PhD Thesis

Investigation of 2D hybrid nanostructures

MÁTÉ KEDVES

Supervisor Dr. Péter Makk
Associate Professor
Department of Physics

Budapest University of Technology and Economics
2025

Contents

List of abbreviations

2D	Two-dimensional
ABS	Andreev bound state
ALD	atomic layer deposition
BLG	bilayer graphene
CNP	charge neutrality point
CNL	charge neutrality line
CPR	current–phase relation
CϕR	current–flux relation
IP	(band-)inverted phase
JJ	Josephson junction
LL	Landau level
MTJJ	multiterminal Josephson junction
MQT	macroscopic quantum tunneling
PC	polycarbonate
PDMS	polydimethylsiloxane
RCSJ	resistively and capacitively shunted junction
RIE	reactive ion etching
SCD	switching current distribution
SLG	single-layer graphene
SOC	spin–orbit coupling
SOI	spin–orbit interaction
SQUID	superconducting quantum interference device
TA	thermal activation
TMD	transition metal dichalcogenide
VTI	variable-temperature insert
WAL	weak anti-localization

Chapter 1

Introduction

The semiconductor industry is approaching a limit where Moore's law [1] is becoming increasingly difficult to sustain [2]. Alternative approaches building on the results of quantum mechanics are required to further enhance the functionality of electronic devices. For example, recent years have seen a surge in encouraging achievements in the field of quantum computation. Most notably, the quantum advantage over classical computers for specific problems was demonstrated using superconducting [3, 4] and photonic [5] quantum computers. Superconducting qubits are among the most promising platforms to create scalable and programmable quantum computers capable of solving practical problems. Furthermore, superconducting hybrid devices are also proposed to host exotic quasiparticles such as Majorana fermions[6–8] that may enable fault-tolerant quantum computing [9]. Majorana fermions are expected to arise if superconducting correlations are induced in the surface states of topological insulators [7].

Graphene has been theoretically predicted as a topological insulator soon after its discovery in 2004 [10]. However, the experimental observation of this exotic phase in graphene has remained elusive due to its very weak intrinsic spin–orbit coupling (SOC) [11]. On the other hand, the family of two-dimensional (2D) materials has grown rapidly over the last two decades, making it possible to tailor the physical porperties of graphene by creating van der Waals heterostructures that combine graphene and other 2D materials. For example, by bringing graphene in close proximity to transition metal dichalcogenides (TMDs) in such heterostructures, a large SOC can be induced in graphene [12]. This, on the one hand, gave a significant boost to the field of spintronics. The combination of the large spin diffusion length in graphene [13–15] and the ability to manipulate spins by electric fields [16–18] are key elements to realize information storage and logic devices that utilize the spins of electrons [19]. On the other hand, this so-called proximity-induced SOC has opened new possibilities to engineer topological phases in graphene [20–22], leading to the experimental observation of a peculiar band-inverted phase hosting helical edge states in bilayer graphene [23, 24]. Furthermore, the induced SOC can also have a strong effect on the correlated states observed in twisted structures [25–27].

In this thesis, I set out to explore the nature and size of induced SOC in graphene/TMD heterostructures, to boost its strength and to incorporate such heterostructures in superconducting circuits. I present the fabrication of van der Waals heterostructures based on graphene and TMDs that allow the investigation of the proximity-induced SOC. Low-temperature transport measurements are used to determine the type and strength of the induced SOC and reveal a large spin-relaxation anisotropy in these heterostructures[28]. Hydrostatic pressure can be used to squeeze the layers of van der Waals heterostructures [29]. By reducing the layer distances, the strength of the induced SOC can be significantly enhanced [30]. The hydrostatic pressure is applied in a pressure cell where kerosene acts as the pressure mediating medium. A measurement in this thesis shows that the electronic quality of graphene is preserved by encapsulating graphene in hexagonal boron nitride (hBN). Furthermore, I also present that the proximity-induced SOC can be enhanced by hydrostatic pressure in a bilayer graphene/TMD

heterostructure and the band-inverted phase can be extended as a result [31]. Furthermore, the effect of SOC on superconductivity in graphene/TMD heterostructures is studied. Josephson junctions are formed by fabricating superconducting electrodes on the heterostructures. SOC is expected to manifest as a phase shift in the current–phase relation (CPR) of the Josephson junctions. For this reason, CPR measurements are presented on graphene/TMD Josephson junctions. Recently, multiterminal Josephson junctions (MTJJs) were proposed theoretically as a platform to artificially engineer topologically non-trivial band structures [32]. Therefore, fabricating multiple superconducting terminals provides an alternative to SOC to engineer topological phases in Josephson junctions. In this thesis, transport measurements on a graphene-based MTJJ are presented. The results are compared to simulations based on a resistively shunted Josephson junction network model. It is shown that self-heating effects have to be considered in the simulation to reproduce the main features of the measurements [33].

The structure of the thesis is the following. The theoretical concepts necessary for understanding this thesis are briefly summarized in Chapter 2. Chapter 3 presents the experimental techniques used throughout this work. These include the fabrication of van der Waals heterostructures and details of the low-temperature transport measurements. In Chapter 4, I present the key results from the investigation of proximity-induced SOC in single-layer graphene/TMD heterostructures that were enabled by the devices I fabricated. I also briefly discuss the measurement showing that hBN can efficiently protect graphene from the kerosene environment in pressure cells, for which I provided the measured device. Furthermore, I summarize the measurements showing that our pressure cell can be used to apply hydrostatic pressure to van der Waals heterostructures and increase the proximity-induced SOC. Building on these results, in Chapter 5, I present the investigation of the inverted-gap phase in a bilayer graphene/TMD heterostructure under hydrostatic pressure. Chapter 6 details the CPR measurements on Josephson junctions based on graphene/TMD heterostructures. In Chapter 7, I discuss the transport measurements on graphene-based MTJJs and the simulation method incorporating self-heating effects. Finally, in Chapter 8, I summarize these findings.

Chapter 2

Theoretical background

2.1 Graphene and 2D materials

Layered materials consist of 2D atomic or molecular sheets with strong in-plane bonds that are weakly coupled by van der Waals forces in the out-of-plane direction. This fundamental property makes it possible to isolate a few or even single-layers from bulk crystals and investigate them in their ultimate thinness limit. Although graphene, the 2D equivalent of graphite, was the first example discovered in 2004 [34–36], the number of 2D materials has increased rapidly over the past two decades. Along with this, the functionality of these materials has also seen a significant broadening. Without claim of completeness, the types of 2D materials include semimetals, metals, insulators, semiconductors, superconductors, magnetic materials and topological insulators [37, 38].

From the point of view of this work, the most important 2D materials are graphene, hexagonal boron nitride (hBN) and transition metal dichalcogenides (TMDs). As mentioned, graphene is the first example of 2D materials. It is a semimetal with exceptional electronic qualities [39]. State-of-the-art graphene devices can have charge carrier mobilites of $\sim 10^6\,\mathrm{cm}^2/\mathrm{Vs}$, matched only by 2D electron gas (2DEG) devices. As a result of high device quality, quantum effects become more easily accessible, demonstrated by the room-temperature observation of the quantum Hall effect [40]. A review of the numerous quantum effects available in graphene can be found in Reference [41]. A key element to obtain large charge carrier mobilities is the encapsulation of graphene in hBN [42, 43] which is a 2D insulator with a crystal structure very similar to graphite. The benefits of using hBN as a substrate for graphene devices is discussed in detail in Section 3.1. Finally, TMDs are layered semiconducting materials with a typical band gap of 1-2 eV. The unit cell of these materials contains one transition metal atom (such as W or Mo) and two chalcogen atoms (e.g. S, Se or Te). More importantly, these materials have strong intrinsic spin–orbit coupling which makes them useful for spintronics applications (Section 2.3).

Reducing the dimensionality of such materials opens up several new possibilities. In many cases, the physical properties of these materials depend heavily on the number of layers and can be strikingly different from their bulk counterparts. Two key examples, which will be discussed in more detail later, are the electric field effect (Section 2.4.1) and the tunable band gap in bilayer graphene (Section 2.2.2). Both of these effects become available by reducing the number of layers towards the 2D limit and are not accessible in bulk graphite.

We can improve or change the functionality of 2D layered materials not only by reducing the number of layers but it is also possible by combining different layers in van der Waals heterostructures as presented in Section 3.1. This method provides unprecedented opportunities for band structure engineering. For example, it is possible to take a layer of graphene, place it on top of a TMD layer and the proximity of the TMD layer will induce a large spin–orbit coupling in graphene while the electronic quality of graphene is mostly preserved. In such heterostructures, additional tuning knobs can also be used to control the band structure. By reducing the distance

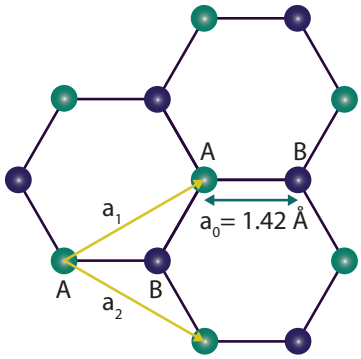

Figure 2.1: Hexagonal lattice structure of single-layer graphene. The lattice vectors are shown in yellow. The unit cell contains two atoms, denoted A and B. The distance between nearest-neighbour atoms is $a_0 = 1.42$ Å, as illustrated by the green arrow.

between the layers, the proximity effect can be enhanced. This can be achieved by applying pressure to such heterostructures as it is discussed in Chapters 4 and 5. Although not covered in this work, it is worth mentioning that the electronic properties of van der Waals heterostructures can also be tuned by applying strain [44–50]. Furthermore, the rotation of the layers can also have a significant effect on the band structure. The most notable examples are the twisted graphene heterostructures where flat bands appear when two graphene layers are rotated by a so-called magic angle [51–58]. The study of twist-angle dependent phenomena is referred to as twistronics.

2.2 Band structure of graphene

2.2.1 single-layer graphene

Graphene is a two-dimensional allotrope of carbon where atoms are arranged in a hexagonal lattice as it is shown in Figure 2.1. The unit cell of the honeycomb lattice contains two carbon atoms, denoted A and B. The lattice vectors $\mathbf{a}_1$ and $\mathbf{a}_2$ can be expressed in real space using the inter-atomic distance $a_0 = 1.42$ Å:

$$\mathbf{a}_1 = \frac{a_0}{2}\begin{pmatrix} 3 \\ \sqrt{3} \end{pmatrix} \qquad \text{and} \qquad \mathbf{a}_2 = \frac{a_0}{2}\begin{pmatrix} 3 \\ -\sqrt{3} \end{pmatrix} \tag{2.1}$$

A free carbon atom has the electronic configuration of $1s^2 2s^2 2p^2$ with a total of six electrons. However, in graphene three of the four valence electrons occupy sp^2 hybrid orbitals while the remaining electron occupies the p_z orbital. The sp^2 electrons form strong σ-bonds localized in the plane of the atoms while the p_z electrons form delocalized π-bonds. The $1s^2$ core electrons do not contribute to chemical bonds.

Although graphene was discovered in 2004, it had already been investigated theoretically in 1947 [59] as a stepping stone to understand the electronic properties of graphite. The electronic band structure of p_z electrons in single-layer graphene (SLG) can be calculated in a tight-binding approximation [59, 60]. Considering only nearest neighbour hopping, this yields:

$$E_{\pm}(\mathbf{q}) = \pm t\sqrt{3 + 2\cos\left(\sqrt{3}q_y a_0\right) + 4\cos\left(\frac{3}{2}q_x a_0\right)\cos\left(\frac{\sqrt{3}}{2}q_y a_0\right)}, \tag{2.2}$$

where $\mathbf{q}$ is the wavenumber vector and $t = 2.61$ eV [61] is the nearest neighbour hopping parameter. This band structure is shown in Figure 2.2.(a) for the first, hexagon-shaped, Brillouin

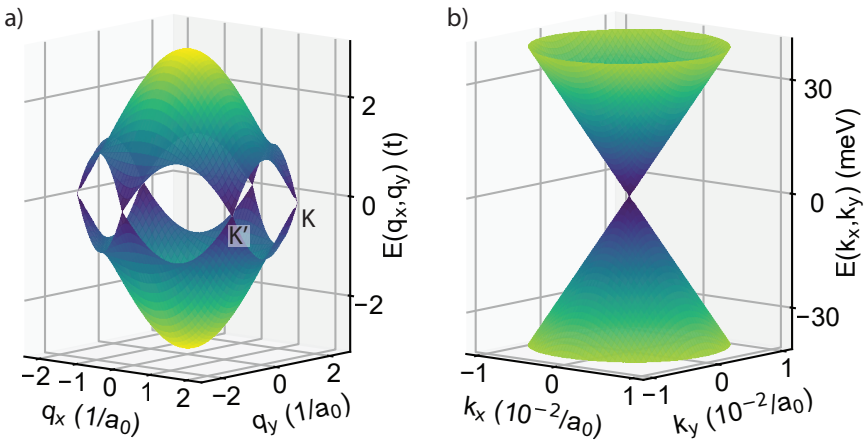

Figure 2.2: a) Band structure of SLG in the first Brillouin zone obtained from tight binding calculation using only nearest neighbour hopping. The valence and conduction bands touch at the corners of the hexagonal Brillouin zone. b) Low-energy part of the band structure around the **K** valley with $t = 2.8$ eV as a function of the quasi-momentum **k** measured from the **K** point.

zone. SLG is a semimetal since the valence and conduction bands touch at the so-called Dirac points in the corners of the Brillouin zone, also referred to as valleys, and the p_z electrons fill the valence band. Two of these valleys are denoted with **K** and **K'** in Figure 2.2.(a). Their positions in the momentum space can be given by:

$$\boldsymbol{K} = \frac{2\pi}{3\sqrt{3}a_0}\begin{pmatrix}\sqrt{3}\\1\end{pmatrix} \quad \text{and} \quad \boldsymbol{K'} = \frac{2\pi}{3\sqrt{3}a_0}\begin{pmatrix}\sqrt{3}\\-1\end{pmatrix}. \tag{2.3}$$

In most cases, it is enough to consider only the low-energy sector of the band structure. This is shown in the vicinity of the **K** valley in Figure 2.2.(b), highlighting the now-famous Dirac cone of graphene. The dispersion relation in the valleys is linear and isotropic which makes it possible to describe the band structure with a linearized Hamiltonian. Considering two inequivalent valleys and neglecting spin degeneracy, it takes the form of:

$$H_0 = \hbar v_F \left(\kappa k_x \hat{\sigma}_x - k_y \hat{\sigma}_y\right), \tag{2.4}$$

where $\hat{\sigma}_i$ are the Pauli matrices acting on the sublattice space and $\kappa = \pm 1$ stands for the **K** and **K'** valley and we introduced $\mathbf{k} = \mathbf{q} - \mathbf{K}$, the quasi-momentum measured from the **K** and **K'** points. This Hamiltonian is equivalent to the Dirac Hamiltonian that describes massless relativistic particles with the Fermi velocity $v_F \approx 10^6$ m/s substituting the speed of light. For this reason, the **K** and **K'** points are commonly known as Dirac points. In the Dirac points, the dispersion relation can be given simply by:

$$E_{\pm}(\mathbf{k}) = \pm\hbar v_F |\mathbf{k}|. \tag{2.5}$$

The positive solution is referred to as conduction band, whereas the negative as valence band.

2.2.2 Bilayer graphene

Two layers of graphene stacked on top of each other is referred to as bilayer graphene (BLG). In most cases, the crystal structure follows the so-called Bernal stacking, also known as AB stacking, shown in Figure 2.3. The unit cell contains four atoms, A1 and B1 are situated on the lower layer, while A2 and B2 sit on the upper layer. The B1 and A2 atoms are aligned vertically, these are called dimer atoms, while A1 and B2 are referred to as non-dimer atoms. The distance between the two layers in pristine BLG is $d = 3.3$ Å.

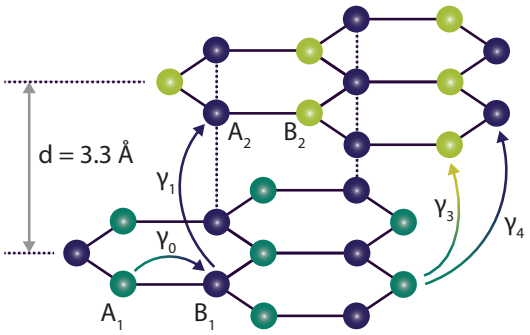

Figure 2.3: Lattice structure of Bernal-stacked bilayer graphene. The A_2 atoms of the upper layer are located above the B_1 atoms of the lower layer. The distance between the layers in pristine BLG is $d = 3.3\,\text{Å}$. The relevant hopping parameters are also indicated by γ_i and the corresponding arrows.

Similarly to SLG, it is possible to construct a linearized tight-binding Hamiltonian to describe the low-energy band structure for BLG, as well. In the basis of the 4 atom unit cell, $(|C_{\text{A1}}\rangle, |C_{\text{B1}}\rangle, |C_{\text{A2}}\rangle, |C_{\text{B2}}\rangle)$ the Hamiltonian is written as:

$$\mathcal{H}_{\text{BLG}} = \begin{pmatrix} u/2 & v_0\pi^\dagger & -v_4\pi^\dagger & v_3\pi \\ v_0\pi & u/2+\Delta' & \gamma_1 & -v_4\pi^\dagger \\ -v_4\pi & \gamma_1 & -u/2+\Delta' & v_0\pi^\dagger \\ v_3\pi^\dagger & -v_4\pi & v_0\pi & -u/2 \end{pmatrix}. \tag{2.6}$$

Here, we use γ_i, with $i = \{0, 1, 3, 4\}$ to describe the intra- and interlayer hoppings in BLG, as illustrated in Figure 2.3. γ_0 is the nearest neighbour intralayer hopping, γ_1 is the interlayer hopping between the dimer sites, γ_3 describes the hopping between the non-dimer sites and γ_4 is the interlayer hopping between the dimer and non-dimer orbitals. $v_i = \sqrt{3}a\gamma_i/2\hbar$ are effective velocities derived from the hopping parameters, with the lattice constant of the graphene $a = 2.46\,\text{Å}$ and Δ' is the dimer on-site energy. $\pi = \hbar(\xi k_x + ik_y)$ and $\pi^\dagger = \hbar(\xi k_x - ik_y)$ are momentum operators measured from the K and K' valleys with the valley indices $\xi = \pm 1$. The parameter u is the interlayer potential difference modelling the effect of an external electric field. The values available in the literature for the hopping parameters are $\gamma_0 = 2.61\,\text{eV}$, $\gamma_1 = 0.361\,\text{eV}$, $\gamma_3 = 0.283\,\text{eV}$, $\gamma_4 = 0.138\,\text{eV}$ and $\Delta' = 0.015\,\text{eV}$ [61].

To illustrate some of its key features, we calculate[1] the BLG band structure using only the γ_0 and γ_1 hopping terms and compare it with the low-energy band structure of SLG in Figure 2.4. For convenience, the low-energy sector of the SLG band structure is shown again in Figure 2.4.(a) and the BLG band structure is plotted in 2.4.(b). The most obvious conclusion from this comparison is that BLG no longer shows linear dispersion but it features quadratic bands that touch at the Dirac points. Even though the unit cell of BLG contains four atoms, the bands are four-fold degenerate in both cases, due to the valley and spin degrees of freedom, since γ_1 splits the bands originating from the dimer atoms A_2 and B_1 from the low-energy subspace. These are not visible in the energy range shown in Figure 2.4.

As mentioned in Section 2.1, a different number of layers can result in strikingly different functionalities for 2D materials. A prime example for this is the appearance of an electric field-tunable band gap in bilayer graphene [62–64]. When an out-of-plane electric field is applied to BLG, the two layers are placed at different potential energies resulting in an interlayer asymmetry. In Equation 2.6, this is taken into account by the interlayer potential difference u

[1]The Python code used for the band structure calculations of BLG was developed by Bálint Szentpéteri.

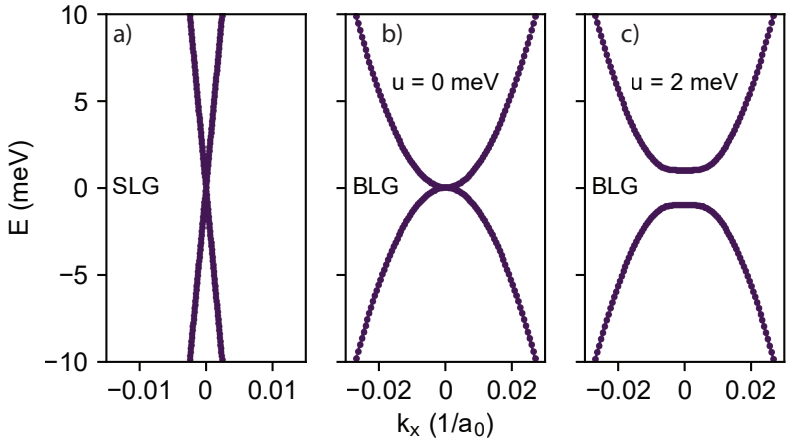

Figure 2.4: a,b) Low-energy band structure of SLG and BLG in the **K** valley as a function of k_x. For the calculation of the BLG band structure only the hopping terms γ_0 and γ_1 were used. c) The opening of a band gap in BLG for $u = 2\,\text{meV}$. The interlayer potential difference can be controlled by a transverse electric field.

and the effect of a finite $u = 2\,\text{meV}$ is demonstrated in Figure 2.4.(c) where the opening of a band gap is clearly visible. This feature is inaccesible in SLG where a transverse electric field does not break the inversion symmetry. The transverse displacement field (D) in the measurements can be converted to the interlayer potential difference using $u = \frac{-ed}{\epsilon_0 \epsilon_{BLG}} D$, where e is the elementary charge, ϵ_0 is the vacuum permittivity, $d = 3.3\,\text{Å}$ is the separation of BLG layers and ϵ_{BLG} is the effective out-of-plane dielectric constant of BLG.

2.3 Spin–orbit coupling in graphene

2.3.1 Spin–orbit coupling basics

Spin–orbit coupling (SOC), or spin–orbit interaction (SOI), is the relativistic effect connecting the spin of a particle to its motion. An electron moving at a speed $\mathbf{v}$ in an external electric field $\mathbf{E}$ experiences an effective magnetic field $\mathbf{B}'$ in its resting frame of reference that is given by the Lorentzian transformation:

$$\mathbf{B}' = -\frac{1}{c^2}\mathbf{v} \times \mathbf{E}. \tag{2.7}$$

Writing this into the Zeeman energy term:

$$H_{SOC} = +g\mu_B \mathbf{S} \cdot \frac{1}{c^2}\mathbf{v} \times \mathbf{E} = \frac{1}{c^2} g\mu_B \mathbf{S} \cdot \frac{\mathbf{p}}{m} \times \mathbf{E}, \tag{2.8}$$

where g is the electron g-factor, $\mu_B = e\hbar/(2m_e)$ is the Bohr-magneton, $\mathbf{S}$ is the spin angular momentum and $\mathbf{p}$ is the momentum. Let us consider a central atomic potential where:

$$\mathbf{E} = \nabla \frac{Ze}{4\pi\varepsilon_0 r} = \frac{\mathbf{r}}{|\mathbf{r}|}\frac{d}{dr}\frac{Ze}{4\pi\varepsilon_0|\mathbf{r}|}. \tag{2.9}$$

Using this in Equation 2.8:

$$H_{SOC} = \frac{1}{c^2} g\mu_B \mathbf{S} \cdot \frac{\mathbf{p}}{m} \times \mathbf{E} \propto \mathbf{S} \cdot (\mathbf{p} \times \mathbf{r}) \propto \mathbf{S} \cdot \mathbf{L}, \tag{2.10}$$

where $\mathbf{L} = (\mathbf{r} \times \mathbf{p})/\hbar$ is the orbital angular momentum. In this case, it is easy to see how the spin and the orbital angular momenta are connected, hence the name spin–orbit interaction can be understood.

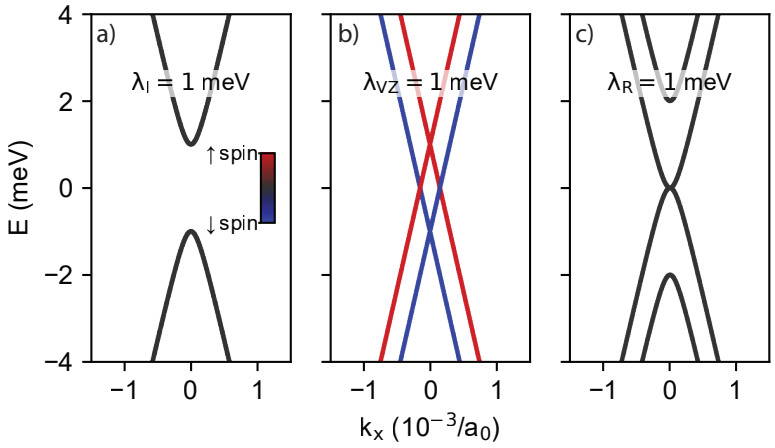

Figure 2.5: Effect of spin–orbit coupling on the low-energy band structure of SLG around the **K** point. The colorscale illustrates the out-of-plane spin polarization of the bands. a) Intrinsic SOC with $\lambda_I = 1\,\text{meV}$. The value of λ_I used here is two orders of magnitude larger than the $12\,\mu\text{eV}$ predicted theoretically [11] to better illustrate the opening of the topological gap. In this case, the bands remain spin and valley degenerate. b) Valley-Zeeman SOC with $\lambda_{VZ} = 1\,\text{meV}$. This SOC term leads to a finite spin-splitting of the bands with opposite sign in the two valleys. c) Rashba SOC with $\lambda_R = 1\,\text{meV}$. The Rashba term leads to the in-plane winding of the spin with no out-of-plane polarization.

In pristine graphene, symmetry allows only one type of spin–orbit coupling [10, 65]. The effective low-energy Hamiltonian of this intrinsic spin–orbit coupling term takes the following form:

$$H_I = \kappa \lambda_I \hat{\sigma}_z \hat{s}_z. \tag{2.11}$$

Here λ_I is the intrinsic spin–orbit strength, $\kappa = \pm 1$ is the usual valley index, while $\hat{\sigma}_z$ and $\hat{s}_z$ are the Pauli matrices acting on the pseudospin and the spin respectively. Combining this with the orbital contributions from Equation 2.4 the low-energy spectrum takes the following form:

$$E_\pm(\mathbf{k}) = \pm\sqrt{\hbar^2 v_F^2 \left(k_x^2 + k_y^2\right) + \lambda_I^2}. \tag{2.12}$$

This intrinsic spin–orbit coupling splits the valence and conduction bands by $2|\lambda_I|$, however, the bands remain spin and valley degenerate. This is illustrated in Figure 2.5.(a) for $\lambda = 1\,\text{meV}$ for better visibility. It is worth noting that the band gap opened by the intrinsic SOC was predicted by Kane and Mele [10] to host a quantum spin Hall state with helical edge states. However, it was found by Gmitra *et al* [11] that the intrinsic SOC strength $\lambda_I \approx 12\,\mu\text{eV}$ is very weak and inaccessible in experiments. On the one hand, this weak SOC allows exceptionally long spin relaxation times in pristine graphene [13–15]. On the other hand, for many spintronic applications, it is desired to have a large spin–orbit coupling to enable manipulation of the electron spins via external electric or magnetic fields. However, other spin–orbit interaction terms are allowed if the symmetry of our system is reduced, which might have a significant impact on the low-energy band structure.

2.3.2 Proximity-induced spin–orbit coupling in single-layer graphene

By combining graphene with other 2D materials that have a large intrinsic spin–orbit coupling, it becomes possible to induce a significant SOC in graphene via the proximity-effect [12, 66–69]. Although other methods have also been proposed to enhance SOC in graphene [19, 60, 70], as mentioned in Section 2.1, TMDs are among the most promising candidates to enable spintronics applications in graphene devices. While TMDs have a large intrinsic SOC,

their low electronic quality results in small spin relaxation lengths that poses severe limitations to their applications. It was found both theoretically [67] and experimentally [12, 69] that graphene/TMD heterostructures make it possible to engineer a large proximity-induced SOC in graphene while preserving its high electronic quality. Among the family of TMD materials, WS_2 [12, 71], MoS_2 [71] and WSe_2 [28, 71] have all been demonstrated to induce a SOC in graphene on the order of $\sim 1 - 10$ meV that is multiple orders of magnitude larger than the intrinsic SOC in pristine SLG.

The induced SOC originates from the hybridization of the graphene and TMD substrate orbitals. The effect of induced SOC on the low-energy band structure can be described by virtual hopping terms [20, 65, 68]. At low energies, neglecting **k**-dependent spin–orbit terms, two relevant SOC terms remain. The Valley-Zeeman term locks spin to valley and introduces a valley-dependent spin-splitting of the bands and the Rashba SOC that originates from the broken inversion symmetry of the heterostructure. The effective Hamiltonians that describe these two SOC terms take the following form [68]:

$$\begin{aligned} H_{VZ} =& \lambda_{VZ} \kappa \hat{\sigma}_0 \hat{s}_z, \\ H_R =& \lambda_R \left(\kappa \hat{\sigma}_x \hat{s}_y - \hat{\sigma}_y \hat{s}_x \right). \end{aligned} \tag{2.13}$$

Here, λ_{VZ} and λ_R are the valley-Zeeman and Rashba spin–orbit strengths, $\kappa = \pm 1$ is the usual valley index and $\hat{\sigma}_i$ and $\hat{s}_i$ are the sublattice and spin Pauli matrices, respectively.

Using these, the low-energy band structure of SLG around the **K** valley in the presence of different SOC terms is illustrated in Figure 2.5. Figure 2.5.(b) shows the spin-splitting of the bands due to the valley-Zeeman SOC term $\lambda_{VZ} = 1\,\text{meV}$. The color corresponds to the out-of-plane spin polarization. It is important to note that this spin-splitting is valley dependent and is opposite in the **K'** valley. Figure 2.5.(c) illustrates the effect of the Rashba SOC with $\lambda_R = 1\,\text{meV}$. This term introduces a finite effective mass in the low-energy band structure. Contrary to the valley-Zeeman term, the Rashba term results in an in-plane spin texture where the spin is perpendicular to the momentum [65, 68].

Finally, two important remarks must be made. First, although the reduced symmetry of the graphene/TMD heterostructure allows the appearance of additional SOC terms, in real devices, the strength and type of proximity-induced SOC show great variation due to sample inhomogeneity. Furthermore, recent theoretical works [72, 73] showed that the strength of induced SOC depends on the relative angle between the graphene and TMD layers. This suggests that heterostructures assembled without controlling the rotation of layers can yield significantly different results even if the device qualities are otherwise similar.

2.3.3 Proximity-induced spin–orbit coupling in bilayer graphene

The proximity-induced SOC in BLG can be treated with the same theoretical tools as in SLG. The relevant SOC terms are again the valley-Zeeman and the Rashba-type SOC terms. Due to historical reasons, the valley-Zeeman term is also referred to as the Ising SOC term and its strength is denoted by λ_I. Although this could cause confusion, since it also labelled the intrinsic SOC in case of SLG, the intrinsic SOC is too small to be experimentally detected and is therefore simply neglected in the following. On the other hand, the larger unit cell and the inequivalence of the two layers add more complexity to the problem. For example, the induced SOC on the two layers can be different if the BLG is encapsulated between two different materials or due to a different rotation angle of the top and bottom TMDs with respect to the BLG layers. This is taken into account by considering different SOC strength parameters for the different layers. In the basis of the 4 atom unit cell, $(|C_{\text{A1}}\rangle, |C_{\text{B1}}\rangle, |C_{\text{A2}}\rangle, |C_{\text{B2}}\rangle) \otimes (|\uparrow\rangle, |\downarrow\rangle)$

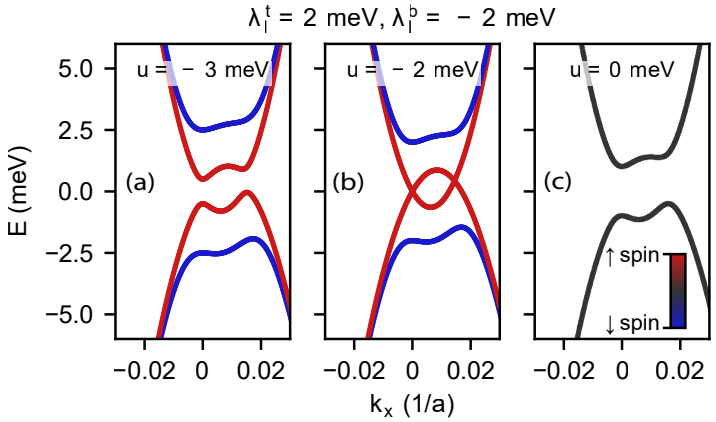

Figure 2.6: a-c) Calculated band structure around the **K**-point for different values of the interlayer potential difference u. Color scale corresponds to the spin polarization of the bands.

the SOC Hamiltonian is written as

$$\mathcal{H}_{\text{SOC}} = \begin{pmatrix} \xi\lambda_I^b s_z/2 & i\lambda_R^b s_-^\xi & 0 & 0 \\ -i\lambda_R^b s_+^\xi & \xi\lambda_I^b s_z/2 & 0 & 0 \\ 0 & 0 & \xi\lambda_I^t s_z/2 & i\lambda_R^t s_-^\xi \\ 0 & 0 & -i\lambda_R^t s_+^\xi & \xi\lambda_I^t s_z/2 \end{pmatrix}, \tag{2.14}$$

where λ_I^t and λ_I^b are the Ising-type SOC strengths on the top and bottom layers, respectively, and the Rashba-type SOC parametrized similarly with λ_R^t and λ_R^b [66, 74]. Here, as before, s_i, with $i = \{0, x, y, z\}$, are the spin Pauli matrices and $s_\pm^\xi = \frac{1}{2}(s_x \pm i\xi s_y)$ with $\xi = \pm 1$ being the valley index.

Combining $\mathcal{H}_{\text{SOC}}$ with $\mathcal{H}_{\text{BLG}}$ from Equation 2.6, the low-energy spectrum of BLG in the presence of arbitrary SOC strengths can be calculated, as it is discussed in detail in Reference [66]. The relative complexity of this system results in many interesting phenomena. From a practical point of view, it is worth mentioning that Gmitra *et al.* predicted that BLG proximitised by WSe_2 could be used as a spin transistor [75]. More importantly from the aspect of this work, Island *et al.* experimentally showed that a band-inverted phase can arise in BLG proximitised by WSe_2 from both sides if the induced Ising SOC strength for the two layers has opposite sign [23].

To reveal this band-inverted phase arising from the Ising SOC in BLG, we show the low-energy band structure of WSe_2/BLG/WSe_2 in Figure 2.6, calculated using $\mathcal{H}_{\text{BLG}}$ and $\mathcal{H}_{\text{SOC}}$. The effect of the WSe_2 layers in proximity of BLG can be described by the Ising SOC terms λ_I^t and λ_I^b that couple only to the closer-lying layer of BLG and act as a valley-dependent effective magnetic field. For WSe_2 layers aligned to the BLG layers, the induced SOC couplings will have opposite sign for the top and bottom layers [73, 74, 76]. This is taken into account by the opposite sign of λ_I^t and λ_I^b.

Figure 2.6.a-c show the calculated band structure around the **K**-point for different values of the interlayer potential difference u, using the parameter values $\lambda_I^t = -\lambda_I^b = 2\,\text{meV}$. First of all, for $|u| > |\lambda_I^t| = |\lambda_I^b|$, we can see the opening of a band gap (Figure 2.6.a), as expected for BLG in a transverse displacement field. On the other hand, as opposed to pristine BLG, the bands are spin-split and the direction of this spin-splitting is opposite for the valence and conduction bands. This is a direct consequence of the opposite sign of λ_I^t and λ_I^b as the valence and conduction bands are localised on different layers due to the large u. The band structure in the **K'**-valley is similar, except that the spin-splittings are reversed due to time-reversal symmetry. For $|u| = |\lambda_I^{t,b}|$ (Figure 2.6.b), the u-induced band gap approximately equals the spin-splitting induced by the Ising SOC and the bands touch. Finally, for $|u| < |\lambda_I^{t,b}|$ (Figure 2.6.c), a band

gap re-opens and we observe spin-degenerate bands for $u = 0$, separated by a gap comparable in size to the Ising SOC terms $\left(\Delta \approx \left|\lambda_I^t - \lambda_I^b\right|/2\right)$. This gapped phase is distinct from the band insulating phase at large u in that the valence and conduction bands are no longer layer polarized, hence it is referred to as the inverted phase (IP). It is worth mentioning that the IP at $|u| < \left|\lambda_I^t\right|$ is topologically different from the trivial band insulating phase. Theoretical [21, 22] and experimental [23, 24] works suggest that the IP hosts helical edge modes.

2.4 Electronic transport in graphene

2.4.1 Electric field effect

It was discovered early-on that graphene exhibits a strong electric field effect [34] that allows the tuning of charge carrier concentration by external gate voltages. This can be understood in a simple planar capacitor model which can be applied to many graphene-based Van der Waals (vdW) heterostructures. A finite voltage difference between the graphene layer and the gate electrode will induce a charge carrier density proportional to the gate capacitance:

$$C = \varepsilon_0 \varepsilon_r \frac{A}{d}, \tag{2.15}$$

where ε_0 is the vacuum permittivity, ε_r is the relative permittivity of the dielectric of thickness d placed between the graphene layer and the gate electrode of area A. From this, the induced charge carrier density as a function of the gate voltage:

$$n = \frac{C}{eA} V_g = \frac{\varepsilon_0 \varepsilon_r}{ed} V_g, \tag{2.16}$$

where e is the electron charge and V_g is the gate voltage.

In a diffusive Drude picture, conductivity can be written as:

$$\sigma = ne\mu = \frac{ne^2 \tau_p}{m}, \tag{2.17}$$

where n is the charge carrier density, μ is charge carrier mobility and τ_p is momentum relaxation time. In graphene, this equation can be brought to the following form:

$$\sigma = \frac{e^2 v_F \tau_p \sqrt{n}}{\hbar \sqrt{\pi}}, \tag{2.18}$$

where we used that $m = \hbar k_F / v_F$ due to the linear dispersion relation and that in two dimensions $k = \sqrt{n\pi}$.

In transport measurements, usually, the conductance G is measured, from which the conductivity can easily be calculated using the geometric factors of the sample. This allows us to obtain basic information about the quality of the sample by extracting the field-effect mobility:

$$\mu = \frac{l}{we} \frac{dG}{dn}, \tag{2.19}$$

where l and w are the length and width of the sample, respectively.

It is also worth mentioning that, even though graphene is a semimetal with zero band gap where electron and hole conduction are both achievable, in a real device it is impossible to set the chemical potential exactly to the Dirac point, also referred to as charge neutrality point (CNP), due to ever-present potential fluctuations. This means that below a certain doping level, the device breaks up into electron and hole regions, commonly referred to as puddles. Therefore, another way to characterize sample quality is to determine the residual doping n^*, which is the lowest homogeneous doping level achievable in the sample.

Considering BLG, the situation becomes slightly more complex. While it is possible to tune the charge carrier density with a single gate electrode as previously presented, it is evident that it will also induce a potential difference between the two graphene layers that eventually opens a gap in the band structure. However, by introducing a second gate electrode to the system, it is possible to control the charge carrier density and the transverse electric field separately. This can easily be realized in a planar system where the bilayer graphene is isolated from a top and a bottom gate electrode by a dielectric as in Reference [77] and [78]. Here, the charge carrier density and the transverse electric field can be calculated by extending the previous planar capacitor model. For this we have to solve the following set of equations:

$$n = \frac{\epsilon_0 \epsilon_b}{e} \cdot \frac{V_b - V_{b0}}{d_b} + \frac{\epsilon_0 \epsilon_t}{e} \cdot \frac{V_t - V_{t0}}{d_t} \tag{2.20}$$

$$E = \frac{V_b - V_{b0}}{d_b} - \frac{V_t - V_{t0}}{d_t}, \tag{2.21}$$

where the index b (t) labels quantities describing the bottom (top) gate electrode, while V_{t0} and V_{b0} account for the shift of the Dirac point due to contaminants in the sample or electric fields built into the structure. From this, one can express the gate voltages at a given charge carrier density and electric field:

$$V_b = V_{b0} + n\left(\frac{d_b}{\alpha_b d_b + \alpha_t d_t}\right) + E\left(\frac{\alpha_t d_b d_t}{\alpha_b d_b + \alpha_t d_t}\right) \tag{2.22}$$

$$V_t = V_{t0} + n\left(\frac{d_t}{\alpha_b d_b + \alpha_t d_t}\right) - E\left(\frac{\alpha_b d_b d_t}{\alpha_b d_b + \alpha_t d_t}\right), \tag{2.23}$$

where we introduced the lever arm $\alpha = \varepsilon_0 \varepsilon_r / (de)$ for each gate electrode.

2.4.2 Weak antilocalisation

In diffusive systems, charge carrier trajectories in a conductor can form closed loops due to a series of scattering events, as it is illustrated in Figure 2.7. In a system with time-reversal symmetry, such a loop and its time-reversed pair will interfere with each other. Let us denote the complex quantum mechanical amplitudes of these paths by A^+ and A^- for a given loop and its time-reversed path, respectively. Now if we calculate the probability of the particle returning to its starting point it reads:

$$P_{qm} = |A^+ + A^-|^2 = |A^+|^2 + |A^-|^2 + A^{+*}A^- + A^+ A^{-*}. \tag{2.24}$$

Since time-reversal symmetry requires that $A^+ = A^- = A$, the above expression simply gives us $P_{qm} = 4A^2 = 2P_{cl}$ which means that the probability of backscattering in a quantum mechanical treatment is twice the probability P_{cl} calculated in a classical picture without taking into account the interference terms. This phenomenon is called weak localization, which eventually results in an increase in resistance compared to the classical case.

By applying an external magnetic field perpendicular to the plane of the conductor, time-reversal symmetry can be broken. Charge carriers moving around the loop in opposite directions will pick up an Aharonov-Bohm phase Φ_{AB} of opposite sign and the quantum mechanical amplitudes will be $A^\pm = Ae^{\pm i\Phi_{AB}}$. As a consequence, the interference condition at the starting point will also depend on the applied magnetic field:

$$P_{qm} = 2A^2 + 2A^2 \cos\left(2eSB/\hbar\right), \tag{2.25}$$

where B is the applied out-of-plane magnetic field and S is the area enclosed by the loops. Since many loops with different areas contribute to the conductance, the interference terms will

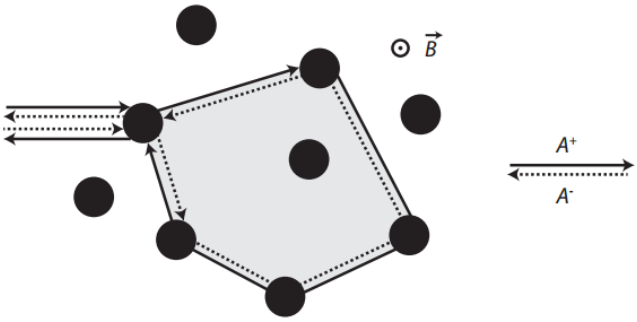

Figure 2.7: Charge carriers in a diffusive picture can form closed loops after several scattering events. In case of time-reversal symmetry, a loop and its time-reversed path can interfere constructively, resulting in an enhanced back-scattering. Figure adapted from Reference [79].

average out at larger magnetic fields. This means that weak localization results in a dip in the magneto-conductance at zero magnetic field.

On the other hand, in the presence of strong spin–orbit coupling, the spin of the electron on such a pair of trajectories rotates in opposite direction during the scattering process. Even though the final spin states are random, on average this will result in a destructive interference and thus in a decreased resistance compared to the classical case [80]. This phenomenon is called weak antilocalization (WAL).

In this work, WAL is employed as an experimental tool to obtain the spin-orbit strengths in SLG as shown in Chapter 4. In the case of single-layer graphene, the quantum correction to the magneto conductivity $\Delta\sigma$ in the presence of strong SOC is given by:

$$\begin{aligned}\Delta\sigma(B) = -\frac{e^2}{2\pi h}\Bigg[F\left(\frac{\tau_B^{-1}}{\tau_\phi^{-1}}\right) - F\left(\frac{\tau_B^{-1}}{\tau_\phi^{-1}+2\tau_{asy}^{-1}}\right) \\ -2F\left(\frac{\tau_B^{-1}}{\tau_\phi^{-1}+\tau_{asy}^{-1}+\tau_{sym}^{-1}}\right)\Bigg],\end{aligned} \tag{2.26}$$

where $F(x) = \ln(x) + \Psi(1/2 + 1/x)$, with $\Psi(x)$ being the digamma function, $\tau_B^{-1} = 4eDB/\hbar$, where D is the diffusion constant, τ_ϕ is the phase coherence time, τ_{asy} is the spin–orbit scattering time due to SOC terms that are asymmetric upon z/-z inversion (H_R) and τ_{sym} is the spin–orbit scattering time due to SOC terms that are symmetric upon z/-z inversion (H_I, H_{VZ}). The total spin–orbit scattering time is given by the sum of the asymmetric and symmetric rate $\tau_{SO}^{-1} = \tau_{asy}^{-1} + \tau_{sym}^{-1}$. In general, Equation 2.26 is only valid if the intervalley scattering rate τ_{iv}^{-1} is much larger than the dephasing rate τ_ϕ^{-1} and the rates due to spin–orbit scattering τ_{asy}^{-1}, τ_{sym}^{-1} [79].

To relate the spin–orbit scattering times to spin–orbit strengths, different spin relaxation mechanisms have to be discussed briefly. Theoretical works [81, 82] showed that the intrinsic and the Rashba SOC relax spins via the Elliot-Yafett mechanism. In this case, scattering events can result in spin-flips due to the presence of SOC. As a consequence, the spin lifetime scales linearly with the momentum scattering time:

$$\tau_s = \frac{\tau_p}{\alpha}, \tag{2.27}$$

where α is a proportionality constant specific to the given type of SOC. For the experimentally relevant Rashba SOC it is given by:

$$\alpha_R = \left(\frac{4\lambda_R}{E_F}\right)^2, \tag{2.28}$$

where E_F is the Fermi energy. Therefore, in principle, Equation 2.27 allows to determine λ_R from the asymmetric spin relaxation time τ_{asy} obtained from magneto conductance measurements.

On the other hand, the Dyakonov-Perel spin relaxation mechanism [83] originates from spin precession between scattering events due to the effective spin-orbit field. Contrary to the Eliott-Yafett mechanism, here, the spin lifetime is inversely proportional to the momentum scattering time, since scattering randomizes the direction of the spin–orbit field and leads to longer spin lifetimes. For the Rashba SOC, the spin relaxation time due to the Dyakonov-Perel mechanism is given by [79]:

$$\tau_s = \left(\frac{\hbar}{2\lambda_R}\right)^2 \tau_p^{-1}. \tag{2.29}$$

Furthermore, it was shown [84] that the valley-Zeeman SOC can also lead to a spin relaxation via the Dyakonov-Perel mechanism. However, in this case intervalley scattering is needed to randomize the spin–orbit field direction and the above expression is modified:

$$\tau_s = \left(\frac{\hbar}{2\lambda_{VZ}}\right)^2 \tau_{iv}^{-1}, \tag{2.30}$$

where τ_{iv} is the intervalley scattering time.

2.4.3 Quantum Hall effect

It is well known that charge carriers moving in a magnetic field experience a Lorentz force according to $\mathbf{F}_L = q\mathbf{v} \times \mathbf{B}$. As a consequence, if we apply a perpendicular magnetic field to a two-dimensional conductor in which a current I is flowing in a given direction, a transverse electric field will appear perpendicular to the direction of the current and the applied magnetic field. This phenomenon is called the classical Hall effect, in which the Hall voltage related to the above electric field can be given by $V_H = IB/(en)$ and the Hall resistance is $R_{xy} = B/(ne)$.

In a quantum mechanical picture, let us consider the problem of a free electron in a magnetic field with the Hamiltonian:

$$H(\mathbf{p}, \mathbf{r}) = \frac{1}{2m} \left[\mathbf{p} + e\mathbf{A}(\mathbf{r})\right]^2, \tag{2.31}$$

where in Landau gauge the vector potential is $\mathbf{A}$=(0,Bx,0) with $\mathbf{B}$=rot$\mathbf{A}$. By introducing the cyclotron frequency $\omega_c = eB/m$ this can be written in the following form:

$$H(\mathbf{p}, \mathbf{r}) = \frac{1}{2m} \left[p_x^2 + (p_y + m\omega_c x)^2 + p_z^2\right]^2. \tag{2.32}$$

By solving the Schrödinger equation with this Hamiltonian one can easily find that the $x - y$ and z directions decouple and the solution to the former part can be described by a simple harmonic oscillator. The energy eigenvalues will then look like:

$$E_N = \frac{\hbar^2 k_z^2}{2m} + \hbar\omega_c \left(N + \frac{1}{2}\right), \tag{2.33}$$

where $N = 0, 1, 2...$ and k_z is the out-of-plane wavenumber. Therefore, in a two-dimensional system, e.g. a 2D electron gas, where one can omit the term describing the z-direction due to confinement, the energy spectrum will consist of equidistant energy levels, commonly known as Landau levels (LLs).

The appearance of Landau levels has a significant impact on transport properties. In a finite sample at large magnetic field the longitudinal resistance R_{xx} becomes zero, while the Hall resistance R_{xy} becomes quantized at values of $h/(e^2\nu)$ with $\nu = 2, 4, 6, ...$ being a positive integer. This can be understood in a simple picture where the confining potential of the sample causes the LLs to bend upwards (or downwards for holes, see Figure 2.8.a) at the edges of the sample leading to the formation of edge channels. Charge carriers on these edge channels

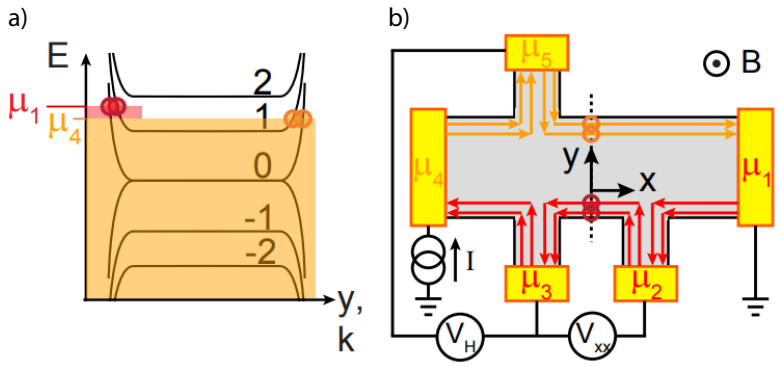

Figure 2.8: a) Landau level structure including the chemical potentials of electrodes 1 and 4 of the setup in b): a Hall-bar geometry at filling $\nu = 6$, with current injected in contact 4 and grounded in 1, and voltmeters between two pairs of floating contacts. Due to LL bending, propagating states (red and orange arrows) are formed at the edges, where the chemical potentials intersect - in this example - the 0th and 1st LLs, as highlighted by red and orange circles. Because of the Landau gap, edge states are spatially separated by insulating regions. Figure adapted from Reference [85].

move in one direction and there is no scattering between channels of opposite directions due to the large spatial separation which results in no backscattering and eventually zero longitudinal resistance (e.g. between contacts 2 and 3 in Figure 2.8.b).

It is worth noting that this quantum mechanical picture is only valid if the electrons can move several times around the cyclotron orbital between two elastic scattering events when $\hbar\omega_c \gg \hbar/\tau_e$. From this, the relation $B \gg 1/\mu$ can be approximately derived which gives us a practical tool to estimate charge carrier mobility from the magnetic field strength at which quantum oscillations in the conductivity are visible. Furthermore, it is also required that the thermal energy $k_B T$, with k_B being the Boltzmann constant, should be negligible compared to the energy spacing of the LLs.

The LLs in single-layer graphene can be obtained by solving the Dirac equation in a perpendicular magnetic field. The energy eigenvalues are the following:

$$E_N = \mathrm{sgn}(N) v_F \sqrt{2e\hbar B|N|}. \tag{2.34}$$

From this, it is easy to see that the lowest LL is at zero energy being half filled by electrons and half filled by holes. Furthermore, the square-root dependence on N results in non-equidistant level spacing. The transverse conductivity takes the form:

$$\sigma_{xy} = \frac{4e^2}{h}(N + \frac{1}{2}), \tag{2.35}$$

where the factor of 4 comes from the valley and spin degeneracy of the conducting channels (Figure 2.9.(a)). At higher magnetic field values, due to the Zeeman effect and electron-electron interactions [86, 87], the spin and valley degeneracy can be lifted and quantized conductance at all integer values of e^2/h can be observed.

Since the charge carriers in bilayer graphene are massive, the Landau level spacing is equidistant and described by [88]:

$$E_N = \pm\hbar\omega_c \sqrt{N(N-1)}. \tag{2.36}$$

From this, it is trivial that the LLs $N = 0$ and $N = 1$ both lie at zero energy which leads to an eight-fold degeneracy, while the other Landau levels are four-fold degenerate. As in single-layer

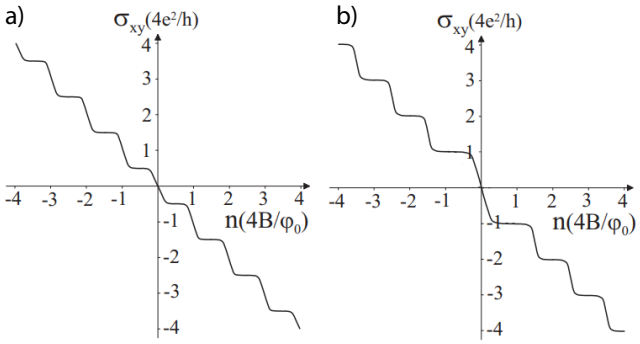

Figure 2.9: Schematic of the dependence of the Hall conductivity σ_{xy} on carrier density n for (a) single-layer graphene and (b) bilayer graphene, where $\varphi_0 = h/e$ is the flux quantum and B is the magnetic field strength. Figure adapted from Reference [89].

graphene, this Landau level is half-filled by holes and half-filled by electrons. For $N \in \mathbb{Z}$, the transverse conductance is given by:

$$\sigma_{xy} = \frac{4e^2}{h} N \tag{2.37}$$

2.5 Superconducting phenomena

Superconductivity was discovered as early as 1911 by H. Kammerlingh Onnes when he measured the temperature dependence of different materials in liqiud helium environment [90]. It is the peculiar phase of matter that is characterized by perfect conductivity and perfect diamagnetism (Meissner–Ochsenfeld effect [91]).

The microscopic theory of conventional superconductors was developed by Bardeen, Cooper and Schrieffer (BCS theory). The basic idea of the theory is that the Fermi-sea of electrons is unstable against the formation of bound electron pairs in the presence of an attractive interaction. Therefore, the result of an effective attraction due to electron-phonon interaction is the formation of Cooper pairs — electron pairs with opposite momenta and spins [92]. From a phenomenological aspect, a superconductor is described by a complex order parameter $\Delta = |\Delta| e^{i\varphi}$, with its absolute value equal to the superconducting gap or, in other words, the binding energy of the Cooper pairs.

2.5.1 Josephson effect

The Josephson effect occurs in so-called Josephson junctions (JJs) where two superconducting leads are connected by a weak link. What Josephson predicted in his original work [93] is that in a superconductor-insulator-superconductor (SIS) tunnel junction a zero voltage supercurrent I_S can flow without voltage drop between the two superconducting electrodes:

$$I_s = I_c \sin(\varphi), \tag{2.38}$$

where I_c is the critical current, the maximum supercurrent that the junction can sustain, and φ is the phase difference of the order parameter in the two leads. This phenomenon is known as the DC Josephson effect. It is common to refer to Equation 2.38 as the current–phase relation (CPR). Furthermore, the voltage V over the junction and the time evolution of the phase difference are also connected by the second Josephson equation:

$$\frac{d\varphi}{dt} = \frac{2eV}{\hbar}. \tag{2.39}$$

This implies that if a DC voltage is applied to the junction, an AC current of frequency $2eV/\hbar$ will flow, also known as the AC Josephson effect. Equations 2.38 and 2.39 are commonly referred to as the first and second Josephson equations, respectively.

Let us consider a magnetic field B applied perpendicular to the plane of the Josephson junction (Figure 2.10). This magnetic field induces a relative phase shift between different supercurrent trajectories which interfere at the contacts and generate an interference pattern that is related to the Fourier transform of the spatial distribution of the supercurrent in the sample.

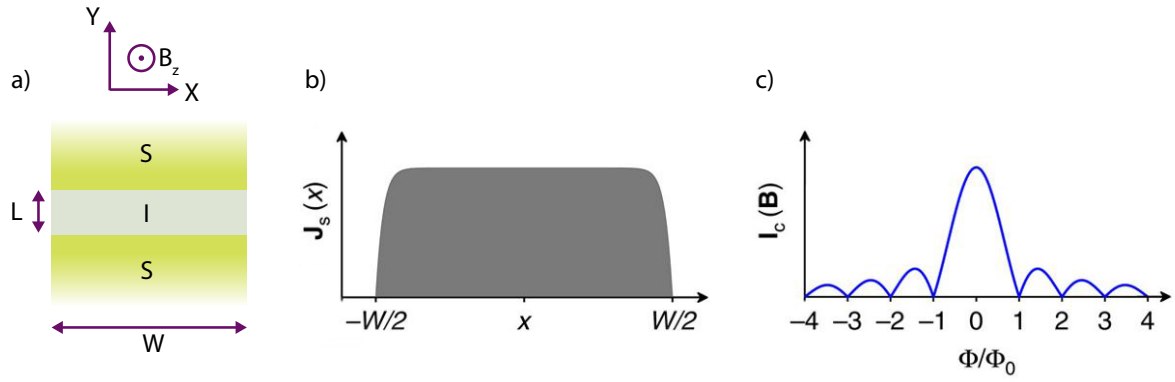

Figure 2.10: a) Schematics of an SIS Josephson junction. In a Josephson interferometry measurement the critical current is measured as a function of the magnetic field applied perpendicular to the plane of the sample. b) For homogeneous distribution of the supercurrent density the resulting pattern is c) the well-known Fraunhofer diffraction pattern. Panels b) and c) adapted from Reference [94]

To be more quantitative, let us consider an ideal junction with sinusoidal CPR, assuming the device size in the plane perpendicular to the field is much larger than the magnetic penetration depth:

$$j_s(x) = j(x)\sin(\varphi(x)), \tag{2.40}$$

where j is the maximum supercurrent density. The relative phase shift between two supercurrent path depends on their enclosed area. Assuming that the Josephson supercurrent does not screen the field within the junction, i.e. the Josephson penetration depth is much larger than the JJ, this means that the superconducting phase at a given position x can be written as:

$$\varphi(x) = \varphi_0 + \frac{2\pi\Phi(x)}{\Phi_0}, \tag{2.41}$$

where $\varphi_0 = \varphi(x=0)$ is a reference phase, $\Phi_0 = h/2e$ is the superconducting flux quantum and $\Phi(x) = B \cdot S(x)$ is the magnetic flux with $S(x) = L \cdot x$ being the area enclosed. From this, the total supercurrent can be given as:

$$J_s(\beta, \varphi_0) = \int_{-W/2}^{W/2} dx j(x)\sin(\varphi_0 + \beta x), \tag{2.42}$$

where $\beta = 2\pi BL/\Phi_0$. Using that j can be written as the sum of an odd j_o and even j_e part, this can be further expressed as:

$$J_s(\beta, \varphi_0) = \sin(\varphi_0)\int_{-W/2}^{W/2} dx j_e(x)e^{i\beta x} - i\cos(\varphi_0)\int_{-W/2}^{W/2} dx j_o(x)e^{i\beta x} \tag{2.43}$$

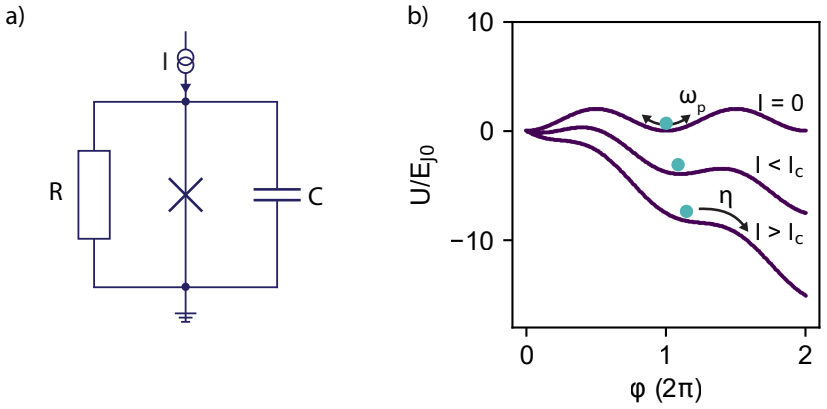

Figure 2.11: a) Equivalent circuit for a realistic Josephson junction consisting of (from left to right) a normal resistance, an ideal JJ and a shunt capacitor. b) Analogy between the phase of the Josephson junction and the motion of a massive particle in the tilted washboard potential.

Assuming an even current distribution, the maximum supercurrent J_c can be given by the Fourier transform of j_e:

$$J_c(\beta) = \int_{-W/2}^{W/2} dx j_e(x) e^{i\beta x}. \tag{2.44}$$

However, measurements can only reveal the absolute value of J_c, such that:

$$I_c(\beta) = |J_c(\beta)| = \left| \int_{-W/2}^{W/2} dx j_e(x) e^{i\beta x} \right|. \tag{2.45}$$

By calculating the inverse Fourier transform of J_c, the spatial distribution of the supercurrent can be calculated. For this reason, measurement of the Fraunhofer diffraction pattern has become a common tool in the analysis of Josephson junctions, from the detection of edge currents [94, 95] to the mapping of the supercurrent distribution in different confinements [96]. For homogeneous current distribution the Fraunhofer diffraction pattern is obtained, as illustrated in Figure 2.10.(b,c).

2.5.2 RCSJ model

The Josephson equations describe an ideal JJ. However, to gain insight into the dynamics of a realistic junction, a more complex model is needed. In the resistively and capacitively shunted junction (RCSJ) model, the physical junction is built up of an ideal junction, shunted by a normal resistor and a capacitor, as it is shown in Figure 2.11.(a). Noise (e.g. thermal noise) can also be included in the model as a fluctuation current source.

Neglecting the noise and using Kirchhoff's law, the current in the junction can be written as:

$$I = I_S + I_N + I_C. \tag{2.46}$$

Using the Josephson equations this can be further expressed as:

$$I = I_c \sin\varphi + \frac{1}{R}\frac{\Phi_0}{2\pi}\frac{d\varphi}{dt} + C\frac{\Phi_0}{2\pi}\frac{d^2\varphi}{dt^2}, \tag{2.47}$$

where R and C are the shunt resistance and capacitance respectively. The usual way to interpret this equation is to draw an analogy with a particle of mass M moving in a potential U with damping η, since it can be rewritten in the following form:

$$M\frac{d^2\varphi}{dt^2} + \eta\frac{d\varphi}{dt} + \nabla U = 0. \tag{2.48}$$

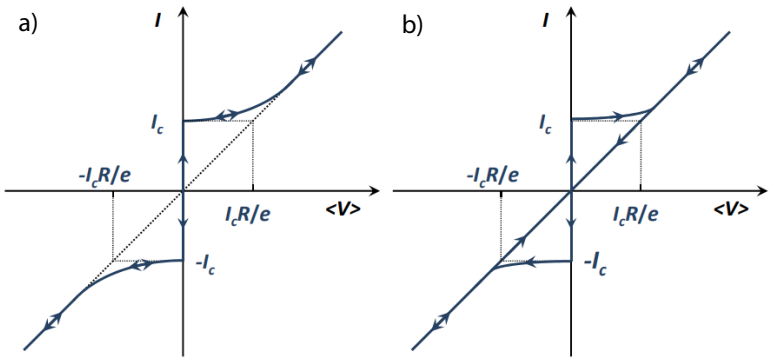

Figure 2.12: Current–voltage characteristics of a) an overdamped and b) underdamped Josephson junction. The arrows indicate the direction of the current variation. Figure adapted from Reference [97].

The mass of the phase particle and the damping can be expressed as:

$$M = \left(\frac{\hbar}{2e}\right)^2 C, \tag{2.49}$$

$$\eta = \left(\frac{\hbar}{2e}\right)^2 \frac{1}{R}, \tag{2.50}$$

and the potential can be written in the form:

$$U = E_{J0}\left[1 - \cos\varphi + \frac{I}{I_c}\varphi\right], \tag{2.51}$$

where $E_{J0} = \hbar I_c/2e$ is the Josephson coupling energy and U is referred to as the tilted washboard potential that is illustrated in Figure 2.11.(b).

In this analogy, two distinct regimes can be discussed. In case of small mass and large damping (small RC product) the junction is *overdamped*. Upon increasing the current, and the tilt of the washboard potential, the junction stays in the zero voltage state until the critical current is reached since the particle is residing in a potential well and there is no time-evolution of the phase. However, at larger currents the phase particle moves down the potential well and the continuous evolution of the phase results in the appearance of a finite voltage on the junction. When reducing the current from above I_c, the particle gets trapped in a potential well when I_c is reached and the junction jumps back to the zero-voltage state. This is shown in Figure 2.12.(a).

In case of an *underdamped* junction, when the mass is large and the damping is small (large RC product), the junction will also stay in the zero voltage state until the current reaches I_c. However, when decreasing the current, the massive particle can move down the potential well even if there are local minima due to the small damping and therefore the junction will stay in the finite-voltage state even below I_c and will only jump back to the zero-voltage state at the so-called retrapping current I_r. As a result, in case of an underdamped junction, the I–V curves become histeretic, as it is illustrated in Figure 2.12.(b).

One important remark about the zero voltage state is that the phase particle is not stationary at the bottom of the potential well but it is oscillating at the plasma frequency [97]:

$$\omega_p = \sqrt{2eI_c/\hbar C}\left[1 - (I/I_c)^2\right]^{1/4}. \tag{2.52}$$

In this state, the time-averaged $d\varphi/dt$ and voltage is zero.

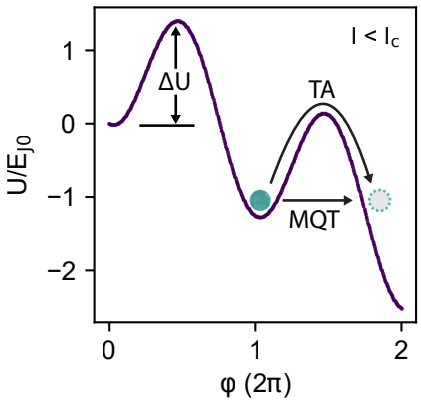

Figure 2.13: Schematic illustration of the macroscopic quantum tunneling and thermal activation. These processes can result in the escape of the phase particle from the potential well when $I < I_c$ and switch the Josephson junction into the finite voltage state.

2.5.3 Stochastic switching in Josephson junctions

The RCSJ model provides a framework for modeling realistic JJs. However, it is important to note that it cannot account for probabilistic events that cause the premature switching of a JJ such as macroscopic quantum tunneling (MQT) and thermal activation (TA) as illustrated in Figure 2.13. MQT is the quantum tunneling of the phase particle at low temperatures through the potential barrier of the tilted washboard potential. If the damping is small, once the phase particle escapes from the potential well, it can run down the washboard potential, and the JJ switches to the finite-voltage state. When the current through the JJ is ramped from zero towards the critical current, the probability distribution of switching at a given current value I_s is given by [98, 99]:

$$P(I_s) = [\Gamma(I_s)/(dI/dt)] \left\{ 1 - \int_0^{I_s} P(I')dI' \right\}, \tag{2.53}$$

where Γ_{I_s} is the escape rate and dI/dt is the current ramp rate. The escape rate in the MQT regime is given by [100]:

$$\Gamma_{MQT} = \left[120\pi \left(\frac{7.2\Delta U}{\hbar\omega_p} \right)^{1/2} \frac{\omega_p}{2\pi} \exp\left(-7.2 \frac{\Delta U}{\hbar\omega_p} \left(1 + \frac{0.87}{Q} \right) \right) \right], \tag{2.54}$$

where $Q = \omega_p RC$ is the quality factor and $\Delta U = 2E_{J0}\left[(1-\gamma^2)^{1/2} - \gamma\cos^{-1}\gamma\right]$ is the potential barrier (see Figure 2.13) with $E_{J0} = \hbar I_c/2e$ being the Josephson energy and $\gamma = I/I_c$. These two equations practically state that when thermal effects are negligible, the phase particle will attempt to escape from the potential well at a rate related to the plasma frequency and the probability of switching is increasing as the current is increased since the height and the width of the potential barrier is gradually decreasing as the washboard potential is tilted. MQT was experimentally detected in both SIS [101] and S-graphene-S (SGS) [102] junctions.

At larger temperatures, the phase particle can get excited out of the potential well by thermal fluctuations. The escape rate in this thermal activation regime is given by [102]:

$$\Gamma_{TA} = a_t(\omega_p/2\pi)\exp[-\Delta U/k_B T], \tag{2.55}$$

where T is the temperature and $a_t = (1 + 1/4Q^2)^{1/2} - 1/2Q$ is a damping dependent factor. It is easy to realize that the escape rate in the thermally activated process increases exponentially with T and it is usually the dominant switching process in experiments above $\sim 100\,\mathrm{mK}$ for typical junctions. More precisely, the cross-over temperature between the MQT and TA regimes

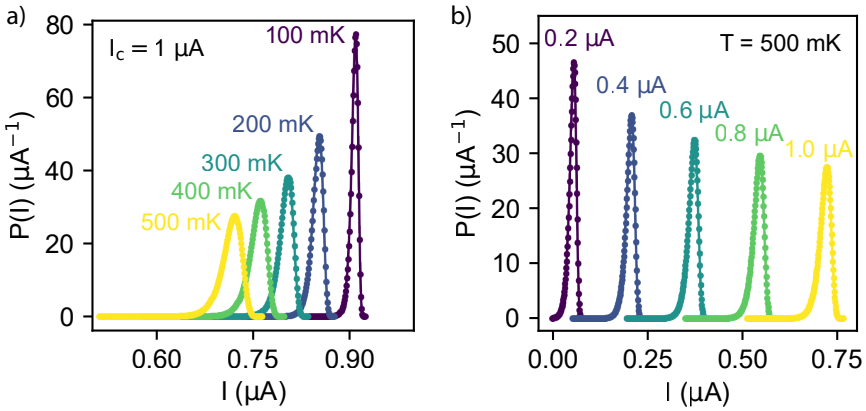

Figure 2.14: Probability of switching $P(I)$ in the thermal activation regime with $dI/dt = 10^{-3}\,\mathrm{A/s}$ for a) different temperatures T and fixed $I_c = 1\,\mu\mathrm{A}$ and b) different values of I_c and fixed $T = 500\,\mathrm{mK}$. As T is increased, the junction switches at lower and lower current values and the width of the probability distribution function is increasing. The width of the distribution also increases with I_c.

is given by $T_{cr} = a_t\hbar\omega_p/k_B$. The probability of switching $P(I)$ is shown for different examples in the thermally activated regime in Figure 2.14.

It is also important to note that, at even higher temperatures, thermally activated retrapping can occur. The phase particle can be excited out of the potential well and retrapped consequently multiple times which results in the appearance of a finite time-averaged voltage below I_c and the narrowing of the SCD with increasing temperature. This phase diffusion regime was predicted by Monte Carlo simulations in Reference [103] and demonstrated experimentally in graphene-based JJs [102].

2.5.4 Current–phase relation

The current–phase relation given in Equation 2.38 is valid for SIS tunnel junctions, the problem originally investigated by Josephson. On the other hand, the weak link does not need to be an insulating barrier. Andreev reflection [104] allows the transport of Cooper pairs through a normal-superconductor (NS) interface. In an SNS junction, a series of Andreev reflections result in the formation of Andreev bound states (ABSs) [105]. For a single conduction channel in the ballistic, short junction limit where the length of the junction (L) is smaller than the superconducting coherence length (ξ), the ABS spectrum takes the following form [106]:

$$E(\varphi) = \pm\Delta\sqrt{1 - \tau\sin^2(\varphi/2)}, \tag{2.56}$$

where τ is the transmission of the channel. From this, the current carried by the single conduction channel can be given by:

$$I_s(\varphi) = -\frac{2e\partial E}{\hbar\partial\varphi} = \frac{e\pi\Delta}{h}\frac{\tau\sin(\varphi)}{\sqrt{1 - \tau\sin^2(\varphi/2)}}. \tag{2.57}$$

For practical purposes (see Chapter 6), it is sometimes useful to normalise the Andreev formula given in Equation 2.57 and use the following form:

$$I_s(\varphi) = I_c\,\frac{\tau\sin(\varphi)}{\sqrt{1 - \tau\sin^2(\varphi/2)}}\Bigg/\max_{\varphi}\left\{\frac{\tau\sin(\varphi)}{\sqrt{1 - \tau\sin^2(\varphi/2)}}\right\}. \tag{2.58}$$

This is shown in Figure 2.15.(b) for different values of τ. In the $\tau \to 0$ limit, the Andreev formula reduces to the sinusoidal CPR predicted by Josephson for SIS junctions. Furthermore,

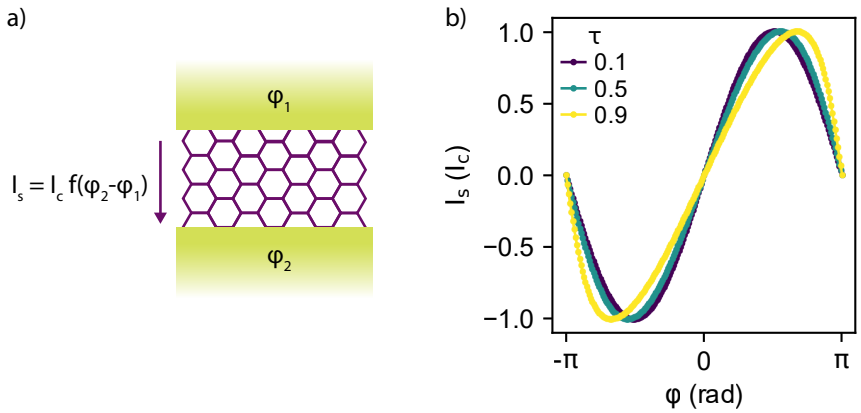

Figure 2.15: a) Schematic illustration of an SGS Josephson junction. Two superconducting leads (yellow) are connected by a short graphene section. The supercurrent flowing in graphene is determined by the macroscopic phase difference of the two leads via the current–phase relation. b) Supercurrent I_s as a function of the phase difference φ according to the Andreev formula given in Equation 2.58 for different values of τ. For $\tau \ll 1$, the CPR is sinusoidal and becomes skewed as τ increases.

as τ increases, the CPR becomes more and more skewed. It is worth mentioning that the non-sinusoidal behaviour can also be described by expressing the CPR as a Fourier series [107, 108]:

$$I_s(\varphi) = \sum_k (-1)^{k-1} a_k \sin(k\varphi). \tag{2.59}$$

Here, higher frequency terms describe higher order Andreev processes that are increasingly sensitive to phase decoherence. Nevertheless, the a_k coefficients and τ contain the same information, the skewness of the CPR.

An important property of CPRs described by both Equations 2.38 and 2.58 is that they yield $I_s(\varphi = 0) = 0$. This means that no supercurrent can flow without a finite phase difference. This property is protected by time-reversal and spatial parity symmetries [109–111]. However, the presence of SOC and magnetic field can break these symmetries. When these symmetries are lifted, a finite phase shift φ_0 can appear in the CPR. This can simply be included e.g. in Equation 2.57 by the substitution $\varphi \to \varphi_t$ with $\varphi_t = \varphi + \varphi_0$. This leads to a finite supercurrent even when $\varphi = 0$, also known as the anomalous Josephson effect. For a ballistic system with Rashba SOC and in–plane magnetic field, the φ_0 phase shift is given by [111]:

$$\varphi_0 = \frac{4 E_Z \alpha_R L}{(\hbar v_F)^2}, \tag{2.60}$$

where E_Z is the Zeeman energy, α_R is the Rashba coefficient, L is the junction length and v_F is the Fermi velocity. Reference [111] also gives an estimate for the φ_0 phase shift in the diffusive regime:

$$\varphi_0 = \frac{\tau_p m^{*2} E_Z (\alpha_R L)^3}{3\hbar^6 D}, \tag{2.61}$$

where τ_p is the momentum scattering time, m^* is the effective mass and D is the diffusion constant. Phase shifts originating from the interplay between in-plane magnetic field and SOC has been experimentally detected in InAs and InSb Josephson junctions [109–112]. To provide similar equations that can be applied to graphene requires further theoretical efforts taking into account the different SOC terms. However, the presence of a φ_0 phase shift is connected to the appearance of the superconducting diode effect [112] (SDE). The SDE refers to the asymmetry of the critical current in the positive and negative current direction and has been demonstrated in a variety of Josephson junctions [113–120].

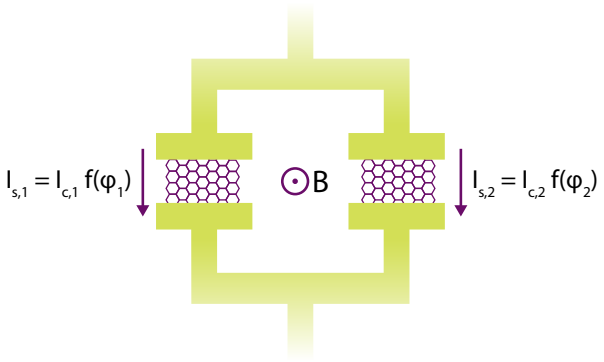

Figure 2.16: Schematics of a DC SQUID. Two Josephson junctions are connected in parallel by a superconducting loop (yellow). The phase differences of the two junctions, φ_1 and φ_2 are connected by the magnetic flux Φ threading the superconducting loop via the relation $\varphi_2 - \varphi_1 = 2\pi\Phi/\Phi_0$, where Φ_0 is the magnetic flux quantum.

2.5.5 SQUID

To measure the CPR of a Josephson junction, it is essential to be able to tune the phase difference across the junction. This is made possible by using a superconducting quantum interference device [121] (SQUID). A DC SQUID is schematically illustrated in Figure 2.16, it consists of two JJs embedded in a superconducting loop. It can be shown that in such a configuration, the phase differences of the two junctions, φ_1 and φ_2, are connected via the relation:

$$2\pi\frac{\Phi}{\Phi_0} = \varphi_2 - \varphi_1, \tag{2.62}$$

where $\Phi = B \cdot A$ is the magnetic flux threading the loop, B is the magnetic field applied perpendicular to the plane of the loop, A is the loop area and $\Phi_0 = h/2e$ is the magnetic flux quantum. Historically, this property enabled the precise measurement of very small magnetic fields that lead to practical applications such as scanning SQUID microscopy [122] and magnetoencephalography [123]. More importantly for us, it also enables the measurement of the CPR [124]. This method is discussed in the following.

For simplicity, let us assume sinusoidal CPR of the form $I_{s,1} = I_{c,1}\sin(\varphi_1)$ ($I_{s,2} = I_{c,2}\sin(\varphi_2)$) for junction 1 (junction 2). Since the two phase differences are connected by Equation 2.62, the supercurrent is junction 2 for a given Φ can be expressed as $I_{s,2}(\varphi_1, \Phi) = I_{c,2}\sin(2\pi\Phi/\Phi_0 + \varphi_1)$. Using these, the total supercurrent in the SQUID is simply $I_s(\varphi_1, \Phi) = I_{s,1}(\varphi_1) + I_{s,2}(\varphi_1, \Phi)$ for a given (φ_1,Φ) pair. From this, the critical current I_c of the SQUID, the maximum allowed supercurrent, can be numerically calculated as:

$$I_c = \max_{\varphi_1}\left\{I_{c,1}\sin(\varphi_1) + I_{c,2}\sin(2\pi\Phi/\Phi_0 + \varphi_1)\right\}. \tag{2.63}$$

The resulting critical current as a function of the magnetic flux is shown in Figure 2.17.(a), calculated numerically for different ratios of $I_{c,1}/I_{c,2}$. In analogy to the CPR of a single JJ, this is often referred to as the current–flux relation (CϕR). For a symmetric configuration with $I_{c,1} = I_{c,2}$, the CϕR can be analytically calculated and is given by:

$$I_c|_{I_{c,1}=I_{c,2}} = 2I_{c,2}|\cos(\pi\Phi/\Phi_0)|. \tag{2.64}$$

In the asymmetric case where $I_{c,1} \ll I_{c,2}$, the critical current can be maximised by keeping $I_{s,2}$ maximal with $\varphi_2 = \pi/2$ and only changing $I_{s,1}$ via φ_1. From this, it follows that the CϕR in the asymmetric configuration contains the CPR of junction 1 offset by $I_{c,2}$:

$$I_c|_{I_{c,1}\ll I_{c,2}} = I_{c,1}\sin(\pi/2 - 2\pi\Phi/\Phi_0) + I_{c,2}. \tag{2.65}$$

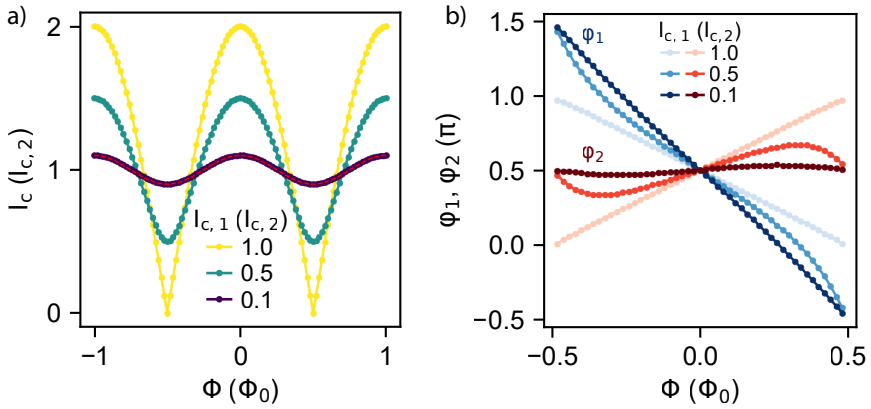

Figure 2.17: a) Numerically calculated critical current–flux relation of a DC SQUID assuming sinusoidal CPRs for the two junctions. The critical current of the SQUID I_c as a function of the magnetic flux for different values of $I_{c,1}$ in units of $I_{c,2}$. Red dashed line shows the function defined by Equation 2.65 with $I_{c,1} = 0.1 I_{c,2}$ for comparison. b) Phase differences φ_1 and φ_2 of the two JJs as a function of Φ for different values of $I_{c,1}$. Shades of blue correspond to φ_1 and red to φ_2.

This is further confirmed in Figure 2.17.(b) where the phase differences are shown as a function of Φ for the three $I_{c,1}/I_{c,2}$ ratios used in Figure 2.17.(a). It can be seen that in the symmetric configuration, φ_1 and φ_2 change simultaneously with the same absolute rate, while in the asymmetric configuration, we obtain $\varphi_2 \approx \pi/2$ and φ_1 changes roughly linearly with Φ. Therefore, the asymmetric SQUID allows the measurement of the CPR of the junction with the smaller critical current if the asymmetry is sufficient. It is important to emphasize that for intermediate asymmetry, the two phase differences evolve nonlinearly with Φ and the resulting CϕR is nonsinusoidal, as it is clearly visible in Figure 2.17 for $I_{c,1}/I_{c,2} = 0.5$.

Although it is challenging to estimate the necessary asymmetry of the critical currents to measure CPR, the ratio used in experimental works typically ranges from $I_{c,1}/I_{c,2} = 0.2$ to 0.01 [124–129]. As detailed in Reference [130], the necessary asymmetry depends on the shape of both CPRs. Generally, more exotic CPRs with sharp features, such as ABS with large τ or saw-tooth functions, require larger asymmetry to be directly measured. For this reason, it is important to carefully analyze the measured CϕR and confirm that the true CPR can be extracted. For the measurements presented in this work, this is detailed in Chapter 6.

2.5.6 Multiterminal Josephson junctions

Multiterminal Josephson junctions (MTJJs) consist of a single scattering region connected to multiple superconducting terminals. This is illustrated in Figure 2.18. In analogy to a simple JJ, an MTJJ with N terminals can be described by $N-1$ independent phase differences and the phase difference between a pair of terminals can be tuned by local magnetic fields using superconducting loops similarly to SQUIDs. These systems gained considerable attention in recent years after theoretical works showed that the ABS spectrum in the $N-1$ dimensional phase space can host Weyl points and, therefore, provide a platform to simulate the band structure of topologically non-trivial materials [32, 131–146]. Furthermore, recent experimental works showed that ABSs can hybridize between multiple terminals [147–150]. Theoretical predictions [151–156] and experimental works [157–161] also suggest that MTJJs can give rise to multiplet supercurrents where supercurrent is carried by multiple entangled Cooper pairs. MTJJs are also ideal systems for realizing the Josephson diode effect since inversion symmetry breaking can be realized simply by current-biasing in a suitable geometry [162] or by small magnetic fields [163–165], regardless of the weak-link material and without the need for large

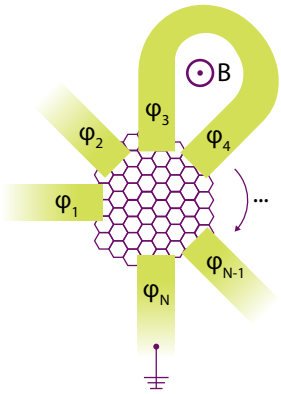

Figure 2.18: Schematic illustration of a multiterminal Josephson junction. N superconducting terminals are connected to a single scattering region. Phase differences between pairs of terminals can be tuned by local magnetic fields using superconducting loops.

SOC.

In spite of the numerous exotic phenomena proposed theoretically, many of the experimental works found that basic transport properties of MTJJs can be described by an RCSJ network, in which each pair of terminals is connected by an RCSJ element. This relatively simple approach is able to qualitatively capture features of current-biased measurements, such as the coexistence of normal and supercurrents between different terminals [159, 160, 166–168] and multiplet resonances [159, 168]. This model, along with its limitations, is investigated in Chapter 7 for three-terminal MTJJs.

Chapter 3

Experimental techniques

In this chapter, the experimental techniques used throughout the rest of this work are presented. First, we discuss the fabrication of electronic devices based on Van der Waals heterostructures. This involves the exfoliation of 2D materials, the assembly of heterostructures and the fabrication of electronic contacts using electron beam lithography. In the second part of the chapter, the measurement techniques are presented, including the typical equipment for low-temperature transport measurements. The measurement of stochastic switching events in Josephson junctions is also discussed.

3.1 Fabrication of Van der Waals heterostructures

3.1.1 Exfoliation of 2D materials

Multiple methods exist for the large scale production of graphene and other 2D materials, such as electrochemical [169] and shear exfoliation in liquids [170]. Furthermore, high-quality few-layer crystals can also be synthesized by chemical vapor deposition (CVD) [171]. These methods are especially promising for the industrial scale production of electronic devices based on Van der Waals heterostructures. However, to this day, mechanical exfoliation remains the easiest and most hassle-free solution to produce thin flakes of 2D materials for research purposes. Mechanical exfoliation is the process of isolating single- or few-layer thick flakes from bulk crystals by repeated peeling using an adhesive tape [34, 36]. Since the layers in 2D materials are held together by weak Van der Waals forces, by pressing a bulk crystal against an adhesive tape multiple times, the tape can be populated with flakes that detach from the remaining bulk part. After this, the tape is pressed onto a Si substrate covered with SiO_2 and, due to the adhesion between the SiO_2 and the flakes of 2D materials, these flakes can be cleaved again and even thinner flakes can be transferred to the substrate.

The choice of a suitable substrate is of the utmost importance in the search for single- or few-layer crystals and particularly for graphene. Few-layer graphene is almost completely transparent. However, it can be identified on the Si/SiO_2 substrate by optical microscopy due to interference effects. The presence of graphene modifies the optical path of the illuminating light and changes the intensity of reflected light. As detailed in Reference [172], the intensity of light reflected from a Si/SiO_2/graphene structure in case of wavelength λ and normal incidence can be calculated using Fresnel's law:

$$I(n_1) = \Big| \Big(r_1 e^{i(\Phi_1+\Phi_2)} + r_2 e^{-i(\Phi_1-\Phi_2)} + r_3 e^{-i(\Phi_1+\Phi_2)} + r_1 r_2 r_3 e^{i(\Phi_1-\Phi_2)} \Big) \times \Big(e^{i(\Phi_1+\Phi_2)} + r_1 r_2 e^{-i(\Phi_1-\Phi_2)} + r_1 r_3 e^{-i(\Phi_1+\Phi_2)} + r_2 r_3 e^{i(\Phi_1-\Phi_2)} \Big)^{-1} \Big|^2 , \quad (3.1)$$

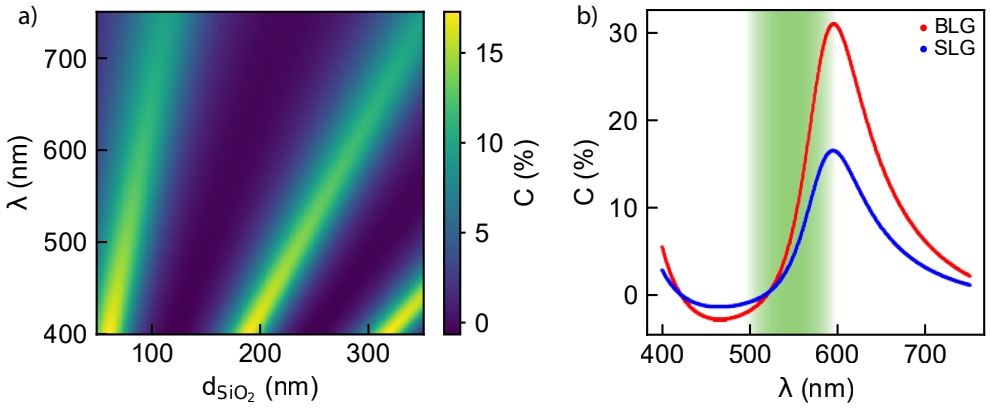

Figure 3.1: a) Optical contrast of SLG as a function of wavelength λ and oxide thickness d_{SiO_2} calculated from Equation 3.1. b) Optical contrast of SLG (blue) and BLG (red) as a function of λ for $d_{SiO_2} = 285\,\text{nm}$ used typically for mechanical exfoliation. In practice, the green channel intensity of optical images is used to determine the contrast. The relevant wavelength range is highlighted in green.

with

$$r_1 = \frac{n_0 - n_1}{n_0 + n_1}, \tag{3.2}$$

$$r_2 = \frac{n_1 - n_2}{n_1 + n_2}, \tag{3.3}$$

$$r_3 = \frac{n_2 - n_3}{n_2 + n_3}, \tag{3.4}$$

$$\Phi_1 = \frac{2\pi n_1 d_1}{\lambda} \quad \text{and} \tag{3.5}$$

$$\Phi_2 = \frac{2\pi n_2 d_2}{\lambda}. \tag{3.6}$$

Here, $n_0 = 1$, n_1, n_2 and n_3 are the refractive indices of air, graphene, SiO_2 and Si, respectively. Furthermore, r_1, r_2 and r_3 are the reflection coefficients from the surface of graphene, SiO_2 and Si, respectively. Si is assumed to be semi-infinite, d_1 and d_2 are the thicknesses of graphene and SiO_2. The contrast of graphene on SiO_2 can be calculated using the reflected intensity in the presence $I(n_1 \neq 1)$ and absence $I(n_1 = 1)$ of graphene as:

$$C = \frac{I(n_1 = 1) - I(n_1)}{I(n_1 = 1)}. \tag{3.7}$$

Using refractive indices for Si and SiO_2 from `refractiveindex.info` [173] and $n_1 = 2.6 - 1.3i$ for graphene [172], the contrast C is shown in Figure 3.1.(a) for SLG with $d_1 = 0.33\,\text{nm}$ as a function of λ in the visible spectrum and $d_2 = d_{SiO_2}$. From this, it is easy to realize that the optical contrast of graphene depends greatly on the thickness of SiO_2. Furthermore, graphene gives a reasonably large contrast for a wide range of d_{SiO_2} and, in principle, can be identified by using appropriate optical filters.

In practice, we use Si wafers with an oxide thickness of $d_{SiO_2} \approx 285 \pm 10\,\text{nm}$ and an optical microscope with white illumination that yields a reasonably good contrast. This not only allows experienced users to find few-layer graphene flakes, but also to distinguish SLG and BLG from thicker flakes. As it is shown in Figure 3.1.(b), the highest calculated contrast for BLG ($d_1 = 0.66$ nm) is almost twice the contrast calculated for SLG ($d_1 = 0.33\,\text{nm}$) for $d_{SiO_2} = 285\,\text{nm}$. For a quantitative analysis of the contrast, we analyze the green channel intensity of optical images and calculate the contrast similarly to Equation 3.7. This method

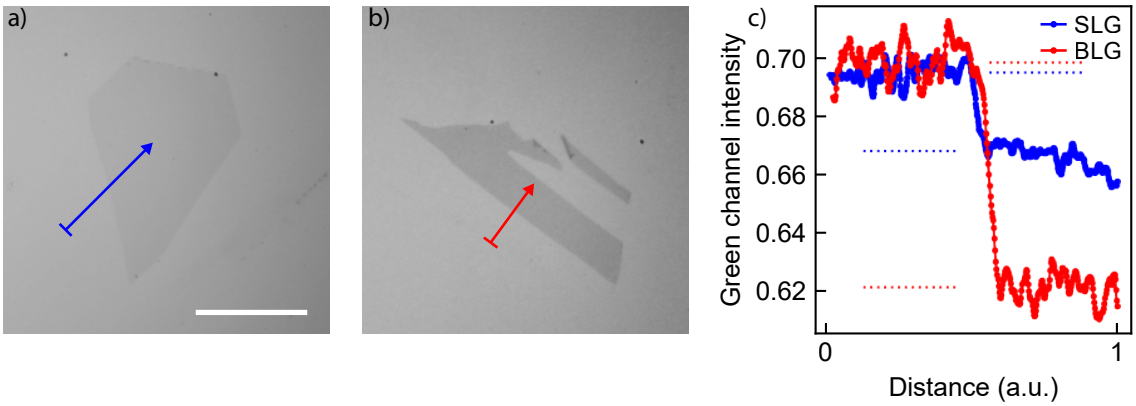

Figure 3.2: a,b) Green channel data from optical microscopic images of SLG and BLG. Scale bar is 25 μm. c) Intensity porfiles along the arrows in panels (a) and (b). SLG and BLG can be clearly distinguished by their optical contrast.

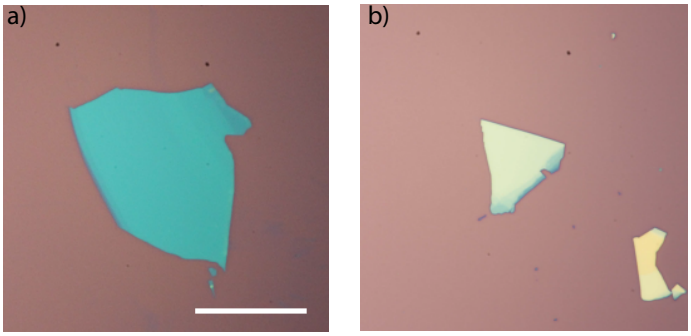

Figure 3.3: a,b) Optical microscopic images of hBN and WSe_2. Thickness are 25 nm and 15 nm, respectively. Scale bar is 25 μm.

yields a typical contrast of $\sim 4-7\%$ for SLG and $\sim 10-15\%$ for BLG, depending on the variation of oxide thickness and camera settings. Figures 3.2.(a) and 3.2.(b) show optical images of an SLG and a BLG flake, respectively. The green channel intensity is shown in a grayscale representation. Figure 3.2.(c) shows line cuts along the respective arrows in panels (a) and (b). The two curves yield a contrast of $\sim 4\%$ for SLG and $\sim 11\%$ for BLG.

In addition to graphene, two other 2D materials are important for this work. Firstly, hexagonal boron nitride (hBN) is an insulator with a crystal structure similar to graphene. The role of hBN in graphene-based van der Waals heterostructures is to isolate graphene from the disordered SiO_2 substrate and protect graphene from contamination. SiO_2 has significant surface roughness on the atomic scale and contains charged surface states and impurities which introduce disorder in graphene and limit charge carrier mobility. On the other hand, hBN can be mechanically exfoliated similarly to graphene, resulting in atomically flat surfaces. Furthermore, the lattice mismatch between graphene and hBN is small, only 1.7%, making hBN an ideal substrate for graphene. By placing graphene on hBN, a significant improvement in device quality can be achieved compared to early graphene/SiO_2 devices [42]. Encapsulating graphene between two layers of hBN can improve device quality even further by protecting graphene from polymer residues during the contact fabrication process [174]. The ideal thickness of hBN flakes is $\sim 20-40$ nm. Thinner flakes cannot efficiently isolate graphene from its environment, while too thick layers complicate the fabrication of electric contacts. The thickness of hBN flakes can be approximately determined by optical microscopy based on the interference color on SiO_2. A 25 nm thick hBN flake is shown in Figure 3.3.(a).

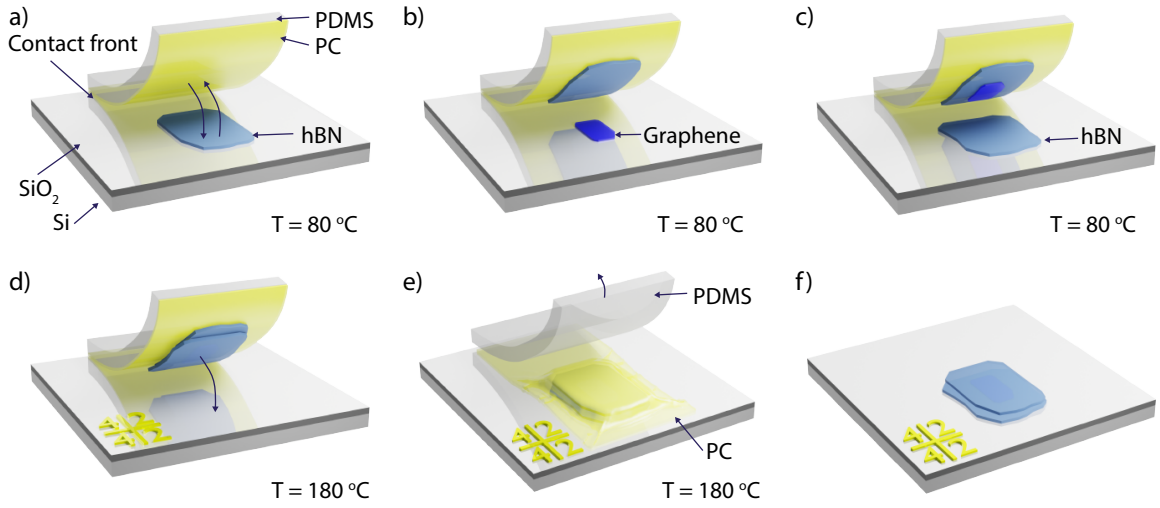

Figure 3.4: Schematic illustration of the stacking process. a) A PDMS/PC structure is brought in contact with the desired 2D material at $T = 80\,°C$. When the PDMS/PC structure is retracted, the flake is picked up from the Si/SiO_2 substrate. b,c) Further layers are picked up sequentially, making use of the van der Waals forces between the flakes. d,e) The assembled heterostructure is placed on a Si/SiO_2 substrate with predefined markers assisting the lithography process. The PC layer is delaminated from the PDMS at $T = 180\,°C$. f) PC is dissolved in chloroform, leaving behind the assembled heterostructure.

As discussed in Section 2.3, by placing graphene close to a TMD layer, a large SOC can be induced via the proximity effect. In this work, we use WSe_2 for the investigation of proximity-induced SOC in graphene. WSe_2 can also be mechanically exfoliated and flakes of suitable thickness (< 20 nm) can be identified by optical microscopy based on their interference color. An example is shown in Figure 3.3.(b). Although some optical applications require the use of monolayer WSe_2 [67, 175], their exfoliation is generally more challenging and experiments suggest that thicker flakes are also suitable to induce SOC in graphene.

3.1.2 Assembly of heterostructures

After selecting the suitable exfoliated layers, the heterostructures are assembled using the dry polymer stacking technique described in Reference [176]. The stacking process is illustrated in Figure 3.4 for a basic hBN/graphene/hBN heterostructure. First of all, a small polydimethylsiloxane (PDMS) cube or hemisphere is placed on a glass microscope slide and coated with a thin layer of polycarbonate (PC). The glass slide and the exfoliated flake on the Si/SiO_2 is placed in a purpose-built transfer microscope. The layers of the heterostructure are picked up from their respective substrate sequentially with the PC/PDMS structure making use of the van der Waals forces between subsequent layers that are stronger than the adhesion to the substrate (Figure 3.4.(a-c)). The substrate is usually heated up to 80 °C to promote adhesion to the PC layer. During the pick-up process, the flakes remain visible since the PC/PDMS structure is transparent and the relative position of the flakes can be precisely controlled by the micromanipulators of the transfer microscope. When the desired layers are all picked up, the PC/PDMS structure with the assembled heterostructure is pressed onto the surface of another Si/SiO_2 substrate (Figure 3.4.(d)). The substrate is heated up to 180 °C, above the glass transition temperature of PC and the PC layer delaminates from the PDMS. The PDMS is then retracted, leaving the heterostructure on the substrate covered with the PC film (Figure 3.4.(e)). Finally, PC is dissolved in chloroform (Figure 3.4.(f)). This stacking process can be extended to

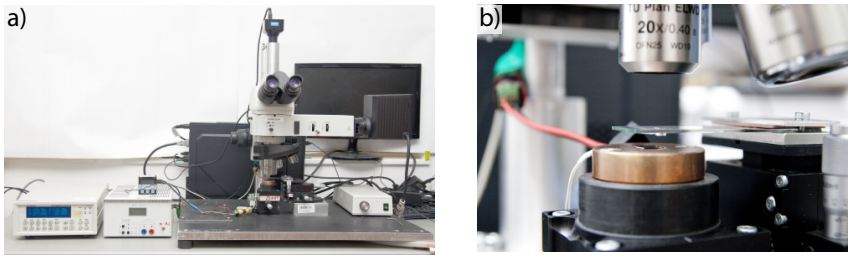

Figure 3.5: a) Photo of the transfer microscope with the temperature control system. b) Close-up of the heated sample holder stage and glass slide holder.

practically any 2D materials and number of layers as long as the van der Waals forces between the layers are strong enough to lift them up from the substrate. It is also worth noting that the process can be partially automated [177].

Although the basic concept of the stacking process is robust, details may vary slightly. For example, different polymers – such as poly(methyl methacrylate) (PMMA), polypropylene carbonate (PPC), polyvinyl chloride (PVC) and polyvinyl alcohol (PVA) – are often used instead of PC with each polymer having slightly different adhesion properties. PDMS acts as a spacer during the stacking process and provides the necessary flexibility to precisely control the assembly of layers. Due to a tilt angle between the PC/PDMS structure and the substrate, after the PC is brought in contact with the substrate the contact front (Figure 3.4.(a)) can be controlled by further lowering the glass slide towards the substrate and deforming the PDMS. As detailed in Reference [176], above 180 °C, contaminants trapped between layers become mobile and can be cleaned from the heterostructure or accumulated into fewer and larger bubbles when the contact front passes over the stacked layers. PDMS cubes or hemispheres can both be used for stacking, however, the contact area for hemispheres is generally smaller and they allow for easier control of the tilt angle between substrate and PDMS around the heterostructure.

The assembled heterostructure is characterized by atomic force microscopy (AFM) measurements. These allow the measurement of the layer thickness with nanometer precision that is necessary for further fabrication steps. Furthermore, the bubbles formed by trapped contaminants can also be located and electronic devices can be designed in clean regions of the heterostructure.

3.1.3 Electron beam lithography

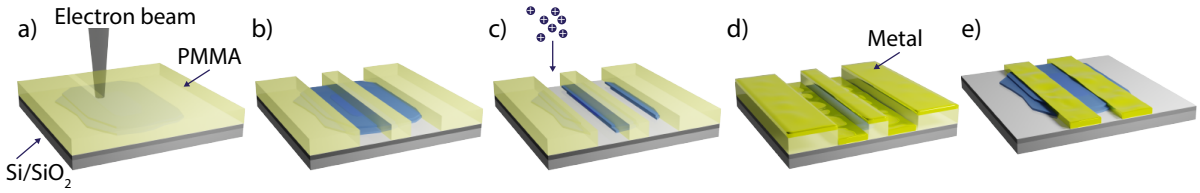

Figure 3.6: Steps of contact fabrication with electron-beam lithography. a) Patterning: the resist layer is selectively exposed by a focused beam of electrons. b) Development: the exposed parts of the resist are chemically dissolved. c) Reactive ion etching of the heterostructure. The remaining part of the resist acts as a mask during the etching process. d) Metal is deposited on the whole substrate. e) Lift-off: the remaining resist is dissolved, taking away the surplus of metal.

In order to conduct transport measurements on van der Waals heterostructures, electronic contacts are fabricated using electron-beam lithography (EBL). This process is illustrated in

Figure 3.6. First, the substrate is spin-coated with a PMMA resist layer and the desired geometry is exposed by a focused electron beam (Figure 3.6.(a)). High-energy electrons break up the polymer chains of PMMA, and the patterned area can be dissolved with a 1:3 mixture of isopropyl alcohol (IPA) and methyl isobutyl ketone (MIBK), called the developer (Figure 3.6.(b)). The development step uncovers parts of the heterostructure, however, graphene is still fully encapsulated in hBN. Therefore, in order to contact graphene, reactive ion etching (RIE) is needed. RIE is a combination of physical and chemical etching. In our case, ions from a CHF_3/O_2 plasma are accelerated towards the substrate, etching away the heterostructure in the patterned area (Figure 3.6.(c)). After this, metal is deposited onto the substrate and one dimensonal contacts are formed along the exposed edges of graphene [174] (Figure 3.6.(d)). Contacts can be fabricated of normal metals or superconducting materials. Typically, normal contacts are made of $\sim 50 - 80$ nm Au with ~ 10 nm Cr or Ti adhesion layer. For superconducting electrodes, we typically use MoRe or NbTiN deposited by DC sputtering. Finally, the remaining resist is dissolved in acetone, removing also the surplus of metal from the substrate and metal is left behind only in the patterned area (Figure 3.6.(e)). Lithography parameters can be found in Appendix A.

To control the charge carrier density and transverse electric field in graphene, gate electrodes are used. In some cases, the highly doped Si substrate can act as a global backgate which does not require additional fabrication steps. However, in many devices, graphite bottom gates and metallic topgates are used simultaneously. Using such a dual-gated structure enables the separate tuning of carrier density and electric field, as described in Section 2.4.1. The fabrication of gate electrodes is also done by EBL, similarly to contacts but without etching. However, some additional details have to be discussed. For example, graphite bottom gates are usually positioned such that they are only partially covered by the rest of the heterostructure. This means that no etching step is required to contact them, which facilitates fabrication. On the other hand, when a graphite bottom gate is used, special care has to be taken during the etching of contacts. If the etching time is too long, then the heterostructure is completely etched through exposing both the graphene and the graphite bottom gate. In this case, if metal is deposited, it creates an electric short circuit between graphene and graphite. This practically makes the device useless for transport measurements. These problems can be prevented by determining the etching rates and layer thicknesses using AFM measurements. To avoid similar issues with topgates, we deposit an aluminium oxide (AlO_x) layer by atomic layer deposition after the contacts are deposited. AlO_x is a high-quality dielectric that uniformly covers the entire substrate. Topgates are deposited on top of this insulating layer to avoid any short circuits with the contact electrodes.

The whole fabrication process is further illustrated in Figure 3.7. The heterostructure consists of six layers, these are shown in Figure 3.7.(a-f). These are – from bottom to top – the following (thickness): graphite (< 5 nm), hBN (40 nm), WSe_2 (15 nm), single-layer graphene, WSe_2 (5 nm), hBN (25 nm). The assembled heterostructure is shown in Figure 3.7.(g) with the outline of each layer shown by dashed lines. The bottom graphite layer is employed as a gate electrode. A Ti/Au (10/60 nm) electrode is fabricated to establish metallic contact to this layer (Figure 3.7.(h)), deposited by electron beam evaporation. Superconducting electrodes are used to form a SQUID and a Josephson junction. These are formed of 50-nm-thick MoRe deposited by DC sputtering following the reactive ion etching step using CHF_3/O_2 mixture (Figure 3.7.(i)). The heterostructure is shaped by another RIE step using SF_6/O_2 mixture to remove parts of the heterostructure and confine the flow of electrons. After this, 30 nm of AlO_x is grown by ALD. Finally, Ti/Au (10/60 nm) electrodes are deposited for the top gates. The finished device is shown in Figure 3.7.(j).

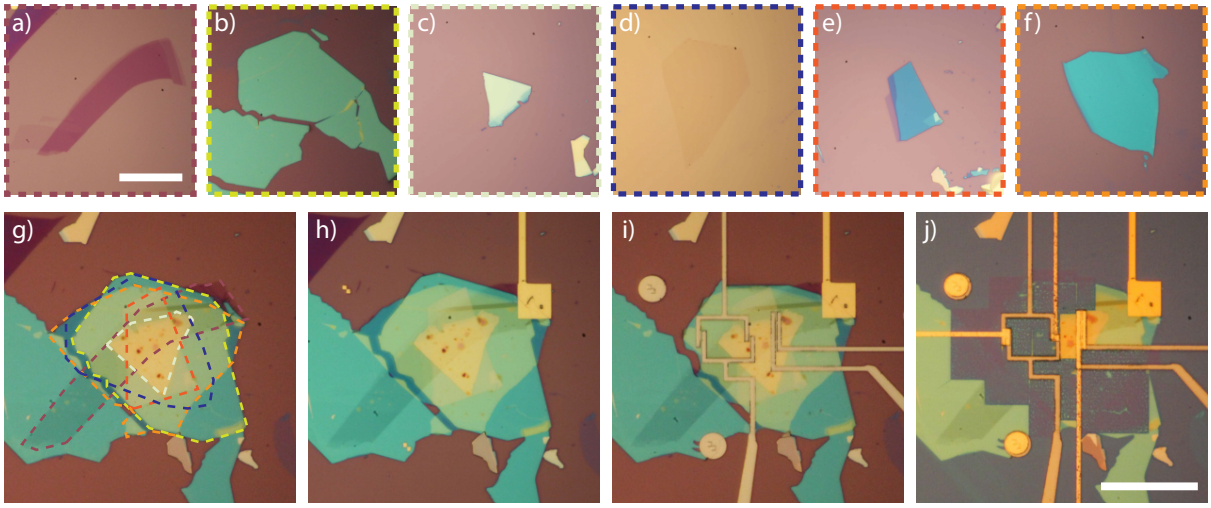

Figure 3.7: Demonstration of the fabrication process for van der Waals heterostructures. Layers of the heterostructure from bottom to top: a) graphite, b) hBN, c) WSe_2, d) SLG, e) WSe_2, f) hBN. g) Assembled heterostructure with the different layers shown by dashed lines. Colors correspond to the borders of panels (a-f). h) Ti/Au electrode is deposited by e-beam evaporation to the graphite layer that acts as a bottom gate. i) Superconducting contacts are deposited by DC sputtering after a RIE step. j) The heterostructure is shaped by another RIE step and Ti/Au top gates are deposited on top of 30 nm AlO_x. Scale bars, corresponding to the top and bottom rows, are 25 μm.

3.2 Transport measurement of van der Waals heterostructures

3.2.1 Cryogenic measurement systems

In order to conduct electronic transport measurements on the fabricated devices, different measurement instruments have to be connected to the electrodes fabricated by lithography. This transition from the nanoscale electronic device to the macroscopic scale is illustrated in Figure 3.8. The electrodes terminate in few-hundred-μm rectangular bonding pads (Figure 3.8.(b)) that can be wire-bonded to chip carriers (Figure 3.8.(c)) or printed circuit boards (PCBs, Figure 3.8.(d)). These macroscopic objects can be connected to the measurement instruments using chip sockets or simple electronic connectors.

The measurement of quantum effects and superconducting phenomena generally requires

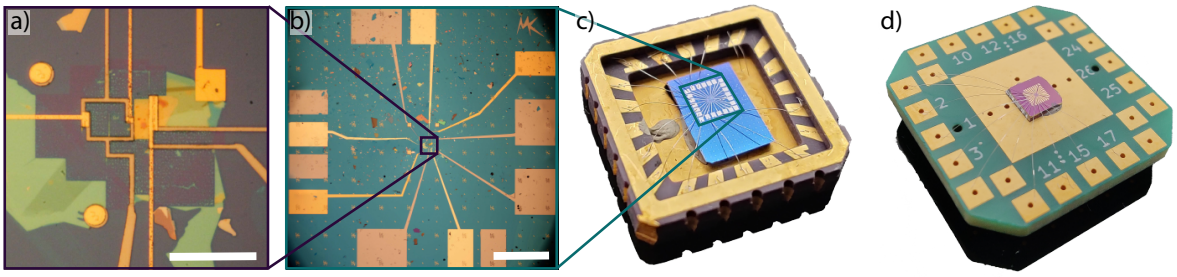

Figure 3.8: a) Optical microscopic image of a nanoelectronic device. Scale bar is 25 μm. b) Zoomed-out image of panel (a). The nanoscale device can be connected to the measurement instruments via bonding pads that terminate the electrodes. Scale bar is 400 μm. c) The metallic pads are wire-bonded to a chip carrier which can be connected to the measurement instruments by a chip socket. d) Alternatively, chips can also be wire-bonded to a printed circuit board.

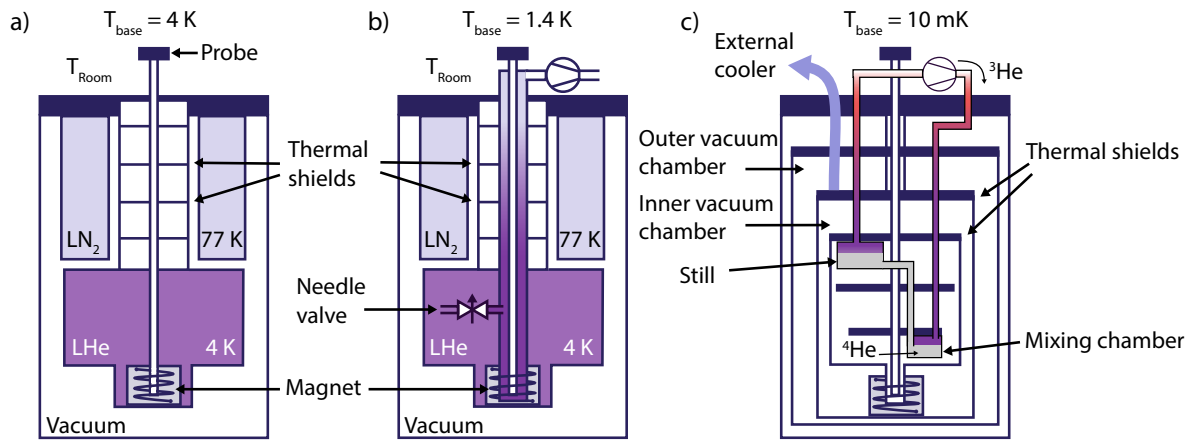

Figure 3.9: Cryogenic systems. a) In a cryostat, devices fixed at the bottom end of a probe can be immersed in liquid helium. The boiling helium results in a base temperature of $T_{base} = 4.2\,\mathrm{K}$. b) Cryostats can be equipped with VTIs. Liquid helium can be injected via a needle valve and gas is continuously evacuated by a pump. The evaporation of helium results in a lower base temperature $T_{base} = 1.4\,\mathrm{K}$. c) Dilution refrigerators use a mixture of ^{3}He/^{4}He to reach a base temperature of $T_{base} = 10\,\mathrm{mK}$. Each cryogenic system can be equipped with superconducting vector magnets.

very low temperatures. For this reason, the measurements are carried out in various cryogenic measurement systems. The simplest examples are cryostats that are essentially vessels of liquid ^{4}He surrounded by chambers of liquid nitrogen and vacuum for thermal isolation. The boiling helium inside the cryostat provides a temperature of $\sim 4\,\mathrm{K}$ at ambient pressure. Devices are fixed to one end of a probe that is immersed in the liquid helium. Electric wires run through the probe and connect the device to the measurement instruments at room temperature. The temperature can be further lowered by using a variable temperature insert (VTI) placed inside the liquid helium bath of a cryostat. The VTI consists of a gas chamber continuously pumped via an external vacuum pump and a needle valve through which helium can be injected to the gas chamber from the helium bath. The injected helium evaporates in the low pressure chamber, further lowering the temperature to $\sim 1.4\,\mathrm{K}$. If an even lower temperature is required, dilution refrigerators provide the solution. Dilution refrigerators are capable of reaching a base temperature of $\sim 10\,\mathrm{mK}$ via a complicated cooling system using ^{3}He/^{4}He mixture. The core principle behind their operation is that the ^{3}He/^{4}He mixture separates into a pure ^{3}He and a dilute ^{3}He/^{4}He (^{4}He-rich) phase at very low temperature and the latent heat of mixing these two phases produces a cooling power.

One benefit of using cryogenic systems is that they can be equipped with superconducting magnets. These are usually solenoid magnets made of type-II superconductors such as NbTi, allowing the generation of magnetic fields without the dissipation of heat. Typical vector magnets can produce a magnetic field of up to ~ 10 T. Vector magnets using multiple solenoids can produce magnetic fields along multiple axes simultaneously.

Nanoelectronic devices can also be investigated under hydrostatic pressure using pressure cells. A method compatible with devices featuring van der Waals heterostructures was developed in our research group by Bálint Fülöp [178]. Devices are wire-bonded to a special PCB that is fitted inside a pressure cell. The pressure cell is filled with kerosene, which acts as the pressure mediating medium, and pressure is applied via a hydraulic press. Details of this technique can be found in References [29, 178]. The pressure cell can also be attached to probes and is compatible with the cryogenic systems of our lab. An important step in the developement of pressure cell measurement technique was to show that hBN can protect van der Waals heterostructures from

the kerosene environment. I fabricated an hBN/SLG/hBN device to test this hypothesis. The device and the related measurement is discussed in Section 4.2.

3.2.2 Transport measurements

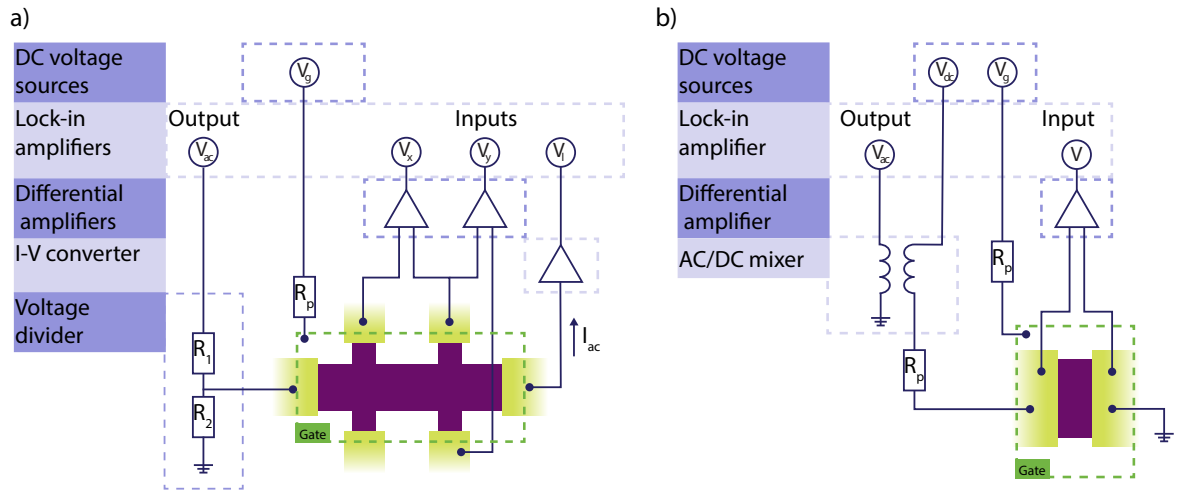

Figure 3.10: Typical transport measurement schemes. a) Voltage-biased measurement in a Hall-bar geometry. The lockin output is applied to the device via a voltage divider. The current through the device is converted to a V_I voltage signal and measured by the lock-in. The V_x longitudinal and V_y transverse voltages are amplified by differential voltage amplifiers and measured by lock-in amplifiers. Gate voltages are supplied by DC voltage sources. b) Current-biased measurement of a superconducting device. A small AC voltage is superimposed to a DC voltage signal with an AC/DC mixer. The voltage drives a current through an R_p pre-resistor and the device to a grounded electrode. The four-terminal voltage is amplified and measured by the lock-in amplifier.

Electronic transport measurements in this work generally consist of the measurement of resistance as a function of external parameters such as charge carrier density, electric and magnetic fields, temperature, or hydrostatic pressure. For this, two typical setups are used that are illustrated in Figure 3.10. Devices with normal contacts are usually measured in a Hall-bar geometry shown in Figure 3.10.(a). This geometry allows the measurement of the four-terminal or longitudinal resistance and the Hall resistance via the longitudinal and transverse voltages. In a voltage-biased setup, an AC voltage with a frequency of $\sim 0.1 - 1\,\mathrm{kHz}$ from a lock-in amplifier is applied to a voltage divider. This scales down the applied voltage by a factor of $10^3 - 10^4$, usually resulting in a voltage bias of $0.1 - 1\,\mathrm{mV}$ on the measured device. The current flowing through the device is converted to a voltage signal by a current–voltage amplifier and is measured by the lock-in amplifier. The longitudinal and transverse voltages are amplified by differential voltage amplifiers and measured by lock-in amplifiers synchronized to the frequency of the drive signal. Additionally, the charge carrier density and transverse electric field can be controlled by gate voltages applied from DC voltage sources via pre-resistors (with typically $R_p \geq 1\,\mathrm{M\Omega}$) to limit leakage currents towards the measured device.

In case of devices with superconducting electrodes, we are usually interested in the response to a well-defined current bias (e.g. to measure the critical current of the device). This is measured in the geometry shown in Figure 3.10.(b). In this case, the AC voltage signal of the lock-in amplifier is superimposed on a DC voltage by an AC/DC mixer. The resulting voltage signal is fed to the device via a pre-resistor with a resistance much larger than the device resistance, typically $R_p = 1\,\mathrm{M\Omega}$. This generates a well-defined DC current bias, modulated by

a small AC component, flowing towards a grounded electrode. The differential resistance of the device is obtained from the four-terminal voltage measured by the lock-in amplifier. Since the electrodes are superconducting, two electrodes are sufficient to apply the current bias and measure the voltage drop over the device. However, it should be noted that the measured voltage contains both the device resistance and the contact resistance when the device is in the normal state. This measurement scheme can be used to measure the I–V curves of superconducting devices.

3.2.3 Measurement of stochastic switching events

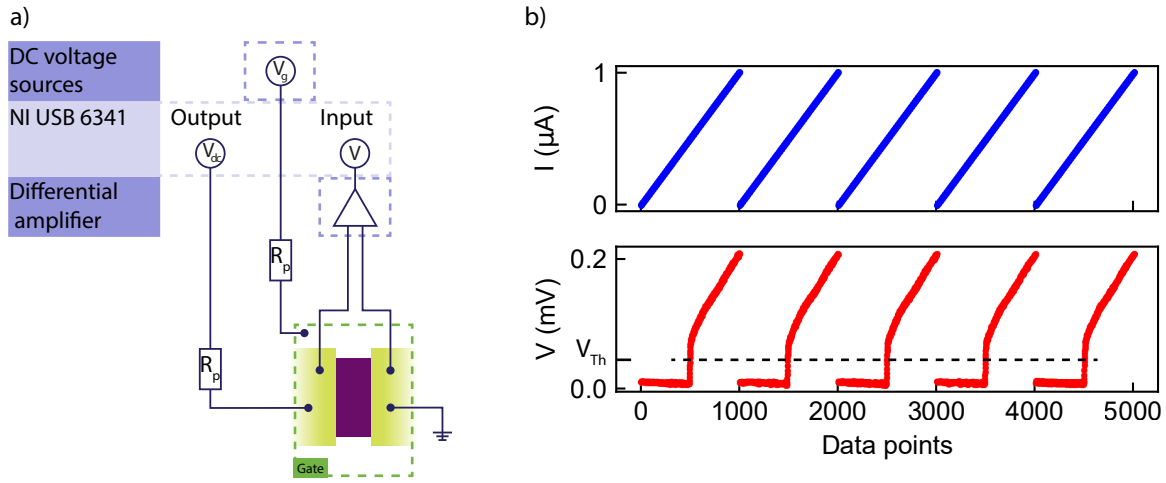

Figure 3.11: a) Measurement setup using the National Instrument USB 6341 measurement card. A DC voltage is applied from the output of the measurement card to the measured device via a R_p pre-resistor. The pre-resistor defines the current-bias that flows towards the grounded electrode. The resulting voltage drop over the device is amplified and measured on the input of the measurement card. b) Typical measurement of the switching current distribution of a superconducting device. A saw-tooth function of bias current is applied from the measurement card (top panel) and the voltage response is measured (bottom panel). The series of switching currents can be determined numerically from the measured voltage data as the current bias values where the measured voltage exceeds a suitably chosen threshold voltage V_{Th}.

The measurement setup shown in Figure 3.10.(b) is often used to measure the I–V curve of superconducting devices. The lock-in technique allows the detection of critical currents below 100 nA. However, as a result of the low frequency of the lock-in signal and the relatively slow communication with the measurement computer, to measure maps of I–V curves as a function of external parameters in this setup can take multiple hours. Furthermore, as discussed in Section 2.5.3, the switching of a Josephson junction is a stochastic process, described by a probability distribution function. The measurement of this distribution function involves the repeated measurement of the switching current, typically 10 000 times. This measurement is incompatible with lock-in technology, where the measurement of a single I–V curve can take minutes.

To enable the measurement of the switching current distribution of superconducting devices, I developed a measurement scheme to obtain several I–V curves in a short time. This setup is shown in Figure 3.11.(a) and is based on a National Instruments USB 6341 data acquisition device, hereafter referred to as the measurement card. The measurement card features multiple analog inputs and outputs. A DC voltage from the measurement card is converted to a current bias by the R_p pre-resistor and the current flows through the device towards a grounded elec-

trode. The voltage drop over the device is measured with the measurement card. A significant speed-up can be achieved with this setup compared to the setup based on lock-in technique by making use of the internal buffer of the measurement card. The measurement card can be programmed to apply a pre-defined set of voltages with a maximum sampling rate of $2 \cdot 10^5\,\mathrm{s}^{-1}$ and simultaneously measure the voltage on its input with the same sample clock frequency. By applying current bias in the form of a saw-tooth function, this allows the measurement of multiple I–V curves that are transferred to the computer in a single communication step. In contrast, when lock-in technique is used, a single current bias value is set and then the lock-in signal is read out by the computer. Therefore, it takes $2N$ communication steps to measure an I–V curve consisting of N data points. On the other hand, using the measurement card, multiple I–V curves can be measured in a single communication step, resulting in a significant speed-up of the measurements. Measurement time in this case is limited by the sampling rate of the device and the time to transfer the large amount of measured data. Even for a single I–V curve, measurement time can be reduced from minutes to seconds.

Measurement of the switching current distribution consists of repeating current bias sweeps several times (usually 10 000) and numerically determining the series of switching currents. This is typically done using a suitably chosen threshold voltage V_{Th}. This method is illustrated in Figure 3.11.(b). In each period of the saw-tooth function, when the applied current bias is below the switching current, the measured voltage is zero. When the device switches to the normal state, the measured voltage rises sharply and the switching current can be numerically determined as the current bias value where the measured voltage exceeds V_{th}. Counting the different switching current values into several narrow bins to create a histogram directly probes the probability distribution function of the switching current. I also developed the required measurement and data processing routines based on the QCodes data acquisition framework and the NI-Daqmx python package.

Although the basic concept of the measurement setup is simple, implementation in a real measurement system is challenging. Special care has to be taken to eliminate all external factors that might cause the fluctuation of the measured signal. Among others, ground loops and even the sensors of the dilution refrigerator can cause noise in the measurements. The elimination of these is highly specific to the measurement system, therefore, we do not discuss it in detail. The key elements include the isolation of the measurement instruments from the computer by optoelectronic isolators, disconnecting all sensors of the dilution refrigerator that are not necessary for its safe operation, and eliminating ground loops.

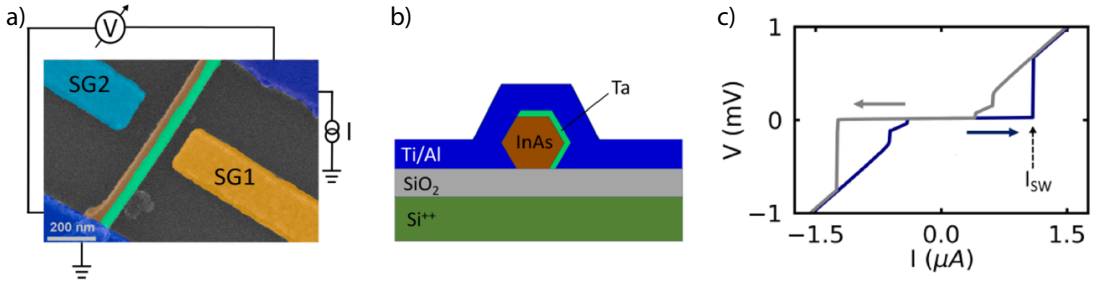

Figure 3.12: a) False-colored electron microscopic image of a superconducting nanobridge device. The Ta/InAs nanowire (green/brown) is contacted with Ti/Al electrodes (blue). Metallic sige gates (orange and light blue) are deposited on the substrate, next to the nanobridge. b) Schematic cross-section of the device under a contact. c) I–V characteristic of the device. A significant hysteresis can be observed in the switching and retrapping currents which is attributed to self-heating in the normal state.

The measurement scheme I developed was first used in the work of Tosson Elalaily [179]. This work investigated the origin of gate-controlled supercurrent (GCS) in superconducting

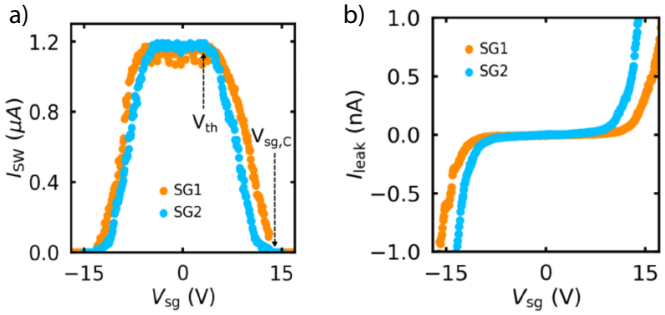

Figure 3.13: a) Switching current as a function of side gate voltages. Above a threshold voltage V_{th}, I_{sw} drops sharply. b) Leakage current between the gate and the nanobridge. The amplitude of the leakage current increases significantly above V_{th}, suggesting the the decrease of I_{sw} is caused by the Joule heat dissipated by the leakage current.

nanobridges. An electron microscopic image of one of the measured devices is shown in Figure 3.12.(a). The device consists of a 20-nm-thick Ta superconducting layer deposited on the surface of an InAs nanowire connecting two Ti/Al contacts. Figure 3.12.(b) shows the cross-section of the device. A typical I–V curve measured in a dilution refrigerator at $T_{base} = 35$mK temperature is presented in Figure 3.12.(c). Here, a large hysteresis can be observed as the switching current I_{sw} is significantly larger than the retrapping current. This is attributed to the Joule heat dissipated in the normal state that heats up the device and temporarily reduces the critical current. As the current sweep direction is reversed and the device returns to the zero voltage state, it cools back to the base temperature, which leads to a significant difference between the switching and retrapping currents.

Devices also feature metallic side gates deposited next to the nanobridges with a horizontal spacing in the range from 30 to 120 nm. Figure 3.13.(a) shows the switching current of a device as a function of the voltage applied to one of its side gates V_{sg}. I_{sw} is constant below a threshold gate voltage ($|V_{sg}| < V_{th}$) and drops rapidly as $|V_{sg}|$ increases. This effect is termed gate-controlled supercurrent which was observed in different superconducting nanostructures. As shown in Figure 3.13.(b), the decrease of I_{sw} correlates with the increase of leakage current from the side gate to the nanobridge. This suggests that heat from the leakage current is responsible for the decrease of I_{sw}. By investigating the switching current distribution (SCD) of such devices, it was possible to reveal the physical process responsible for the GCS.

SCDs were obtained by extracting I_{sw} from 10 000 I-V curves and counting the different values. The obtained histograms are normalized and shown in Figure 3.14. Figure 3.14.(a) shows the obtained SCDs for different $|V_{sg}|$ measured with positive and negative gate voltage polarity. Here, a significant difference can be seen between the two polarities. The measured I_{sw} values are significantly smaller for negative V_{sg} (blue) than for positive polarity (red) with equal $|V_{sg}|$. In contrast to this, Figure 3.14.(b) shows SCDs measured at equal dissipated power, calculated as $P_G = I_{leak}V_{sg}$, for both gate voltage polarities. Here, the measured SCDs are closely matched, indicating that the decrease of I_{sw} is almost independent of the direction of the leakage current. These findings can be explained by the injection of high-energy electrons into the substrate and the generation of phonons during the relaxation process. The process for positive V_{sg} is illustrated in Figure 3.14.(c). High-energy electrons leave the nanobridge and undergo a series of relaxation events. Due to the small energy relaxation length in the insulating substrate, they loose most of their energy close to the nanobridge. For opposite gate voltages, energy relaxation takes place closer to the gate electrode but phonons can still propagate towards the nanobridge. This explains the slight difference in the measured SCDs for opposite gate voltage polarities with equal P_G.

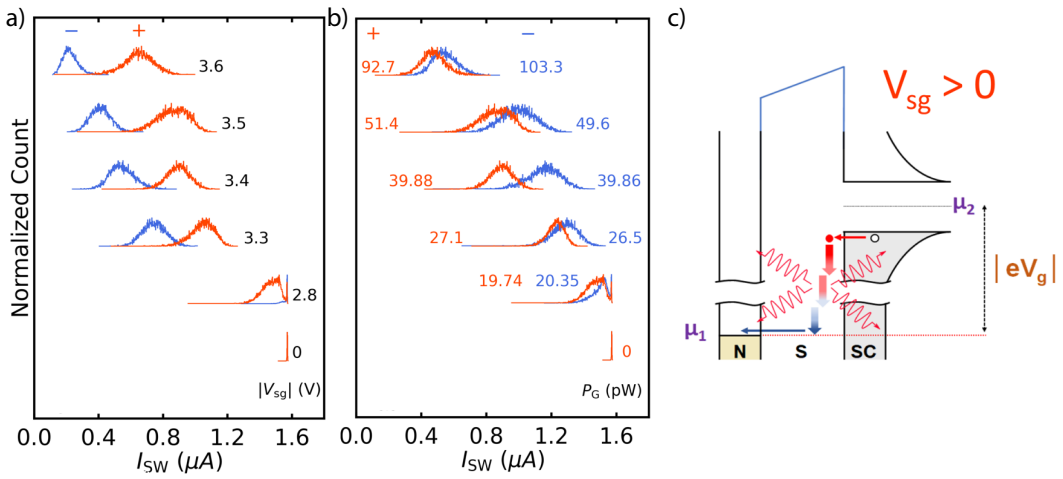

Figure 3.14: Switching current distributions for a) different $|V_{sg}|$ and b) different heating power $P_G = I_{leak}V_{sg}$ with positive (red) and negative (blue) gate voltage polarity. c) Illustration of the physical process responsible for the GCS. For $V_{SG} > 0$, high-energy electrons are injected from the nanobridge into the substrate where phonons are generated close to the nanobridge by a series of relaxation events.

Chapter 4

Experimental investigation of spin–orbit coupling in single-layer graphene

4.1 Introduction

SOC in graphene is a key element for spintronics applications [19] as it allows to control the spin information via electric fields [16–18]. Furthermore, both the intrinsic [10] and proximity-induced SOC [20] was predicted to give rise to topological states in graphene. In this chapter, I summarize the key aspects of References [28] and [29]. I was involved in the discussions on the measurements and contributed to these two works by fabricating different graphene-based Van der Waals heterostructures. Reference [28] concerns the experimental characterisation of proximity-induced SOC in SLG. In this work, four hBN/SLG/WSe_2 devices were investigated by our collaborators and my supervisor at the University of Basel, I fabricated one of them, device C (using the notations of the article). This device enabled the investigation of spin–orbit scattering times related to SOC as a function of the momentum relaxation time, as it will be discussed below. Furthermore, the investigation of proximity-induced SOC in our research group was significantly boosted by the development of a measurement technique detailed in Reference [29] that allowed the transport measurement of nanoelectronic devices under hydrostatic pressure. I contributed to this project by fabricating an hBN/SLG/hBN device that was used to prove that hBN can be effectively used to protect such heterostructures from the pressure mediating medium (device A in the corresponding article). I also present here the experimental results that are beneficial for the understanding of the following chapters.

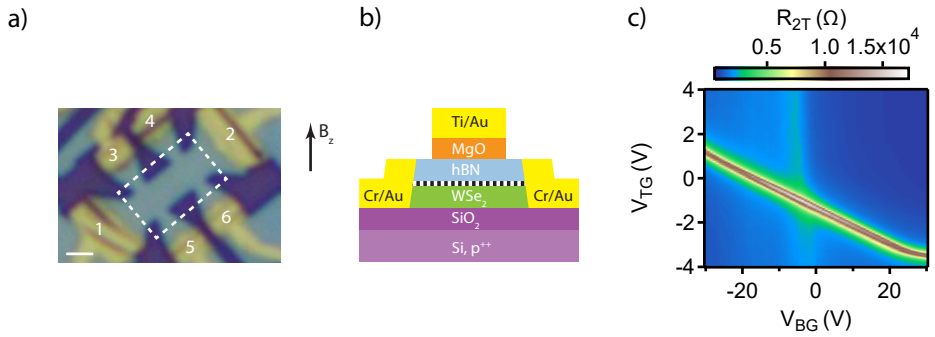

Figure 4.1: a) Optical microscopic image of Device A. The outline of the topgate electrode is illustrated by white dashed line. Scale bar is 1 μm. b) Schematic cross-section the device. c) Two-terminal resistance R_{2T} as a function of V_{TG} topgate and V_{BG} backgate voltages.

4.2 Characterisation of proximity-induced spin–orbit coupling

As mentioned earlier, in Reference [28], the proximity-induced SOC was investigated in four hBN/SLG/WSe_2 heterostructures (devices A-D). Figure 4.1.(a) shows the optical microscopic image of device A. All other devices featured similar geometries. As it is also illustrated in Figure 4.1.(b), single-layer graphene is encapsulated between a WSe_2 and an hBN layer. Cr/Au normal electrodes are fabricated using electron beam lithography and the heterostructure is etched into a Hall-bar geometry using reactive ion etching. An MgO dielectric layer is deposited on top of the device to isolate the Ti/Au top gates from the contacts. The outline of the topgate electrode is illustrated by white dashed line in Figure 4.1.(a). The highly doped Si substrate is employed as backgate electrode. The two-terminal resistance measured between contacts 1 and 2 of device B as a function of V_{TG} topgate and V_{BG} backgate voltages is shown in Figure 4.1.(c). Here, the diagonal, high-resistance feature corresponds to the charge neturality point that is tunable by both V_{TG} and V_{BG}. An additional, vertical line of higher resistance independent of V_{TG} is also visible. This is due to the dual-gated structure since the topgate electrode covers the heterostructure only partially, therefore, there is a region that is tuned only by the backgate. More importantly, the simultaneous application of V_{TG} and V_{BG} allows the independent tuning of charge carrier density n and transverse electric field, as detailed in Section 2.4.1.

As discussed in Section 2.4.2, the spin–orbit coupling strengths can be extracted from magneto-conductance measurements. The presence of strong SOC in a diffusive conductor causes the precession of electron spin between scattering events which leads to weak anti-localization (WAL), manifesting in a peak in the magneto-conductance at low temperatures. Figure 4.2 shows the quantum correction to the magneto-conductance of device A as a function of out-of-plane magnetic field B_z. Here, the classical magneto-conductance background measured at 30 K is subtracted from the magneto-conductance curve measured at 0.25 K and the resulting curve yields the correction from WAL. To eliminate the effect of universal conductance fluctuations, an average is taken over multiple charge carrier densities in the range $-2.5\times10^{11} < n < 2.5\times10^{11}\,\mathrm{cm}^{-2}$. It is important to note that, in this device, WAL can only be investigated close to the CNP where the mean free path is small and the device is diffusive. The resulting curves can be fitted by the following formula:

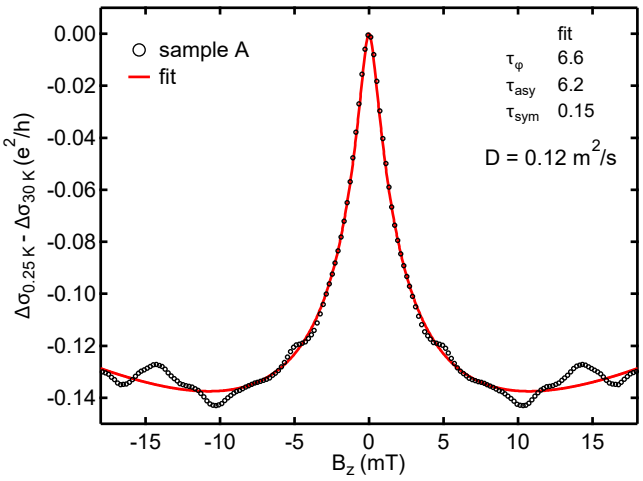

Figure 4.2: Quantum correction to the conductance as a function of out-of-plane magnetic field B_z. The curve is obtained by subtracting the classical magneto-conductance background measured at 30 K from the magneto-conductance curve measured at 0.25 K. To eliminate the effect of universal conductance fluctuations, an average is taken over multiple charge carrier densities around the CNP. A fit to the measured data is also shown (red solid line) using Equation 4.1. The obtained fit parameters (in units of ps) are also illustrated.

$$\Delta\sigma(B) = \frac{e^2}{2\pi h}\left[F\left(\frac{\tau_B^{-1}}{\tau_\phi^{-1}}\right) - F\left(\frac{\tau_B^{-1}}{\tau_\phi^{-1}+2\tau_{asy}^{-1}}\right) - 2F\left(\frac{\tau_B^{-1}}{\tau_\phi^{-1}+\tau_{asy}^{-1}+\tau_{sym}^{-1}}\right)\right], \tag{4.1}$$

where $F(x) = \ln x + \Psi\left(1/2 + 1/x\right)$ with $\Psi(x)$ being the digamma function, $\tau_B^{-1} = 4eDB/\hbar$, where D is the diffusion constant, τ_ϕ is the phase coherence time and τ_{asy} (τ_{sym}) is the spin–orbit scattering time related to SOC terms that are asymmetric (symmetric) upon z/-z inversion [180], as also discussed in Section 2.4.2. By fitting the curve shown in Figure 4.2 with Equation 4.1, it can be shown that the symmetric SOC is significantly stronger than the asymmetric SOC, since $\tau_{sym} \ll \tau_{asy}$.

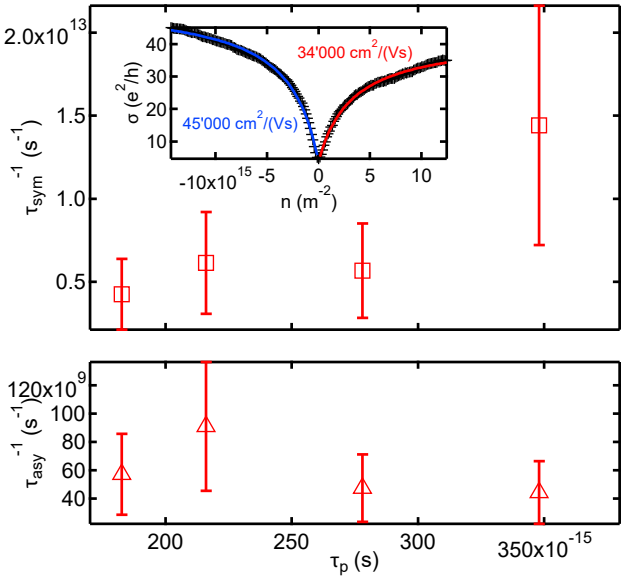

Figure 4.3: The dependence of the symmetric τ_{sym}^{-1} (top) and asymmetric τ_{sym}^{-1} (bottom) spin–orbit scattering rates on the momentum relaxation time τ_p. The inset shows the two-terminal conductivity as a function of n. The extracted charge carrier mobilities for the electron (red) and hole (blue) sides are also illustrated.

Since the analysis shown above can only be performed in the diffusive regime, the high quality of device A and B limited the available charge carrier density range. On the other hand, device C enabled measurements at larger carrier densities in the diffusive regime due to its more modest charge carrier mobility. Since the momentum relaxation time τ_p can be tuned by the carrier density, these measurements allowed the investigation of spin–orbit scattering times as a function of τ_p, extracted from electric field effect measurement. Figure 4.3 shows the dependence of the spin–orbit scattering rates τ_{sym}^{-1} and τ_{asy}^{-1} on τ_p, corresponding to different charge carrier densities. The inset shows the two-terminal conductivity as a function of n. From this, the charge carrier mobility μ can be determined. Assuming constant μ, τ_p can be calculated for a given n, according to the Drude model (see Section 2.4.1). The dependence of τ_{sym}^{-1} on τ_p allows to exclude the intrinsic SOC from the contributing SOC types since, as detailed in Section 2.4.2, it is expected to relax spins via the Eliott-Yafett mechanism, where the spin relaxation time scales linearly with τ_p. However, as it is visible in Figure 4.3, the relaxation rate τ_{sym}^{-1} increases with τ_p which does not support the Eliott-Yafett mechanism.

To briefly summarize, these measurements allowed the estimation of SOC strengths in SLG/WSe_2 heterostructes. As discussed in Section 2.4.2, the spin–orbit scattering times can be used to calculate the SOC strengths. The main contribution to the symmetric SOC scattering rate τ_{sym}^{-1} was found to be the Valley-Zeeman SOC term with an estimated strength from

$\lambda_{VZ} \sim 0.23$ to 2.3 meV. Furthermore, the asymmetric SOC scattering rate around the CNP is determined by the Rashba SOC which was found to be much weaker, around $\lambda_R \sim 0.35$ meV. It is also important to note that, in this system, the Rashba SOC is responsible for the relaxation of out-of-plane spins and τ_{asy}^{-1} represents the out-of-plane spin relaxation rate $\tau_{\perp}^{-1}$, while the overall spin-orbit scattering rate $\tau_{SO}^{-1} = \tau_{asy}^{-1} + \tau_{sym}^{-1}$ represents the in-plane spin relaxation rate $\tau_{\parallel}^{-1}$ [84]. Using the extracted spin–orbit scattering times, a lower bound for the spin relaxation anisotropy $\tau_{\perp}/\tau_{\parallel} \sim 20$ can be given. These measurements are also the first experimental demonstrations of the large spin-relaxation anisotropy in these systems using WAL measurements.

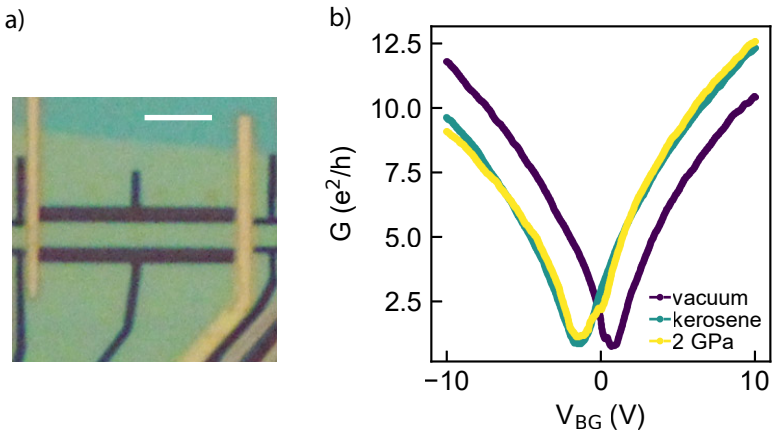

Figure 4.4: a) Optical microscopic image of an hBN/SLG/hBN heterostructure with Cr/Au contacts in a two-terminal geometry. Dark regions were etched away defining a straigth channel with a width of $W = 1.7\,\mu$m and a length of $L = 12.7\,\mu$m. Scale bar is $5\,\mu$m. b) Two-terminal conductance of the device as a function of V_{BG} backgate voltage in three different cases: before exposing the heterostructure to kerosene, in kerosene and under a hydrostatic pressure of 2 GPa.

4.3 Boosting proximity spin–orbit coupling with pressure

Having established that a sizable SOC can be induced in graphene by placing it in close proximity to WSe_2, we have focused on tuning this induced SOC via hydrostatic pressure. To this end, a measurement technique was developed in our research group that allows the measurement of nanoelectronic devices under hydrostatic pressure [29]. An important step in the development of the pressure cell measurement technique was to test whether the kerosene which acts as a pressure mediating medium influences the properties of Van der Waals heterostructures. Figure 4.4.(a) shows the optical microscopic image of an hBN/SLG/hBN heterostructure with Cr/Au contacts in a two-terminal geometry I fabricated to enable this measurement. The doped Si substrate is used as a global backgate. Figure 4.4.(b) shows the two-terminal conductance of the device as function of V_{BG} backgate voltage in three different scenarios: before placing it in kerosene, in kerosene environment and after a hydrostatic pressure of 2 GPa had been applied to the heterostructure. As it is easily visible, although the presence of kerosene slightly shifts the position of the CNP, indicating a small doping effect, it does not affect the overall quality of the device. To further quantify this, the charge carrier mobility was extracted in all cases and found to vary less than 10%, reaching 55 000 $\mathrm{cm}^2/\mathrm{Vs}$ and 50 000 $\mathrm{cm}^2/\mathrm{Vs}$ for electrons and holes, respectively. Furthermore, contact resistances were also found to be independent of

the applied pressure. In conclusion, these measurements suggested that hBN can be efficiently used to isolate graphene-based heterostructures from the kerosene environment and that the electronic quality of such devices is not influenced by the applied hydrostatic pressure.

To showcase the efficiency of tuning the proximity-induced SOC by hydrostatic pressure, in Reference [30], Bálint Fülöp et al. investigated the magneto-conductance of hBN/SLG/WSe_2 devices similar to device A under pressure. Such a WAL measurement is shown in Figure 4.5.(a). Here, similarly to Figure 4.2, the low-temperature quantum correction to the conductivity is shown, averaged over multiple densities to eliminate universal conductance fluctuations. It can be seen that without applied pressure, the device shows weak localization indicative of weak induced SOC. However, as the pressure is increased, a clear WAL peak appears in the magneto-conductance as a result of increased SOC as the layers are compressed. The resulting curves can be once again fit according to Equation 4.1 as shown by blue solid lines in Figure 4.5.(a). In this case, the Valley-Zeeman SOC term could not be extracted reliably from the fits. However, the extracted Rashba SOC strength shows an increase from $\lambda_R \sim 250\,\mu$eV to $450\,\mu$eV for an applied pressure of 1.8 GPa. These measurements showed that the proximity-induced SOC can be efficiently increased by applying hydrostatic pressure to Van der Waals heterostructures.

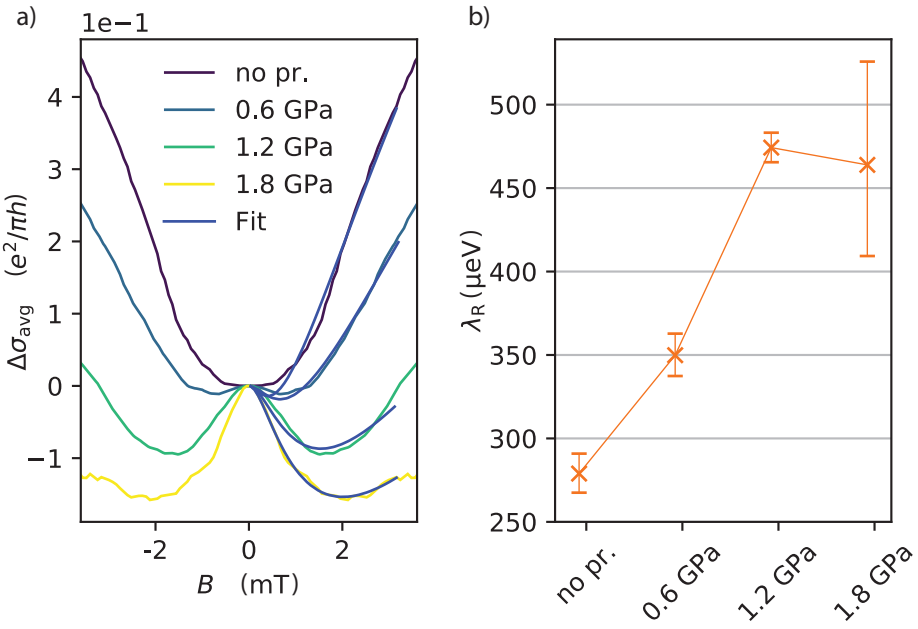

Figure 4.5: a) Quantum correction of the magneto-conductance of an hBN/SLG/WSe_2 heterostructure for different hydrostatic pressures. A large WAL conductance peak develops, indicating that the proximity-induced SOC is increased by the pressure. Solid blue lines are fits to Equation 4.1. b) Extracted Rashba SOC strength as a function of pressure.

Chapter 5

Experimental investigation of spin–orbit interaction in WSe_2/BLG/WSe_2 heterostructures

5.1 Introduction

Using bilayer graphene instead of single-layer graphene provides additional tuning knobs, such as the tunable band gap that can be opened by a transverse electric field. The additional layer adds significant complexity also to the proximity-induced SOC. Since the induced SOC depends strongly on the distance between the graphene and TMD layers, as also shown by the pressure cell studies discussed in the previous chapter, it is expected that the SOC induced by a TMD layer will be significantly different for the two layers of BLG. This layer-dependent SOC was proposed to be used in a spin transistor [75]. Furthermore, theoretical works also predicted that BLG encapsulated in TMD layers from both sides can host a band-inverted phase (IP) with helical edge states. The inverted phase was also experimentally demonstrated in Reference [23]. Building on our previous experience with SLG/WSe_2 devices, in collaboration with TU Delft, we investigated the effect of hydrostatic pressure on this inverted phase in WSe_2/BLG/WSe_2 heterostructures. The samples were fabricated at TU Delft while the pressure cell studies were conducted in Budapest.

In this chapter, I present transport measurements that demonstrate the formation of the band-inverted phase in a BLG device encapsulated symmetrically in WSe_2 from both sides. By applying a hydrostatic pressure of 1.65 GPa, I show that this inverted phase can be stabilized. I determine the strength of induced Ising SOC from thermal activation measurements and show that it increases by almost a factor of two due to the hydrostatic pressure. Finally, I present the measurement of Landau level crossings in the quantum Hall regime and show that these crossings also indicate the increase of proximity-induced SOC with applied pressure. These results were published in Reference [31].

5.2 Device geometry and measurement setup

The measured sample is shown in Figure 5.1. The dry-transfer technique with PC/PDMS hemispheres is employed to stack, from top to bottom, hBN (35 nm)/WSe_2 (19 nm)/BLG/WSe_2 (19 nm)/hBN (60 nm)/graphite. To fabricate electrical contacts to the Hall bar, we use e-beam lithography patterning followed by a reactive ion etching step using CHF_3/O_2 mixture and finally deposit Ti (5nm)/NbTiN (100 nm) by dc sputtering. We deposit Al_2O_3 (30 nm) using ALD which acts as the gate dielectric. Finally, the top gate is defined by e-beam lithography and deposition of Ti (5 nm)/Au (100 nm). The schematic cross-section of the device is shown

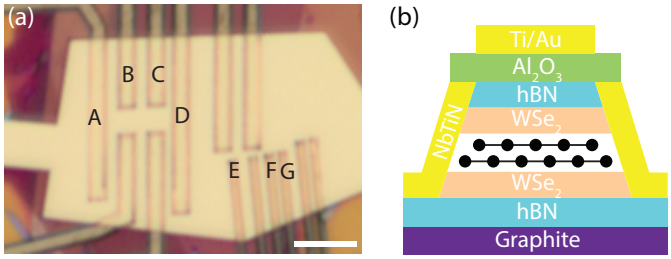

Figure 5.1: a) Optical image of the measured device. The scale bar is 4 μm. b) Schematic representation of the cross-section of the measured device. Bilayer graphene is symmetrically encapsulated in WSe_2 and hBN.

in Figure 5.1.(b).

Transport measurements were carried out in an Oxford cryostat equipped with a variable temperature insert (VTI) at a base temperature of 1.4 K (unless otherwise stated). Measurements were performed using lock-in technique with 0.1 mV AC voltage excitation at 1171 Hz frequency. Measurements presented in the main text were conducted on device S1: the AC voltage bias was applied between contacts A and D while the four-terminal voltages were measured between B and C. The results on similar devices with very similar findings are also shown in Appendix B.3.

5.3 Experimental observation of the band-inverted phase

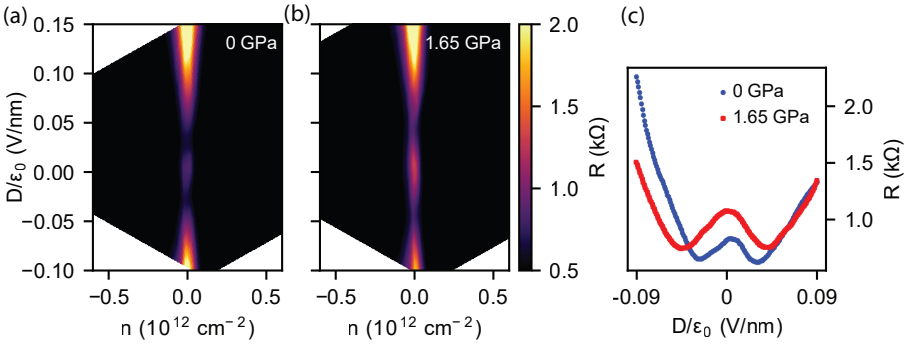

Figure 5.2: a, b) Four-terminal resistance map as a function of charge carrier density n and displacement field D measured at ambient pressure and an applied pressure of 1.65 GPa, respectively. The alternating low and high resistance regions along the CNL indicate the closing and re-opening of a band gap in the bilayer graphene. c) Line trace of the four-terminal resistance along the CNL for ambient pressure (blue) and $p = 1.65$ GPa (red).

As discussed in Section 2.2.2, a transverse displacement field D applied to BLG results in a potential difference u between the layers. This interlayer potential difference leads to the opening of a band gap in pristine BLG. As shown in Section 2.3.3, the presence of an Ising SOC induced by the two WSe_2 layers modifies this picture. If $|u|$ is larger than the Ising SOC strength λ_I, a band gap opens similarly to pristine BLG. However, as the displacement field is decreased, the band gap closes for $|u| = \lambda_I$ and reopens for $|u| < \lambda_I$ as the IP is reached. The effect of Ising SOC and u on the band structure is further illustrated in Appendix B.1.

Figure 5.2.(a) shows the resistance measured in a four-terminal geometry as a function of n and D at ambient pressure at 1.4 K temperature. As expected for BLG, we observe the opening of a band gap at large displacement fields along the charge neutrality line (CNL) at $n = 0$, indicated by an increase of resistance. In accordance with the theoretical model and previous compressibility measurements [23], we also observe two local minima separated by a resistance peak at $D = 0$ in agreement with the closing and re-opening of the band gap signalling the transition between the band insulator and the IP. This observation is further emphasized in Figure 5.2.(c), where a line trace (blue) of the resistance is shown as a function of D, measured along the CNL. It is important to note that during the fabrication process the rotation of WSe_2 layers was not controlled. However, from theoretical predictions [73, 74, 76], we only expect to observe signatures of the IP for a suitable range of rotation angles between the two WSe_2 layers (e.g. $\sim 180°$). This is further supported by the fact that not all devices fabricated showed the IP. An example for this case is shown in Appendix B.4 where only the band insulating regime can be observed in the resistance map.

To boost the induced SOC and stabilize the IP, we applied a hydrostatic pressure of $p = 1.65$ GPa and repeated the previous measurement. To apply hydrostatic pressure, the sample is placed in a piston-cylinder pressure cell as discussed in Chapter 3.2 and detailed in Ref. [29], where kerosene acts as the pressure mediating medium. To change the applied pressure, the sample is warmed up to room temperature, where the pressure is applied using a hydraulic press and the sample is cooled down again.

Figure 5.2.(b) shows the n–D map of the resistance after applying the pressure. Although the basic features of the resistance map are similar, two consequences of applying the pressure are clearly visible. First, as it is also illustrated in Figure 5.2.(c), the peak resistance in the IP at $D = 0$ increased by $\sim 25\%$. Secondly, the displacement field required to close the gap of the IP increased significantly, by about 50%. Both of these observations can be accounted for by an increase of the Ising SOC term that results in a larger gap at $D = 0$ and subsequently in a larger displacement field needed to close the gap. Altough the shift of resistance minima could be explained by the increase of ϵ_{BLG} or the decrease of interlayer separation d, these altogether are not expected to have greater effect than $\sim 20\%$ [181, 182]. It is also worth mentioning that the lever arms also change due to the applied pressure, changing the conversion from gate voltages to n and D, however, we have corrected for this effect by experimentally determining them from quantum Hall measurements (see Appendix B.2).

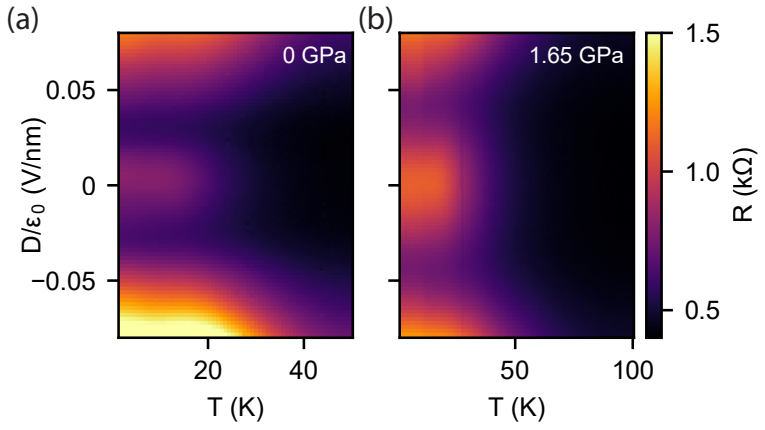

Figure 5.3: Temperature dependence of the resistance R as a function of D at $n = 0$ for a) $p = 0$ and b) $p = 1.65$ GPa.

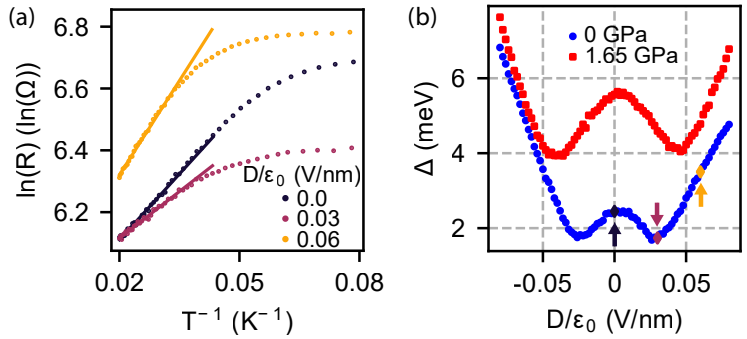

Figure 5.4: Thermal activation measurements along the charge neutrality line. a) Arrhenius plot of the resistance at ambient pressure for selected values of D. Solid lines are fits to the linear parts of the data from which the band gap values were obtained. b) Gap Δ as a function of displacement field at ambient pressure (blue) and an applied pressure of 1.65 GPa (red). Arrows indicate the D values for which the activation data is shown in a).

5.4 Thermal activation measurements

To quantify the increase of SOC gap due to hydrostatic pressure, we performed thermal activation measurements along the CNL for several values of D. Raw measurement data obtained while cooling the device is shown in Figure 5.3 for $p = 0$ and $p = 1.65\,\text{GPa}$. Similar maps were recorded while warming up the device from base temperature (not shown).

Figure 5.4.(a) demonstrates the evolution of resistance as a function of $1/T$ for selected values of D at ambient pressure. From this, we extract the band gap using a fit to the high-temperature, linear part of the data where thermal activation – $\ln(R) \propto \Delta/2k_BT$ – dominates over hopping-related effects [183]. Figure 5.4.(b) shows the extracted gap values as a function of D with and without applied pressure. First of all, a factor of 2 increase is clearly visible in the gap at $D = 0$ for $p = 1.65\,\text{GPa}$, that is consistent with the observed increase of resistance. Secondly, the higher D needed to reach the gap minima is also confirmed. We also note that the band gap cannot be fully closed which we attribute to spatial inhomogeneity in the sample.

The experimentally determined band gaps allow us to quantify the SOC parameters. By adjusting the theoretical model to match the positions of the gap minima and the opening of the trivial gap for $p = 0$, we extract $\lambda_I^t = -\lambda_I^b = 2.2 \pm 0.4\,\text{meV}$. Similarly, we can extract the SOC parameters at $p = 1.65\,\text{GPa}$. For these, we obtain $\lambda_I^t = -\lambda_I^b = 5.6 \pm 0.6\,\text{meV}$. The SOC parameters extracted from the minima give the same order of magnitude estimate as the gaps at $D = 0$ extracted from thermal activation directly. A more detailed discussion on the extraction and possible errors is given in Section 5.6. We expect that all layer distances (e.g. hBN-hBN, BLG-WSe_2 and d) change due to the applied pressure as it is also reflected in the change of lever arms. The extracted increase of SOC strength due to the change of BLG-WSe_2 distances is consistent with theoretical predictions in Ref. [30] where almost a factor of 3 increase was predicted for an applied pressure of 1.8 GPa. Importantly, we have found similar results in two further devices shown in Appendix B.3.

5.5 Displacement field-driven Landau level crossings

The quantum Hall effect in BLG provides us another tool to investigate the Ising SOC induced by the WSe_2 layers. The two-fold degeneracy of valley isospin ($\xi = +, -$), the first two orbitals ($N = 0, 1$) and spin ($\sigma = \uparrow, \downarrow$) give rise to an eight-fold degenerate Landau level (LL) near zero-energy [88, 184, 185]. This degeneracy is weakly lifted by the interlayer potential difference,

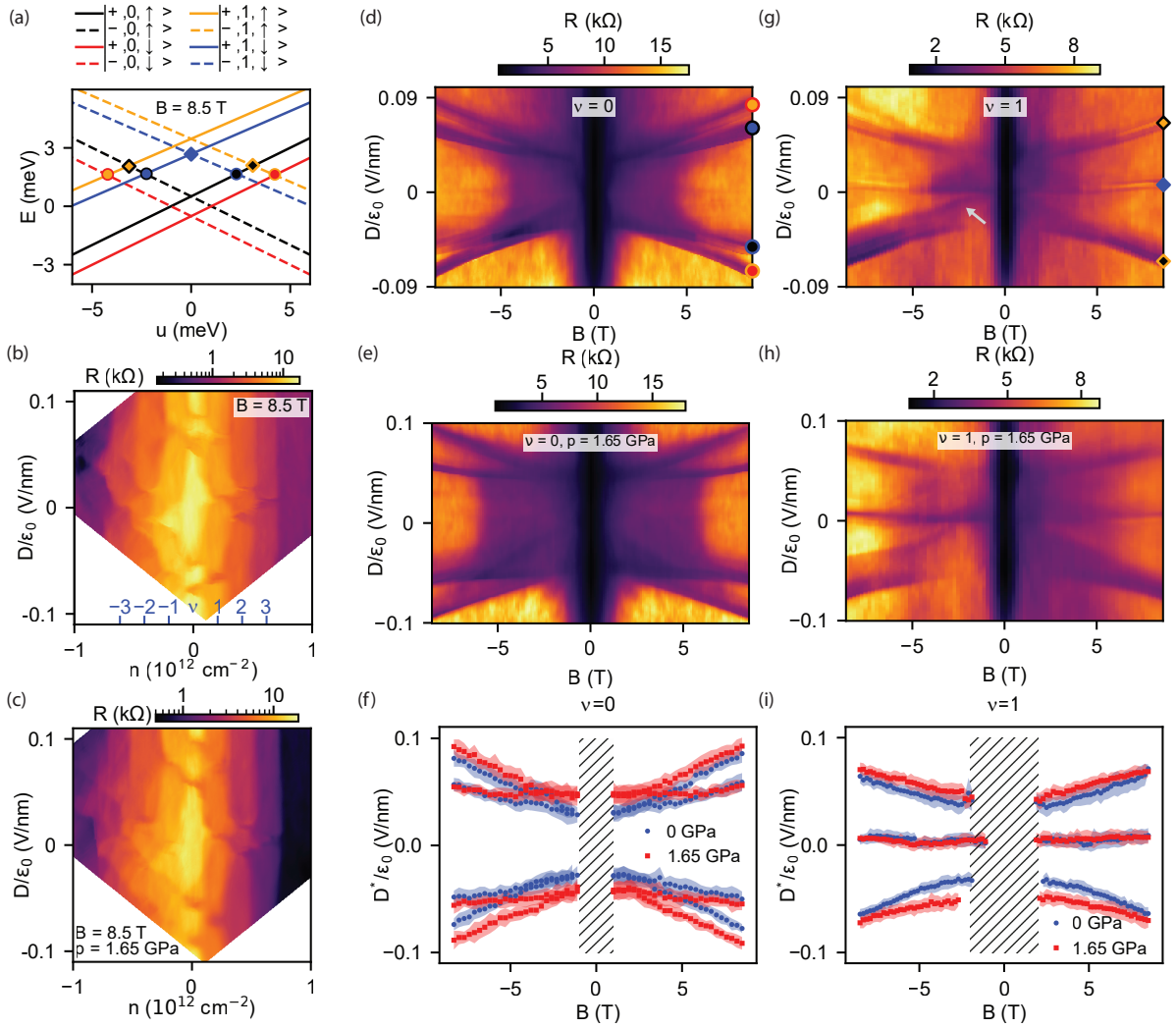

Figure 5.5: a) Low energy Landau level spectrum at $B = 8.5$ T obtained from single-particle continuum model with $\lambda_I^t = -\lambda_I^b = 2\,\text{meV}$. b,c) Four-terminal resistance as a function of n and D measured at $B = 8.5\,\text{T}$ out-of-plane magnetic field and ambient pressure for $p = 0$ and $1.65\,\text{GPa}$, respectively. Resistance plateaus correspond to different ν filling factors. Abrupt changes in resistance at a given ν as a function of D indicate the crossings of LLs. d,g) Measurements of LL crossings as a function of B for $\nu = 0$ and $\nu = 1$, respectively, for $p = 0$. Symbols denote LL crossings shown in (a). e,h) Measurements of LL crossings as a function of B for $\nu = 0$ and $\nu = 1$, respectively, for $p = 1.65\,\text{GPa}$. f,i) Critical displacement field D^* corresponding to LL crossings for $\nu = 0$ and $\nu = 1$ extracted from $D - B$ maps measured at $p = 0$ (blue) and $p = 1.65$ GPa (red).

Zeeman energy, coupling elements between the BLG layers [186] and the induced Ising SOC [45]. We can obtain the energy spectrum of this set of eight closely-spaced sublevels – labeled by $|\xi, N, \sigma\rangle$ – by introducing a perpendicular magnetic field in our continuum model, as detailed in [186]. This is shown in Figure 5.5.(a) for $B = 8.5\,\mathrm{T}$ as a function of the interlayer potential (u)[1]. LLs with different ξ reside on different layers of the BLG, therefore u induces a splitting between these levels. Secondly, the finite magnetic field causes the Zeeman-splitting of levels with different σ. Finally, the Ising SOC induces an additional effective Zeeman field associated to a given layer, further splitting the levels. The key feature that should be noted here is that for a given filling factor ν, crossings of LLs can be observed and the position of crossing points along the u axis depend on SOC parameters as well as on the magnetic field. These level crossings manifest as sudden changes of resistance in our transport measurements, as it is illustrated in Figure 5.5.(b). Here, the $n - D$ map of the resistance is shown as measured at $B = 8.5\,\mathrm{T}$ with fully developed resistance plateaus corresponding to the sublevels of $\nu \in [-4, 4]$. We note that the heterostructure was not etched into a Hall-bar shape after the contacts were deposited. Therefore, current can flow along the pristine edges of the BLG layer. For the quantum Hall measurements, this results in a non-trivial sample geometry which could result in the mixing of longitudinal and transverse resistances. For a given filling factor ν, we observe $4-|\nu|$ different D values where the resistance deviates from the surrounding plateau corresponding to the crossing of LLs, as expected from the model. The same measurement performed at an applied pressure of 1.65 GPa is shown in Figure 5.5.(c).

The evolution of LL crossings with B can be observed by performing measurements at fixed filling factors, as it is shown in Figure 5.5.(d) and 5.5.(g) for $\nu = 0$ and $\nu = 1$, respectively. During the latter measurement, the carrier density n was tuned such that the filling factor given by $\nu = nh/eB$ was kept constant, i.e. the magnetic field and both gate voltages were simultaneously swept to keep the filling factor constant. On both panels, we can observe $4 - \nu$ LL crossings that evolve as B is tuned, until they disappear at low magnetic fields where we can no longer resolve LL plateaus. Similar maps corresponding to $p = 1.65\,\mathrm{GPa}$ are shown in Figures 5.5.(e) and 5.5.(h). This B-dependent behavior enables us to investigate the effect of SOC on the LL structure. Figures 5.5.f and 5.5.i show the critical displacement field D^* values – where LL crossings can be observed – extracted from Figures 5.5.(d), 5.5.(g), 5.5.(e) and 5.5.(h). For $\nu = 0$ (Figure 5.5.(f)), the most important observation is that the crossing points do not extrapolate to zero as $B \to 0\,\mathrm{T}$ which is a direct consequence of the induced Ising SOC. It is also clearly visible that due to the applied pressure, $|D^*|$ is generally increased, especially at lower B-fields, indicating that the Ising SOC has increased, in agreement with our thermal activation measurements. For $\nu = 1$ (Figure 5.5.(i)), similar trends can be observed. The two LL crossings at finite D saturate for small B, while the third crossing remains at $D = 0$. We note that the $D^*(B)$ curves for $p = 1.65$ GPa cannot be scaled down to the $p = 0$ curves, which confirms that our observations cannot simply be explained by an increased ϵ_{BLG} or decreased interlayer separation distance, but are the results of enhanced SOC. We also point out that some lines which extrapolate to $D = 0$ can also be observed (e.g. Figure 5.5.(g), grey arrow). This could also be explained by sample inhomogeneity. It is also important to note that our single-particle model fails to quantitatively predict the B-dependence of the LL crossings indicating the importance of electron-electron interactions (see Appendix B.1).

5.6 Determination of the SOC parameters

To obtain the SOC strength from thermal activation measurements, we fit the band structure calculations to the measurements to match the observed band gaps. For this, the transverse displacement field (D) in our measurements is modeled by introducing an interlayer potential difference $u = -\frac{ed}{\epsilon_0 \epsilon_{\mathrm{BLG}}} D$, where e is the elementary charge, ϵ_0 is the vacuum permittivity, d is

[1] Calculations were performed by Bálint Szentpéteri.

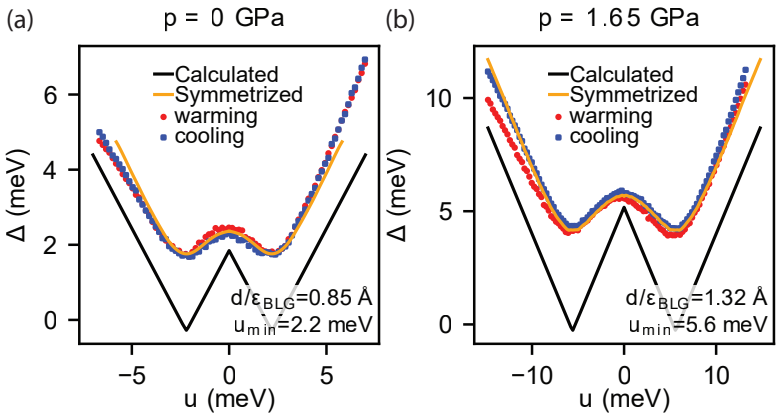

Figure 5.6: Band gaps determined from thermal activation measurements performed while warming up (red) and cooling down (blue) the device for a) $p = 0$ and b) $p = 1.65\,\mathrm{GPa}$, respectively. Symmetrized curve with respect to $u = 0$ is shown in orange (see text for details) and the band gap calculated from the theoretical model is shown with the solid black line.

the separation of BLG layers and ϵ_{BLG} is the effective out-of-plane dielectric constant of BLG. For ambient pressure, $d = 3.3\,\text{Å}$ can be taken, similarly to pristine BLG. On the other hand, the value of ϵ_{BLG} available in the literature ranges from 2.6 [187] to 6 [188]. Since in the large u limit, the band gap induced by the displacement field is independent of the SOC parameters, by varying ϵ_{BLG}, we can effectively "fit" our model to the experimental data. Figure 5.6.(a) shows the extended thermal activation data (partially presented in Figure 5.4) measured while warming up (red symbols) and cooling down (blue symbols) the sample for $p = 0$. As it is visible, in the band insulator regimes for $u \ll 0$ and $u \gg 0$, the data have different slopes. We take this effect into account by averaging the two measurements and symmetrizing it with respect to $u = 0$ (solid orange line). In the next step, we determine ϵ_{BLG} by matching the slope of the high-u part of the data to match the slope of the theoretical model (solid black line), resulting in $\epsilon_{\mathrm{BLG}} \approx 3.9$. Finally, we numerically determine the position u_{min} of the band gap minimum of the symmetrized curve and take the Ising SOC parameters as $\lambda_t = -\lambda_b = u_{min}$. We estimate the lower and upper bounds of the SOC parameter by fitting the slope of the theoretical curve to the $u \ll 0$ and $u \gg 0$ parts of averaged band gaps, respectively, yielding $\lambda_t = -\lambda_b = 2.2 \pm 0.4\,\mathrm{meV}$ for $p = 0$.

In contrast to ambient pressure, at $p = 1.65\,\mathrm{GPa}$, we expect both d and ϵ_{BLG} to change due to applied pressure. From theoretical predictions [181, 182], we expect a change in the BLG interlayer distance of $\Delta d < 5\%/\mathrm{GPa}$. However, to estimate the change in ϵ_{BLG} is more challenging. To be able to extract the SOC strength at $p = 1.65\,\mathrm{GPa}$, we vary the $d/\epsilon_{\mathrm{BLG}}$ ratio to match the experimental data to the model using the method described above. This way, for $p = 1.65\,\mathrm{GPa}$, we extract $\lambda_t = -\lambda_b = 5.6 \pm 0.6\,\mathrm{meV}$. The extracted increase in SOC strength is comparable to theoretical predictions using ab initio calculations[30]. Furthermore, the SOC parameters extracted from the minima give the same order of magnitude estimate as the extracted gaps at $u = 0$. Therefore, it is clear that the relative increase of the positions of band gap minima in D cannot alone stem from changes in the $d/\epsilon_{\mathrm{BLG}}$ ratio.

To estimate the robustness of our method, we extracted the band gaps from the thermal activation measurements at $p = 1.65\,\mathrm{GPa}$ using linear fits to different temperature ranges of the $\ln R$–$1/T$ curves. These are shown in Figure 5.7. for ranges of $40\,\mathrm{K} < T < 70\,\mathrm{K}$ (blue) and $40\,\mathrm{K} < T < 100\,\mathrm{K}$. The error bars on the figure show the error of the fit for given u and fixed temperature range. From this, we conclude that the uncertainty of the extracted band gaps is $< 20\%$. More importantly, the uncertainty of the slope of the $u \ll 0$ and $u \gg 0$ regimes and the positions of band gap minima is even less. Since in our analysis, these are the parameters that

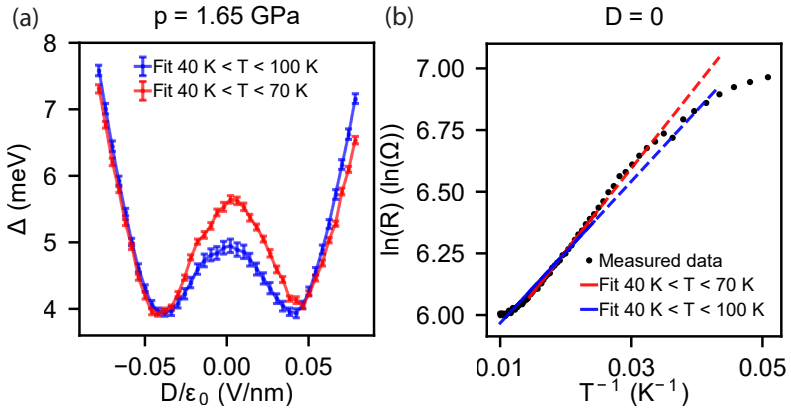

Figure 5.7: a) Band gaps determined from thermal activation measurements performed while cooling down the device at $p = 1.65\,\mathrm{GPa}$, using a linear fit to the data according to the Arrhenius formula ($\ln R \propto \Delta/2k_BT$) in the temperature range $40\,\mathrm{K} < T < 70\,\mathrm{K}$ (red) and $40\,\mathrm{K} < T < 100\,\mathrm{K}$ (blue). Error bars represent the uncertainty of the fits. b) Examples for linear fits at $D = 0$ in the temperature range $40\,\mathrm{K} < T < 70\,\mathrm{K}$ (red) and $40\,\mathrm{K} < T < 100\,\mathrm{K}$ (blue) are shown with solid lines and are extended with dashed lines for better visibility. In this case, the difference in the slopes stems from the saturation of the resistance around 100 K.

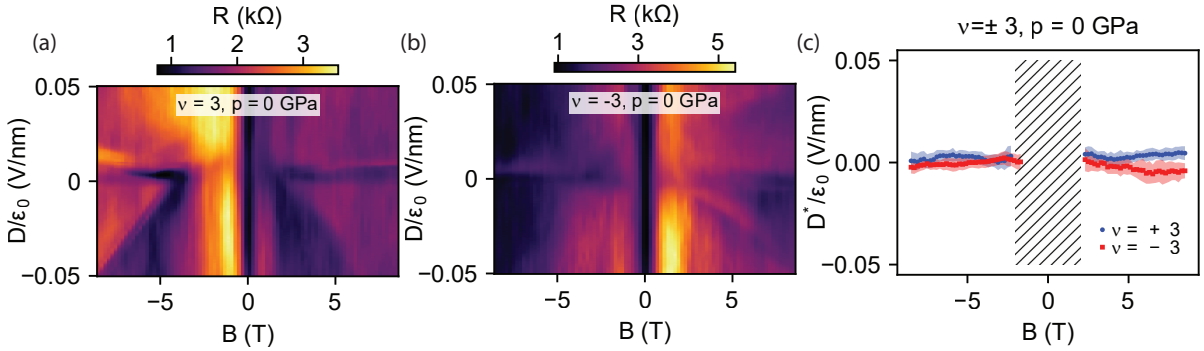

Figure 5.8: a,b) Measurements of LL crossings as a function of B for $\nu = +3$ and $\nu = -3$, respectively, for $p = 0$. c) Positions of the LL crossings extracted from the maps in a) and b) for $\nu = +3$ (blue) and $\nu = -3$ (red).

determine the extracted SOC strength, this results in an uncertainty of the $d/\epsilon_{\mathrm{BLG}}$ ratio and the SOC strength of $\sim 10\%$ that is comparable to the uncertainty estimated from the difference in the slopes of the $u \ll 0$ and $u \gg 0$ regimes.

We also have to note that, although we assumed that $|\lambda_I^b| = |\lambda_I^t|$, our method of determining the SOC parameters is only sensitive to the absolute difference of the two parameters since this quantity defines the closing of the band gap. In other words, the minima of the $\Delta(u)$ functions shown in Figure 5.6 are insensitive to a difference in the absolute values of $|\lambda_I^{b,t}|$ as long as $\left|\lambda_I^t - \lambda_I^b\right|/2$ is constant. However, we can estimate the asymmetry of $|\lambda_I^{b,t}|$ by measuring the $\nu = \pm 3$ LL crossings since, within our model, the positions of these crossings in u are separated by $u_{+3}^* - u_{-3}^* \approx |\lambda_I^t| - |\lambda_I^b|$, nearly insensitive to the magnetic field. Measurements of the LL crossings as a function of D and B for $\nu = +3$ and $\nu = -3$ are shown in Figure 5.8.(a,b), respectively. Figure 5.8.(c) shows the extracted positions D^* of the crossings for $\nu = \pm 3$. As it is visible, for the most part of our magnetic field range, the positions of the crossings are indistinguishable. At higher magnetic field we see crossings at $u_{\pm 3}^* \neq 0$, indicating a small asymmetry of the SOC parameters. From these, we can estimate the upper bound of the asymmetry as $|\lambda_I^t| - |\lambda_I^b| < 0.4\,\mathrm{meV}$ for $p = 0$.

5.7 Conclusions

In conclusion, we showed that the IP observed in BLG symmetrically encapsulated between twisted WSe_2 layers can be stabilized by applying hydrostatic pressure which enhances the proximity induced SOC. We presented thermal activation measurements as a means to quantify the Ising SOC parameters in this system and showed an increase of approximately 150% due to the applied pressure. In order to gain more information on the twist angle dependence of the SOC, a more systematic study with several samples with well-controlled twist angles is needed. The enhancement of Ising SOC with pressure was further confirmed from quantum Hall measurements. However, to extract SOC strengths from these measurements, more complex models are needed that also take into account interaction effects. Our study shows that the hydrostatic pressure is an efficient tuning knob to control the induced Ising SOC, thereby the topological phase in WSe_2/BLG/WSe_2.

The IP has a distinct topology from the band insulator phase at large D, and edge states are expected [22]. The presence of these states should be studied in better defined sample geometries [189, 190] or using supercurrent interferometry [95, 191]. This has recently been demonstrated by our collaborators in Reference [24]. Opposed to the weak protection of the edge states in this system, a strong topological insulator phase is predicted in ABC trilayer graphene [21, 192]. Furthermore, pressure could also be used in case of magic-angle twisted BLG, in which topological phase transitions between different Chern insulator states are expected as a function of SOC strength [47].

Chapter 6

Current–phase relation measurements

6.1 Introduction

The CPR is the most fundamental property of a Josephson junction. It provides information on the process underlying the supercurrent transport in the junction. It is also expected to be influenced by the SOC in the weak link [106]. As discussed in Section 2.5.4, the presence of SOC can result in the appearance of a φ_0 phase shift of the CPR [109–112] and the superconducting diode effect that manifests in the asymmetry of the critical current for different current directions [112–120].

In this chapter, I present the measurement of the CPR of a WSe_2/SLG/WSe_2 heterostructure using an asymmetric SQUID design, as discussed in Section 2.5.5. First, I present the characterization of the SQUID device in the normal state. The high quality of the device is confirmed by the observation of ballistic Fabry-Perot oscillations. After this, I show the gate-tunability of the supercurrent and the measurement of the Fraunhofer pattern. Furthermore, I discuss the measurement of the CPR as a function of gate voltages. From the measured CPR, I determine the gate-dependence of the critical current and transparency of the device junction, along with the phase shifts of the CPR. I also show that the Fabry-Perot oscillations can also be observed in the critical current of the device junction. After this, I investigate the dependence of the junction parameters on the in-plane magnetic field. Finally, I discuss the limitations of these measurements regarding the extraction of very small phase shifts. This project was also carried out in collaboration with TU Delft. The fabrication of the device presented and the measurements in this chapter were performed in Budapest. Measurements on additional devices are shown in Appendix C.

6.2 Device geometry and measurement setup

The measured device is shown in Figure 6.1. The Van der Waals heterostructure consists of six layers. As shown in Figure 6.1(a)-(f), these are – from bottom to top – the following, with the thickness indicated in brackets: graphite (< 5 nm), hBN (40 nm), WSe_2 (15 nm), single-layer graphene, WSe_2 (5 nm), hBN (25 nm). The assembled structure is shown in Figure 6.1(g) with the outline of each layer shown by dashed lines. The bottom graphite layer is used as a gate electrode. A Ti/Au (10/60 nm) electrode is fabricated to establish metallic contact to this layer (Figure 6.1(h)), deposited by electron beam evaporation. The superconducting electrodes are formed of 50-nm-thick MoRe deposited by DC sputtering following a reactive ion etching step using CHF_3/O_2 mixture (Figure 6.1(i)). The heterostructure is shaped by a RIE step using SF_6/O_2 mixture and covered by 30 nm of ALD-grown aluminium oxide. Finally, Ti/Au (10/60

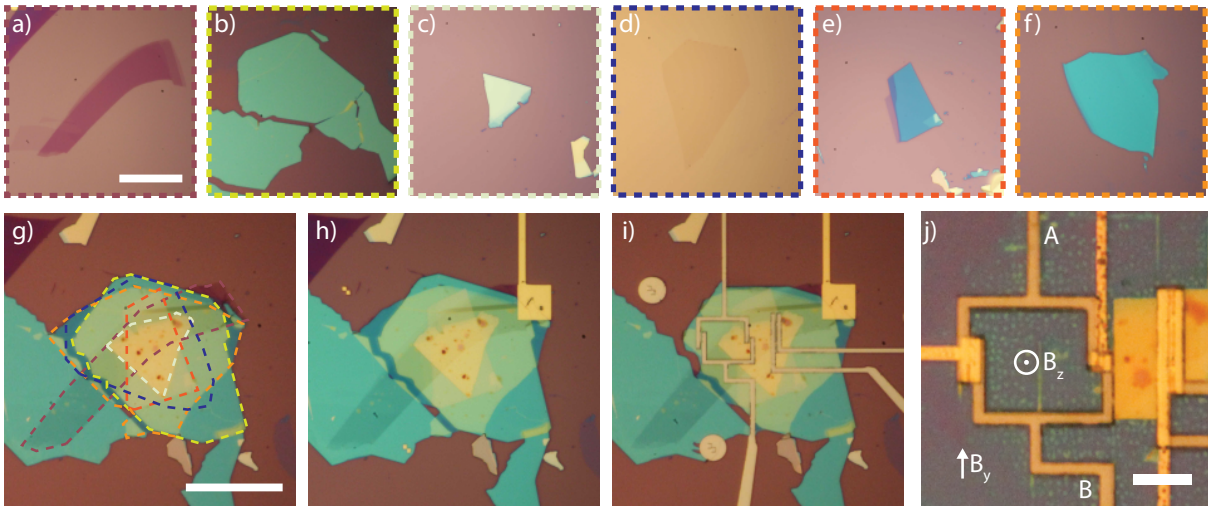

Figure 6.1: a-f) The investigated heterostructure consists of six layers. From bottom to top these are: a) graphite, b) hBN, c) WSe_2, d) single-layer graphene, e) WSe_2 and f) hBN. Scale bar for the top row is 25 μm. g) Assembled heterostructure. Scale bar is 25 μm. Dashed lines show the contours of each layer. The colors of dashed lines correspond to the colors of the borders of panels a-f). h) In the first lithography step, a metallic contact to the bottom graphite gate electrode is fabricated. i) Secondly, the SC electrodes are deposited. j) The heterostructure after the final etching step and aluminium oxide growth with the top gates fabricated. (See main text for fabrication details.) Scale bar is 5 μm.

nm) electrodes are deposited for the top gates. The finished device is shown in Figure 6.1(j).

The SQUID consists of two Josephson junctions embedded in a 10 μm×10 μm loop. To ensure a large asymmetry in their critical currents, the junctions have different geometries. The smaller junction is 500 nm×1.4 μm and the larger one is 500 nm×4.4 μm by design. From here, we refer to these junctions as the device and reference junctions and to the corrresponding top gates as device and reference top gates, respectively. The SQUID loop is positioned such that the graphite bottom gate extends only below the device junction and that the WSe_2 layers are not present in the reference junction. An additional, larger Josephson junction is also fabricated next to the SQUID loop that serves as a reference and will not be discussed here.

To measure electronic transport through the SQUID, contact B (see Figure 6.1.(j)) is grounded and a DC current I is applied to contact A via a 1 MΩ pre-resistor while the DC voltage drop V over the SQUID is measured. Charge carrier density in the reference junction is tuned by the voltage $V_{TG,ref}$ applied to the reference top gate and the device junction is tuned by the voltages V_{BG} and $V_{TG,dev}$ applied to the graphite bottom gate and the device top gate, respectively. Transport measurements were carried out in a dilution refrigerator with a base temperature of $\sim$ 40 mK.

6.3 Measurements

6.3.1 Normal state resistance

To obtain a general understanding of the graphene-based Josephson junctions embedded in the SQUID loop, we first investigate the normal state resistance $R_N = V/I$ as a function of gate voltages at a current bias of $I = 10\,\mu$A, well above the critical current of the device. These measurements are shown in Figure 6.2.(a) and 6.2.(b). Figure 6.2.(a) shows R_N as a function of $V_{TG,dev}$ and $V_{TG,ref}$. Two distinct features, a horizontal and a vertical line of high resistance can be observed. These correspond to the charge neutrality points (CNPs) of the

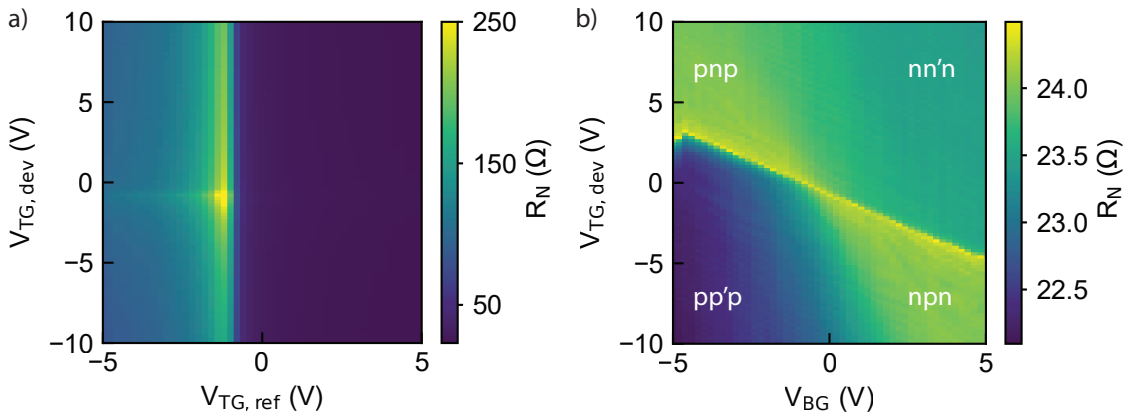

Figure 6.2: a) Normal state resistance R_N as a function of $V_{TG,dev}$ and $V_{TG,ref}$ at $V_{BG} = 0\,\mathrm{V}$. The horizontal and vertical lines correspond to the CNP of the device and reference junctions, respectively. b) R_N as a function of $V_{TG,dev}$ and V_{BG} at $V_{TG,ref} = 5\,\mathrm{V}$. The diagonal, large-resistance feature correcponds to the CNP of the device junction. The segments with different resistances can be explained by the formation of p–n junctions originating from the dual-gated structure (see main text for details).

device and reference junctions, respectively. The most essential conclusion to be drawn from Figure 6.2.(a) is that the two top gates are essentially independent since the CNPs are only tuned by their respective top gates. It is also visible that the resistance is larger for hole doping of the reference junction ($V_{TG,ref} < -1.5\,\mathrm{V}$) which is a consequence of electron doping of graphene from the MoRe contacts which results in the formation of p–n junctions near the contacts [193]. Figure 6.2.(b) shows a somewhat more complicated map of R_N as a function of $V_{TG,dev}$ and V_{BG} measured at $V_{TG,ref} = 5\,\mathrm{V}$. Although the two junctions are connected in parallel and R_N contains a contribution from both the device and the reference junction, by fixing $V_{TG,ref}$ the changes in the normal state resistance originate from the device junction only. Here, a high-resistance line corresponding to the CNP of the device junction can also be observed. Here, however, the CNP depends both on the device top gate and the bottom gate, indicating the both gates tune the charge carrier density of the device junction. The remaining part of the resistance map can be divided into four quadrants of different resistances. We attribute the appearance of these regions to the formation of p–n junctions in the device. This could be explained by the asymmetry of the device gates. While the graphite bottom gate extends below the SC contacts, the top gates are fabricated on top of them and the 30-nm-thick aluminium oxide layer and are inherently less effective near the contacts. Therefore, the doping in the device junction near the contacts can be different from the central parts and p–n junctions might form resulting in a larger normal resistance. The doping scenario corresponding to each quadrant is shown in Figure 6.2.(b).

Since the two junctions constituting the SQUID are connected in parallel by the SC loop, it is challenging to investigate their individual qualities. Nevertheless, faint oscillations can be observed in Figure 6.2.(b) which we attribute to Fabry-Perot oscillations. These periodic oscillations are better visible in Figure 6.3.(a) where a subset of the previous normal resistance map is shown in the *nn'n* doping configuration, remeasured at $V_{TG,ref} = -1.5\,\mathrm{V}$, near the CNP of the reference junction. We attribute the appearance of Fabry-Perot oscillations also to the formation of p–n junctions. As illustrated in Figure 6.3.(b), the incoming electrons are reflected with a finite probability from the p–n junctions forming around the contacts. These p–n junctions form a cavity that acts as a Fabry-Perot interferometer [194, 195]. By converting the gate voltages to charge carrier density n (see Section 2.4.1 and Appendix C), the distance between two neighboring interference fringes yields a cavity length of $l_c = \pi / \left(\sqrt{n_{i+1}} - \sqrt{n_i}\right) \approx$

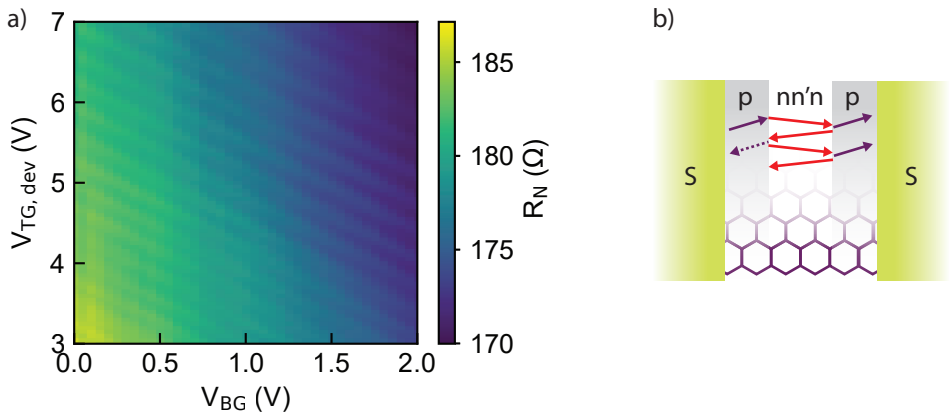

Figure 6.3: a) R_N as a function of $V_{TG,dev}$ and V_{BG} at $V_{TG,ref} = -1.5\,\mathrm{V}$. Periodic modulation of the normal resistance can be observed which is attributed to Fabry-Perot oscillations originating from the formation of different doping regions in the device. b) Illustration of the p–n junctions leading to the Fabry-Perot oscillations.

400 nm that is consistent with the length of the junction, where n_{i+1} and n are the carrier densities where the i^{th} and $(i+1)^{\mathrm{th}}$ interference fringe is observed. Most notably, the presence of Fabry-Perot interference means that electronic transport in the device junction is phase coherent and ballistic, indicating its high quality.

6.3.2 Supercurrent measurements

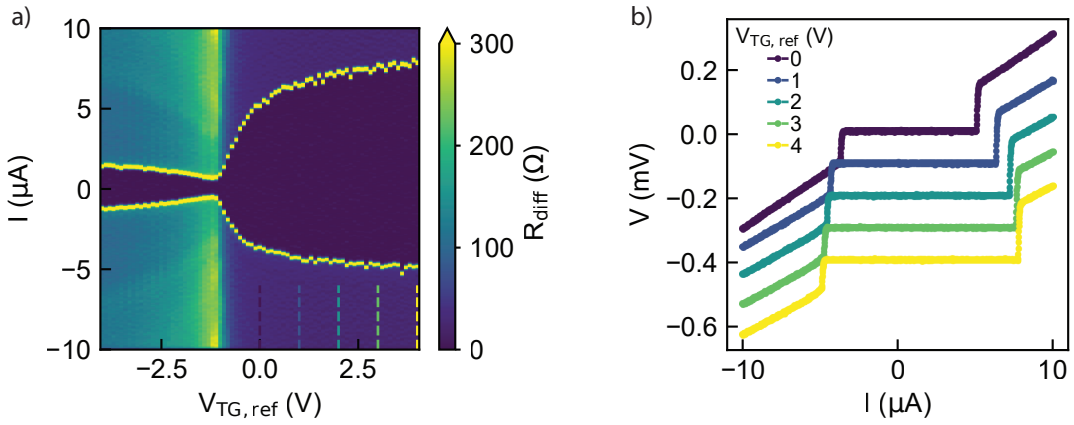

Figure 6.4: a) Differential resistance R_{diff} as a function of current bias I and reference top gate voltage $V_{TG,ref}$ measured at $V_{TG,dev} = V_{BG} = 0\,\mathrm{V}$. b) Raw $I-V$ curves measured at the gate voltages shown by dashed lines in panel a). Curves are offset for better visibility.

Having obtained the general behaviour of the normal resistance, we turn our attention towards the basic characterisation of supercurrent in the SQUID. Introduction to SQUIDs is given in Section 2.5.5. Without any applied magnetic fields, we expect that the total critical current of the SQUID is equal to the sum of critical currents of the device and reference junctions. Since the reference junction is intentionally designed to be ~ 3 times wider than the device junction, the reference top gate has a significantly larger effect on the total critical current than the other gates. For this reason, in Figure 6.4.(a), we present the differential resistance $R_{\mathrm{diff}} = dV/dI$ as a function of current bias I and $V_{TG,ref}$ measured at $V_{TG,dev} = V_{BG} = 0\,\mathrm{V}$, close to the CNP of the device junction. As it is common for similar graphene-based Josephson

junctions, a largely tunable critical current is observable that is smallest around the CNP ($V_{TG,ref} \approx -1.5\,\mathrm{V}$) of the reference junction and increases towards larger positive and negative gate voltages. The criticial current for $V_{TG,ref} \ll -1.5\,\mathrm{V}$ is consistently smaller than what is observed for $V_{TG,ref} \gg -1.5\,\mathrm{V}$. We attribute this also to the formation of p–n junctions due to negative doping from the MoRe contacts, in agreement with previous observations on similar devices [193]. This smaller critical current is also consistent with the larger normal resistance observed in Figure 6.2.(a). Figure 6.4.(b) shows the raw measured voltage V as a function of the current bias I for selected reference top gate voltages illustrated by dashed lines in Figure 6.4.(a). These I–V curves demonstrate the underdamped characteristics of the SQUID since a large hysteresis in the switching and retrapping currents can be observed.

Additional information can be gained about the flow of supercurrent by studying its magnetic field dependence (see Section 2.5.1). This is presented in Figure 6.5 where R_{diff} is shown as a function of I and out-of-plane magnetic field B_z (see also Figure 6.1.(j) for magnetic field orientation) measured at $V_{TG,ref} = V_{BG} = 0\,\mathrm{V}$ and $V_{TG,dev} = 2\,\mathrm{V}$. Due to the geometric difference between the device and reference junctions, we assume that the main contribution to the supercurrent originates from the reference junction. Most importantly, a regular Fraunhofer pattern can be observed which indicates that the ditribution of supercurrent in the reference junction is homogeneous. The expected periodicity of the Fraunhofer pattern for the reference junction is $\Phi_0/(4.4\,\mu\mathrm{m}\times 500\,\mathrm{nm}) \approx 1\,\mathrm{mT}$. The observed periodicity is about a factor of two smaller than expected. We attribute this to flux focusing due to the Meissner effect that expels the magnetic field from the MoRe contacts and leads to the increase of flux in the Josephson junctions [196] and results in a smaller periodicity than what is expected merely from geometric considerations. It is also worth noting that the Fraunhofer pattern is not centered around $B_z = 0$. This is a measurement artefact and the consequence of trapped fluxes in the superconducting vector magnet used to generate the external magnetic field. This could also explain the discrepancy between the largest critical current values observed in the magnetic field dependence (Figure 6.5) and the reference top gate dependence measurements (Figure 6.4.(a)). Even though no external magnetic field is applied during the measurement presented in Figure 6.4.(a), the presence of a trapped magnetic flux can cause the reduction of the critical current of the SQUID.

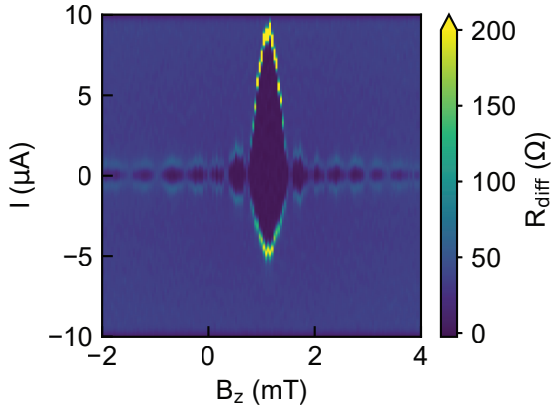

Figure 6.5: Differential resistance R_{diff} as a function of current bias I and out-of-plane magnetic field B_z measured at $V_{TG,ref} = V_{BG} = 0\,\mathrm{V}$ and $V_{TG,dev} = 2\,\mathrm{V}$. The magnetic field dependence of the critical current exhibits a regular Fraunhofer pattern indicative of homogeneous supercurrent distribution in the reference junction.

6.3.3 Current–phase relation measurements

As detailed in Section 2.5.5, to measure the current-phase relation of the device junction, a large asymmetry between the critical currents of the two junctions has to be ensured. For this reason, we set the reference top gate voltage to $V_{TG,ref} = -0.4\,\mathrm{V}$ which results in a switching current of $\sim 7\,\mu\mathrm{A}$. Furthermore, to ensure that the CPR is measured around the *net zero* magnetic field, an iterative procedure is used to locate the center of the Fraunhofer pattern by repeatedly measuring the pattern while gradually decreasing the magnetic field range around its central lobe. This step is necessary to eliminate the effect of any trapped magnetic flux or hysteresis in the magnetic field. When the magnetic field range is sufficiently small, the SQUID oscillations become visible. This is illustrated in Figure 6.6.(a) where the measured switching current I_s is shown around the effective zero magnetic field for different values of $V_{TG,dev}$ and $V_{BG} = 5\,\mathrm{V}$. The switching current is determined as the current bias value where the measured voltage becomes larger than a pre-defined threshold voltage of $10\,\mu\mathrm{V}$. In Figure 6.6.(a), oscillations of I_s are clearly visible as a function of B_z with a periodicity of $\sim 24\,\mu\mathrm{T}$. This corresponds to an effective loop area of $86\,\mu\mathrm{m}^2$. The obtained value is slightly smaller than the expected $100\,\mu\mathrm{m}^2$ which could also be explained by magnetic flux focusing of the MoRe leads. Figure 6.6.(a) also illustrates that the amplite of the SQUID oscillation is efficiently tunable by the device top gate.

To gain separate information about the device and reference junctions from the measured switching current oscillations, we fit the raw curves using the function:

$$I_s(B_z) = I_{c,dev}\widetilde{f}(\varphi(B_z, p_B), \varphi_0, \tau), \tag{6.1}$$

where $\widetilde{f}$ is the normalised Andreev formula (Equation 2.58) for a single conduction channel with transmission τ. Here, we assume that the conditions detailed in Section 2.5.5 hold and the measured current–flux relation (CϕR) curves contain the CPR offset simply by the value of the reference critical current $I_{c,ref}$. To fit the measured curves with the above function, we subtract $I_{c,ref}$ and the magnetic field strength is converted to the SC phase difference of the device junction using $\varphi = -2\pi B_z/p_B$, where p_B is the periodicity of the SQUID oscillations. Figure 6.6.(b) shows an example for a CPR curve after these transformations as a function of φ. Here, the $\varphi = 0$ reference point is arbitrarily chosen. As it is illustrated in Figure 6.6.(b), the measured curve can be fitted well by the Andreev formula.

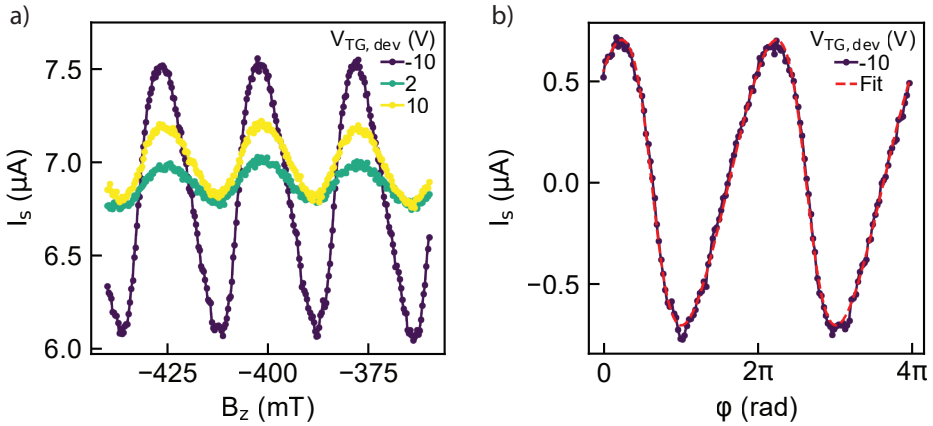

Figure 6.6: a) Raw measurements of the switching current of the SQUID I_s as a function of B_z (CϕR) around the main lobe of the Fraunhofer pattern for different values of $V_{TG,dev}$ with $V_{BG} = 5\,\mathrm{V}$ and $V_{TG,ref} = -0.4\,\mathrm{V}$. b) CPR curve after the subtraction of $I_{c,ref}$ as a function of the SC phase difference φ of the device junction.

We measure the CPR as a function of $V_{TG,dev}$ and V_{BG} for $V_{TG,ref} = -0.4\,\mathrm{V}$ and extract

$I_{c,dev}$, $I_{c,ref}$, τ and φ_0 using the previous fit procedure. Figure 6.7.(a) shows the fit results for $I_{c,dev}$. The obtained gate map shows a clear trend in agreement with the normal resistance map shown in Figure 6.2.(b) and the four quadrants corresponding to different doping configurations can be easily identified. Figure 6.7.(b) shows the gate map obtained for $I_{c,ref}$. Here, contrary to our expectations, we observe a dependence of the critical current of the reference junction on the applied gates. This could be explained by a non-negligible cross-talk between the reference top gate and the other two gates due to parasitic capacitances. On the other hand, the observed change in $I_{c,ref}$ is below 10% and our assumption for large asymmetry in the device and reference critical currents is justified.

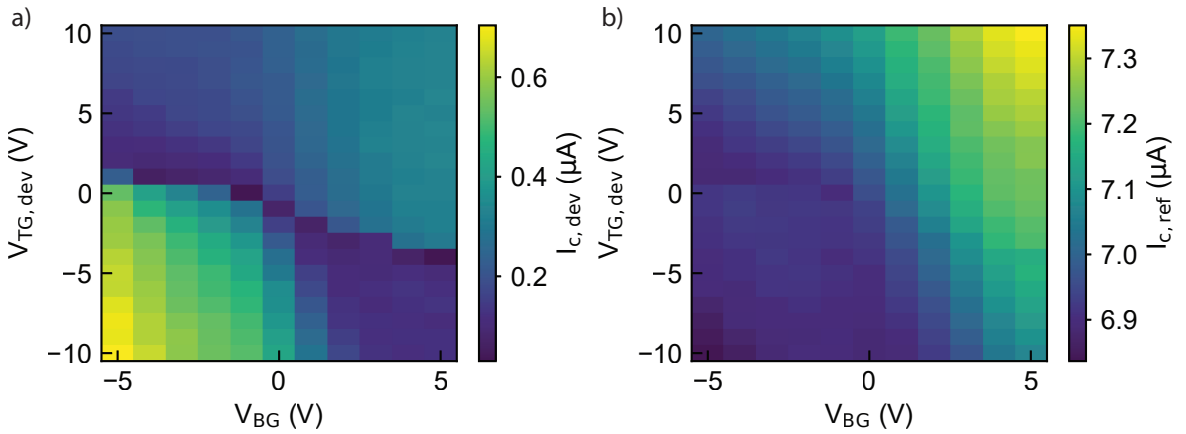

Figure 6.7: a) Device and b) reference junction critical current, $I_{c,dev}$ and $I_{c,ref}$ as a function of V_{BG} and $V_{TG,dev}$ for $V_{TG,ref} = -0.4\,\mathrm{V}$. $I_{c,dev}$ changes in agreement with the normal resistance shown in Figure 6.2.(b)

Figure 6.8.(a) shows the gate map of τ. As mentioned earlier, we fit the CPR curves with the Andreev formula for a single conduction channel with transmission τ. Although our graphene Josephson junctions are wide and may contain hundreds of channels, τ can be interpreted as an average transmission. Furthermore, since the measured curves can be fitted reasonably well with the formula, τ can be used as a measure of skewness (see Section 2.5.4). From Figure 6.8.(a), we can conclude that τ and consequently the skewness of the measured CPR increases drastically as $I_{c,dev}$ increases. This can also be seen in Figure 6.6.(a) where the curve measured at $V_{TG,dev} = 2\,\mathrm{V}$ is sinusoidal, whereas the one measured at $V_{TG,dev} = -10\,\mathrm{V}$ exhibits a significant skewness.

Figure 6.8.(b) shows the extracted gate map of the φ_0 phase shift. As discussed earlier, the absolute value of the extracted φ_0 is difficult to interpret since it contains a contribution from the offset of the magnetic field. On the other hand, we expect that any φ_0 phase shift originating from the spin–orbit interaction should depend on the charge carrier density. For this reason, we choose the φ_0 value extracted at $V_{BG} = V_{TG,ref} = 0$ as a reference point and in Figure 6.8.(b) plot the difference with respect to this value. Although no change in φ_0 is expected, a clear dependence on the applied gate voltages can be observed. We attribute this to inductance effects arising from the change in $I_{c,ref}$. This is discussed in detail in Section 6.5.

We also repeat this procedure with larger resolution in gate voltages in a smaller range where Fabry-Perot oscillations are visible in the normal resistance. Figure 6.9.(a) shows the gate map of $I_{c,dev}$. Here, oscillations are clearly visible in agreement with the oscillations present in the normal resistance map shown in Figure 6.3.(a). On the other hand, Figure 6.9.(b) shows the gate map of τ where no oscillations are visible. This suggests that the interference pattern is modulated by the charge carrier density while the transmission of the channels is not influenced.

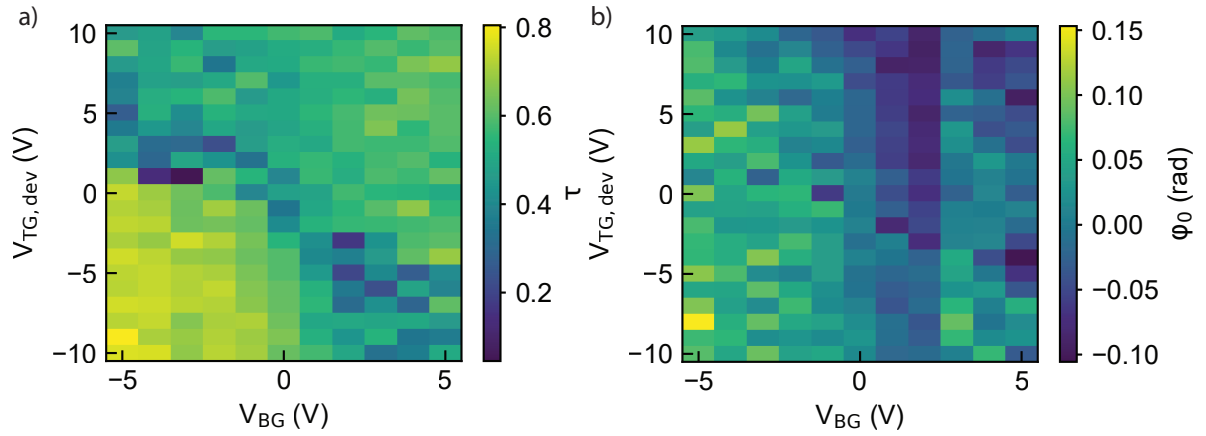

Figure 6.8: a) Transmission τ and b) phase shift φ_0 of the CPR curves as a function of V_{BG} and $V_{TG,dev}$ for $V_{TG,ref} = -0.4\,\mathrm{V}$. φ_0 phase shift is shown with respect to the value extracted for $V_{BG} = V_{TG,dev} = 0$.

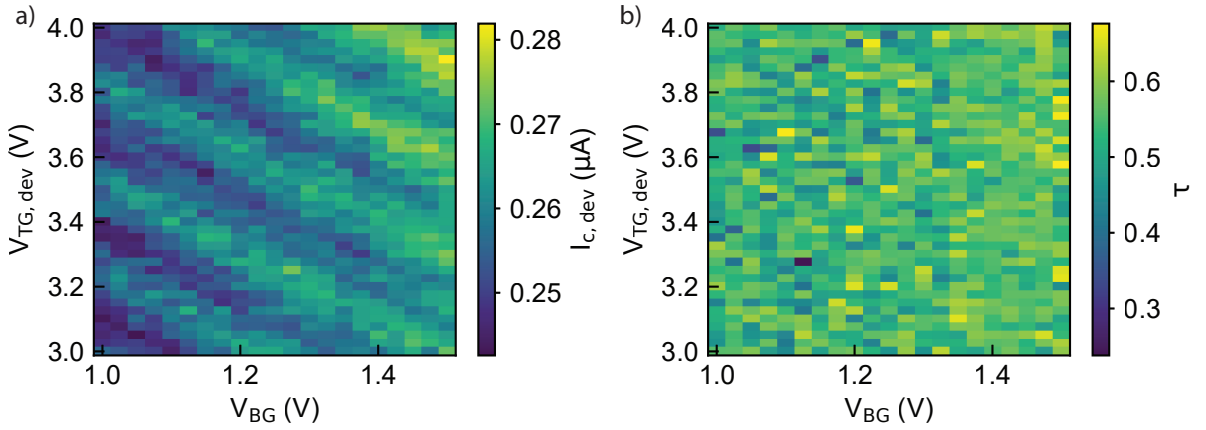

Figure 6.9: a) $I_{c,dev}$ and b) τ as a function of $V_{TG,dev}$ and V_{BG} in the gate voltage range where Fabry–Perot oscillations are visible in the normal resistance. $I_{c,dev}$ shows clear oscillations while no clear trend in τ can be observed.

6.4 Effects of in-plane magnetic field

To investigate the effects of in-plane magnetic field on the junction parameters, we apply a B_y magnetic field in the direction perpendicular to the direction of current in the Josephson junctions (see Figure 6.1.j). It must be emphasized that the investigation of such 2D heterostructures in an in-plane magnetic field is a complicated task. First of all, a small tilt angle between the horizontal axis of the magnetic field and the device plane is always present. Therefore, an out-of-plane magnetic field component will appear when the B_y magnetic field is applied. This out-of-plane component results in an additional shift of the Fraunhofer pattern and can be compensated. On the other hand, the in-plane magnetic field bends around the SC electrodes due to the Meissner effect. Depending on device geometry and orientation, this can result in local out-of-plane magnetic field components that cannot be compensated and lead to the rapid decay of critical current as B_y is increased [196]. Furthermore, out-of-plane corrugations of the graphene sheet can also lead to local, random out-of-plane magnetic field components [197].

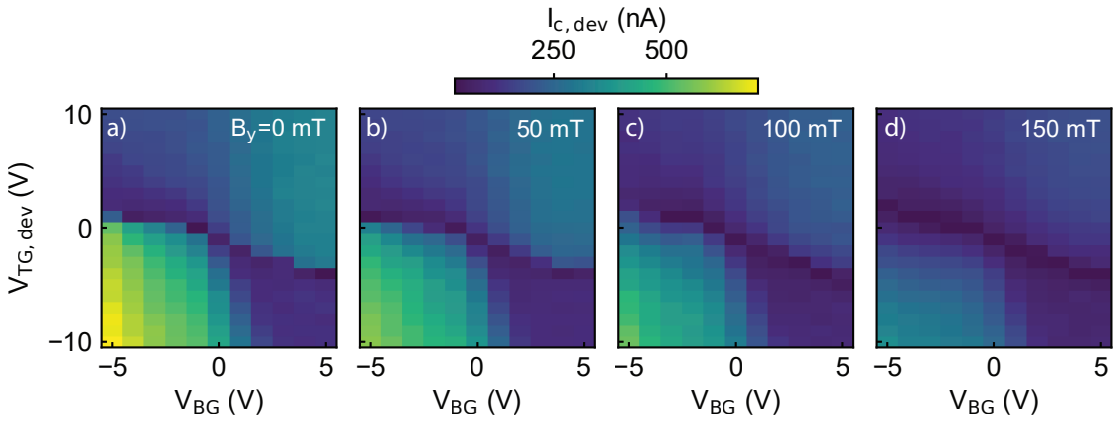

Figure 6.10: a-d) $I_{c,dev}$ as a function of $V_{TG,dev}$ and V_{BG} for an in-plane magnetic field of $B_y = 0$, 50, 100 and 150 mT.

We repeat the previous measurements for $B_y = 50$, 100 and 150 mT and extract the same junction parameters: $I_{c,dev}$, $I_{c,ref}$, τ and φ_0. To compensate for the decrease of $I_{c,ref}$ and ensure that we remain in the true CPR measurement regime, we tune $V_{TG,ref}$ individually for each in-plane magnetic field value and set a suitably large critical current.

More importantly, Figure 6.10 shows the evolution of the gate map of $I_{c,dev}$ for different B_y. The four quadrants corresponding to the different doping configurations discussed earlier can be easily observed for all B_y. Furthermore, as B_y is increased to 150 mT, $I_{c,dev}$ decreases by a factor of 2. Even though this decreasing trend is in agreement with our expectations, the relative decrease in $I_{c,dev}$ is smaller than the change in $I_{c,ref}$. This could be attributed to the different geometry of the two junctions. Similar trends can be observed in the gate map of τ (Figure 6.11). For $B_y = 0$, a clear evolution of τ is visible in agreement with the gate maps of $I_{c,dev}$, as discussed in the previous section. This gate dependence can also be observed for $B_y = 50$ mT. However, for larger B_y, as $I_{c,dev}$ decreases the extracted τ is also generally smaller and the resulting gate maps become noisy since the error of the fit increases as τ decreases. A similar decrease of τ was observed for Al/InAs Josephson junctions [198].

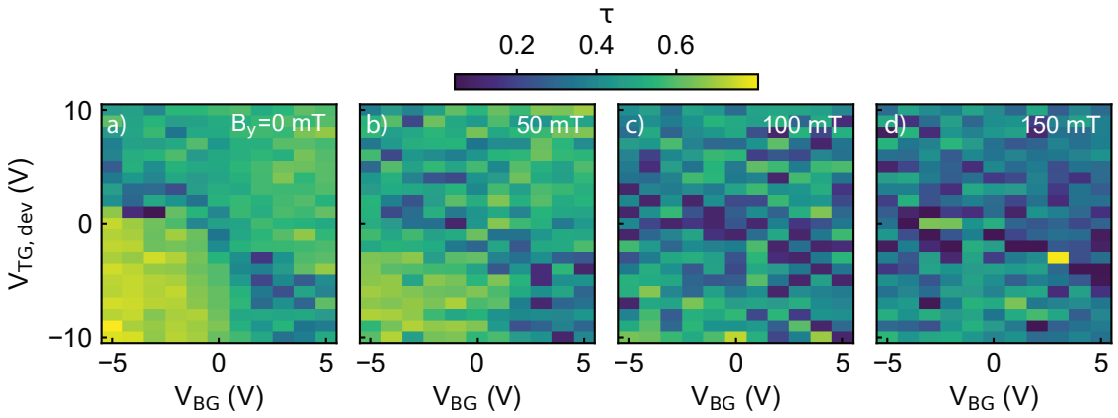

Figure 6.11: a-d) τ as a function of $V_{TG,dev}$ and V_{BG} for $B_y = 0$, 50, 100 and 150 mT.

Figure 6.12 shows the extracted gate maps of φ_0 for different values of B_y. As earlier, the phase shift obtained for $V_{BG} = V_{TG,ref} = 0$ is subtracted from the gate map for each B_y. For $B_y = 0$, 50 and 100 mT, the observed gate dependence of φ_0 can be explained by inductance effects due to the variations in $I_{c,ref}$. However, for $B_y = 150$ mT, we observe relatively large

phase shifts around the charge neutrality line which cannot be attributed to these inductance effects. The appearance of these phase shifts around small charge carrier densities could be a consequence of diffusive conduction. No such phase shifts are visible for larger charge carrier densities.

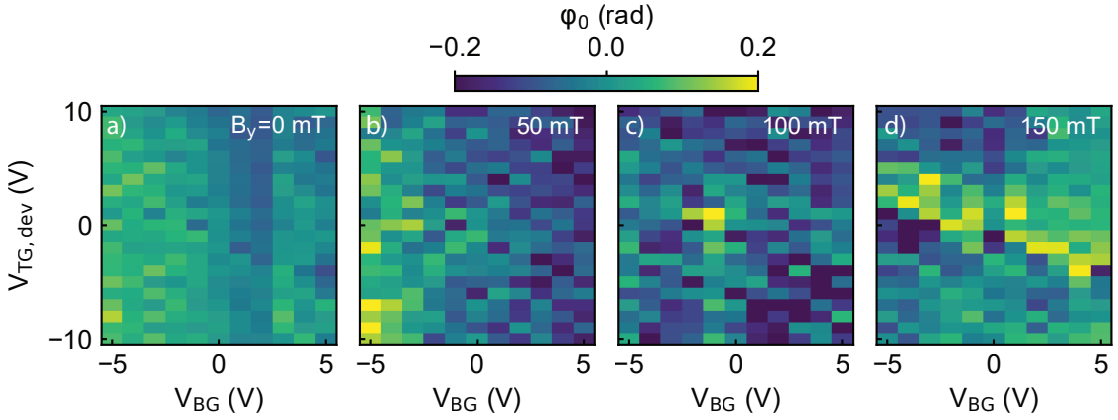

Figure 6.12: a-d) φ_0 phase shift as a function of $V_{TG,dev}$ and V_{BG} for $B_y = 0, 50, 100$ and 150 mT. For each B_y in-plane magnetic field, the relative phase shift is shown with respect to the value extracted for $V_{BG} = V_{TG,ref} = 0$.

6.5 Limitiations of current-phase relation measurements

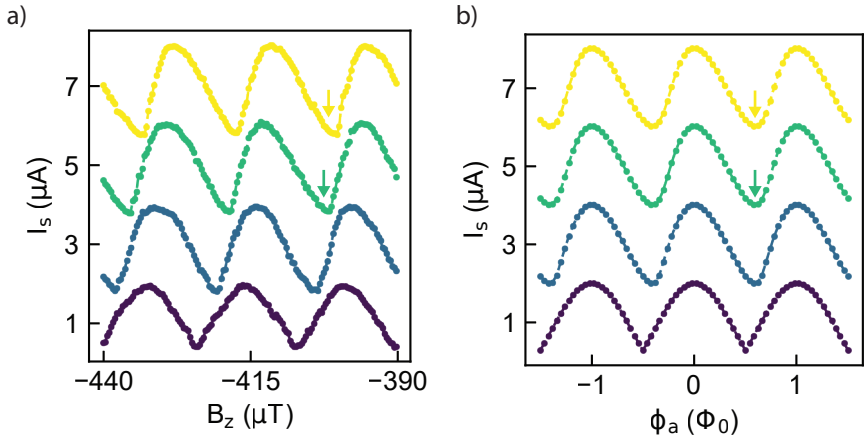

Figure 6.13: a) CϕR of sample B for $I_{c,ref} = 1, 3, 5$ and $7\,\mu$A with $I_{c,dev} = 1\,\mu$A. b) Numerical calculations of the CϕR with the critical currents obtained from panel a) and $\tau_{dev} = \tau_{ref} = 0.7$.

To help the interpretation of the experimental results presented in the previous section, it is necessary to discuss the limitations of these CPR measurements. First of all, as mentioned in Section 2.5.5, to measure the true CPR of the device junction, a large asymmetry between $I_{c,dev}$ and $I_{c,ref}$ has to be ensured. Although it is commonly argued that an $I_{c,ref}/I_{c,dev}$ ratio of 10 is sufficient, the necessary asymmetry depends on both the device and reference CPRs [130] and also on the loop inductance [199]. To illustrate this, Figure 6.13 shows the CϕR, the switching current I_s of sample B (see Appendix C for sample details) as a function of B_z for different values of $I_{c,ref}$ with $I_{c,dev} \approx 1\,\mu$A. The curve with $I_{c,ref} \approx 1\,\mu$A (dark blue) corresponds to the symmetric SQUID configuration and the curve with $I_{c,ref} \approx 7\,\mu$A (yellow) is supposed to be in the true CPR regime. This is further supported by numerical calculations of the

CϕR presented in Figure 6.13.(b) where the switching current I_s is shown as a function of the externally applied flux ϕ_a. The junction critical currents used for the calculations were obtained from Figure 6.13.(a) while conservative values of $\tau_{dev} = \tau_{ref} = 0.7$ were used for the junction transparencies. Although the qualitative trends and the transition from the symmetric to the asymmetric configuration is captured well, some differences between measurement and simulation can be observed. First of all, the calculations suggest that an asymmetry of ~ 7 (yellow curve) is sufficient to measure the device CPR. On the other hand, the measurements show sharp features not present in the calculated curves (see arrows in Figure 6.13). Secondly, the measured curves for different $I_{c,ref}$ appear shifted compared to each other. Although the latter could be explained by an increase in τ_{ref}, we argue that both phenomena are caused by the finite inductance of the MoRe loop.

To investigate these inductance effects, it is helpful to introduce the notion of circulating current. The DC current bias I applied to the SQUID loop is split between the two junctions according to their CPRs and the applied magnetic flux:

$$I = I_{dev} + I_{ref} = I_{c,dev} f(\varphi_{dev}) + I_{c,ref} f(\varphi_{ref}). \tag{6.2}$$

As illustrated in Figure 6.14, I_{dev} and I_{ref} can be decomposed into a sum of a transport component I_t and a circulating component I_{circ}. I_t flows in the same direction in both arms while I_{circ} is the current flowing around the SQUID loop. The latter, I_{circ} becomes relevant if the loop has a finite inductance L. In this case, the circulating current induces a magnetic flux LI_{circ} opposing the externally applied flux. As a result, the condition for the phase differences is modified:

$$\varphi_{ref} - \varphi_{dev} = \frac{2\pi}{\Phi_0} \left(\phi_a - LI_{circ}\right). \tag{6.3}$$

If the loop inductance is large then the flux inside the loop can become a multivalued function of the applied flux [200] due to this screening effect. More importantly, for moderate values of the loop inductance, the conditions for a true CPR measurement become modified.

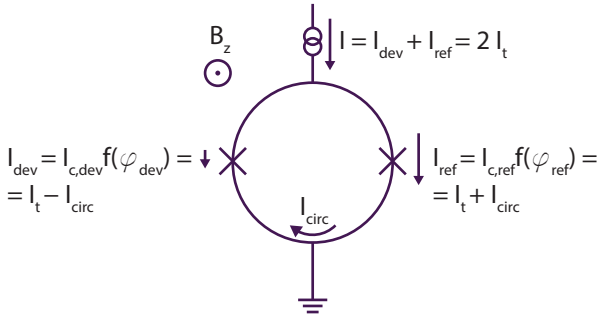

Figure 6.14: Schematic illustration of an asymmetric SQUID device under current bias I. The currents flowing in the arms of the device and reference junctions can be decomposed into the sum of a transport and a circulating component.

To estimate the effect of loop inductance L on our CPR measurements, we determine its value for sample A. To obtain L, we measure the CϕR at a fixed $V_{BG} = V_{TG,dev} = 5\,\mathrm{V}$ for different $V_{TG,ref}$, similarly to Figure 6.13. Some of these curves are shown in Figure 6.15.(a). As it also illustrated by arrows and the corresponding marks on the horizontal axis, the position of the CϕR curves clearly shift as $I_{c,ref}$ is increased which is a consequence of the finite loop inductance. It is also important to note that the CPRs measured at different $I_{c,ref}$ are qualitatively similar which confirms that the asymmetry of the critical currents is sufficient to measure the true CPR of the device junction. To determine the value of the loop inductance, we extract $I_{c,ref}$ from the measured CϕRs and calculate the average circulating current for a given CϕR curve as $I_{circ} = I_{c,ref}/2$. Using this, the loop inductance L can be obtained from a simple linear fit,

since the phase shift is given by $\varphi_0 = 2\pi L I_{circ}/\Phi_0$, assuming that the variation of I_{circ} with B_z is small. This analysis yields $L \approx 130\,\text{pH}$ which is close to the value obtained for similar devices [127].

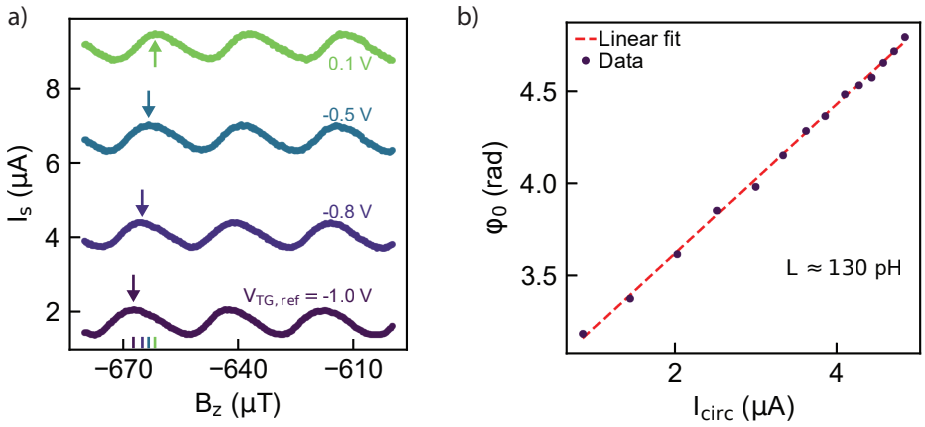

Figure 6.15: a) CϕR curves measured for diffent $V_{TG,ref}$ at $V_{BG} = V_{TG,dev} = 5\,\text{V}$. b) Phase shift φ_0 of the CϕR curves as a function of the current circulating in the SQUID loop I_{circ}. The phase shift is proportional to the loop inductance. A linear fit yields $L \approx 130\,\text{pH}$.

Using the obtained value of L, we can investigate the effect of loop inductance on the measured CϕRs. Figure 6.16.(a) shows the numerically calculated CϕR for $L = 0$ and the experimentally determined value of $L = 130\,\text{pH}$ (see Appendix C for details of the calculation). The junction parameters are chosen based on our measurements: $I_{c,dev} = 0.7\,\mu\text{A}$, $I_{c,ref} = 7\,\mu\text{A}$ and $\tau_{dev} = \tau_{ref} = 0.7$. As it is clearly visible, the curves are shifted compared to each other as a consequence of the finite inductance, in agreement with our previous observations. More importantly, the loop inductance also modifies the shape of the CϕR curve, visibly increasing its skewness. In more extreme cases, this can lead to the appearance of sharp features such as those visible in Figure 6.13.(a). This is also further illustrated in Figure 6.16.(b) where the calculated phases of the device and reference junctions – φ_{dev} and φ_{ref} – are plotted as a function of the applied magnetic flux ϕ_a. In the $L = 0$ case (pale blue and red markers), the calculated phases are consistent with our expectations for a true CPR measurement such that φ_{ref} is approximately constant and φ_{dev} changes linearly with ϕ_a. On the other hand, for $L = 130\,\text{pH}$, a clear deviation from the expected behaviour can be observed and the two phases change simultaneously around an applied flux of $\sim 0.1\,\Phi_0$ (arrows in Figure 6.16.(b)). This simultaneous winding of the two phases is a consequence of the screening of magnetic flux due to the current circulating in the SQUID loop. Since the circulating current and the screening depends on the applied magnetic flux, a magnetic field-dependent phase shift appears and the measured CϕR becomes more skewed. From these, we can conclude that inductance effects are not necessarily negligible and the interpretation of the fit parameters τ and φ_0 requires a more careful analysis.

From the previous arguments, it is easy to see that any change in $I_{c,ref}$ causes a shift of the measured CϕR curve. As it is visible in Figure 6.7, even though the gates of the device and reference junctions are in principle well separated, a small change in $I_{c,ref}$ is visible in the gate maps. The phase shift due to this change in $I_{c,ref}$ can easily be compensated using the previously determined value of $L = 130\,\text{pH}$. Figure 6.17 shows the gate maps of the extracted phase shift for different B_y in-plane magnetic fields with the phase shifts due to the inductance subtracted. This compensation has a clearly visible effect on the gate map for $B_y = 0$. However, it is essentially negligible for larger B_y as the magnitude of the change in $I_{c,ref}$ becomes smaller. It is also important to note that in some cases the device and reference junctions share a common bottom gate (see e.g. sample B in Appendix C). In this case, during the measurement

of gate maps, $I_{c,ref}$ has to be kept constant by continuously compensating the effect of the common bottom gate with the reference top gate which makes the measurement significantly more challenging.

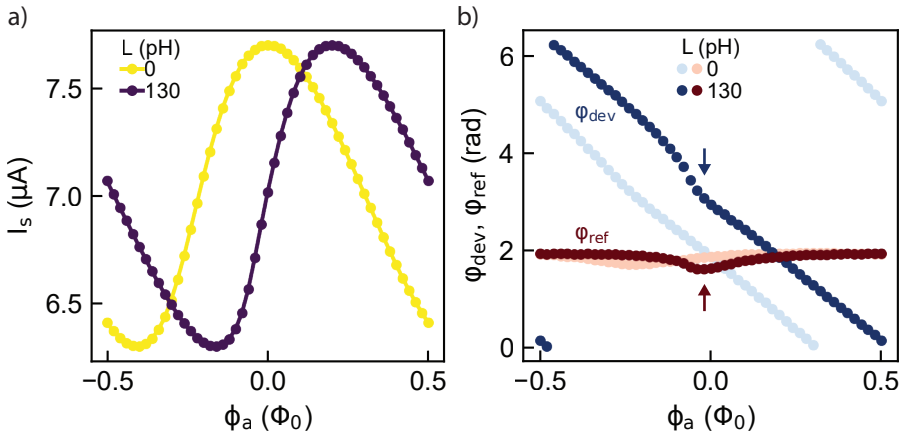

Figure 6.16: a) Numerically calculated current–phase relation with the parameters $\tau_{dev} = \tau_{ref} = 0.7$, $I_{c,ref} = 7\,\mu$A and $I_{c,dev} = 0.7\,\mu$A for $L = 0$ and 130 pH. b) φ_{dev} device and φ_{ref} reference junction phases as a function of the applied magnetic flux ϕ_a for $L = 0$ and 130 pH.

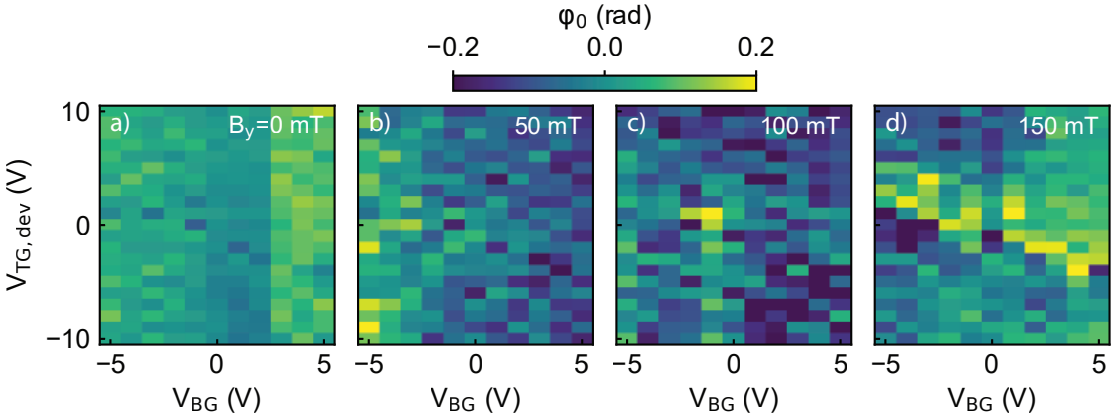

Figure 6.17: a-d) φ_0 phase shift with the change due to the variations of $I_{c,ref}$ subtracted as a function of $V_{TG,dev}$ and V_{BG} for $B_y = 0$, 50, 100 and 150 mT. For each B_y in-plane magnetic field, the relative phase shift is shown with respect to the value extracted for $V_{BG} = V_{TG,ref} = 0$.

The effect of loop inductance on the fit parameter τ is more subtle. In Figure 6.16.(a), it is visible that the finite inductance introduces an additional skewness. Therefore, we expect that, at least for large $I_{c,dev}$, the extracted τ is overestimated. To investigate this, we numerically calculate the CϕR with $I_{c,ref} = 7\,\mu$A and $\tau_{ref} = 0.7$ taking into account a finite loop inductance of $L = 130$ pH for different $I_{c,dev}$ and τ_{dev} in the range of our measurements and fit the resulting curves applying the fit procedure used for the analysis of the measured CϕR curves. Although in extreme cases, due to inductance effects [199] or an insufficient asymmetry [130], it is possible that the magnitude of the oscillation is smaller than $I_{c,dev}$, we find that $I_{c,dev}$ and $I_{c,ref}$ can be confidently extracted from the simulated CϕRs for our parameter range. Furthermore, Figure 6.18.(a) shows the extracted relative phase shift φ_0 which illustrates that the additional skewness of the CϕR curves results in an effective phase shift for large $I_{c,dev}$ and τ_{dev} which increases the uncertainty of the extracted values of φ_0. On the other hand, this effective phase shift is smaller than the observed variations of φ_0 presented in Figure 6.17.

Figure 6.18.(b) shows the extracted transparency τ_{fit} for different values of $I_{c,dev}$ and τ_{dev}. It is clearly visible that the finite inductance has a significant effect on τ_{fit} causing it to deviate from the input parameter τ_{dev}, especially for small values of τ_{dev}. For example, a fitted transparency of ~ 0.6 can be achived by using $\tau_{dev} = 0.2$, if $I_{c,dev}$ is sufficiently large. This is due to the fact that the additional skewness is caused by the change in I_{circ} with B_z which results in a change of the screening of magnetic flux with B_z and is governed by the change in I_{dev} since I_{ref} is approximately constant. This effect obviously increases with $I_{c,dev}$. However, it is also visible that the effect of inductance is less significant if the input τ_{dev} is larger. From these observations we can conclude that the increase in τ_{dev} observed for $B_y = 0$ (Figure 6.12) cannot be explained solely by inductive effects and the transparency increases as the charge carrier density is tuned away from the charge neutrality line. This is consistent with previous observations for ballistic graphene Josephson junctions [127]. On the other hand, the extracted values for τ_{dev} are overestimated because of the apparent skewing of the measured CϕRs originating from the screening of the applied magnetic flux due to a finite loop inductance.

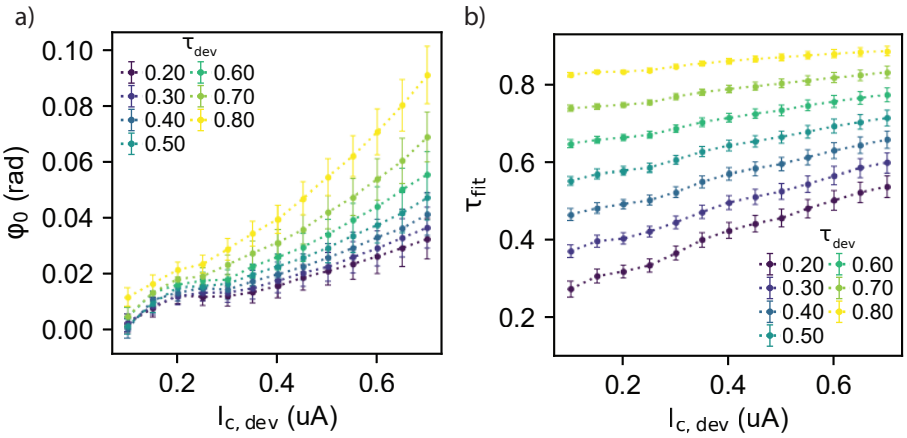

Figure 6.18: a) Relative phase shift φ_0 caused by the increased skewness due to loop inductance. φ_0 is obtained by performing the fit procedure used for the measured CϕR curves for calculated CϕRs with different $I_{c,dev}$ and τ_{dev}, taking into account a finite $L = 130$ pH. b) Transparency τ_{fit} obtained from the fit procedure. The deviation of τ_{fit} from the input parameter τ_{dev} is caused by the increased skewness of the measured CϕR due to the inductive screening of magnetic flux.

6.6 Conclusions

In conclusion, we have shown that the CPR of a JJ based on a WSe_2/SLG/WSe_2 heterostructure can be measured using an asymmetric SQUID design. The high quality of the device was confirmed by the observation of Fabry-Perot oscillations in both the normal resistance and the superconducting critical current. We showed that the measured CPR becomes highly skewed for high doping of the graphene, indicative of large junction transparency. It was also shown that, due to the formation of p–n junctions that are also responsible for the Fabry-Perot oscillations, the skewness of the CPR decreases in the bipolar regime. We also investigated the phase shifts of the CPR in in-plane magnetic fields. By increasing the magnetic field, I showed phase shifts that cannot be explained by imperfect sample orientation or inductive effects. In connection with these measurements, I demonstrated the practical limitations of the measurement of phase shifts.

To connect such small phase shifts to the proximity-induced SOC requires further theoretical and experimental work. From a theoretical point of view, the expected phase shifts should be calculated in both the ballistic and diffusive regimes, using the experimentally obtained SOC

parameters. On the experimental side, more precise fabrication is desired as the alignment of the WSe_2 layers can significantly influence the induced SOC. Furthermore, the measurement of the superconducting diode effect could provide an additional tool to investigate the effect of SOC on the CPR.

Chapter 7

Multiterminal Josephson junctions

7.1 Introduction

MTJJs consisting of a single scattering region connected to multiple superconducting terminals attracted significant attention in recent years. Theoretical works showed that MTJJs may enable multiplet supercurrents [151–156], and the Andreev bound state (ABS) spectra of MTJJs can exhibit non-trivial topology and simulate the band structure of Weyl semimetals [32, 131–146]. Although some of the theoretically proposed key features remain unobserved, recent experimental advances led to the observation of hybridized ABSs [147–150], broken spin degeneracy and ground state parity transitions [201], signatures of quartet supercurrents [157–161], the Josephson diode effect [162–165] and topological phase transitions [202], highlighting the versatility of MTJJ devices.

On the other hand, several experimental works found that the transport characteristics of MTJJs can be reasonably well modeled by a network of resistively and capacitively shunted Josephson junctions (RCSJ), in which each pair of terminals is connected by an RCSJ element. This relatively simple approach is able to qualitatively capture features of current-biased measurements, such as the coexistence of normal and supercurrents between different terminals [159, 160, 166–168] and multiplet resonances [159, 168]. In spite of some agreement between simulations and measurements, these models in general fail to quantitatively capture the observations when normal and supercurrents coexist in the scattering region. This lack of agreement can be attributed to heating effects due to the presence of normal currents [166] that influence the supercurrent flowing in other parts of the device. Furthermore, the observation of more exotic phenomena, such as multiplet supercurrents [159, 168] and quantized transconductance [32, 131], also rely on the presence of finite voltages between some of the terminals that necessarily imply the existence of normal currents and heating effects. Due to the large superconducting gap Δ of the terminals which prevents the outflow of hot electrons, these heating effects can significantly modify the superconducting properties of MTJJs. Moreover, heating effects can have an impact on the switching dynamics of single Josephson junctions [101, 102] which could be enhanced in the case of MTJJs, due to the complex geometry and the non-trivial current distribution.

In this chapter, I present the experimental investigation of a three-terminal graphene Josephson junction[1] and compare the current-biased measurements to an RCSJ network model which allows to identify the limitations of these models. Next, I present an improved simulation method[2], incorporating heating effects due to the presence of normal currents which results in a significantly better agreement with the measurements. Furthermore, I investigate the switching dynamics of our device and observe a non-trivial behaviour of the switching current distribution (SCD) at low temperatures that is governed by phase diffusion. This behaviour is modified by

[1] The device was fabricated by Pápai Tamás and myself.

[2] The simulation method was developed together with Gergő Fülöp.

the heating effects due to normal currents and I–V curves develop overdamped characteristics. Finally, I investigate the charge carrier density dependence of the measured and simulated resistance maps which gives us further insight into the possible cooling mechanisms by which the dissipated heat escapes from the device.

7.2 Device geometry and measurement setup

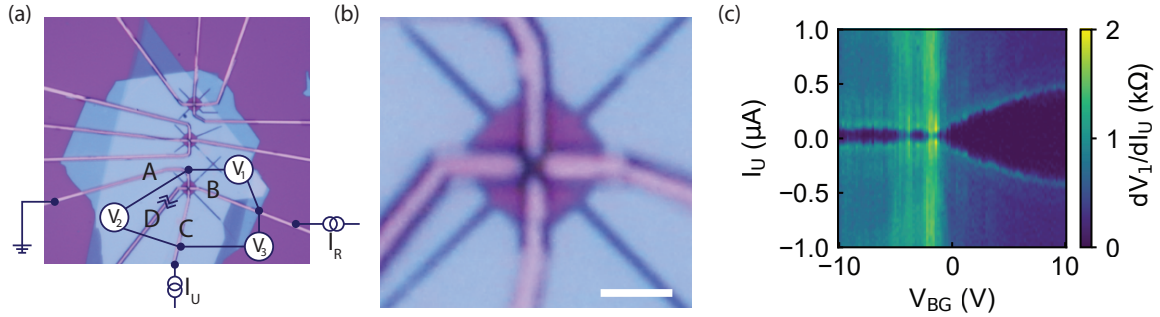

Figure 7.1: a) Optical microscopic image of the device with the schematic illustration of the measurement geometry. Electrode D failed to contact the graphene, resulting in a three-terminal device. b) Zoomed-in optical image of the measured MTJJ device. Darker regions are etched away, defining a cross-shaped area in the center, connecting the terminals. Scale bar is 2 μm. c) Differential resistance of junction 1 dV_1/dI_U as a function of current bias I_U and backgate voltage V_{BG} for $I_R = 0$.

The measured device is shown in Figure 7.1.(a). The dry-transfer technique with PC/PDMS stamps was employed to stack hBN (20 nm, top)/SLG/hBN (35 nm, bottom). To fabricate electrical contacts, we used electron beam lithography patterning followed by a reactive ion etching step using CHF_3/O_2 mixture and finally deposited MoRe (50 nm) by dc sputtering. As it is visible on the optical microscopic image in Figure 7.1.(a), four MoRe contacts were fabricated, however, one of the contacts failed to contact the graphene layer, resulting in a three-terminal device. The separation of neighbouring contacts is around 150 nm. The heterostructure around the cross-shaped region was etched away using reactive ion etching with SF_6/O_2 mixture.

Transport measurements were carried out in a Leiden dilution refrigerator at a base temperature of 40 mK (unless otherwise stated). Measurements were performed using a NI USB 6341 measurement card. In each measurement, contact A was grounded and the DC current biases I_R and I_U were applied via 1 MΩ preresistors to contact B and C, respectively. Differential voltages – V_1, V_2 and V_3 – between the three different pairs of terminals are measured. The charge carrier density n in graphene can be tuned via the voltage applied to the doped Si substrate that acts as a global backgate, while a 300 nm thick SiO_2 layer forms the gate dielectric. Figure 7.1.(c) shows the differential resitance V_1 measured between contacts A and B as a function of the backgate voltage V_{BG} and I_U showing a highly tunable critical current with V_{BG} as it is common for graphene devices. The critical current can be tuned to zero near the CNP and we observe a significantly smaller critical current for negative V_{BG} which we attribute to doping from the MoRe contacts and formation of a p-n junction at the MoRe interface [193].

7.3 Characterization of supercurrent in a multiterminal device

Figure 7.2.(a) shows the schematic representation of our device. As detailed in the previous section, the cross-shaped hBN/SLG/hBN heterostructure is connected to three MoRe superconducting electrodes. Figure 7.2.(b) (7.2.(c)) shows the differential resistance dV_1/dI_U (dV_2/dI_U)

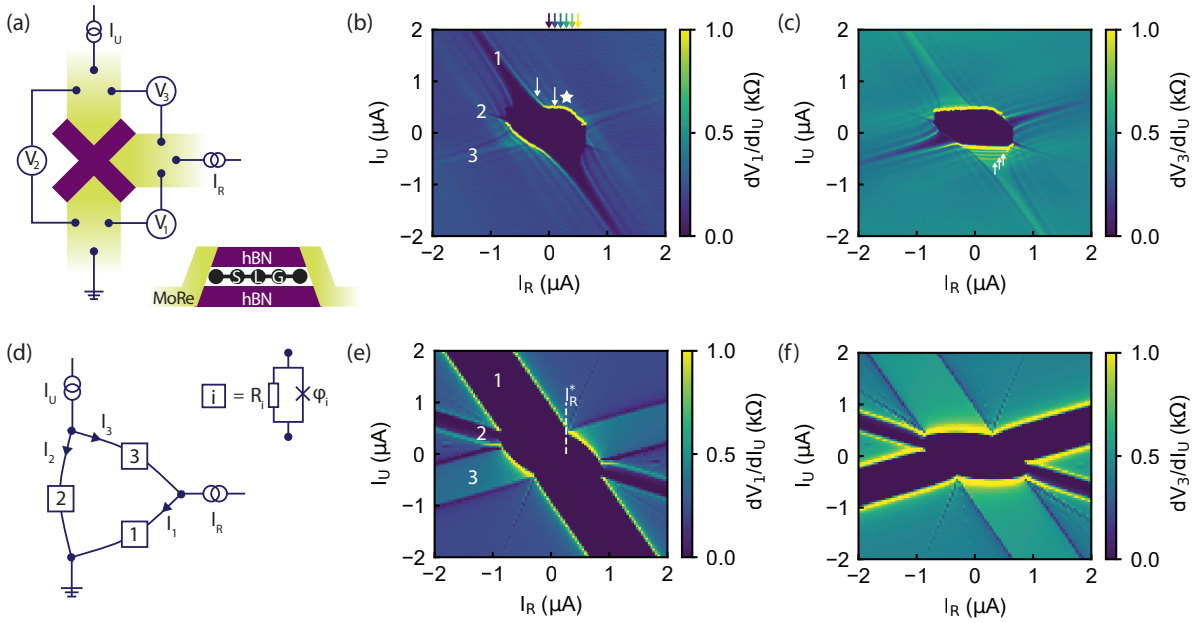

Figure 7.2: a) Schematic representation of the multiterminal Josephson junction. Current biases I_U and I_R are applied via two separate contacts and the third contact is grounded. Voltages V_i are measured between the three pairs of contacts. b,c) Differential resistance dV_1/dI_U and dV_3/dI_U as a function of the current biases. In panel b), white arrows illustrate the position of T-dependent measurement of $I-V$ curves (Figure 7.4.(d)) and colored arrows correspond to bias values where SCD measurements were performed (Figure 7.4.b). White star symbol shows the extended region where a finite voltage develops between all terminals simultaneously. White arrows in panel c) point to resonant features attributed to MAR. d) RSJ network model of our device. e,f) Simulated differential resistance maps analogous to panels b) and c), respectively. I_R^* corresponds to the single current bias value of I_R where all three junctions switch to normal state simultaneously as I_U is ramped.

– obtained from the measured V_1 (V_2) voltage by numerical differentiation with respect to the current bias I_U – as a function of I_U and I_R at a backgate voltage of $V_{BG} = 10\,\mathrm{V}$. Two main features can be identified in such a differential resistance map, similarly to previous experiments [159, 160, 162, 163, 166, 167, 203, 204]. First, in the center, around small current bias values an extended superconducting region of zero resistance can be observed. Second, superconducting arms (labeled by 1, 2 and 3 in Figure 7.2.(b)) are spreading out from this central superconducting region in multiple directions. Comparing differential resistance maps obtained from the measurements of V_1 (Figure 7.2.(b)), V_2 (Appendix D.1) and V_3 (Figure 7.2.(c)), it is easy to realise that the central superconducting region is present in all cases indicating that the whole sample is superconducting and supercurrent can flow between all of the terminals. On the other hand, each of the superconducting arms correspond to supercurrent flowing between only two terminals, resulting in zero resistance in only one of the differential resistance maps while a finite voltage develops between the remaining pairs of terminals (e.g. the SC arm labeled by 1 shows zero resistance in Figure 7.2.(b) and a finite voltage develops in Figure 7.2.(c)). This indicates that both normal and supercurrents can flow in the sample simultaneously.

7.3.1 RSJ simulation

Previous works [160, 166, 167, 204] showed that MTJJs can be described to a large extent by a network of RCSJ elements (see Section 2.5.2). Here, we neglect capacitive effects and model our three-terminal JJ with three resistively shunted junctions (RSJs), one between any pair of

contacts, as shown in Figure 7.2.(d). First, we present the results of this model and highlight its limitations in comparison with our measurements. Later, we show that the agreement between measurement and simulation can be improved by including self-heating effects in the model. As detailed in Appendix D.2, the differential equations of this network model can be constructed from the Josephson equations and Kirchhoff's laws. The necessary input parameters of the model are the resistances (R_i with $i \in \{1, 2, 3\}$) and the critical currents ($I_{c,i}$) of the individual junctions. R_i can be obtained from the measured differential resistances in the normal state, at large bias currents. For these, we obtain $R_1 = 420\,\Omega$, $R_2 = 1355\,\Omega$ and $R_3 = 815\,\Omega$. Furthermore, assuming that our junctions are in the short junction limit and using $I_{c,i}R_i \propto \Delta$, it is possible to extract $I_{c,i}$ from the measured differential resistance maps as well. For these, we get $I_{c,1} = 545\,\text{nA}$, $I_{c,2} = 170\,\text{nA}$ and $I_{c,3} = 280\,\text{nA}$, respectively. (See Appendix D.2 for details on the extraction of parameters.)

By numerically solving the set of differential equations for the network of Josephson junctions and resistors, we obtain differential resistance maps as shown in Figs. 7.2.(e) and 7.2.(f). The model is capable of capturing the most prominent features of the measured differential resistance map: (i) the central superconducting region and (ii) the superconducting arms, corresponding to the coexistence of normal current and supercurrent. In the context of this model, the SC arms can be further discussed. The total current between any pair of terminals (I_1, I_2 and I_3) is determined by the Kirchhoff and Josephson equations for a given I_U and I_R. It can be shown that for arbitrary I_R, a single value of I_U exists for each junction for which the total junction current $I_i = 0$ (see Appendix D.2). The ratio of I_U/I_R for which $I_i = 0$ is determined solely by the normal resistances and is independent of I_U and I_R. Therefore, we expect to observe superconductivity in the vicinity of lines with slopes defined by the normal resistances. We also note that, in this particular geometry, due to Kirchhoff's law which states that the sum of voltages in a closed loop has to be zero, a single junction cannot switch to the normal state alone, a voltage drop has to appear on either two or all three junctions simultaneously. Therefore, outside the central SC region, the SC arms correspond to a configuration where only a single junction is superconducting and the other two reside in the normal state.

On the other hand, several missing features can also be identified in the simulated resistance maps. The most prominent example is the decay of superconductivity that can be observed in the measurements along the superconducting arms. While the width of these arms in the simulated maps is constant towards higher current bias values, in the measurements a clear narrowing of the zero-resistance regions can be observed. Furthermore, in the measured resistance maps an extended region exists where all three junctions switch to the normal state simultaneously (e.g. marked by star symbol in Figure 7.2.(b)), whereas in the simulated maps, this simultaneous switching of all three junctions can only be observed for a single bias value I_R^* (marked also by vertical dashed line in Figure 7.2.(e)). Finally, multiple resonant features (e.g. marked by white arrows in Figure 7.2.(c)) are visible in the measurements parallel to the superconducting arms that are attributed to multiple Andreev reflections (MAR) [203] which cannot be accounted for by our simple model.

7.4 Self-heating effects

The narrowing of the superconducting arms is attributed to Joule heating from the dissipative normal currents in the scattering region [166]. Due to the large superconducting gap of the MoRe that prevents hot electron diffusion towards the leads, the electron system can only dissipate heat via electron-phonon coupling. In this case, the dissipated power towards the substrate is given by $P_{e-ph} = \Sigma(T_e^\delta - T^\delta)$ [205], where Σ is the electron-phonon coupling constant, T_e and T are the electron and phonon bath temperatures, respectively. Following along the lines of Ref. [166], we determine Σ from the temperature dependence of $I_{c,1}$ along the corresponding SC arm. For this, we measure the switching current $I_{s,1}$ for junction 1 by

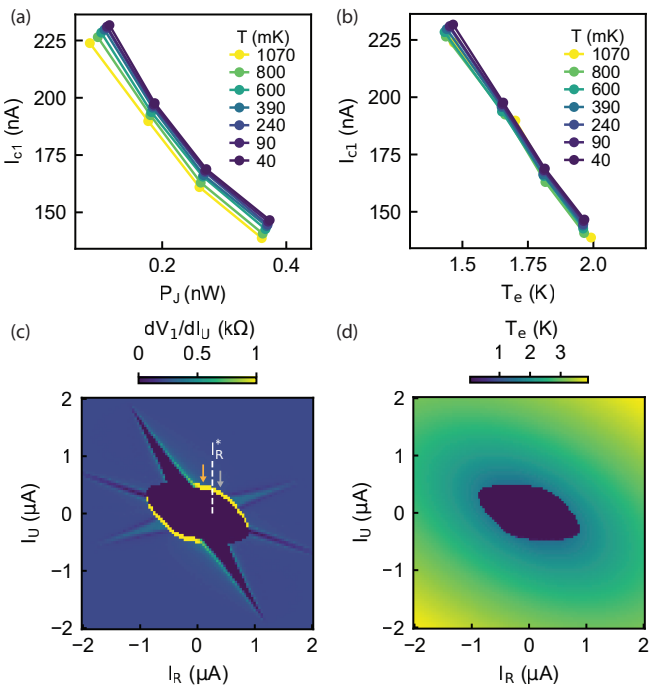

Figure 7.3: Critical current of junction 1 $I_{c,1}$ along the corresponding superconducting arm as a function of a) heating power P_J and b) electronic temperature T_e calculated assuming only phonon cooling. c) Simulated differential resistance map taking into account the elevated electronic temperature due to normal current flowing in the device. d) Simulated map of T_e as a function of current biases.

sweeping I_U at different values of I_R and bath temperatures. $I_{s,1}$ is then defined as the value of I_U where V_1 crosses a certain threshold voltage (20 μV) corresponding to the switching from the SC to the normal state. As mentioned earlier, in this current-biasing scheme, I_U and I_R do not directly correspond to the junction currents I_1, I_2 or I_3. However, since along the SC arm supercurrent only flows in junction 1, it is possible to calculate the junction's critical current $I_{c,1}$ from $I_{s,1}$ (see Appendix D.2). Moreover, as it is detailed later, the switching current of a Josephson junction is prone to fluctuations due to thermal effects. To eliminate these fluctuations, we take the average of 10 000 measurements to determine the average switching current $\overline{I}_{s,1}$. Next, we calculate the power P_J dissipated in the normal regions from Joule heating as $P_J = I_U V_2$. Since junction 1 is superconducting, I_R does not contribute to Joule heating. Figure 7.3.(a) shows the measured critical current $I_{c,1}$ as a function of P_J for different T bath temperatures. As it can be seen from the figure, the increased heating power leads to the decrease of the switching current, similarly to the increased bath temperature. Our assumption is that T_e is homogeneous in the device and the critical current value is defined by T_e independently from whether it originates from bath heating or current dissipation. We then determine the value of Σ for which $I_{c,1}$ as a function of the calculated equilibrium electron temperature T_e scales onto a single curve. As it is discussed later, by assuming $\delta = 4$, we obtain $\Sigma = 25\,\mathrm{pW/K^4}$. This is shown in Figure 7.3.(b), where all the curves fall on top of each other. Although it is challenging to determine the exact active area of our device, we estimate that Σ scaled by the graphene's area yields $\sim 100\,\mathrm{W/m^2K^4}$. This is an order of magnitude larger than the value obtained in reference [166] ($\sim 10\,\mathrm{W/m^2K^3}$) and significantly larger than the value obtained for large-area, nonencapsulated graphene devices [205] ($< 50\,\mathrm{mW/m^2K^4}$). The authors of reference [166] also speculate that electron-phonon coupling can be enhanced by the presence of the hBN substrate and by scattering at the edges of the graphene layer. Since our device area is about an order of

magnitude smaller than the device studied in reference [166], scattering at the edges could be even more significant and could explain the larger value obtained for Σ scaled by the graphene's area.

To take the effects of self-heating into account in our simulations, we perform a fixed-point iteration based on the RSJ model introduced previously. First, we perform the previous simulation with the experimentally determined R_i and $I_{c,i}$ parameters for all I_U and I_R. We then calculate the Joule heat dissipated in the whole network as $P_J = \sum_i V_i^2/R_i$. From P_J, we can obtain the equilibrium electron temperature T_e using the electron-phonon coupling model for all I_U and I_R bias currents. Finally, we take into account the elevated temperature using an $I_c(T_e)$ function which we reconstruct from the temperature dependent measurements shown previously in Figure 7.3.(a,b) and from the temperature dependence of the central superconducting region (see Appendix D.2 for more details). We then iterate this process to achieve a self-consistent solution, using the modified $I_{c,i}$ values in our RSJ model which now also depend on the applied I_U and I_R current biases.

Figure 7.3.(c) shows the simulated dV_1/dI_U map obtained in our model with self-heating. Compared to Figure 7.2.(d), several improvements can be observed. First of all, the narrowing of the SC arms is qualitatively reproduced. The remaining quantitative difference could be explained by the incorrect reconstruction of the $I_c(T_e)$ function or an inhomogeneous temperature profile. Secondly, the improved simulation method is capable of producing an extended edge on the contour of the central SC region where all three junctions switch to the normal state simultaneously. It is also worth noting that the simulated resistance map is inversion symmetric in contrast to the measurements where the sweep direction of the bias currents results in a slightly asymmetric central SC region. Finally, Figure 7.3.(d) shows the map of T_e, illustrating that the heating outside the central SC region is significant, increasing the equilibrium temperature to a few Kelvins, an order of magnitude above the bath temperature, in agreement with our measurements shown in Figure 7.3.(b).

7.5 Switching dynamics

In the following, we further investigate the interplay between the three junctions in the regions where all junctions switch to the normal state simultaneously around I_R^* (also shown in Figure 7.3.(c)). Figure 7.4.(a) shows the current in each junction as a function of I_U for $I_R = 0.1\,\mu\text{A} \lesssim I_R^*$ (orange arrow in Figure 7.3.(c)) obtained from our simulation with self-heating (dashed lines). Although, I_i cannot be obtained from our measurements, we can also calculate the current in each junction as long as all junctions are superconducting by numerically minimizing the Josephson energy (symbols). Here, the Josephson energy for junction i is given by $E_{J,i} = \hbar I_{c,i}/2e \sin\varphi_i$, where φ_i is the phase difference of junction i. For a given I_U, I_R and φ_1, the other two phase differences φ_2 and φ_3 can be calculated. Therefore, by minimizing $\sum_i E_{J,i}$ with respect to φ_1, φ_i and, as a result, I_i can be determined. As it is visible in Figure 7.4.(a), this method is consistent with our simulation. The dotted horizontal lines show the critical current of the respective junctions. As it is visible also in Figure 7.2.(e), junction 1 is far below its critical current when junction 2 and 3 reach their respective critical currents. Therefore, without taking self-heating into account, we only expect junction 2 and 3 to switch together. However, when heating is included (Figure 7.3.(c) and measurements on Figure 7.2.(b) and 7.2.(c)), all three junctions switch at the same I_U. From these, we can infer that junction 2 and 3 switch together and junction 1 switches immediately afterwards due to heating from the other junctions. On the other hand, for $I_R \sim I_R^*$, all three junctions reach their critical currents simultaneously and heating should play no role in the switching process, while for $I_R \gtrsim I_R^*$ (gray arrow in Fig 7.3.c), junction 1 and 2 switch together and junction 3 switches due to heating. Based on the previous arguments, we emphasize that the observation of this correlated switching of all three junctions in an extended region along the border of the central

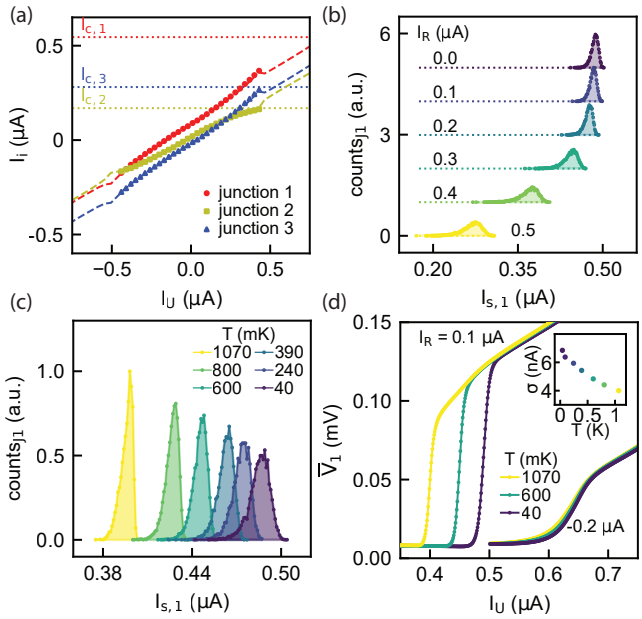

Figure 7.4: a) Current distribution between the three junctions in the central superconducting region obtained from the RSJ model (dashed lines) and from numerically minimising the Josephson energy of the whole network (symbols) for $I_R = 0.1\,\mu$A. Dotted lines show the critical current of each junction. b) SCD for junction 1 measured at different I_R in the central superconducting region obtained from 10 000 measurements. c) Temperature dependence of the SCD at $I_R = 0.1\,\mu$A. The narrowing of the SCD with increasing temperature is consistent with phase diffusion. d) Averaged I-V curves obtained from 10 000 individual measurements in the central SC region ($I_R = 0.1\,\mu$A) and in the SC arm of junction 1 ($I_R = -0.2\,\mu$A) for different temperatures. Inset: standard deviation σ of the SCD as a function of T for $I_R = 0.1\,\mu$A.

SC region is strong evidence for self-heating effects.

To gain insight into the dynamics of these correlated switchings, it is essential to investigate not only the average switching current but also its distribution. Figure 7.4.(b) shows the switching current distribution (SCD) obtained from the measurement of V_1 for different I_R at 40 mK base temperature. The investigated values of I_R are also indicated on top of Figure 7.2.(b) by coloured arrows. Each distribution is obtained by sweeping I_U and detecting the switching current using the previously defined threshold voltage. This process is repeated 10 000 times and a distribution of switching current values is obtained. Interestingly, we observe that the width of the SCD is greatly tunable by I_R (Figure 7.4.(b)). We find that the standard deviation σ of the SCD, which describes the width of the distribution, increases by a factor of 2. This broadening of the SCD could be explained by the different junctions that switch simultaneously at different I_R. As junction 1 takes over the role of junction 3 with increasing I_R, the sum of the critical currents of the two junctions that switch simultaneously increases which could lead to a wider distribution. It is also important to note that during the measurement of the SCD of junction 1, we simultaneously recorded the SCD of junction 2 obtained from the appearance of a finite V_2 and find that the distributions are identical and the switching events of the two junctions are indistinguishable within the time-scales of our measurement (see Appendix D.5). This suggests that the thermalisation of the device is faster than our data acquisition.

To further investigate the escape dynamics of our device, we measure the temperature dependence of the SCD along the contour of the central SC region. This is shown in Figure 7.4.(c) for $I_R = 0.1\,\mu$A and a similar trend is observed for all investigated values of I_R inside the central SC region. It is clearly visible that the SCD gets narrower with increasing T which is in stark contrast to the thermally activated behaviour as the SCD is expected to broaden with

temperature. This is further confirmed by calculating σ as a function of bath temperature for $I_R = 0.1\,\mu$A that is shown in the inset of Figure 7.4.(d). Here, a $\sim 40\%$ decrease of σ is visible in the investigated temperature range. The observed narrowing of the SCD with increasing T is a consequence of phase diffusion due to thermally activated escape and retrapping and is consistent with previous observations in moderately damped Josephson junctions [103] and planar Josephson junctions [206]. However, it is important to note that we observe the narrowing of the SCD in the whole available temperature range and do not find the broadening of the SCD due to thermally activated escape even for the lowest temperatures. This suggests that phase diffusion is significant even at base temperature.

We performed similar measurements along the SC arm of junction 1. Here, we find a different behaviour and we cannot resolve a clear SCD. Figure 7.4.(d) shows the averaged I-V curves of the 10 000 individual measurements for $I_R = -0.2\,\mu$A and $I_R = 0.1\,\mu$A (white arrows in Figure 7.2.(b)) for different temperatures. In the central SC region, for $I_R = 0.1\,\mu$A, a sharp transition between the SC and normal states can be seen. In this case, the curvature of the averaged I-V curves results from averaging curves with fluctuating switching currents. On the other hand, for $I_R = -0.2\,\mu$A, along the SC arm of junction 1, a smooth transition is observed indicating that a finite voltage develops below the switching current. This is also consistent with the theoretical expectations for moderately damped Josephson junctions at higher temperatures [103]. As T increases, the thermally activated retrapping results in a significant damping and the junctions become overdamped. This is further confirmed by the T-dependence of the curves. For $I_R = 0.1\,\mu$A, as T is increased, the switching current decreases (also visible in Figure 7.4.(c)). However, for $I_R = -0.2\,\mu$A, along the SC arm of junction 1, the effect of increasing T is negligible, the increase of T rather makes the transition between the SC and normal states smoother, as it is expected for overdamped junctions. It is also consistent with the self-heating picture, since increasing the bath temperature has less effect on the electronic temperature when a large heating power is already present due to the normal currents in the device. Therefore, we conclude that the switching of our multiterminal device is determined by phase diffusion at lower temperatures along the contour of the central SC region and show overdamped characteristics along the SC arm of junction 1 due to the increased temperature.

7.6 Charge carrier density dependence

Finally, we investigate the dependence of the differential resistance maps on the applied backgate voltage V_{BG}. As mentioned earlier, the exponent of the electron-phonon cooling power formula δ can be 3 or 4, depending on electronic mean free path l_{mfp} and temperature [205]. At the relatively low temperatures accessed in our measurements, $\delta = 4$ describes phonon cooling in clean devices where l_{mfp} is large, while $\delta = 3$ corresponds to phonon cooling modified by impurity scattering in devices with small l_{mfp}. Furthermore, the expression for Σ is also different in the two limits. In the clean limit $\Sigma = \pi^2 D^2 |E_F| k_B^4 / 15 \rho_M \hbar^5 v_F^3 s^3$, where D is the deformation potential of graphene which describes the electron-phonon coupling strength, ρ_M is the mass density of graphene, $v_F = 10^6\,\mathrm{m/s}$ is the Fermi velocity, $E_F = \hbar v_F \sqrt{\pi n}$ is the Fermi energy and $s = 2 \times 10^4\,\mathrm{m/s}$ is the speed of sound in graphene. It can easily be shown that in the clean limit $\Sigma \propto \sqrt{n}$, while in the dirty limit the expression is modified and Σ becomes independent of n [205]. Figure 7.5 shows the measured and simulated resistance maps for different V_{BG} and $\delta = 4$. We scale Σ according to the $\sqrt{n}$-dependence and n is calculated according to a planar capacitor model based on the hBN and SiO_2 dielectrics (see Appendix D.3). From Figure 7.5, it is visible that the qualitative trend is reproduced well. Here, we assumed $\delta = 4$, but note that a reasonably good agreement can also be achieved by taking $\delta = 3$ and a constant $\Sigma = 30\,\mathrm{pW/K^3}$ (see Appendix D.3). Although the overall qualitative agreement between measurement and simulation is good, some differences can still be observed. Most notably, some of the SC arms persist up to larger current bias values in the measurements, especially noticeable for $V_{BG} = 2\,\mathrm{V}$.

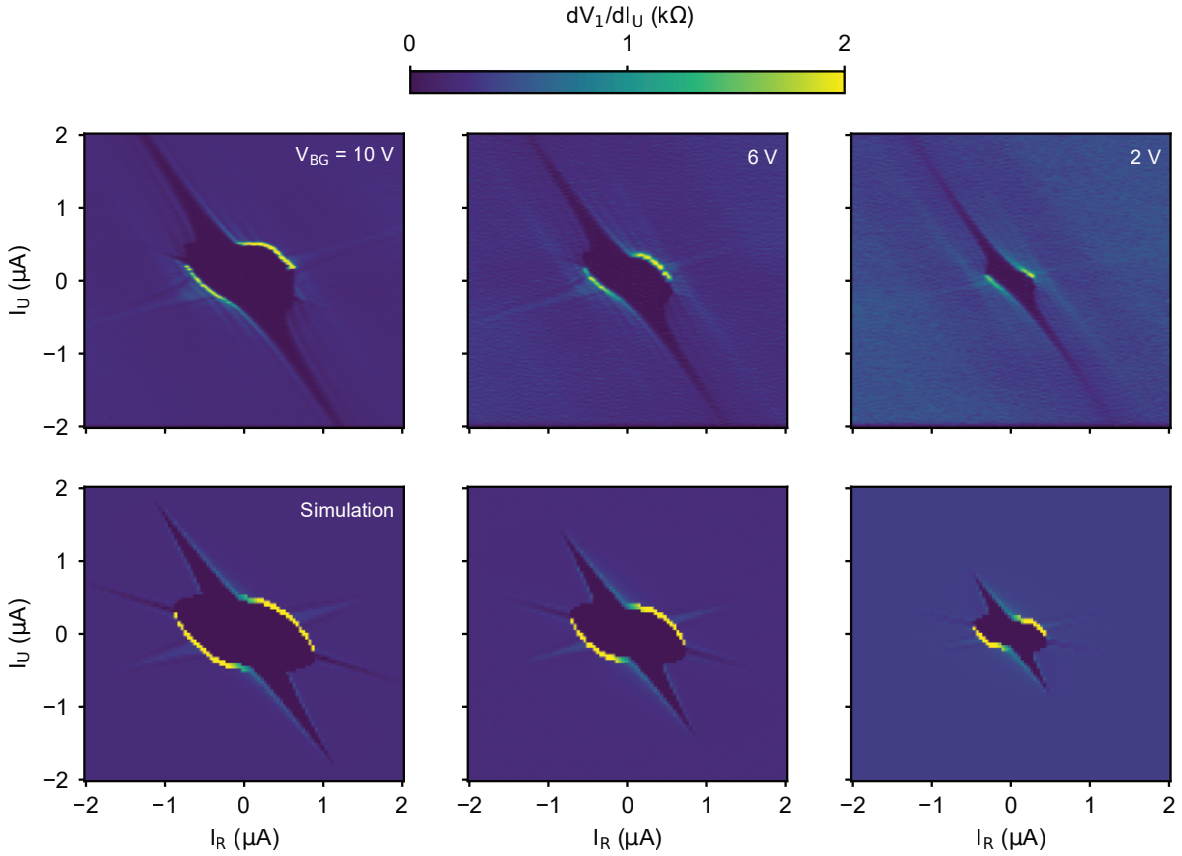

Figure 7.5: Backgate dependence of the measured (top) and simulated (bottom) differential resistance maps. Simulations were performed with $\delta = 4$ and $\Sigma = 25\,\mathrm{pW/K^4}$ for $V_{BG} = 10\,\mathrm{V}$ and Σ was scaled according to the $\sqrt{n}$-dependence expected for the clean limit of electron-phonon coupling.

This could be explained by the appearance of additional cooling paths. As T_e is increased up to a few Kelvins, $k_B T_e$ becomes comparable to Δ, allowing quasiparticles to diffuse into the MoRe leads. Furthermore, we assumed that T_e is homogeneous in the whole device which does not necessarily hold for large heating powers. The inhomogeneity of T_e could significantly modify the ratio of normal and SC segments of the scattering region and, as a result, the estimated input parameters of our model would become increasingly inaccurate with increasing heating powers.

7.7 Superconducting diode effect

Previous works showed that MTJJs are a suitable platform to realise the Josephson diode effect [162, 163, 165] where the amplitude of the critical current depends on the direction of the current flow. Figure 7.6 shows the differential resistance as a function of out-of-plane magnetic field B and I_R for $I_U = 0$. The differential resistance is measured between contacts A and B using lock-in technique at 177 Hz frequency using 10 nA AC current bias applied via a 1 MΩ preresistor. During the measurement, I_R is ramped from $-1\,\mu$A to $1\,\mu$A for fixed B. As it is visible in Figure 7.6, the maximum switching and retrapping currents are observed for different B (orange and white dashed lines, respectively) which is a signature of the Josephson diode effect, where the switching current depends on the direction of the current sweep.

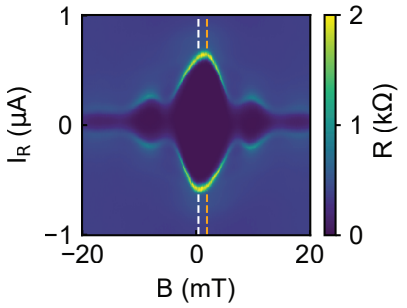

Figure 7.6: Differential resistance R as a function of out-of-plane magnetic field B and I_R for $I_U = 0$. Orange and white dashed lines show the maximum of the switching and retrapping currents, respectively.

7.8 Conclusions

In conclusion, we have measured three-terminal graphene Josephson junctions and investigated the heating effects and junction dynamics in this multiterminal system. We have shown that a significant improvement can be achieved over existing RCSJ models for MTJJs by incorporating heating effects into the simulation method. By considering only Joule heating from the normal currents in the device and electron-phonon coupling as cooling mechanism, we were able to obtain the narrowing of the SC arms that is commonly observed in experiments and the simultaneous switching of all junctions. By measuring the charge carrier density dependence of the differential resistance maps, we could infer the limitations of our model, and suggest that, for significantly increased electronic temperatures, new cooling mechanisms might become available. We propose that by including additional cooling terms, such as the outflow of hot electrons via the SC terminals, our model could be further improved. Furthermore, from the investigation of the SCD, we concluded that the switching from the central SC region to the normal state is governed by phase diffusion even at very low temperatures. As the temperature is increased due to self-heating, this phase diffusion modifies the characteristics of the device, resulting in smooth I-V curves resembling overdamped Josephson junctions. Building on these results, future experiments could focus on the phase-biasing of MTJJs and inductance measurements using RF techniques in the SC state, where self-heating effects are absent.

Chapter 8

Summary

Here, the key results from this thesis are briefly summarized. I investigated nanoelectronic devices based on van der Waals heterostructures built up of graphene, hBN and WSe_2. The motivation behind this work is that graphene is expected to host a quantum spin Hall state if an appropriate spin–orbit coupling is present. Furthermore, if superconducting correlations are induced in such a state, it could lead to the realization of topological superconducting states. Therefore, the objectives of our work was twofold. On the one hand, we set out to investigate the SOC induced in graphene when placed in close proximity to WSe_2. On the other hand, we investigated graphene-based superconducting devices.

In Chapter 4, I discussed the experimental investigation of proximity-induced SOC in single-layer graphene devices. Our collaboration with the Nanoelectronics group at the University of Basel in Switzerland resulted in measurements on SLG/WSe_2 heterostructures that allowed us to determine the strength and type of the proximity-induced SOC. The transport measurements showed a large spin-relaxation anisotropy originating from the induced valley-Zeeman SOC term. The device I fabricated allowed the measurement of the relevant spin-relaxation times as a function of the momentum-relaxation time that made it possible to reveal the Dyakonov-Perel mechanism as the dominant cause of spin-relaxation. Building on these results, our research group showed that the proximity-induced SOC can be enhanced by applying hydrostatic pressure in a pressure cell to these van der Waals heterostructures that reduces the interlayer distances. A major step in the development of the pressure cell measurement technique was to show that hBN can protect the electronic quality of graphene from the pressure mediating medium. For this purpose, I provided a hBN/SLG/hBN device that was used to demonstrate that hBN can efficiently isolate graphene from the kerosene inside the pressure cell.

The next step in the investigation of hydrostatic pressure on the proximity-induced SOC in graphene-based van der Waals heterostructures involved WSe_2/BLG/WSe_2 devices discussed in Chapter 5. In a collaboration with the Technical University of Delft, we were provided with a sample that showed a peculiar band-inverted phase originating from the proximity-induced Ising-type SOC. By transport measurements, I showed that this inverted phase can be stabilized by enhancing the SOC with hydrostatic pressure. The strength of SOC was determined by thermal activation measurements. I also showed that the measurement of Landau level crossings in the quantum Hall regime can also be utilized to show the increase of SOC.

Another aspect of our collaboration with TU Delft was to examine the interplay of proximity-induced SOC and superconductivity in graphene/WSe_2 heterostructures, as detailed in Chapter 6. For this reason, I assembled heterostructures with different combinations of graphene, WSe_2 and hBN and fabricated SQUIDs on these structures using MoRe electrodes. Similar devices were also fabricated at TU Delft. I performed current–phase relation measurements on these devices as phase shifts are expected to appear in the CPR, if SOC and an in-plane magnetic field are present. I showed that the CPR of a WSe_2/SLG/WSe_2 device becomes highly skewed at large dopings, indicating the large transparency of the conduction channels. Further-

more, I detected ballistic Fabry-Perot oscillations in the normal resistance of the device and demonstrated that these oscillations are also observable in the CPR measurements. Finally, I measured the phase shifts of the CPR in in-plane magnetic fields and explored the limitations of such measurements.

Finally, in Chapter 7, I presented transport measurements on a multiterminal Josephson junction. I fabricated a three-terminal Josephson junction on an hBN/SLG/hBN heterostructure. I showed that normal and supercurrents can coexist in such a device and that this behavior can be described by a network of resistively shunted Josephson junctions. I also showed that the agreement between measurement and simulation can be significantly increased if self-heating effects originating from the normal currents are taken into account. I investigated the switching dynamics of this multiterminal system by measuring its switching current distribution. These measurements showed that the switching process is governed by phase diffusion even at low temperatures where the entire device is superconducting. On the other hand, if normal currents are also present, the switching dynamics change and the I–V curves develop overdamped characteristics.

The field of 2D materials is rapidly evolving. This thesis captures only a small fraction of the research directions of the past decade. In the meantime, many new and exciting phenomena were uncovered that pave the way for future experiments. As it is also evident from our measurements, having a precise control over the rotation angle of layers in van der Waals heterostructures is inevitable to regulate proximity-induced SOC in graphene. Advances in twistronics also showed that graphene is a promising platform to study correlated electron phases that can host, among others, exotic superconducting and correlated insulator phases.

Thesis points

1. I created van der Waals heterostructures based on single-layer graphene, hexagonal boron nitride (hBN), and tungsten diselenide (WSe_2) to induce spin—orbit coupling in graphene. One of these devices allowed for the investigation of the spin relaxation times related to the spin—orbit coupling induced by WSe_2 in graphene as a function of momentum relaxation time, which enabled the identification of the relevant spin relaxation mechanism and the large spin-relaxation anisotropy. I also fabricated a heterostructure consisting of single-layer graphene and hBN, to test if hBN can protect graphene from kerosene used in a pressure cell. Furthermore, using low-temperature transport measurements, I showed that the band-inverted phase formed in bilayer graphene due to double-sided WSe_2 encapsulation can be stabilized using hydrostatic pressure. By activation measurements, I determined the magnitude of the induced spin-orbit coupling with and without hydrostatic pressure. I also confirmed the increase of the spin—orbit coupling strength due to hydrostatic pressure by measuring Landau level crossing points. [T1, T2, T3]

2. I fabricated superconducting quantum interference devices (SQUIDs) from Josephson junctions based on heterostructures containing single-layer and bilayer graphene, hBN, and WSe_2, which allowed me to perform current-phase relation (CPR) measurements. In the case of a Josephson junction containing a WSe_2/single-layer graphene/WSe_2 heterostructure, I showed by CPR measurements that resistance oscillations caused by ballistic Fabry-Perot (FP) interference are also detectable in the superconducting critical current. Furthermore, I demonstrated with these measurements that the skewness of the CPR is enhanced at high doping, indicating high transparency of the conduction channels. Moreover, I have shown that the p-n junctions formed in the junction that also led to the formation of the FP oscillations, led to decreased skewness in the bipolar regime. Additionally, I investigated the phase shifts of the current—phase relation in an in-plane magnetic field. By increasing the magnetic field, I showed phase shifts that cannot be explained by imperfect sample orientation or inductive effects. In connection with these measurements, I demonstrated the practical limitations of the measurement of phase shifts. [T4]

3. I fabricated three-terminal Josephson junctions based on graphene and hBN and performed low-temperature transport measurements on a device. I showed that the behavior of these samples can be described in the measurements by a network model containing three resistively shunted Josephson junctions. In connection with the model, I showed that a more accurate agreement with measurements can be achieved if self-heating effects due to normal currents are also taken into account using electron-phonon coupling. I investigated the behavior of the switching current distribution of the three-terminal Josephson junction. Using this, I showed that its switching dynamics are governed by phase diffusion when the entire sample is in the superconducting state. Furthermore, I showed that if supercurrents and normal currents coexist in the sample, the switching dynamics change, and the damping increases due to the increased temperature. [T5]

Publications related to thesis points

T1 Simon Zihlmann, Aron W. Cummings, José H. Garcia, Máté Kedves, Kenji Watanabe, Takashi Taniguchi, Christian Schönenberger, and Péter Makk, Large spin relaxation anisotropy and valley-Zeeman spin-orbit coupling in WSe_2/Gr/hBN heterostructures, Phys. Rev. B 97, 075434 (2018)

T2 Bálint Fülöp, Albin Márffy, Endre Tóvári, Máté Kedves, Simon Zihlmann, David Indolese, Zoltán Kovács-Krausz, Kenji Watanabe, Takashi Taniguchi, Christian Schönenberger, István Kézsmárki, Péter Makk, and Szabolcs Csonka. New method of transport measurements on van der Waals heterostructures under pressure, J. Appl. Phys, 130(6):064303 (2021)

T3 Máté Kedves, Bálint Szentpéteri, Albin Márffy, Endre Tóvári, Nikos Papadopoulos, Prasanna K. Rout, Kenji Watanabe, Takashi Taniguchi, Srijit Goswami, Szabolcs Csonka, and Péter Makk, Stabilizing the inverted phase of a WSe_2/BLG/WSe_2 heterostructure via hydrostatic pressure, Nano Letters 23 (20), 9508-9514 (2023)

T4 Máté Kedves, Prasanna K. Rout, Nikos Papadopoulos, Kenji Watanabe, Takashi Taniguchi, Szabolcs Csonka, Srijit Goswami, Péter Makk, Current–phase relation measurements of WSe_2/graphene heterostructures, *manuscript under preparation*

T5 Máté Kedves, Tamás Pápai, Gergő Fülöp, Kenji Watanabe, Takashi Taniguchi, Péter Makk, and Szabolcs Csonka, Self-heating effects and switching dynamics in graphene multiterminal Josephson junctions, Phys. Rev. Research 6, 033143 (2024)

Other unrelated publications

T6 Simon Zihlmann, Péter Makk, Mirko K. Rehmann, Lujun Wang, Máté Kedves, David Indolese, Kenji Watanabe, Takashi Taniguchi, Dominik M. Zumbühl, and Christian Schönenberger, Out-of-plane corrugations in graphene based van der Waals heterostructures, Phys. Rev. B 102, 195404 (2020)

T7 Bálint Fülöp, Albin Márffy, Simon Zihlmann, Martin Gmitra, Endre Tóvári, Bálint Szentpéteri, Máté Kedves, Kenji Watanabe, Takashi Taniguchi, Jaroslav Fabian, Christian Schönenberger, Péter Makk, Szabolcs Csonka, Boosting proximity spin orbit coupling in graphene/WSe_2 heterostructures via hydrostatic pressure, npj 2D Mater Appl 5, 82 (2021)

T8 Tosson Elalaily, Martin Berke, Máté Kedves, Gergő Fülöp, Zoltán Scherübl, Thomas Kanne, Jesper Nygård, Péter Makk, and Szabolcs Csonka, Signatures of gate-driven out of equilibrium superconductivity in Ta/InAs nanowires, ACS Nano 17, 6, 5528–5535 (2023)

T9 Bálint Szentpéteri, Albin Márffy, Máté Kedves, Endre Tóvári, Bálint Fülöp, István Kükemezey, András Magyarkuti, Kenji Watanabe, Takashi Taniguchi, Szabolcs Csonka, Péter Makk, Tuning the proximity induced spin-orbit coupling in bilayer graphene/WSe_2 heterostructures with pressure, arXiv:2409.20062, submitted to Phys. Rev. B

Acknowledgements

In the end, I would like to express my gratitude to the people who made this entire work possible.

First and foremost, to my supervisor, Péter Makk for guiding me throughout the years since my master studies. His devotion to physics has motivated me to a great extent. I am also grateful to him for dealing with scientific and more personal problems with the same enthusiasm. I would also like to thank Szabolcs Csonka for his enlightening ideas and positive attitude. It is due to their tireless effort that the nanoelectronics lab is thriving and continuously expanding.

I am also thankful to my experienced colleagues: Zoltán Balogh, Bálint Fülöp, Gergő Fülöp, Endre Tóvári and Zoltán Scherübl. Their help in scientific and everyday problems has been invaluable. Zoltán Scherübl is specifically acknowledged for keeping the dilution refridgerators in order. I am grateful for Zoltán Kovács-Krausz, Albin Márffy, Tamás Pápai and Bálint Szentpéteri for their contributions to this work. Everyday life in the lab and group excursions would not have been the same without the humor and positivity of the past and present members of the BME Nanoelectronics group. To name but a few: Olivér Kürtössy, Mátyás Kocsis, Tosson Elalaily and Tamás Kalmár.

During this work, I had the opportunity to work at the University of Basel. For this, I am thankful to Christian Schönenberger who made these scientific visits possible. I am also grateful to Simon Zihlmann, David Indolese, Lujun Wang and Roy Haller for sharing their knowledge with me.

I also had the possibility to visit TU Delft for which I am grateful to Srijit Goswami. I thank Nikos Papadopoulos and Prasanna Rout for the help with sample fabrication and current–phase relation measurements. I would also like to thank their entire group for lifting my spirits during the worst of Covid times.

I thank the Institute of Technical Physics and Materials Science of the HUN-REN Centre for Energy Research for sharing their cleanroom facilities with us. Kenji Watanabe and Takashi Taniguchi is acknowlegded for producing the hBN crystals.

This work would have been impossible without the hard work of Béla Horváth and Márton Hajdu in the workshop and the bureaucratic support of Edina Beck, Tímea Varga and Lawson Bich Thuy.

Finally, I would also like to thank my family for their support and tolerance (not only) during this period of my life.

This research was supported by the Ministry of Innovation and Technology and the National Research, Development and Innovation Office within the Quantum Information National Laboratory of Hungary, and by the Quantum Technology National Excellence Program (Project Nr. 2017-1.2.1-NKP-2017-00001).

Appendix A

Sample fabrication parameters

A.1 E-beam lithography parameters

Resist type: 950k PMMA

- Spin-coating:
  - 4000 rpm, 40 s
  - Nominal thickness: 300 nm
  - Heat treatment: 180 °C, 3 min
- Patterning parameters:
  - Extractor voltage: 20 kV
  - Dose: 450 μC/cm^2
- Development:
  - Developer: IPA:H_2O (7:3), 1 min at 0 °C
  - N_2 blow-dry

Resist type: 600k PMMA

- Spin-coating:
  - 4000 rpm, 40 s
  - Nominal thickness: 300 nm
  - Heat treatment: 150 °C, 3 min
- Patterning parameters:
  - Extractor voltage: 20 kV
  - Dose: 240 μC/cm^2
- Development:
  - Developer: IPA:MIBK (1:3), 1 min at room temperature
  - Stopper: IPA, 30 s
  - N_2 blow-dry

A.2 Reactive ion etching

- Gases: CHF_3 (40 sccm), O_2 (4 sccm)
- $p_{base} = 5e - 5$ mBar
- $p_{background} = 60$ mTorr
- $P = 60$ W
- Etching rates:
  - hBN: 24 nm/min
  - WSe_2: 18 nm/min
  - SiO_2: ∼10 nm/min

A.3 Sputtering parameters

MoRe

- Target: MoRe
- Pressure: $p_{bg} = 2$ mTorr
- Gases: Ar (35 sccm)
- Rf power: $P = 100$ W
- Plasma ignition: 35 mTorr, 100 W
- Rate: 3 Å/s

A.4 ALD parameters

Aluminium oxide

- 1 min O_2 plasma cleaning before deposition
- Precursors: trimethylaluminium (TMA) and water
- Temperature: 225 °C
- 300 cycles → 30 nm

Appendix B

WSe_2/BLG/WSe_2 heterostructures

B.1 Continuum model of WSe_2/BLG/WSe_2

B.1.1 Low-energy Hamiltonian

We model the studied heterostructure with the low-energy Hamiltonian of bilayer graphene with an additional spin–orbit coupling term, which is different on the two graphene layers, induced by the proximity of the two WSe_2 layers. In the basis of the 4 atom unit cell, $(|C_{\mathrm{A1}}\rangle, |C_{\mathrm{B1}}\rangle, |C_{\mathrm{A2}}\rangle, |C_{\mathrm{B2}}\rangle) \otimes (|\uparrow\rangle, |\downarrow\rangle)$, where the $A1$ and $B1$ sites are located on the bottom layer and the $A2$ and $B2$ sites are on the top layer, the Hamiltonian is written as

$$\mathcal{H} = \mathcal{H}_{\mathrm{BLG}} + \mathcal{H}_{\mathrm{SOC}}, \tag{A1}$$

$$\mathcal{H}_{\mathrm{BLG}} = \begin{pmatrix} u/2 & v_0\pi^\dagger & -v_4\pi^\dagger & v_3\pi \\ v_0\pi & u/2+\Delta' & \gamma_1 & -v_4\pi^\dagger \\ -v_4\pi & \gamma_1 & -u/2+\Delta' & v_0\pi^\dagger \\ v_3\pi^\dagger & -v_4\pi & v_0\pi & -u/2 \end{pmatrix} \otimes s_0, \tag{A2}$$

$$\mathcal{H}_{\mathrm{SOC}} = \begin{pmatrix} \xi\lambda_I^b s_z/2 & i\lambda_R^b s_-^\xi & 0 & 0 \\ -i\lambda_R^b s_+^\xi & \xi\lambda_I^b s_z/2 & 0 & 0 \\ 0 & 0 & \xi\lambda_I^t s_z/2 & i\lambda_R^t s_-^\xi \\ 0 & 0 & -i\lambda_R^t s_+^\xi & \xi\lambda_I^t s_z/2 \end{pmatrix}, \tag{A3}$$

where $\mathcal{H}_{\mathrm{BLG}}$ is the Hamiltonian of the BLG[89] and $\mathcal{H}_{\mathrm{SOC}}$ is the spin–orbit coupling term describing the layer-specific proximity induced Ising-type SOC with the parameters of λ_I^i and Rashba-type SOC parametrized with λ_R^i [66, 74]. Here, s_i, with $i = \{0, x, y, z\}$, are the spin Pauli matrices and $s_\pm^\xi = \frac{1}{2}(s_x + i\xi s_y)$. In $\mathcal{H}_{\mathrm{BLG}}$, γ_i, with $i = \{0, 1, 3, 4\}$ describe the intra- and interlayer hoppings in BLG, as illustrated in Figure 5.1.(b), $v_i = \sqrt{3}a\gamma_i/2\hbar$ are effective velocities, with the lattice constant of the graphene $a = 2.46\,\text{Å}$ and Δ' is the dimer on-site energy. γ_0 is the nearest neighbour intralayer hopping, γ_1 is the interlayer hopping between the dimer sites, γ_3 describes the hopping between the non-dimer sites and γ_4 is the interlayer hopping between the dimer and non-dimer orbitals. In $\mathcal{H}$, $\pi = \hbar(\xi k_x + i k_y)$ and $\pi^\dagger = \hbar(\xi k_x - i k_y)$ are momentum operators measured from the K and K' valleys with the valley indices $\xi = \pm 1$. The parameter u is the interlayer potentials difference modelling the effect of an external electric field.

In our simulations we have used the following parameters: $\gamma_0 = 2.61\,\text{eV}$, $\gamma_1 = 0.361\,\text{eV}$, $\gamma_3 = 0.283\,\text{eV}$, $\gamma_4 = 0.138\,\text{eV}$ and $\Delta' = 0.015\,\text{eV}$ [61].

In the main text, we show the spectrum near the K valley. Here, we show the difference between the K and K' valleys in Fig B.1. The main difference, besides the opposite tilting due to the trigonal warping, is the opposite spin polarization of the bands, which is the manifestation of the Kramers theorem, since the valley-Zeemann terms generate an opposite effective magnetic

field in the two valleys. In the figures, we calculate the spin polarization as

$$\zeta_n = \sum_{X=A1,A2,B1,B2} |c_{X,\uparrow}|^2 - |c_{X,\downarrow}|^2. \tag{A4}$$

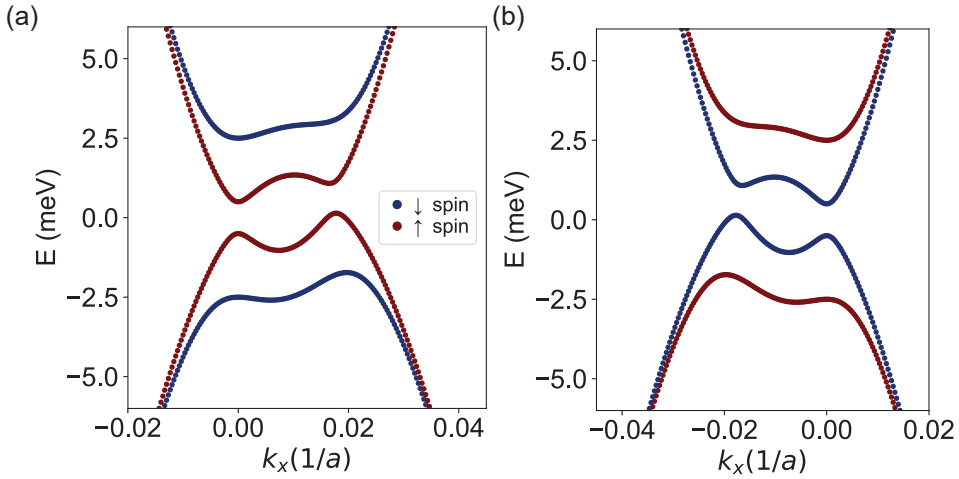

Figure B.1: Calculated band structure using the parameters of $u = 3\,\text{meV}$ and $\lambda_I^b = -\lambda_I^t = 2\,\text{meV}$ (a) near the K valley and (b) near the K' valley.

Besides the spin polarization, the layer polarization α_n is also an important parameter of the model, which is defined as

$$\alpha_n = \sum_{s=\uparrow,\downarrow} |c_{A1,s}|^2 + |c_{B1,s}|^2 - |c_{A2,s}|^2 - |c_{B2,s}|^2. \tag{A5}$$

As shown in Figure B.2, at $u = 0$ the bands have no layer polarization, which can be lifted by increasing u. For $|u| > |\lambda_I^b|$, the low energy part of the conductance and valence bands becomes layer polarized with the opposite layer polarization of the valence and conduction bands.

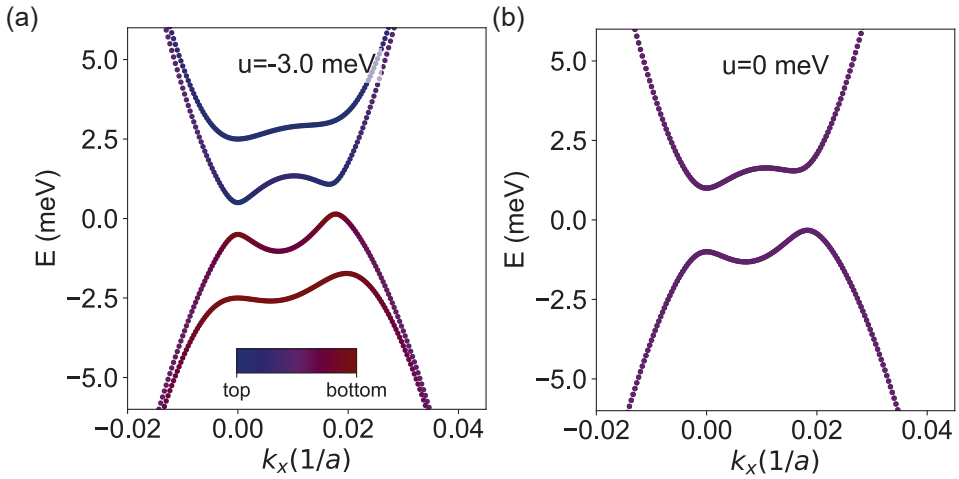

Figure B.2: Calculated band structure using the parameter of $\lambda_I^b = -\lambda_I^t = 2\,\text{meV}$ (a) at $u = -3\,\text{meV}$ and (b) at $u = 0\,\text{meV}$. The color of the line corresponds to the layer polarization: the blue (red) points are fully polarized to the top (bottom) layer and the purple points are layer degenerated.

For completeness, the band structure near the K-point is shown in Figure B.3. with $\lambda_I^b = \lambda_I^t$. In this case, the bands are spin split due to the SOC, which can be considered here as a Zeeman

splitting in an effective magnetic field. Moreover, in this case, there is no gap at $u = 0$ and a gap only opens if $|u| > |\lambda_I^{b,t}|$.

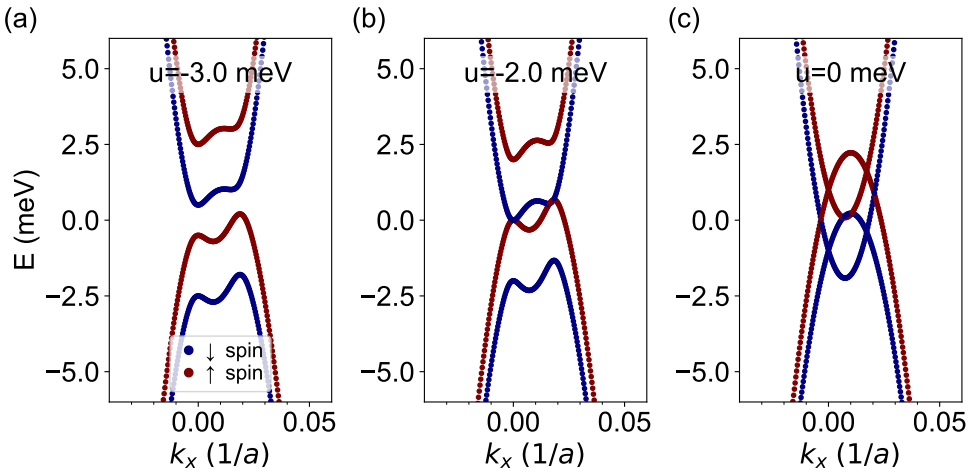

Figure B.3: Calculated band structure using the parameter of $\lambda_I^b = \lambda_I^t = 2\,\text{meV}$ (a) at $u = -3\,\text{meV}$, (b) at $u = -2\,\text{meV}$ and (c) at $u = 0\,\text{meV}$. The color of the lines corresponds to the spin polarization.

B.1.2 Landau level calculations

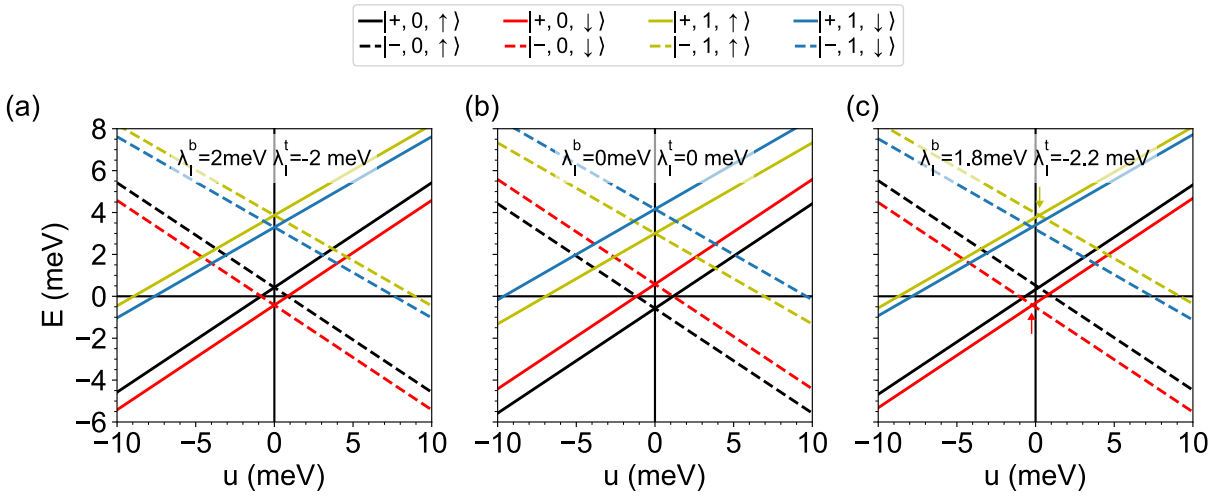

Figure B.4: Single-particle zeroth LL spectrum as a function of u at $B = 10\,\text{T}$ for (a) $\lambda_I^b = -\lambda_I^t = -2\,\text{meV}$, (b) $\lambda_I^b = \lambda_I^t = -0$ and (c) $\lambda_I^b = 1.8\,\text{meV}$ and $\lambda_I^t = -2.2\,\text{meV}$.

The Landau level calculations were performed by Bálint Szentpéteri along the lines of Reference [186]. In Figure 5.5.(a), we plot the lowest 8 LLs with respect to u at $B = 8.5\,\text{T}$. These LLs would be degenerate if we set every parameter to zero except γ_0 and γ_1, including the interlayer potential. In Figure B.4, we show the LLs in three different scenarios of λ_I: in panel (b) the LLs are shown if $\lambda_I = 0$. In this case, the LLs are spin-split due to the Zeeman term and also split in the orbital index due to γ_0 and Δ'. A finite u further splits these LLs and their energy is linear in u. Since for the two lowest LL the spin and layer index become effectively the same, different valleys shift oppositely with a displacement field. By introducing a finite Ising-type SOC λ_I^b shifts the energies of the eigenstates of $|K, n, \sigma\rangle$ and λ_I^t shifts the energies of the eigenstates of $|K', n, \sigma\rangle$. Comparing panel (a) and (b), if $\lambda_I^t = -\lambda_I^b$, at high magnetic field, the spectrum seems very similar to the case without SOC, however, the order of the spin up

and spin down levels flip. Moreover, the positions (u^*) where two LLs cross also change, which we defined as D^* crossings in the measurements in the main text. In the third case, shown in panel (c), when λ_I^t and λ_I^b have an opposite sign but their magnitudes are different, the u, $-u$ symmetry is lost, leading to a non-zero $u^*_{\pm 3}$ crossings (indicated by arrows in Figure B.4.(c)).

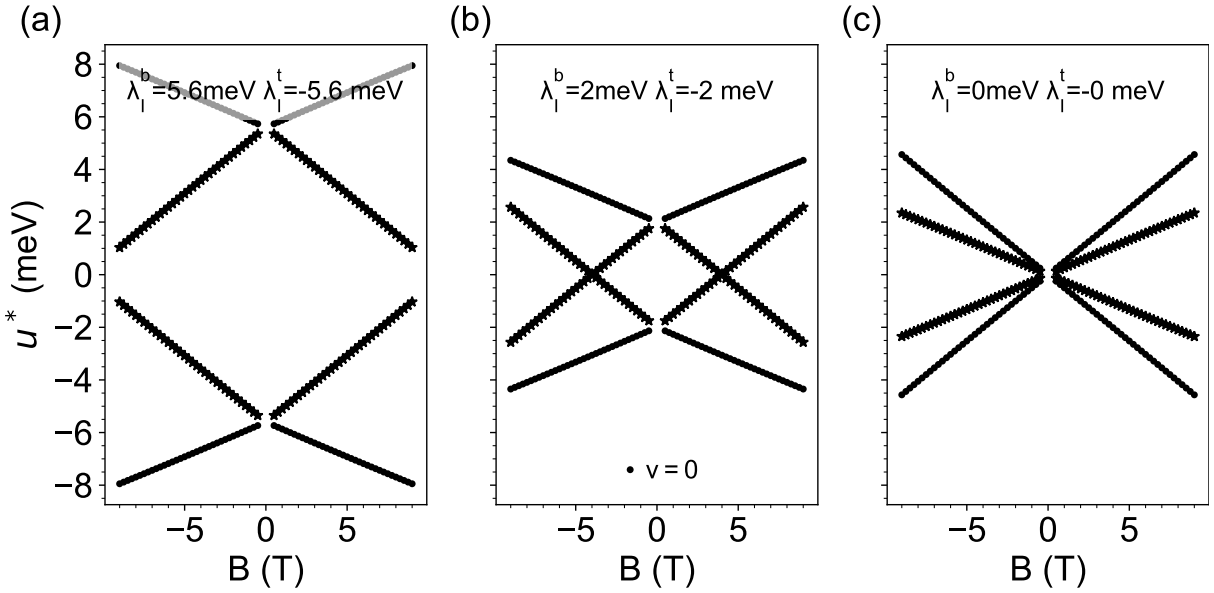

Figure B.5: Landau level crossings at $\nu = 0$ as a function of B with (a) $\lambda_I^b = -\lambda_I^t = -5.6\,\text{meV}$, (b) $\lambda_I^b = -\lambda_I^t = -2\,\text{meV}$ and (c) $\lambda_I^b = \lambda_I^t = -0$.

In Figure B.5 and Figure B.6, we plot the Landau level crossings, with SOC and without SOC, for $\nu = 0$ and $\nu = \pm 1$, respectively. Without SOC the crossings go to zero as $B \to 0$ as opposed to the case of $\lambda_I^b = -\lambda_I^t \neq 0$. Comparing these figures with Fig 4. in the main text, the experiments show similarities to the model: the $\nu = 1$ crossings show similar tendency, so do the higher u_0^* branches in the $\nu = 0$ crossings. Likely the discrepancy between the model calculated in a single-particle picture and the experiment comes from the fact that in our calculations we neglect electron-electron interactions [185].

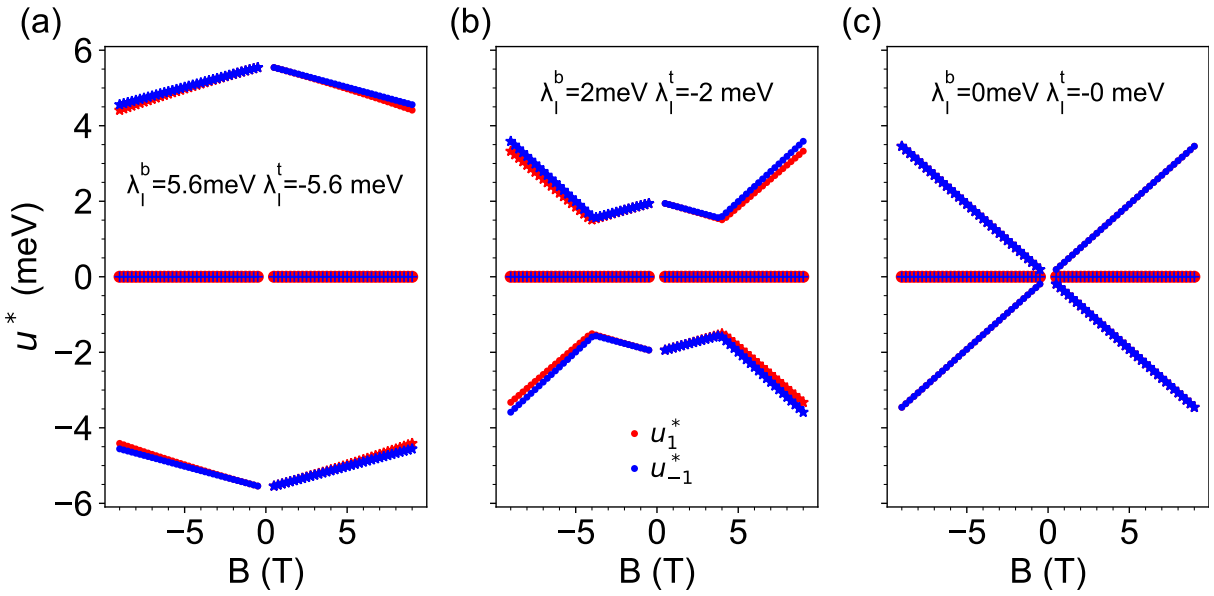

Figure B.6: Landau level crossings at $\nu = \pm 1$ as a function of B with (a) $\lambda_I^b = -\lambda_I^t = -5.6\,\text{meV}$, (b) $\lambda_I^b = -\lambda_I^t = -2\,\text{meV}$ and with (c) $\lambda_I^b = \lambda_I^t = 0$.

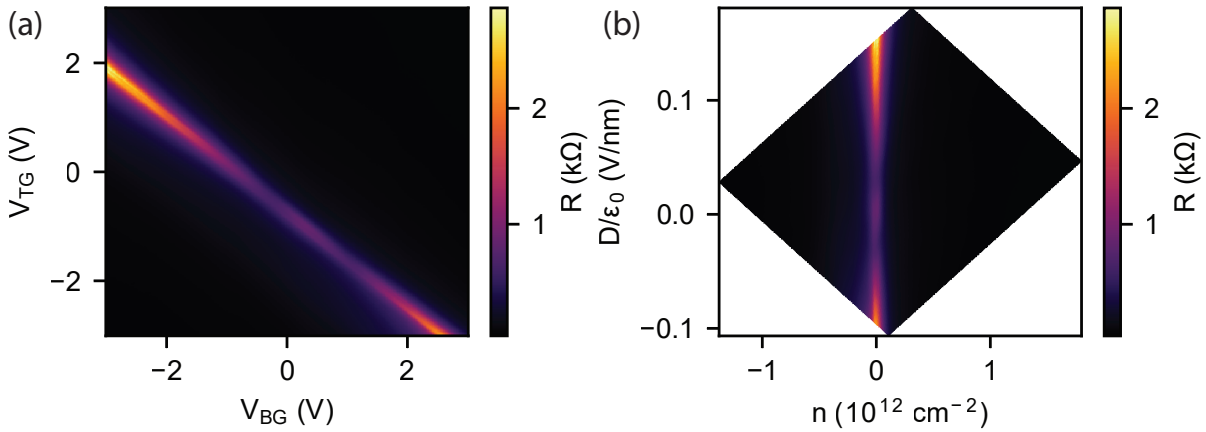

Figure B.7: Conversion from a) gate voltages to b) charge carrier density n and transverse displacement field D.

p (GPa)	α_{BG} $(10^{15}$ V^{-1}m$^{-2})$	α_{TG} $(10^{15}$ V^{-1}m$^{-2})$
0	2.47 ± 0.08	2.81 ± 0.10
1.65	2.82 ± 0.07	3.12 ± 0.09

Table A1: Lever arms determined from quantum Hall measurements.

B.2 Determination of the lever arms

As discussed in the main text, to tune the charge carrier density n and the transverse displacement field D in the sample, gate voltages are applied to the metallic topgate (V_{TG}) and the graphite bottom gate (V_{BG}). The conversion from gate voltages to n and D is shown in Figure B.7 and is given by the following relation:

$$\begin{aligned} n &= \alpha_{TG} V_{TG} + \alpha_{BG} V_{BG} + n_0 \\ \frac{D}{\epsilon_0} &= \frac{e}{2\epsilon_0} \left(\alpha_{TG} V_{TG} - \alpha_{BG} V_{BG}\right) + \frac{D_0}{\epsilon_0}, \end{aligned} \tag{A6}$$

where ϵ_0 is the vacuum permittivity, e is the elementary charge, $\alpha_{BG,TG}$ are the lever arms of the bottom and topgate, respectively, while n_0 and D_0 are the offset charge carrier density and displacement field. Since the lever arms are subject to change after the hydrostatic pressure is applied, originating from the compression of dielectricts, we determine them experimentally. First, the ratio of lever arms α_{BG}/α_{TG} can be obatined from gate voltage maps of the resistance (e.g. Figure B.7.(a)), as it is given by the slope of the charge neutrality line. Secondly, by measuring the fan diagram of Landau levels for $D = 0$, we determine the lever arms via the relation $\nu = nh/eB$ between the filling factor ν and the carrier density n for a given magnetic field B, where h is Planck's constant. The values of the lever arms can be found in Table A1.

B.3 Additional measurements on two-terminal devices

We performed additional measurements on two-terminal devices also shown in Figure 5.1.(a). Two different devices were measured between contacts E-F (device S2) and F-G (device S3) in separate pressurization and cool-down cycles. Two-terminal resistance maps of the devices as a function of n and D are shown in Figure B.9 at $p = 0$ and $p = 1.2$ GPa. These results are consistent with our observations on device S1 in that the inverted phase is clearly visible and is enhanced by the applied pressure. Figure B.9.(c) and B.9.(f) shows the comparison between

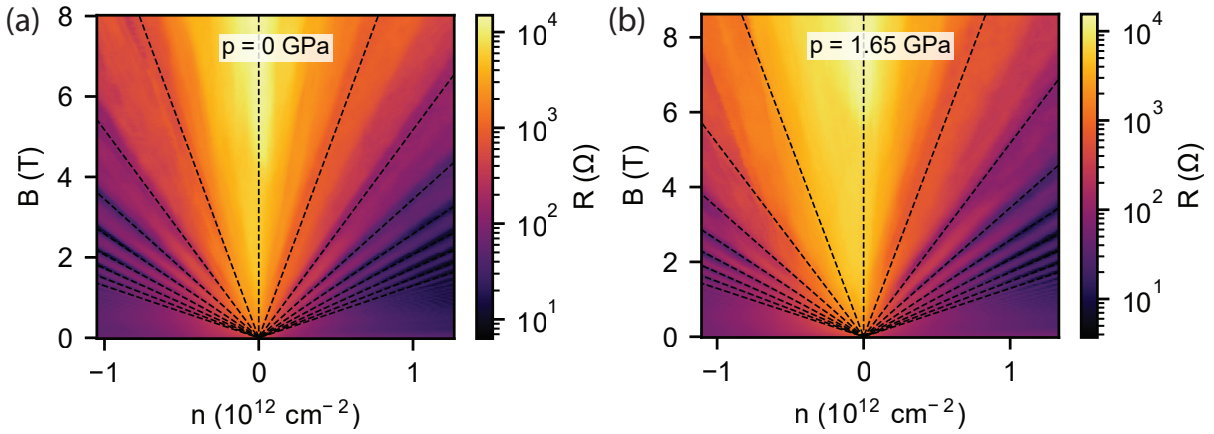

Figure B.8: Landau fan daigram of the resistance for a) $p = 0$ and b) $p = 1.65\,\mathrm{GPa}$ at $D = 0$. Dashed lines correspond to carrier densities with filling factors $\nu = 4k$, where $k \in \mathbb{Z}$.

line traces of the resistance measured at $n = 0$ as a function of D at $p = 0$ and $p = 1.2\,\mathrm{GPa}$ for device S2 and S3, respectively. In both cases, the resistance at $D = 0$ is increased due to the applied pressure and the location of resistance minima (D^*) is increased by $\sim 25\%$.

We also performed thermal activation measurements on both devices. For reference, the raw measurement data is shown for device S2 in Figure B.10.(a) for $p = 0$ obtained while cooling the sample from 100 K to base temperature. Due to the two-terminal geometry of these devices a large jump in resistance is visible that corresponds to the superconducting phase transition of the NbTiN contacts.

In order to extract the band gaps from these measurements additional data processing is required and the normal resistance of the contacts have to be subtracted from the high temperature parts of the data. We subtract $R_{N,S2} = 5.90\,\mathrm{k\Omega}$ and $R_{N,S3} = 5.38\,\mathrm{k\Omega}$ for device S2 and S3, respectively. The thermal activation data after the subtraction of the contact normal resistance is shown in Figure B.10.(b) and B.10.(c) for device S2 at $p = 0$ and $p = 1.2\,\mathrm{GPa}$, respectively. After the subtraction, a vertical line is visible that originates from the phase transition. We exclude these outliers from further analysis. Although this makes our data analysis less reliable, we can nevertheless extract the SOC strength using the same method as described in section 5.6. This yields $\lambda_t = -\lambda_b = 1.6 \pm 0.4\,\mathrm{meV}$ for $p = 0$ and $\lambda_t = -\lambda_b = 2.4 \pm 0.5\,\mathrm{meV}$ for $p = 1.2\,\mathrm{GPa}$ and $\lambda_t = -\lambda_b = 1.0 \pm 0.3\,\mathrm{meV}$ for $p = 0$ and $\lambda_t = -\lambda_b = 2.0 \pm 0.4\,\mathrm{meV}$ for $p = 1.2\,\mathrm{GPa}$ for device S2 and S3, repsectively. These results also reproduce our findings for device S1 as a significant increase in the extracted SOC strength is seen in all cases.

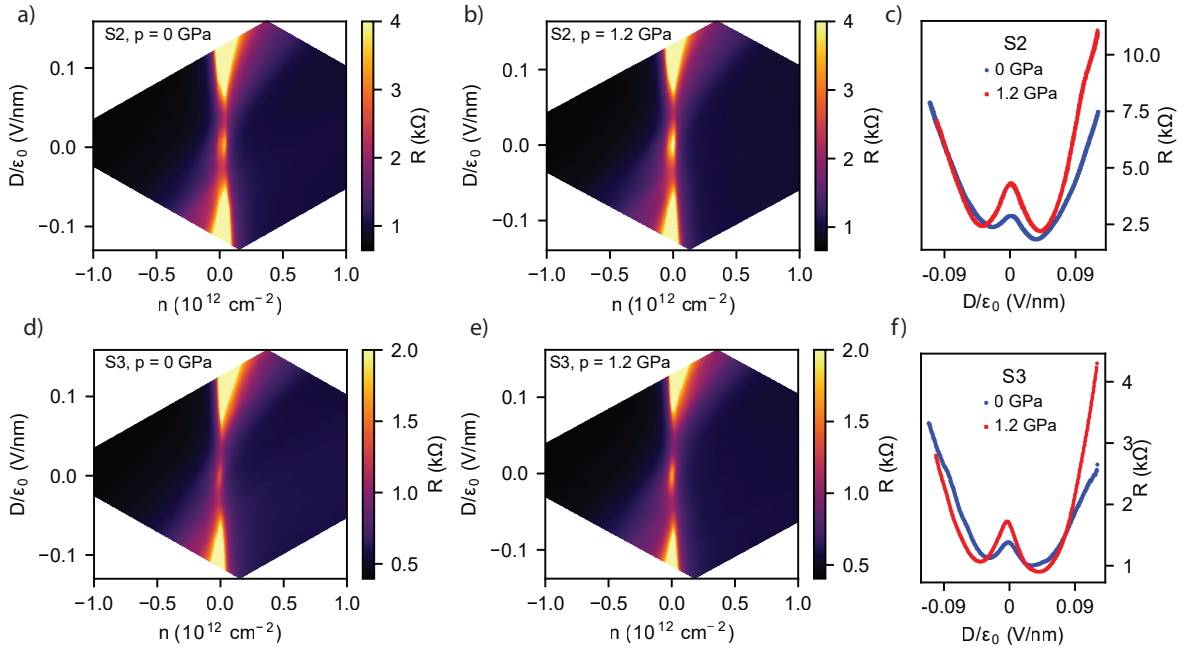

Figure B.9: a,b) 2-terminal resistance map of device S2 for a) ambient pressure and b) $p = 1.2\,\mathrm{GPa}$. c) Line traces of resistance for device S2 as a function of D at $n = 0$ for ambient pressure (blue) and $p = 1.2\,\mathrm{GPa}$ (red). d,e,f) Similar resistance maps and comparison for device S3.

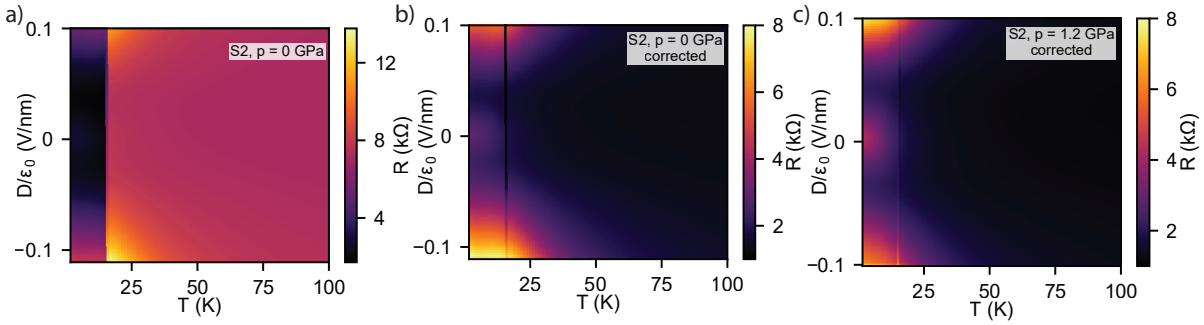

Figure B.10: Temperature dependence of the resistance of device S2 as a function of D at $n = 0$ for a) $p = 0$. The jump in the resistance around 15 K corresponds to the superconducting phase transition of the NbTiN leads. Corrected data after the contact normal resistance was subtracted for b) $p = 0$ and c) $p = 1.2\,\mathrm{GPa}$.

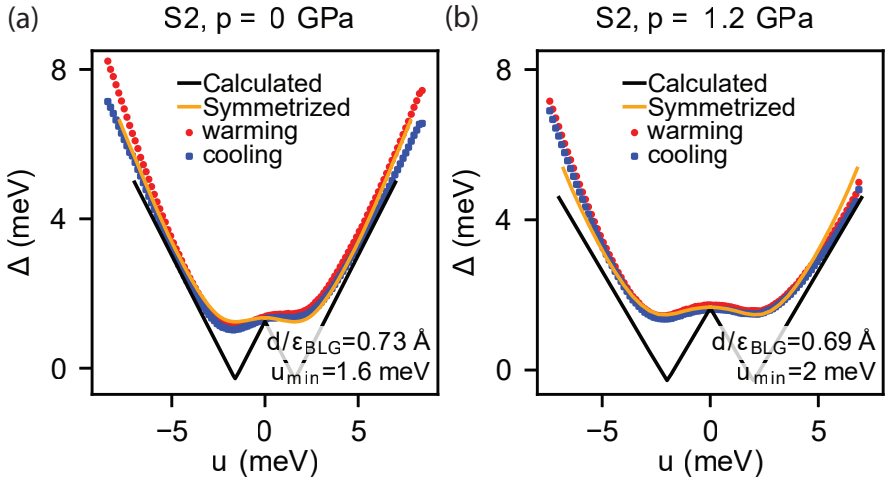

Figure B.11: Band gaps determined from thermal activation measurements performed while warming up (red) and cooling down (blue) device S2 for a) $p = 0$ and b) $p = 1.2\,\mathrm{GPa}$, respectively. Symmetrized curve with respect to $u = 0$ is shown in orange and the band gap calculated from the theoretical model is shown with the solid black line.

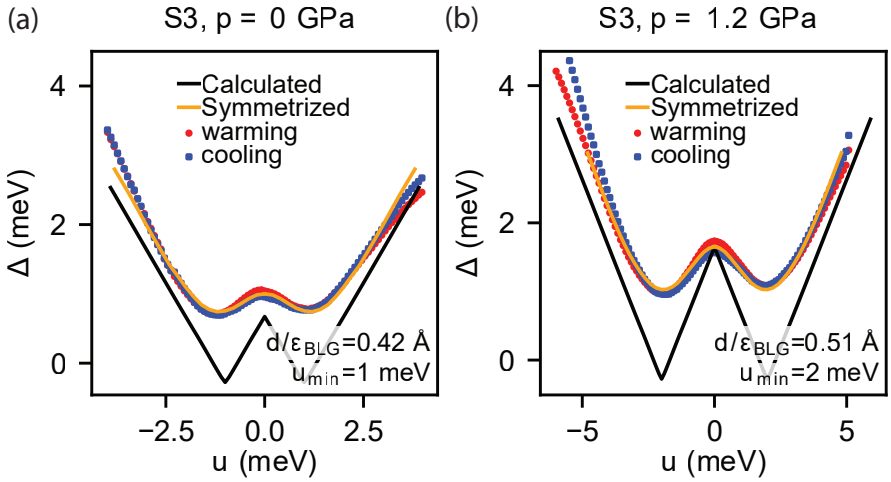

Figure B.12: Band gaps determined from thermal activation measurements performed while warming up (red) and cooling down (blue) device S3 for a) $p = 0$ and b) $p = 1.2\,\mathrm{GPa}$, respectively. Symmetrized curve with respect to $u = 0$ is shown in orange and the band gap calculated from the theoretical model is shown with the solid black line.

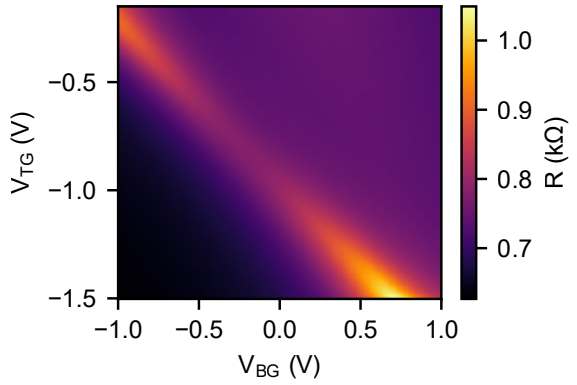

Figure B.13: Differential resistance of a two-terminal device as a function of V_{BG} and V_{TG} that shows no signatures of band inversion.

B.4 Additional data from Sample S4

As mentioned in section 5.3, not all samples showed signatures of band inversion. We attribute this to the lack of control over the rotation of WSe_2 layers. Based on theoretical predictions[72, 76], we argue that for certain rotation angles of the two WSe_2 layers (e.g. 0°), the sign of λ_I^b and λ_I^t can be the same which leads to the situation discussed section B.1 and shown in Figure B.3 where no band gap is present at $D = 0$. For reference, in Figure B.13, we show measurement data of a two-terminal device measured at 4 K, where no signatures of band inversion can be observed in the resistance map.

Appendix C

Current–phase relation measurements

C.1 Conversion from gate voltages to n and D

Here, we show the normal state resistance R_N as a function of $V_{TG,dev}$ and V_{BG} in Figure C.1.(a), as presented in Figure 6.2 in the main text. As discussed in Section 2.4.1 and Appendix B, we can calculated the charge carrier density n and the transverse displacement field D from the gate voltages. In this case, we calculate the lever arms using the layer thicknesses determined from AFM measurements and the ratio of lever arms from the slope of the CNL. Figure C.1.(b) shows R_N as a function of the calculated n and D.

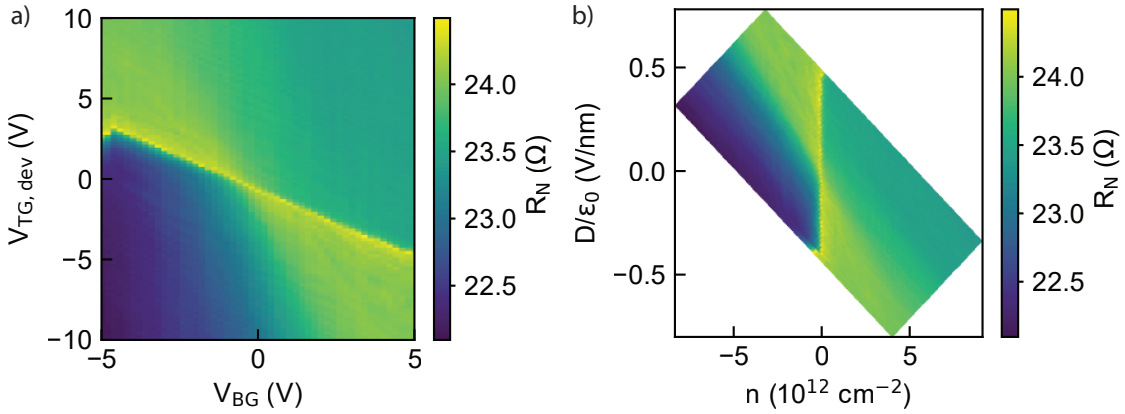

Figure C.1: a) Normal state resistance R_N as a function of $V_{TG,dev}$ and V_{BG} at $V_{TG,ref} = 5\,\mathrm{V}$. b) R_N as a function of n and D.

Similarly, the normal resistance map showing the Fabry-Perot oscillations in Figure 6.3 in the main text can be represented as a function of n and D. This is shown in Figure C.2.

C.2 Additional CPR devices

The devices uses for current–phase relation measurements are listed in Table A1. Layer thicknesses obtained from AFM measurements are also given in parentheses where known. Furthermore, schematic illustrations of the different measured heterostructures and corresponding optical microscopic images are shown in Figure C.3. Each device features metallic top gate electrodes. Independent tuning of the charge carrier density and transverse electric field is enabled by either a graphite bottom gate or the doped Si substrate utilised as a global backgate

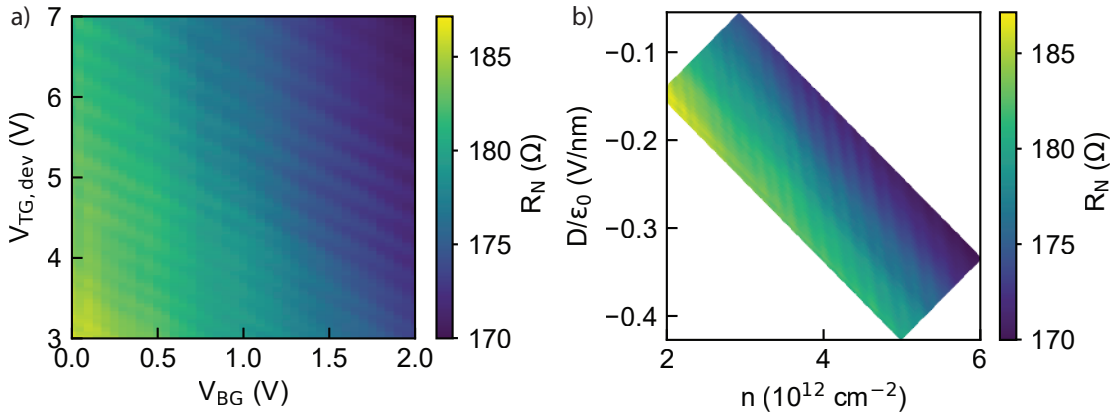

Figure C.2: a) Normal state resistance R_N as a function of $V_{TG,dev}$ and V_{BG} at $V_{TG,ref} = -1.5\,\mathrm{V}$, showing the Fabry-Perot oscillations. b) R_N as a function of n and D.

electrode. Superconducting electrodes were fabricated by DC sputtering of MoRe or NbTiN. Loop size in every instance is $\sim 10 \times 10\,\mu\mathrm{m}^2$.[1]

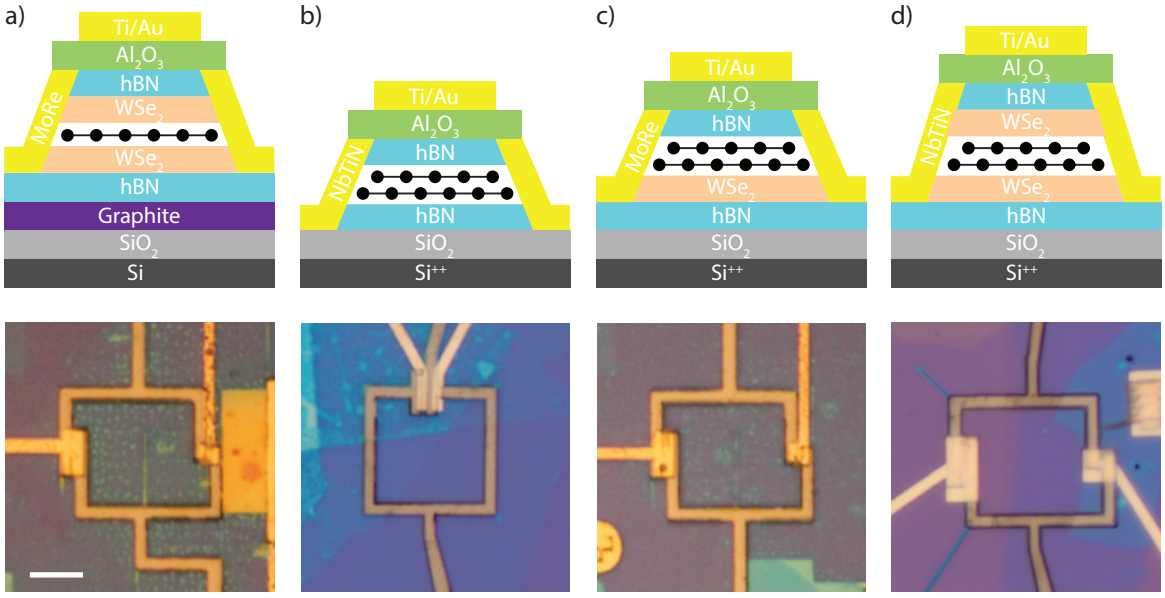

Figure C.3: (a-d) Top: schematic illustration of the heterostructures fabricated for CPR measurements. Bottom: optical microscopic images of devices corresponding to the schematic depictions in the top row. Scale bar is 5 μm.

C.3 In-plane magnetic field dependence of the device critical current

To further illustrate that the rapid decrease of critical current is not unique to device A, we present here the gate maps of the device critical current as a function of top and bottom gates for samples $A - D$. $I_{c,dev}$ is extracted from CPR measurements as described in section 6.3.3 of the main text. Figure C.4 shows the gate maps of $I_{c,dev}$ for samples $A - D$ for $B_y = 0$. The

[1] I fabricated devices A and C in Budapest. I also fabricated Device B with the help of Nikos Papadopulos at TU Delft. Device D was fabricated at TU Delft by Prasanna Rout and Nikos Papadopulos.

Device	Substrate	heterostructure layers (d (nm))
A	Si/SiO_2	graphite gate/hBN (40)/WSe_2 (15)/SLG/WSe_2 (5)/hBN (25)
B	Si^{++}/SiO_2	hBN/BLG/hBN
C	Si^{++}/SiO_2	hBN (20)/WSe_2 (20)/BLG/hBN (10)
D	Si^{++}/SiO_2	hBN/WSe_2/BLG/WSe_2/hBN
E	Si^{++}/SiO_2	graphite gate/hBN (30)/WSe_2 (20)/SLG/hBN (40)

Table A1: List of devices used for current–phase relation measurements. Layer thicknesses obtained from AFM measurements are indicated in parentheses.

gate maps of $I_{c,dev}$ show similar features in all cases. Although signatures of p–n junctions can only be seen for device A, the charge neutrality line where the critical current is minimal can be identified in all cases. The maximum of $I_{c,dev}$ is similar for devices $A-C$ and significantly smaller for device D. This suggests that the quality of device D is lower than the other devices.

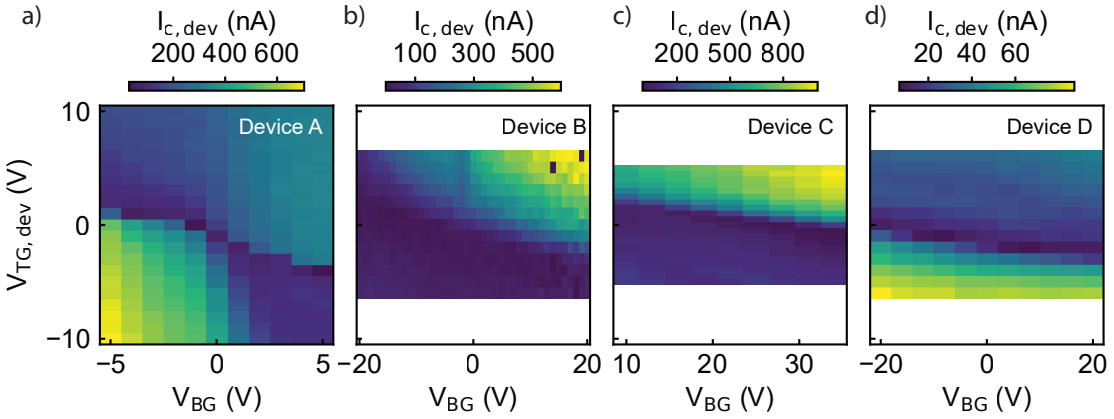

Figure C.4: (a-d) Device critical current $I_{c,dev}$ as a function of $V_{TG,dev}$ and V_{BG} for $B_y = 0$ in case of device $A-D$, respectively.

Figure C.5 shows similar gate maps of $I_{c,dev}$ for samples $A-D$ measured in finite in-plane magnetic field. The values of B_y were chosen such that the reference critical current remained large enough to ensure true CPR measurements. The direction of B_y was perpendicular to the direction of current in the Josephson junctions. A significant decrease in $I_{c,dev}$ is observed for device $A-C$. No decrease of $I_{c,dev}$ was found for device D which might be explained by the low sample quality that results in inhomogeneous supercurrent flow already without in-plane magnetic field.

C.4 In-plane magnetic field dependence of the reference critical current

Figure C.6 shows the extracted values of $I_{c,ref}$ of device A as a function of $V_{TG,dev}$ and V_{BG} for different values of B_y. In Figure C.6.(a) the measurement for $B_y = 0$ is shown again for convenience. $V_{TG,ref}$ is set to $-0.4\,\mathrm{V}$ ($B_y = 0\,\mathrm{mT}$), $0\,\mathrm{V}$ ($50\,\mathrm{mT}$), $2\,\mathrm{V}$ ($100\,\mathrm{mT}$) and $5\,\mathrm{V}$ ($150\,\mathrm{mT}$). A small change in $I_{c,ref}$ is observable in all cases as a function of gate voltages and a significant decrease in the amplitude of $I_{c,ref}$ is visible despite of increasing $V_{TG,ref}$ with B_y. For $B_y = 100\,\mathrm{mT}$, the gate dependence is qualitatively different from the other measurements. This could be attributed to sample inhomogeneity and the different gate setting. However, the relative amplitude of the change in $I_{c,ref}$ is similar in all cases.

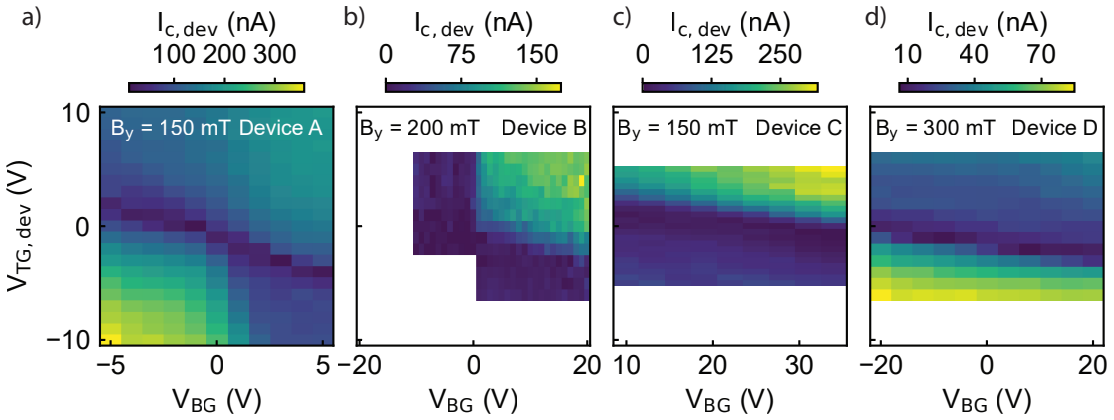

Figure C.5: (a-d) Critical current of the device junction $I_{c,dev}$ as a function of $V_{TG,dev}$ and V_{BG} for relatively large B_y in case of device $A-D$, respectively.

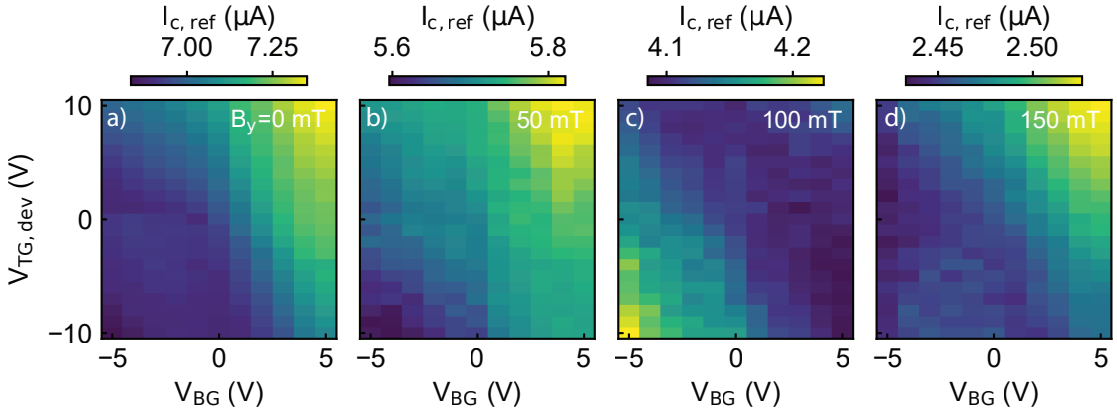

Figure C.6: (a)-(d) Critical current of the reference junction $I_{c,ref}$ of device A as a function of $V_{TG,dev}$ and V_{BG} for $B_y = 0$, 50, 100 and 150 mT. To compensate for the decrease in $I_{c,ref}$ due to the in-plane magnetic field the reference topgate voltage was tuned to $V_{TG,ref} = -0.4$ V (0 mT), 0 V (50 mT), 2 V (100 mT) and 5 V (150 mT), respectively.

C.5 Additional data for device *C*

The measurement of current–phase relation becomes more challenging if the two Josephson junctions share a common gate, such as the doped Si backgate in case of devices $B-D$. In this instance, the two junctions are tuned simultaneously by the backgate electrode and the measurement of gate maps (similarly to device A, presented in the main text) requires additional care. To ensure that the true CPR of the device junction is measured and to avoid unwanted phase shifts related to the change of $I_{c,ref}$, we keep $I_{c,ref}$ constant by simultaneously tuning the reference topgate ($V_{TG,ref}$) and backgate (V_{BG}) voltages. To this end, we first measure CPR as a function of $V_{TG,ref}$ and V_{BG} and extract $I_{c,ref}$ using the fit procedure described in the main text. The extracted $I_{c,ref}$ as a function of $V_{TG,ref}$ and V_{BG} is shown in Figure C.7.(a). The measurement of the CPR of the device junction requires that $I_{c,ref} \gg I_{c,dev}$. By interpolating the gate map of $I_{c,ref}$ shown in Figure C.7.(a), the required value of $V_{TG,ref}$ can be found for a given V_{BG} and $I_{c,ref}$, assuming that $I_{c,ref}$ is independent of $V_{TG,dev}$. This allows us to keep $I_{c,ref}$ constant during the CPR measurement of the device junction and compensate the effect of changing V_{BG} on $I_{c,ref}$.

Using the previously described compensation method, we performed CPR measurements on device C as a function of $V_{TG,dev}$ and V_{BG} with $I_{c,ref} \approx 6\,\mu$A. The effectiveness of the

compensation method is further illustrated in Figure C.7.(b) where the extracted $I_{c,ref}$ is shown as a function of $V_{TG,dev}$ and V_{BG} during the CPR measurement of the device junction. From here, it is easily visible that $I_{c,ref}$ can effectively be kept constant during the measurement and this method results in a relative change of $I_{c,ref}$ smaller than what is observed for device A. This means that, assuming that τ_{ref} is also kept constant along with $I_{c,ref}$, using this compensation method the relative phase shifts can be more precisely measured even though the gates are not independent. On the other hand, it is also important to note that the available range of V_{BG} is constrained by the required value of $I_{c,ref} \approx 6\,\mu$A since a suitable $V_{TG,ref}$ can only be found for a subset of the V_{BG} range.

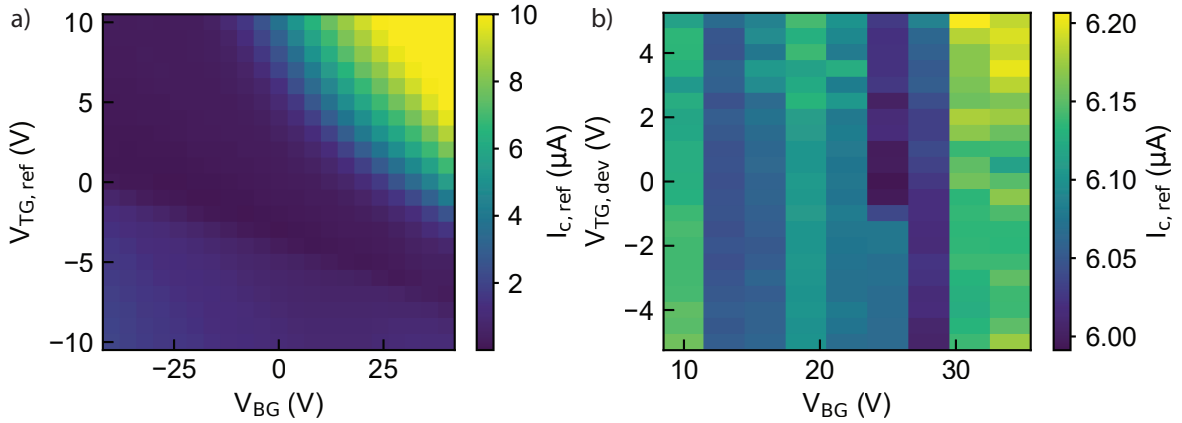

Figure C.7: (a) Reference critical current of device C as a function of $V_{TG,ref}$ and V_{BG}. (b) $I_{c,ref}$ as a function of $V_{TG,dev}$ and V_{BG} during the CPR measurements of the device junction. $I_{c,ref} \approx 6\,\mu$A is kept constant by simultaneously tuning V_{BG} and $V_{TG,ref}$. The required gate voltages are determined using the measurement in panel (a).

Figure C.8.(a) and C.8.(b) shows the measured gate map of $I_{c,dev}$ for $B_y = 0$ and $B_y = 200\,$mT, respectively. As discussed earlier, we generally observe the decrease of $I_{c,dev}$ as B_y is increased for multiple devices. It is also visible in Figure C.8.(a) that the minimum of $I_{c,dev}$ is decreasing along the charge neutrality line which is a consequence of the opening of a band gap in the device junction. Furthermore, similarly to device A, we fit the measurements using the effective single channel Andreev formula and observe a large transparency τ where $I_{c,dev}$ is large and a rapid decrease of τ with B_y, as illustrated in Figure C.9.

Figure C.10.(a) and C.10.(b) shows the extracted phase shift φ_0 for $B_y = 0$ and $B_y = 200\,$mT. Here, due to the appearance of an uncontrolled external flux during the measurement, the relative phase shift compared to the value obtained for $V_{TG,dev} = -5\,$V for each value of V_{BG} is shown. For both $B_y = 0$ and $B_y = 200\,$mT, outliers around the CNL appear. In this case, this is attributed to the unreliability of the fit procedure due to the very small $I_{c,dev}$ around the gapped region.

C.6 Numerical calculation of the current–phase relation

As mentioned in the main text, it is possible to numerically calculate the CϕR of a SQUID device. In the absence of inductance effects, this is a straightforward task. We model our devices with two Josephson junctions, each hosting a single Andreev bound state. Using the previously introduced notation of device and reference junctions, the CPRs of the junctions are given by:

$$\begin{aligned} I_{dev}(\varphi_{dev}) &= I_{c,dev}\widetilde{f}(\tau_{dev}, \varphi_{dev}) \\ I_{ref}(\varphi_{ref}) &= I_{c,ref}\widetilde{f}(\tau_{ref}, \varphi_{ref}), \end{aligned} \tag{A1}$$

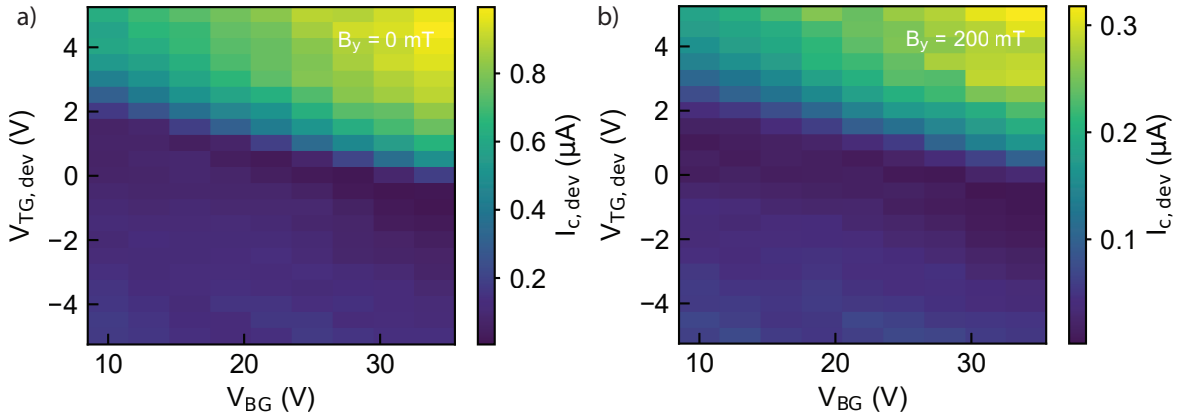

Figure C.8: (a,b) Critical current of the device junction $I_{c,dev}$ of device C as a function of $V_{TG,dev}$ and V_{BG} for $B_y = 0$ and $B_y = 200\,\mathrm{mT}$, respectively.

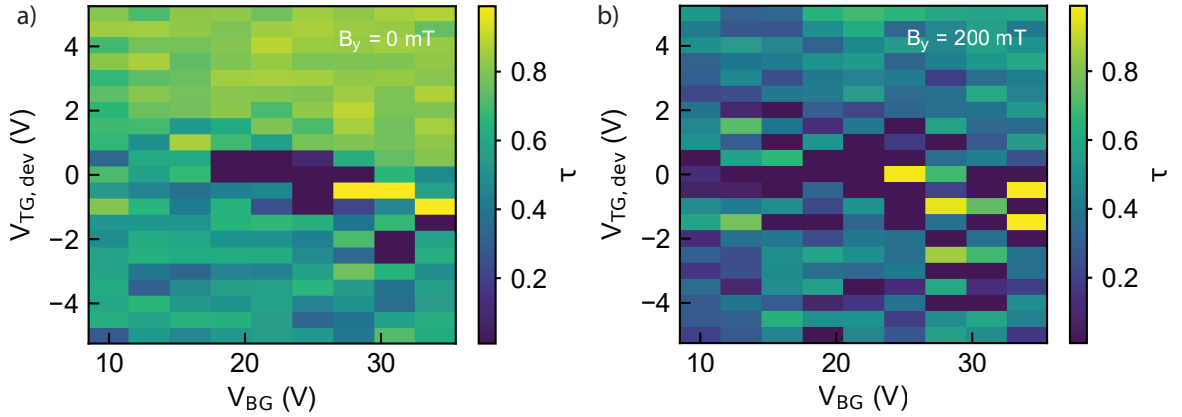

Figure C.9: (a,b) Transparency τ of device C as a function of $V_{TG,dev}$ and V_{BG} for $B_y = 0$ and $B_y = 200\,\mathrm{mT}$, respectively.

where $I_{c,dev}$ ($I_{c,ref}$) is the device (reference) critical current, φ_{dev} (φ_{ref}) is the phase difference, τ_{dev} (τ_{ref}) is the transparency of the device (reference) junction and $\widetilde{f}$ is the normalised Andreev formula introduced in Section 2.5.4. The two phase differences are connected by the applied magnetic flux Φ_a via:

$$\varphi_{ref} - \varphi_{dev} = 2\pi \frac{\Phi}{\Phi_0}. \tag{A2}$$

Combining equation A1 and A2, the critical current of the SQUID for a given magnetic flux – the CΦR – can be found as:

$$I_c(\Phi) = \max_{\varphi_{dev} \in [0, 2\pi[} \left\{ I_{c,dev} \widetilde{f}(\tau_{dev}, \varphi_{dev}) + I_{c,ref} \widetilde{f}\left(\tau_{ref}, \varphi_{dev} + 2\pi \frac{\Phi}{\Phi_0}\right) \right\}. \tag{A3}$$

As detailed in Section 6.5, if a finite inductance L is present, the applied magnetic flux is screened by the circulating current. In this case, in order to calculate the switching current as a function of the applied external magnetic flux Φ_a, equation A2 has to be modified:

$$\varphi_{ref} - \varphi_{dev} = \frac{2\pi}{\Phi_0} \left(\phi_a - L I_{circ}\right). \tag{A4}$$

Using the notation introduced in Section 6.5, the circulating current is given by:

$$I_{circ} = \left(I_{ref} - I_{dev}\right)/2.$$

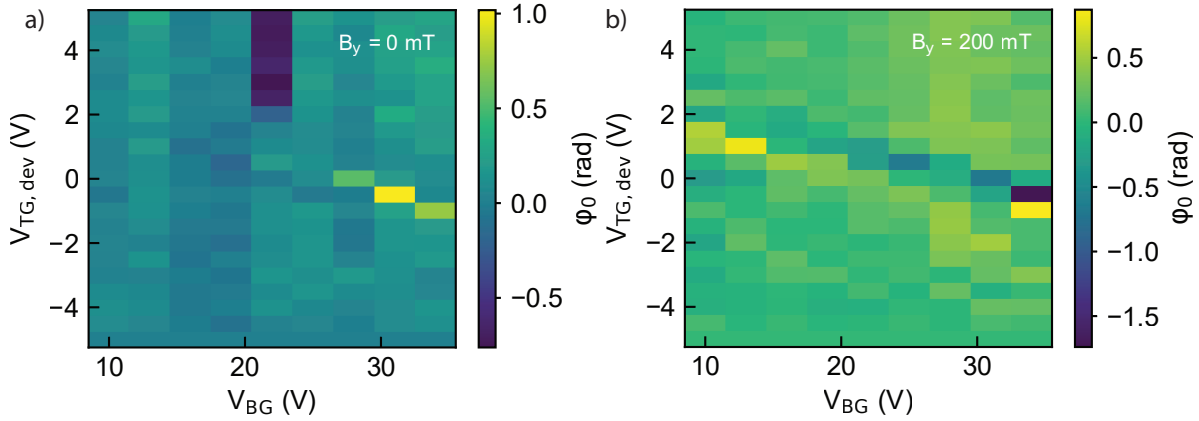

Figure C.10: (a,b) Phase shift φ_0 of device C as a function of $V_{TG,dev}$ and V_{BG} for $B_y = 0$ and $B_y = 200\,\mathrm{mT}$, respectively. In this case, the phase shift relative to the value at $V_{TG,dev} = -5\,\mathrm{V}$ for each V_{BG} is shown.

Following in the footsteps of Reference [199], I_{circ} can be eliminated from equation A4 and φ_{ref} can be expressed for a given current bias I as:

$$\varphi_{ref} = \varphi_{dev} + \frac{2\pi}{\Phi_0}\left(\phi_a + LI_{dev} - LI/2\right). \tag{A5}$$

We then introduce the function:

$$F(I, \varphi_{dev}) = I - I_{c,dev}\widetilde{f}(\tau_{dev}, \varphi_{dev}) - I_{c,ref}\widetilde{f}(\tau_{ref}, \varphi_{dev}). \tag{A6}$$

Using this, the critical current of the SQUID for a given Φ_a and L can be found as the maximal value of I for which there exists some $\varphi_{dev} \in [0, 2\pi[$ where $F(I, \varphi_{dev}) = 0$.

Appendix D

Multiterminal Josehpson junctions

D.1 Raw measurement data

Here, we show the complete set of raw measured voltages V_1, V_2 and V_3, and the corresponding differential resistance maps, as a function of I_U and I_R. The differential resistance maps were partially presented in Figure 7.2.

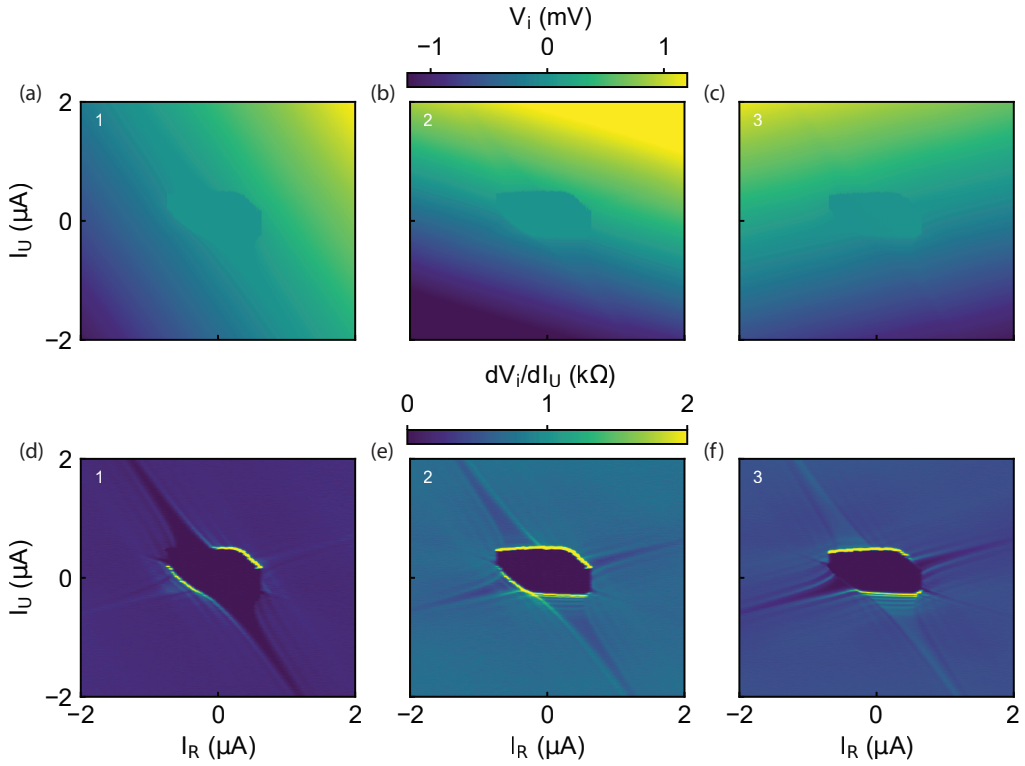

Figure D.1: a-c) Raw measured voltages V_1, V_2 and V_3 as a function of I_U and I_R. e-f) Differential resistances calculated from panels a-c)

D.2 RSJ simulations

As discussed in Section 7.3.1, we start our simulation by solving an RSJ network model. For our three-terminal device, this consists of three blocks of resistively shunted Josephson junctions as shown in Figure D.2.(a). The $i-$th block is described by a resistor with resistance R_i and the phase difference of the Josephson junction φ_i. The normal current flowing in the

resistor is given by $I_{N,i} = V_i/R_i$, where V_i is the voltage drop on the RSJ block. We employ a sinusoidal current-phase relation and the supercurrent flowing in the Josephson junction is given by $I_{s,i} = I_{c,i} \sin \varphi_i$. According to the corresponding Josephson equation, the time derivative of the phase difference is given by $\dot{\varphi}_i = 2eV_i/\hbar$. With these, one can obtain the differential equation of a single RSJ block:

$$I_i = I_{c,i} \sin \varphi_i + \frac{\hbar}{2eR_i} V_i,$$

where I_i is the total current flowing in the $i-$th block. Introducing the external current biases I_U and I_R and the superconducting phases of the corresponding leads φ_U and φ_R according to Figure D.2.(a), choosing the phase of the grounded terminal as zero and applying Kirchhoff's law, one can end up with a set of coupled differential equations for the complete RSJ network:

$$\begin{aligned} \frac{da_1}{dt} &= \frac{2e}{\hbar} \left[I_U - I_{c,2} \sin\left(-\varphi_U\right) - I_{c,3} \sin\left(\varphi_R - \varphi_U\right) \right], \\ \frac{da_2}{dt} &= \frac{2e}{\hbar} \left[I_R - I_{c,1} \sin\left(-\varphi_R\right) + I_{c,3} \sin\left(\varphi_R - \varphi_U\right) \right], \end{aligned} \tag{A1}$$

where

$$\begin{aligned} a_1 &= \frac{\varphi_R - \varphi_U}{R_3} - \frac{\varphi_U}{R_2}, \\ a_2 &= -\frac{\varphi_R - \varphi_U}{R_3} - \frac{\varphi_U}{R_1} \end{aligned}$$

and we made use of the fact that $\varphi_3 = \varphi_R - \varphi_U$. By numerically solving equation system A1, we obtain the stationary φ_i phase differences and V_i voltages from which both the normal $I_{n,i}$ and supercurrents $I_{s,i}$ in each block can be calculated for a given I_U and I_R.

D.2.1 Determination of junction parameters

As mentioned in the main text, to quantitatively match the simulations to our measurement, we determine R_i and $I_{c,i}$ from the measured differential resistance maps. First of all, it is easy to show that the ratio I_U/I_R for which $I_{s,i} = 0$, corresponding to the slope of the SC arms, is determined by the normal resistances as:

$$\begin{aligned} \alpha &= -\frac{R_2 + R_3}{R_2}, \\ \beta &= -\frac{R_1}{R_1 + R_2}, \\ \gamma &= \frac{R_1}{R_2}, \end{aligned} \tag{A2}$$

for junctions 1, 2 and 3 respectively. For these, we obtain $\alpha = -1.6$, $\beta = -0.34$ and $\gamma = 0.31$ from the measured differential resistance maps at $V_{BG} = 10\,\mathrm{V}$. These are shown with dashed lines in Figure D.2.(b). Since these equations are not independent, we also calculate the differential resistances in the normal state where only normal currents are flowing as:

$$\begin{aligned} R_I &= \frac{dV_1}{dI_U} = \frac{R_1 R_2}{R_1 + R_2 + R_3}, \\ R_{II} &= \frac{dV_2}{dI_U} = \frac{R_2(R_1 + R_3)}{R_1 + R_2 + R_3}, \\ R_{III} &= \frac{dV_2}{dI_U} = \frac{R_2 R_3}{R_1 + R_2 + R_3}. \end{aligned} \tag{A3}$$

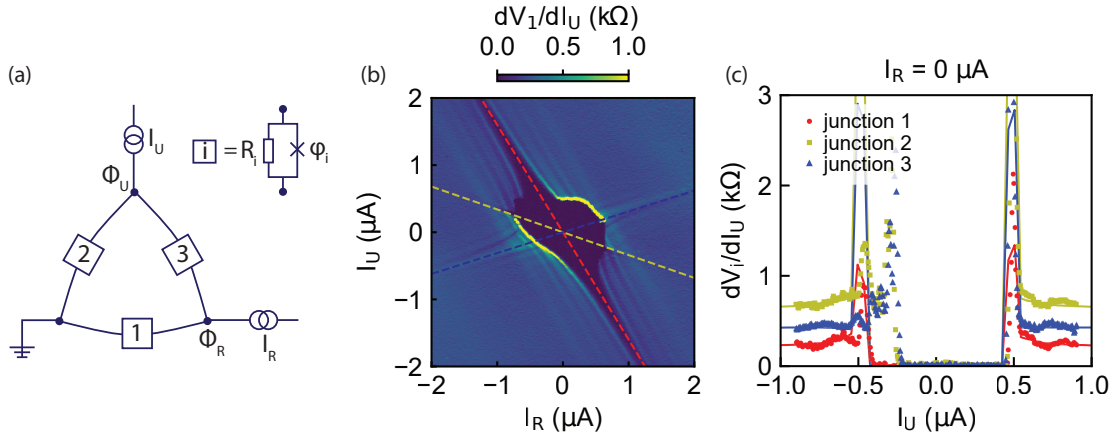

Figure D.2: a) Differential resistance maps dV_1/dI_U. Dashed lines illustrate the obtained slopes of the SC arms. b) Measured differential resistances for $I_R = 0$ (markers). Solid lines show the simulated differential resistances with our improved method, taking self-heating effects into account.

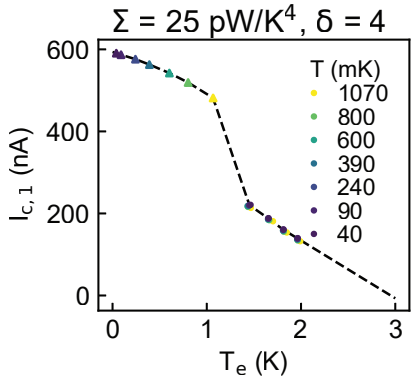

Figure D.3: a) The experimentally obtained $I_{c,1}(T_e)$ function. Triangles show $I_{c,1}$ obtained from the central SC region and circles correspond to the values extracted from the SC arm of junction 1.

Combining equation systems A2 and A3, one can show that $R_2 = R_I(\gamma - \alpha)/\gamma$ and the normal resistances can be calculated. For these, we obtain $R_1 = 420\,\Omega$, $R_2 = 1355\,\Omega$ and $R_3 = 815\,\Omega$, respectively. Having obtained the normal resistances, it is also possible to calculate the junction critical currents $I_{c,i}$. First, we calculate the superconducting coherence length in graphene. Since the length of our junctions is smaller than 200 nm, well below the typical mean free path for similar graphene devices, we assume ballistic conduction. Using $\Delta = 1.2\,\text{meV}$ for the SC gap of the MoRe contacts [95, 207], the coherence length is given by $\xi = \hbar v_F/\pi\Delta \approx 200\,\text{nm}$. Therefore, we conclude that our junctions are in the short, ballistic limit which implies that $I_{c,i}R_i = \Delta \cdot \text{const}$. This allows us to calculate $I_{c,i}$ from the measured differential resistance maps, using the previously calculated normal resistances. Using this, assuming that $I_{c,1} > I_{c,3}$, it can be shown that for $I_R = 0$, the total critical current is given by $I_{c,tot} = I_{c,2} + I_{c,3} = I_{c,2}(1 + R_2/R_3)$ and the individual junction critical currents $I_{c,i}$ can be calculated using the R_i normal resistances. We associate $I_{c,i}$ with the values obtained from the differential resistance maps measured at base temperature. For these, we obtain $I_{c,1} = 545\,\text{nA}$, $I_{c,2} = 170\,\text{nA}$ and $I_{c,3} = 280\,\text{nA}$.

D.2.2 Determination of $I_{c,i}(T_e)$

As discussed in the main text, to include heating effects in our simulations, we perform a fixed-point iteration. The pseudocode for this algorithm is shown in Algorithm 1. First, we solve the RSJ network model with the experimentally obtained parameters and calculate the Joule heating power as $P_J = \sum_i V_i^2/R_i$ and the equilibrium electron temperature as $T_e = \sqrt[4]{T^4 + P_J/\Sigma}$, using $\Sigma = 25\,\mathrm{pW/K^4}$ as obtained from the temperature-dependent measurements (see Figure 7.3. of the main text) and assuming homogeneous temperature distribution in the device. The next step is to take the effect of the elevated electron temperature into account via the $I_c(T_e)$ dependence. We construct this function from our temperature dependent measurements. For this, we have to consider two different regimes. First, in the central SC region, as discussed previously, the individual junction critical currents can be calculated using the normal resistances. Assuming that the ratio of the resistances does not change with temperature, we can obtain $I_{c,1}$ by taking $I_{c,tot}$ as the mean of the SCDs measured at $I_R = 0$ for different T (Figure 7.4.(c) of the main text). Moreover, since in this region all junctions are superconducting, we can take $T_e = T$ as there is no Joule heating.

Next, we consider the SC arm of junction 1. Utilizing the previous definition of the slope α of the SC arm of junction 1, for a given I_R the supercurrent in junction 1 is zero for $I_U = \alpha I_R$. Furthermore, since along the SC arm, only junction 1 is superconducting and the remaining two junctions are in the normal state, we can calculate the ratio of I_U that is flowing towards junction 1. Combining these, the net current of junction 1 is given by $I_1 = (I_U - \alpha I_R)R_2/(R_2 + R_3)$. In this case, we define the average switching current of junction 1 $\overline{I}_{s,1}$ as the value of I_U for which $\overline{V}_1$ exceeds the pre-defined threshold voltage ($20\,\mu\mathrm{V}$), where $\overline{V}_1$ is the average voltage obtained from averaging 10000 individual measurements. From this, we calculate the critical current of junction 1 as $I_{c,1} = (\overline{I}_{s,1} - \alpha I_R)R_2/(R_2 + R_3)$. The obtained values of $I_{c,1}$ for different T_e are shown in Figure D.3. To find the value of $I_{c,1}$ for any T_e, we linearly interpolate and extrapolate. Finally, to get $I_{c,2}$ and $I_{c,3}$, we simply scale the $I_{c,1}(T_e)$ function according to the ratio of normal resistances, based on our previous arguments.

The simulated differential resistances for $I_R = 0$ are shown with solid lines in Figure D.2.(c). As it is visible, the simulated curves qualitatively match the measured points for $I_U > 0$. For negative I_U, the retrapping to the SC state happens later in the measurements than in the simulations. We attribute this also to the elevated temperature due to self-heating, as the simulated curves do not take into account the sweep direction of the current bias.

Algorithm 1 Iterative procedure for the self-consistent calculation of junction currents and electronic temperature

function CALCULATE_MTJJ($n_{\mathrm{iter}} = 10$, δ, Σ, R_i, $I_{c,i}(T_e)$ for $i \in \{1,2,3\}$, T_{bath})
  $T_e \leftarrow T_{\mathrm{bath}}$ for all I_U, I_R ▷ Initialization
  for n_{iter} repetitions **do**
    for all I_U, I_R in the range **do**
      $V_i, I_i \leftarrow$ solve ODE set using $I_{c,i} = I_{c,i}(T_e)$ ▷ Eq. system A1
      $P \leftarrow V_1^2/R_1 + V_2^2/R_2 + V_3^2/R_3$
      $T_e^{\mathrm{new}} \leftarrow$ solve $P = \Sigma \cdot \left(T_e^{\delta} - T_{\mathrm{bath}}^{\delta}\right)$ for T_e ▷ Assumes $P_{e-ph} = P_J$
    end for
  end for
  return $I_i(I_U, I_R), V_i(I_U, I_R), T_e(I_U, I_R)$
end function

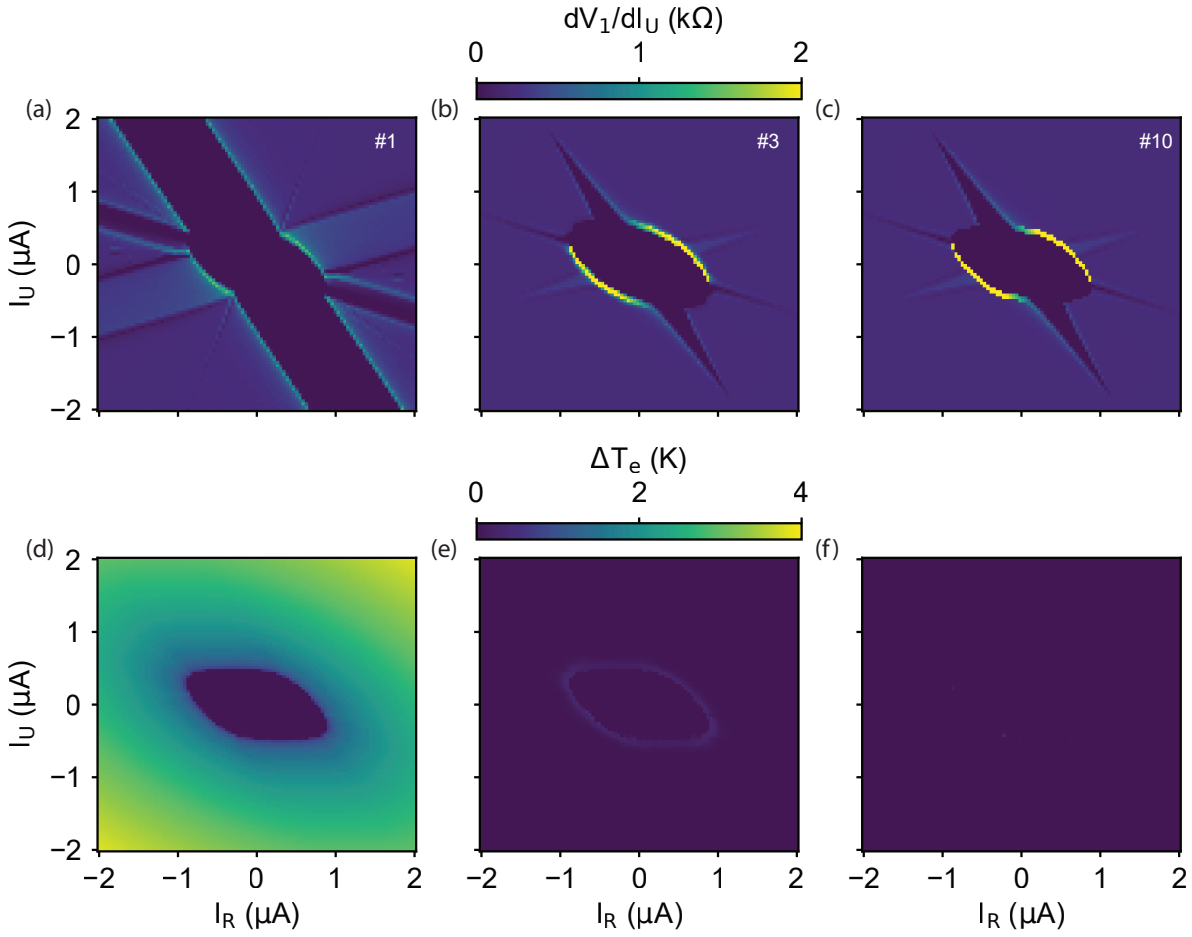

Figure D.4: a-c) Simulated differential resistance maps after 1, 3 and 10 iterations, respectively. d-e) Change of electronic temperature $\Delta T_e = T_n - T_{n-1}$, where n is the iteration step.

D.2.3 Iteration process

To further illustrate the fixed-point iteration method, we show the simulated differential resistance map dV_1/dI_U after different numbers of iteration in Figure D.4. The first step (Figure D.4.(a)) corresponds to the simulation without taking heating into account, also shown in Figure 7.2.(e) and 7.2.(f) of the main text. After three iterations (Figure D.4.(b)), the main features of the measured resistance maps are well reproduced. Figure D.4.(c) shows the final result after 10 rounds of iteration which only shows minor differences compared to Figure D.4.(b). Figure D.4.(d-f) shows the change of electronic temperature $\Delta T_e = T_n - T_{n-1}$, where n is the iteration step and $T_0 = 40\,\mathrm{mK}$ is the base temperature. It can be seen that while the electronic temperature is drastically modified for the first step, later iterations only result in minor changes indicating the convergence of our simulations.

D.3 Additional simulations

As mentioned in the main text, we can also perform the scaling of $I_{c,1}$ along the SC arm of junction 1 using $\delta = 3$ corresponding to the dirty limit of electron-phonon coupling. This scaling yields $\Sigma = 30\,\mathrm{pW/K^3}$. We also construct the $I_c(T_e)$ function using this modified Σ and simulate the differential resistance maps analogous to Figure 7.5. In this case, the expression for Σ is modified, it is given by $\Sigma = \frac{2\zeta(3)D^2|E_F|k_B^3}{\pi^2\rho_M\hbar^4 v_F^3 s^2 l_{mfp}}$. It can be shown that, in this case, Σ is independent of n. The simulated resistance maps for $\delta = 3$ and $\Sigma = 30\,\mathrm{pW/K^3}$ are shown in

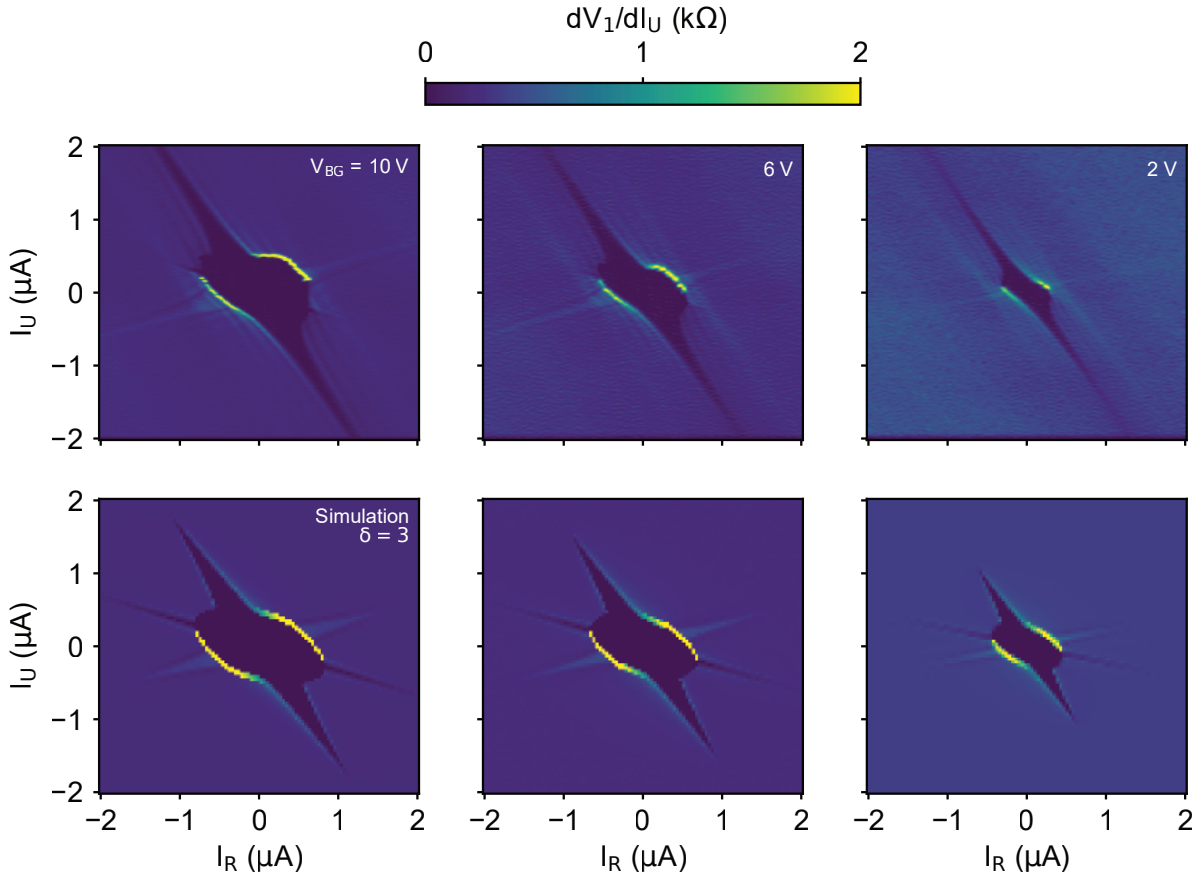

Figure D.5: Backgate dependence of the measured (top) and simulated (bottom) differential resistance maps. Simulations were performed with $\delta = 3$ and constant $\Sigma = 30\,\mathrm{pW/K^3}$.

Figure D.5.

V_{BG} (V)	n ($10^{12}\,\mathrm{cm^{-2}}$)	$\Sigma_{\delta=4}$ ($\mathrm{pW/K^4}$)
10	0.74	25
6	0.48	20
2	0.22	14

Table A1: Charge carrier densities n and Σ in case of $\delta = 4$ corresponding to the values of V_{BG} for which the differential resistance maps were measured and simulated.

As detailed in the main text, for $\delta = 4$, Σ is scaled according to a $\sqrt{n}$-dependence. The Σ values for each V_{BG} can be found in Table A1. We also present the charge carrier densities n for the different V_{BG} values where the differential resistance maps were measured and simulated in Table A1. We determine the backgate voltage of the charge neutrality point $V_{CNP} = -1.4\,\mathrm{V}$ from the gate-dependent measurement shown in Figure 7.1.(c). Using this, the carrier density is given by $n = \alpha_{BG}(V_{BG} - V_{CNP})$. The lever arm of the backgate is calculated according to a planar capacitor model as $\alpha_{BG} = \varepsilon_0/e \cdot (d_{\mathrm{SiO2}}/\varepsilon_{\mathrm{SiO2}} + d_{\mathrm{hBN}}/\varepsilon_{\mathrm{hBN}})^{-1}$, where ε_0 is the vacuum permittivity, e is the elementary charge, $\varepsilon_{\mathrm{SiO2}} = 4$ ($\varepsilon_{\mathrm{hBN}} = 3.3$) and $d_{\mathrm{SiO2}} = 300\,\mathrm{nm}$ ($d_{\mathrm{hBN}} = 35\,\mathrm{nm}$) are the dielectric constant and thickness of SiO_2 (hBN), respectively.

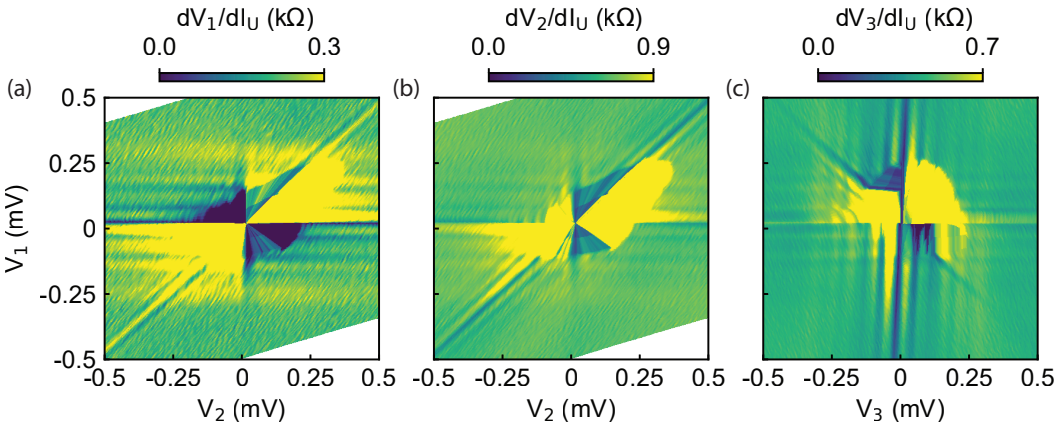

Figure D.6: a) Measured differential resistances dV_i/dI_U as a function of the measured voltages.

D.4 Multiple Andreev reflections

Figure D.6 shows the differential resitances dV_i/dI_U plotted as a function of the measured voltages V_i. We observe resonant features that are attributed to multiple Andreev reflections [203]. Each resistance map is plotted as a function of the two voltages that were measured simultaneously.

D.5 Extended SCD data

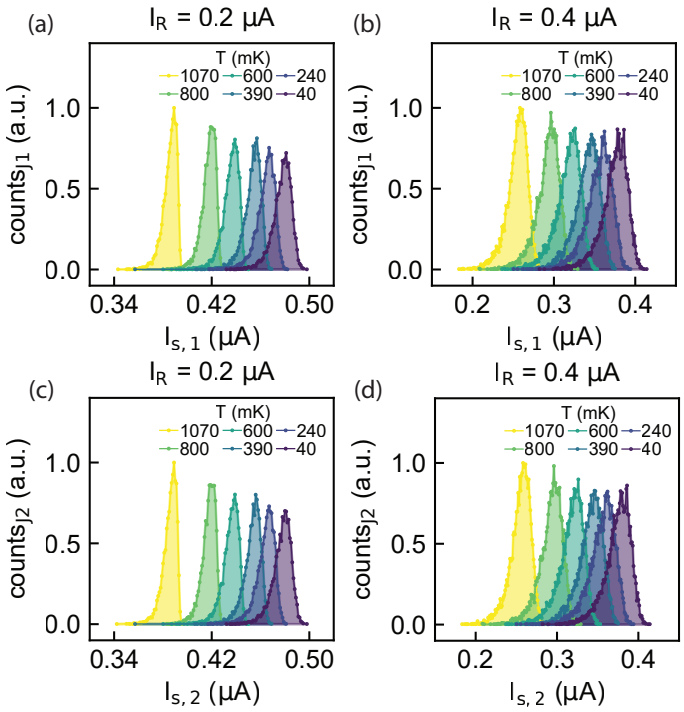

Figure D.7: a-b) Additional SCD data for junction 1 measured at $I_R = 0.2\,\mu$A and $I_R = 0.4\,\mu$A, respectively, for different temperatures. c-d) SCDs for junction 2, simultaneously measured with the SCDs for junction 1.

As mentioned earlier, we performed the SCD measurements simultaneously for two different junctions. Figure D.7.(a) and D.7.(b) shows additional SCDs for junction 1, while Figure D.7.(c)

and D.7.(d) shows the SCDs measured for junction 2. As mentioned in the main text, we observe similar tendencies for all investigated SCDs in the range of $0\,\mu\text{A} < I_R < 0.5\,\mu\text{A}$. The narrowing of the SCDs with temperature can be observed for both junctions in the whole investigated temperature range. Furthermore, the SCDs obtained for junction 1 and 2 are almost identical, further showing that the two junctions switch in a correlated manner.

References

[1] Gordon E. Moore. Cramming more components onto integrated circuits. *Electronics*, 38 (8):114–117, 1965.

[2] M. Mitchell Waldrop. The chips are down for moore's law. *Nature*, 530(7589):144–147, February 2016. ISSN 1476-4687. doi: 10.1038/530144a.

[3] Frank Arute, Kunal Arya, Ryan Babbush, Dave Bacon, Joseph C. Bardin, Rami Barends, Rupak Biswas, Sergio Boixo, Fernando G. S. L. Brandao, David A. Buell, Brian Burkett, Yu Chen, Zijun Chen, Ben Chiaro, Roberto Collins, William Courtney, Andrew Dunsworth, Edward Farhi, Brooks Foxen, Austin Fowler, Craig Gidney, Marissa Giustina, Rob Graff, Keith Guerin, Steve Habegger, Matthew P. Harrigan, Michael J. Hartmann, Alan Ho, Markus Hoffmann, Trent Huang, Travis S. Humble, Sergei V. Isakov, Evan Jeffrey, Zhang Jiang, Dvir Kafri, Kostyantyn Kechedzhi, Julian Kelly, Paul V. Klimov, Sergey Knysh, Alexander Korotkov, Fedor Kostritsa, David Landhuis, Mike Lindmark, Erik Lucero, Dmitry Lyakh, Salvatore Mandrà, Jarrod R. McClean, Matthew McEwen, Anthony Megrant, Xiao Mi, Kristel Michielsen, Masoud Mohseni, Josh Mutus, Ofer Naaman, Matthew Neeley, Charles Neill, Murphy Yuezhen Niu, Eric Ostby, Andre Petukhov, John C. Platt, Chris Quintana, Eleanor G. Rieffel, Pedram Roushan, Nicholas C. Rubin, Daniel Sank, Kevin J. Satzinger, Vadim Smelyanskiy, Kevin J. Sung, Matthew D. Trevithick, Amit Vainsencher, Benjamin Villalonga, Theodore White, Z. Jamie Yao, Ping Yeh, Adam Zalcman, Hartmut Neven, and John M. Martinis. Quantum supremacy using a programmable superconducting processor. *Nature*, 574(7779):505–510, October 2019. ISSN 1476-4687. doi: 10.1038/s41586-019-1666-5.

[4] Dongxin Gao, Daojin Fan, Chen Zha, Jiahao Bei, Guoqing Cai, Jianbin Cai, Sirui Cao, Fusheng Chen, Jiang Chen, Kefu Chen, Xiawei Chen, Xiqing Chen, Zhe Chen, Zhiyuan Chen, Zihua Chen, Wenhao Chu, Hui Deng, Zhibin Deng, Pei Ding, Xun Ding, Zhuzhengqi Ding, Shuai Dong, Yupeng Dong, Bo Fan, Yuanhao Fu, Song Gao, Lei Ge, Ming Gong, Jiacheng Gui, Cheng Guo, Shaojun Guo, Xiaoyang Guo, Lianchen Han, Tan He, Linyin Hong, Yisen Hu, He-Liang Huang, Yong-Heng Huo, Tao Jiang, Zuokai Jiang, Honghong Jin, Yunxiang Leng, Dayu Li, Dongdong Li, Fangyu Li, Jiaqi Li, Jinjin Li, Junyan Li, Junyun Li, Na Li, Shaowei Li, Wei Li, Yuhuai Li, Yuan Li, Futian Liang, Xuelian Liang, Nanxing Liao, Jin Lin, Weiping Lin, Dailin Liu, Hongxiu Liu, Maliang Liu, Xinyu Liu, Xuemeng Liu, Yancheng Liu, Haoxin Lou, Yuwei Ma, Lingxin Meng, Hao Mou, Kailiang Nan, Binghan Nie, Meijuan Nie, Jie Ning, Le Niu, Wenyi Peng, Haoran Qian, Hao Rong, Tao Rong, Huiyan Shen, Qiong Shen, Hong Su, Feifan Su, Chenyin Sun, Liangchao Sun, Tianzuo Sun, Yingxiu Sun, Yimeng Tan, Jun Tan, Longyue Tang, Wenbing Tu, Cai Wan, Jiafei Wang, Biao Wang, Chang Wang, Chen Wang, Chu Wang, Jian Wang, Liangyuan Wang, Rui Wang, Shengtao Wang, Xiaomin Wang, Xinzhe Wang, Xunxun Wang, Yeru Wang, Zuolin Wei, Jiazhou Wei, Dachao Wu, Gang Wu, Jin Wu, Shengjie Wu, Yulin Wu, Shiyong Xie, Lianjie Xin, Yu Xu, Chun Xue, Kai Yan, Weifeng Yang, Xinpeng Yang, Yang Yang, Yangsen Ye, Zhenping Ye, Chong Ying, Jiale Yu, Qinjing Yu, Wenhu Yu, Xiangdong Zeng, Shaoyu Zhan, Feifei Zhang, Haibin Zhang, Kaili Zhang, Pan Zhang, Wen Zhang,

Yiming Zhang, Yongzhuo Zhang, Lixiang Zhang, Guming Zhao, Peng Zhao, Xianhe Zhao, Xintao Zhao, Youwei Zhao, Zhong Zhao, Luyuan Zheng, Fei Zhou, Liang Zhou, Na Zhou, Naibin Zhou, Shifeng Zhou, Shuang Zhou, Zhengxiao Zhou, Chengjun Zhu, Qingling Zhu, Guihong Zou, Haonan Zou, Qiang Zhang, Chao-Yang Lu, Cheng-Zhi Peng, Xiaobo Zhu, and Jian-Wei Pan. Establishing a new benchmark in quantum computational advantage with 105-qubit zuchongzhi 3.0 processor. *Physical Review Letters*, 134(9):090601, March 2025. ISSN 1079-7114. doi: 10.1103/physrevlett.134.090601.

[5] Han-Sen Zhong, Hui Wang, Yu-Hao Deng, Ming-Cheng Chen, Li-Chao Peng, Yi-Han Luo, Jian Qin, Dian Wu, Xing Ding, Yi Hu, Peng Hu, Xiao-Yan Yang, Wei-Jun Zhang, Hao Li, Yuxuan Li, Xiao Jiang, Lin Gan, Guangwen Yang, Lixing You, Zhen Wang, Li Li, Nai-Le Liu, Chao-Yang Lu, and Jian-Wei Pan. Quantum computational advantage using photons. *Science*, 370(6523):1460–1463, December 2020. ISSN 1095-9203. doi: 10.1126/science.abe8770.

[6] A Yu Kitaev. Unpaired majorana fermions in quantum wires. *Physics-Uspekhi*, 44(10S): 131–136, October 2001. ISSN 1468-4780. doi: 10.1070/1063-7869/44/10s/s29.

[7] Liang Fu and C. L. Kane. Superconducting proximity effect and majorana fermions at the surface of a topological insulator. *Physical Review Letters*, 100(9):096407, March 2008. ISSN 1079-7114. doi: 10.1103/physrevlett.100.096407.

[8] Roman M. Lutchyn, Jay D. Sau, and S. Das Sarma. Majorana fermions and a topological phase transition in semiconductor-superconductor heterostructures. *Physical Review Letters*, 105(7):077001, August 2010. ISSN 1079-7114. doi: 10.1103/physrevlett.105.077001.

[9] A.Yu. Kitaev. Fault-tolerant quantum computation by anyons. *Annals of Physics*, 303 (1):2–30, January 2003. ISSN 0003-4916. doi: 10.1016/s0003-4916(02)00018-0.

[10] C. L. Kane and E. J. Mele. Quantum spin hall effect in graphene. *Physical Review Letters*, 95(22):226801, nov 2005. doi: 10.1103/physrevlett.95.226801.

[11] M. Gmitra, S. Konschuh, C. Ertler, C. Ambrosch-Draxl, and J. Fabian. Band-structure topologies of graphene: Spin-orbit coupling effects from first principles. *Physical Review B*, 80(23), dec 2009. doi: 10.1103/physrevb.80.235431.

[12] Zhe Wang, Dong–Keun Ki, Hua Chen, Helmuth Berger, Allan H. MacDonald, and Alberto F. Morpurgo. Strong interface-induced spin–orbit interaction in graphene on WS2. *Nature Communications*, 6(1):8339, sep 2015. ISSN 2041-1723. doi: 10.1038/ncomms9339. URL `https://doi.org/10.1038/ncomms9339`.

[13] J. Ingla-Aynés, M. H. D. Guimarães, R. J. Meijerink, P. J. Zomer, and B. J. van Wees. $24-\mu$m spin relaxation length in boron nitride encapsulated bilayer graphene. *Phys. Rev. B*, 92:201410, Nov 2015. doi: 10.1103/PhysRevB.92.201410. URL `https://link.aps.org/doi/10.1103/PhysRevB.92.201410`.

[14] Marc Drögeler, Christopher Franzen, Frank Volmer, Tobias Pohlmann, Luca Banszerus, Maik Wolter, Kenji Watanabe, Takashi Taniguchi, Christoph Stampfer, and Bernd Beschoten. Spin lifetimes exceeding 12 ns in graphene nonlocal spin valve devices. *Nano Letters*, 16(6):3533–3539, may 2016. doi: 10.1021/acs.nanolett.6b00497.

[15] Simranjeet Singh, Jyoti Katoch, Jinsong Xu, Cheng Tan, Tiancong Zhu, Walid Amamou, James Hone, and Roland Kawakami. Nanosecond spin relaxation times in single layer graphene spin valves with hexagonal boron nitride tunnel barriers. *Applied Physics Letters*, 109(12):122411, sep 2016. doi: 10.1063/1.4962635.

[16] Bowen Yang, Min-Feng Tu, Jeongwoo Kim, Yong Wu, Hui Wang, Jason Alicea, Ruqian Wu, Marc Bockrath, and Jing Shi. Tunable spin–orbit coupling and symmetry-protected edge states in graphene/ws_2. *2D Materials*, 3(3):031012, sep 2016. doi: 10.1088/2053-1583/3/3/031012.

[17] André Dankert and Saroj P. Dash. Electrical gate control of spin current in van der waals heterostructures at room temperature. *Nature Communications*, 8(1):16093, jul 2017. ISSN 2041-1723. doi: 10.1038/ncomms16093. URL `https://doi.org/10.1038/ncomms16093`.

[18] S. Omar and B. J. van Wees. Spin transport in high-mobility graphene on ws_2 substrate with electric-field tunable proximity spin-orbit interaction. *Phys. Rev. B*, 97:045414, Jan 2018. doi: 10.1103/PhysRevB.97.045414. URL `https://link.aps.org/doi/10.1103/PhysRevB.97.045414`.

[19] Wei Han, Roland K. Kawakami, Martin Gmitra, and Jaroslav Fabian. Graphene spintronics. *Nature Nanotechnology*, 9(10):794–807, October 2014. ISSN 1748-3395. doi: 10.1038/nnano.2014.214.

[20] Martin Gmitra, Denis Kochan, Petra Högl, and Jaroslav Fabian. Trivial and inverted dirac bands and the emergence of quantum spin hall states in graphene on transition-metal dichalcogenides. *Physical Review B*, 93(15):155104, April 2016. ISSN 2469-9969. doi: 10.1103/physrevb.93.155104.

[21] Michael P. Zaletel and Jun Yong Khoo. The gate-tunable strong and fragile topology of multilayer-graphene on a transition metal dichalcogenide. *arXiv (Condensed Matter, Mesoscale and Nanoscale Physics)*, January 2019. doi: 10.48550/ARXIV.1901.01294. January 9, 2019, `https://arxiv.org/abs/1901.01294` (accessed 2023-09-01).

[22] Fernando Peñaranda, Ramón Aguado, Elsa Prada, and Pablo San-Jose. Majorana bound states in encapsulated bilayer graphene. *SciPost Phys.*, 14:075, 2023. doi: 10.21468/SciPostPhys.14.4.075. URL `https://scipost.org/10.21468/SciPostPhys.14.4.075`.

[23] J O Island, X Cui, C Lewandowski, J Y Khoo, E M Spanton, H Zhou, D Rhodes, J C Hone, T Taniguchi, K Watanabe, L S Levitov, M P Zaletel, and A F Young. Spinorbit-driven band inversion in bilayer graphene by the van der waals proximity effect. *Nature*, 571:85–89, 6 2019. doi: 10.1038/s41586-019-1304-2.

[24] Prasanna Rout, Nikos Papadopoulos, Fernando Peñaranda, Kenji Watanabe, Takashi Taniguchi, Elsa Prada, Pablo San-Jose, and Srijit Goswami. Supercurrent mediated by helical edge modes in bilayer graphene. *Nature Communications*, 15(1), January 2024. ISSN 2041-1723. doi: 10.1038/s41467-024-44952-6.

[25] Jiang-Xiazi Lin, Ya-Hui Zhang, Erin Morissette, Zhi Wang, Song Liu, Daniel Rhodes, K Watanabe, T Taniguchi, James Hone, and J I A Li. Spin-orbitdriven ferromagnetism at half moiré filling in magic-angle twisted bilayer graphene. *Science*, 375(6579):437–441, 1 2022. ISSN 1095-9203. doi: 10.1126/science.abh2889.

[26] Saisab Bhowmik, Bhaskar Ghawri, Youngju Park, Dongkyu Lee, Suvronil Datta, Radhika Soni, K. Watanabe, T. Taniguchi, Arindam Ghosh, Jeil Jung, and U. Chandni. Spin-orbit coupling-enhanced valley ordering of malleable bands in twisted bilayer graphene on wse2. *Nature Communications*, 14(1), July 2023. ISSN 2041-1723. doi: 10.1038/s41467-023-39855-x.

[27] Yang-Zhi Chou, Yuting Tan, Fengcheng Wu, and Sankar Das Sarma. Topological flat bands, valley polarization, and interband superconductivity in magic-angle twisted bilayer graphene with proximitized spin-orbit couplings. *Physical Review B*, 110(4):l041108, July 2024. ISSN 2469-9969. doi: 10.1103/physrevb.110.l041108.

[28] Simon Zihlmann, Aron W. Cummings, Jose H. Garcia, Máté Kedves, Kenji Watanabe, Takashi Taniguchi, Christian Schönenberger, and Péter Makk. Large spin relaxation anisotropy and valley-zeeman spin-orbit coupling in wse_2/graphene/h-bn heterostructures. *Phys. Rev. B*, 97:075434, Feb 2018. doi: 10.1103/PhysRevB.97.075434. URL `https://link.aps.org/doi/10.1103/PhysRevB.97.075434`.

[29] Bálint Fülöp, Albin Márffy, Endre Tóvári, Máté Kedves, Simon Zihlmann, David Indolese, Zoltán Kovács-Krausz, Kenji Watanabe, Takashi Taniguchi, Christian Schönenberger, István Kézsmárki, Péter Makk, and Szabolcs Csonka. New method of transport measurements on van der waals heterostructures under pressure. *Journal of Applied Physics*, 130: 64303, 8 2021. doi: 10.1063/5.0058583.

[30] Bálint Fülöp, Albin Márffy, Simon Zihlmann, Martin Gmitra, Endre Tóvári, Bálint Szentpéteri, Máté Kedves, Kenji Watanabe, Takashi Taniguchi, Jaroslav Fabian, Christian Schönenberger, Péter Makk, and Szabolcs Csonka. Boosting proximity spin-orbit coupling in graphene/wse2 heterostructures via hydrostatic pressure. *npj 2D Materials and Applications*, 5(1):82, 9 2021. ISSN 2397-7132. doi: 10.1038/s41699-021-00262-9. URL `https://doi.org/10.1038/s41699-021-00262-9`.

[31] Máté Kedves, Bálint Szentpéteri, Albin Márffy, Endre Tóvári, Nikos Papadopoulos, Prasanna K. Rout, Kenji Watanabe, Takashi Taniguchi, Srijit Goswami, Szabolcs Csonka, and Péter Makk. Stabilizing the inverted phase of a wse2/blg/wse2 heterostructure via hydrostatic pressure. *Nano Letters*, 23(20):9508–9514, October 2023. ISSN 1530-6992. doi: 10.1021/acs.nanolett.3c03029.

[32] Roman-Pascal Riwar, Manuel Houzet, Julia S. Meyer, and Yuli V. Nazarov. Multi-terminal Josephson junctions as topological matter. *Nature Communications*, 7(1), apr 2016. doi: 10.1038/ncomms11167.

[33] Máté Kedves, Tamás Pápai, Gergő Fülöp, Kenji Watanabe, Takashi Taniguchi, Péter Makk, and Szabolcs Csonka. Self-heating effects and switching dynamics in graphene multiterminal josephson junctions. *Physical Review Research*, 6(3):033143, August 2024. ISSN 2643-1564. doi: 10.1103/physrevresearch.6.033143.

[34] K. S. Novoselov, A. K. Geim, S. V. Morozov, D. Jiang, Y. Zhang, S. V. Dubonos, I. V. Grigorieva, and A. A. Firsov. Electric field effect in atomically thin carbon films. *Science*, 306(5696):666–669, October 2004. ISSN 1095-9203. doi: 10.1126/science.1102896.

[35] K. S. Novoselov, A. K. Geim, S. V. Morozov, D. Jiang, M. I. Katsnelson, I. V. Grigorieva, S. V. Dubonos, and A. A. Firsov. Two-dimensional gas of massless dirac fermions in graphene. *Nature*, 438(7065):197–200, November 2005. ISSN 1476-4687. doi: 10.1038/nature04233.

[36] K. S. Novoselov, D. Jiang, F. Schedin, T. J. Booth, V. V. Khotkevich, S. V. Morozov, and A. K. Geim. Two-dimensional atomic crystals. *Proceedings of the National Academy of Sciences*, 102(30):10451–10453, July 2005. ISSN 1091-6490. doi: 10.1073/pnas.0502848102.

[37] K. S. Novoselov, A. Mishchenko, A. Carvalho, and A. H. Castro Neto. 2d materials and van der waals heterostructures. *Science*, 353(6298), July 2016. ISSN 1095-9203. doi: 10.1126/science.aac9439.

[38] M. Gibertini, M. Koperski, A. F. Morpurgo, and K. S. Novoselov. Magnetic 2d materials and heterostructures. *Nature Nanotechnology*, 14(5):408–419, May 2019. ISSN 1748-3395. doi: 10.1038/s41565-019-0438-6.

[39] A. K. Geim and K. S. Novoselov. The rise of graphene. *Nature Materials*, 6(3):183–191, March 2007. ISSN 1476-4660. doi: 10.1038/nmat1849.

[40] K. S. Novoselov, Z. Jiang, Y. Zhang, S. V. Morozov, H. L. Stormer, U. Zeitler, J. C. Maan, G. S. Boebinger, P. Kim, and A. K. Geim. Room-temperature quantum hall effect in graphene. *Science*, 315(5817):1379–1379, March 2007. ISSN 1095-9203. doi: 10.1126/science.1137201.

[41] Himadri Chakraborti, Cosimo Gorini, Angelika Knothe, Ming-Hao Liu, Péter Makk, François D Parmentier, David Perconte, Klaus Richter, Preden Roulleau, Benjamin Sacépé, Christian Schönenberger, and Wenmin Yang. Electron wave and quantum optics in graphene. *Journal of Physics: Condensed Matter*, 36(39):393001, July 2024. ISSN 1361-648X. doi: 10.1088/1361-648x/ad46bc.

[42] C. R. Dean, A. F. Young, I. Meric, C. Lee, L. Wang, S. Sorgenfrei, K. Watanabe, T. Taniguchi, P. Kim, K. L. Shepard, and J. Hone. Boron nitride substrates for high-quality graphene electronics. *Nature Nanotechnology*, 5(10):722–726, August 2010. ISSN 1748-3395. doi: 10.1038/nnano.2010.172.

[43] Wendong Wang, Nicholas Clark, Matthew Hamer, Amy Carl, Endre Tovari, Sam Sullivan-Allsop, Evan Tillotson, Yunze Gao, Hugo de Latour, Francisco Selles, James Howarth, Eli G. Castanon, Mingwei Zhou, Haoyu Bai, Xiao Li, Astrid Weston, Kenji Watanabe, Takashi Taniguchi, Cecilia Mattevi, Thomas H. Bointon, Paul V. Wiper, Andrew J. Strudwick, Leonid A. Ponomarenko, Andrey V. Kretinin, Sarah J. Haigh, Alex Summerfield, and Roman Gorbachev. Clean assembly of van der waals heterostructures using silicon nitride membranes. *Nature Electronics*, 6(12):981–990, December 2023. ISSN 2520-1131. doi: 10.1038/s41928-023-01075-y.

[44] Loïc Huder, Alexandre Artaud, Toai Le Quang, Guy Trambly de Laissardière, Aloysius G.M. Jansen, Gérard Lapertot, Claude Chapelier, and Vincent T. Renard. Electronic spectrum of twisted graphene layers under heterostrain. *Physical Review Letters*, 120(15): 156405, April 2018. ISSN 1079-7114. doi: 10.1103/physrevlett.120.156405.

[45] Lujun Wang, Simon Zihlmann, Andreas Baumgartner, Jan Overbeck, Kenji Watanabe, Takashi Taniguchi, Péter Makk, and Christian Schönenberger. In situ strain tuning in hbn-encapsulated graphene electronic devices. *Nano Letters*, 19(6):4097–4102, May 2019. ISSN 1530-6992. doi: 10.1021/acs.nanolett.9b01491.

[46] Zhen Bi, Noah F. Q. Yuan, and Liang Fu. Designing flat bands by strain. *Physical Review B*, 100(3):035448, July 2019. ISSN 2469-9969. doi: 10.1103/physrevb.100.035448.

[47] Lujun Wang, Péter Makk, Simon Zihlmann, Andreas Baumgartner, David I. Indolese, Kenji Watanabe, Takashi Taniguchi, and Christian Schönenberger. Mobility enhancement in graphene by in situ reduction of random strain fluctuations. *Physical Review Letters*, 124(15):157701, April 2020. ISSN 1079-7114. doi: 10.1103/physrevlett.124.157701.

[48] Lujun Wang, Andreas Baumgartner, Péter Makk, Simon Zihlmann, Blesson Sam Varghese, David I. Indolese, Kenji Watanabe, Takashi Taniguchi, and Christian Schönenberger. Global strain-induced scalar potential in graphene devices. *Communications Physics*, 4 (1), June 2021. ISSN 2399-3650. doi: 10.1038/s42005-021-00651-y.

[49] Marwa Mannaï and Sonia Haddad. Twistronics versus straintronics in twisted bilayers of graphene and transition metal dichalcogenides. *Physical Review B*, 103(20):l201112, May 2021. ISSN 2469-9969. doi: 10.1103/physrevb.103.l201112.

[50] Daniel E. Parker, Tomohiro Soejima, Johannes Hauschild, Michael P. Zaletel, and Nick Bultinck. Strain-induced quantum phase transitions in magic-angle graphene. *Physical Review Letters*, 127(2):027601, July 2021. ISSN 1079-7114. doi: 10.1103/physrevlett.127.027601.

[51] Rafi Bistritzer and Allan H. MacDonald. Moiré bands in twisted double-layer graphene. *Proceedings of the National Academy of Sciences*, 108(30):12233–12237, July 2011. ISSN 1091-6490. doi: 10.1073/pnas.1108174108.

[52] Yuan Cao, Valla Fatemi, Shiang Fang, Kenji Watanabe, Takashi Taniguchi, Efthimios Kaxiras, and Pablo Jarillo-Herrero. Unconventional superconductivity in magic-angle graphene superlattices. *Nature*, 556(7699):43–50, March 2018. ISSN 1476-4687. doi: 10.1038/nature26160.

[53] Yuan Cao, Valla Fatemi, Ahmet Demir, Shiang Fang, Spencer L. Tomarken, Jason Y. Luo, Javier D. Sanchez-Yamagishi, Kenji Watanabe, Takashi Taniguchi, Efthimios Kaxiras, Ray C. Ashoori, and Pablo Jarillo-Herrero. Correlated insulator behaviour at half-filling in magic-angle graphene superlattices. *Nature*, 556(7699):80–84, March 2018. ISSN 1476-4687. doi: 10.1038/nature26154.

[54] Leon Balents, Cory R. Dean, Dmitri K. Efetov, and Andrea F. Young. Superconductivity and strong correlations in moiré flat bands. *Nature Physics*, 16(7):725–733, May 2020. ISSN 1745-2481. doi: 10.1038/s41567-020-0906-9.

[55] Mengya Liu, Liping Wang, and Gui Yu. Developing graphene-based moiré heterostructures for twistronics. *Advanced Science*, 9(1), November 2021. ISSN 2198-3844. doi: 10.1002/advs.202103170.

[56] Eva Y. Andrei, Dmitri K. Efetov, Pablo Jarillo-Herrero, Allan H. MacDonald, Kin Fai Mak, T. Senthil, Emanuel Tutuc, Ali Yazdani, and Andrea F. Young. The marvels of moiré materials. *Nature Reviews Materials*, 6(3):201–206, March 2021. ISSN 2058-8437. doi: 10.1038/s41578-021-00284-1.

[57] Dante M. Kennes, Martin Claassen, Lede Xian, Antoine Georges, Andrew J. Millis, James Hone, Cory R. Dean, D. N. Basov, Abhay N. Pasupathy, and Angel Rubio. Moiré heterostructures as a condensed-matter quantum simulator. *Nature Physics*, 17(2):155–163, February 2021. ISSN 1745-2481. doi: 10.1038/s41567-020-01154-3.

[58] Jianpeng Liu and Xi Dai. Orbital magnetic states in moiré graphene systems. *Nature Reviews Physics*, 3(5):367–382, April 2021. ISSN 2522-5820. doi: 10.1038/s42254-021-00297-3.

[59] P. R. Wallace. The band theory of graphite. *Physical Review*, 71(9):622–634, May 1947. ISSN 0031-899X. doi: 10.1103/physrev.71.622.

[60] A. H. Castro Neto, F. Guinea, N. M. R. Peres, K. S. Novoselov, and A. K. Geim. The electronic properties of graphene. *Reviews of Modern Physics*, 81(1):109–162, January 2009. ISSN 1539-0756. doi: 10.1103/revmodphys.81.109.

[61] Jeil Jung and Allan H. MacDonald. Accurate tight-binding models for the π bands of bilayer graphene. *Phys. Rev. B*, 89:035405, Jan 2014. doi: 10.1103/PhysRevB.89.035405. URL `https://link.aps.org/doi/10.1103/PhysRevB.89.035405`.

[62] Edward McCann and Vladimir I. Fal'ko. Landau-level degeneracy and quantum hall effect in a graphite bilayer. *Phys. Rev. Lett.*, 96:086805, Mar 2006. doi: 10.1103/PhysRevLett.96.086805. URL https://link.aps.org/doi/10.1103/PhysRevLett.96.086805.

[63] Eduardo V. Castro, K. S. Novoselov, S. V. Morozov, N. M. R. Peres, J. M. B. Lopes dos Santos, Johan Nilsson, F. Guinea, A. K. Geim, and A. H. Castro Neto. Biased bilayer graphene: Semiconductor with a gap tunable by the electric field effect. *Phys. Rev. Lett.*, 99:216802, Nov 2007. doi: 10.1103/PhysRevLett.99.216802. URL https://link.aps.org/doi/10.1103/PhysRevLett.99.216802.

[64] Yuanbo Zhang, Tsung-Ta Tang, Caglar Girit, Zhao Hao, Michael C. Martin, Alex Zettl, Michael F. Crommie, Y. Ron Shen, and Feng Wang. Direct observation of a widely tunable bandgap in bilayer graphene. *Nature*, 459(7248):820–823, June 2009. ISSN 1476-4687. doi: 10.1038/nature08105.

[65] Denis Kochan, Susanne Irmer, and Jaroslav Fabian. Model spin-orbit coupling hamiltonians for graphene systems. *Physical Review B*, 95(16):165415, apr 2017. ISSN 2469-9969. doi: 10.1103/physrevb.95.165415.

[66] Sergej Konschuh, Martin Gmitra, Denis Kochan, and Jaroslav Fabian. Theory of spin-orbit coupling in bilayer graphene. *Phys. Rev. B 85, 115423 (2012)*, 85:115423, 11 2012. doi: 10.1103/PhysRevB.85.115423. URL https://link.aps.org/doi/10.1103/PhysRevB.85.115423.

[67] Martin Gmitra and Jaroslav Fabian. Graphene on transition-metal dichalcogenides: A platform for proximity spin-orbit physics and optospintronics. *Phys. Rev. B*, 92:155403, Oct 2015. doi: 10.1103/PhysRevB.92.155403. URL https://link.aps.org/doi/10.1103/PhysRevB.92.155403.

[68] Jose H. Garcia, Marc Vila, Aron W. Cummings, and Stephan Roche. Spin transport in graphene/transition metal dichalcogenide heterostructures. *Chemical Society Reviews*, 47 (9):3359–3379, 2018. doi: 10.1039/c7cs00864c.

[69] A. Avsar, J. Y. Tan, T. Taychatanapat, J. Balakrishnan, G.K.W. Koon, Y. Yeo, J. Lahiri, A. Carvalho, A. S. Rodin, E.C.T. O'Farrell, G. Eda, A. H. Castro Neto, and B. Özyilmaz. Spin–orbit proximity effect in graphene. *Nature Communications*, 5(1): 4875, sep 2014. ISSN 2041-1723. doi: 10.1038/ncomms5875. URL https://doi.org/10.1038/ncomms5875.

[70] Conan Weeks, Jun Hu, Jason Alicea, Marcel Franz, and Ruqian Wu. Engineering a robust quantum spin hall state in graphene via adatom deposition. *Physical Review X*, 1 (2):021001, October 2011. ISSN 2160-3308. doi: 10.1103/physrevx.1.021001.

[71] Zhe Wang, Dong-Keun Ki, Jun Yong Khoo, Diego Mauro, Helmuth Berger, Leonid S. Levitov, and Alberto F. Morpurgo. Origin and magnitude of 'designer' spin-orbit interaction in graphene on semiconducting transition metal dichalcogenides. *Physical Review X*, 6(4):041020, October 2016. ISSN 2160-3308. doi: 10.1103/physrevx.6.041020.

[72] Yang Li and Mikito Koshino. Twist-angle dependence of the proximity spin-orbit coupling in graphene on transition-metal dichalcogenides. *Phys. Rev. B*, 99:075438, Feb 2019. doi: 10.1103/PhysRevB.99.075438. URL https://link.aps.org/doi/10.1103/PhysRevB.99.075438.

[73] Alessandro David, Péter Rakyta, Andor Kormányos, and Guido Burkard. Induced spin-orbit coupling in twisted graphene–transition metal dichalcogenide heterobilayers: Twistronics meets spintronics. *Phys. Rev. B*, 100:085412, Aug 2019. doi:

10.1103/PhysRevB.100.085412. URL https://link.aps.org/doi/10.1103/PhysRevB.100.085412.

[74] Klaus Zollner and Jaroslav Fabian. Bilayer graphene encapsulated within monolayers of ws_2 or $cr_2ge_2te_6$: Tunable proximity spin-orbit or exchange coupling. *Phys. Rev. B*, 104: 075126, Aug 2021. doi: 10.1103/PhysRevB.104.075126. URL https://link.aps.org/doi/10.1103/PhysRevB.104.075126.

[75] Martin Gmitra and Jaroslav Fabian. Proximity effects in bilayer graphene on monolayer wse2 : Field-effect spin valley locking, spin-orbit valve, and spin transistor. *Physical Review Letters*, 119(14):146401, October 2017. ISSN 1079-7114. doi: 10.1103/physrevlett.119.146401.

[76] Csaba G. Péterfalvi, Alessandro David, Péter Rakyta, Guido Burkard, and Andor Kormányos. Quantum interference tuning of spin-orbit coupling in twisted van der waals trilayers. *Phys. Rev. Res.*, 4:L022049, May 2022. doi: 10.1103/PhysRevResearch.4.L022049. URL https://link.aps.org/doi/10.1103/PhysRevResearch.4.L022049.

[77] Marius Eich, Riccardo Pisoni, Hiske Overweg, Annika Kurzmann, Yongjin Lee, Peter Rickhaus, Thomas Ihn, Klaus Ensslin, František Herman, Manfred Sigrist, Kenji Watanabe, and Takashi Taniguchi. Spin and valley states in gate-defined bilayer graphene quantum dots. *Physical Review X*, 8(3), jul 2018. doi: 10.1103/physrevx.8.031023.

[78] Luca Banszerus, Benedikt Frohn, Alexander Epping, Daniel Neumaier, Kenji Watanabe, Takashi Taniguchi, and Christoph Stampfer. Gate-defined electron-hole double dots in bilayer graphene. *arXiv:1803.10857*, March 2018.

[79] Simon Zihlmann. *Spin and charge relaxation in graphene*. PhD thesis, University of Basel, 2018.

[80] G. Bergmann. Weak anti-localization—an experimental proof for the destructive interference of rotated spin. *Solid State Communications*, 42(11):815–817, jun 1982. doi: 10.1016/0038-1098(82)90013-8.

[81] D. Huertas-Hernando, F. Guinea, and Arne Brataas. Spin-orbit-mediated spin relaxation in graphene. *Physical Review Letters*, 103(14):146801, September 2009. ISSN 1079-7114. doi: 10.1103/physrevlett.103.146801.

[82] H. Ochoa, A. H. Castro Neto, and F. Guinea. Elliot-yafet mechanism in graphene. *Physical Review Letters*, 108(20):206808, May 2012. ISSN 1079-7114. doi: 10.1103/physrevlett.108.206808.

[83] Michel Dyakonov and V.I. Perel. Spin relaxation of conduction electrons in noncentrosymmetric semiconductors. *Solid State Physics*, 13:3023, 01 1972.

[84] Aron W. Cummings, Jose H. Garcia, Jaroslav Fabian, and Stephan Roche. Giant spin lifetime anisotropy in graphene induced by proximity effects. *Physical Review Letters*, 119 (20):206601, November 2017. ISSN 1079-7114. doi: 10.1103/physrevlett.119.206601.

[85] Endre Tóvári. *Conducting Channels and Localization in Graphene in a Magnetic Field*. PhD thesis, Budapest University of Technology and Economics, 2017.

[86] Y. Zhang, Z. Jiang, J. P. Small, M. S. Purewal, Y.-W. Tan, M. Fazlollahi, J. D. Chudow, J. A. Jaszczak, H. L. Stormer, and P. Kim. Landau-level splitting in graphene in high magnetic fields. *Physical Review Letters*, 96(13):136806, April 2006. ISSN 1079-7114. doi: 10.1103/physrevlett.96.136806.

[87] Z. Jiang, Y. Zhang, H. L. Stormer, and P. Kim. Quantum hall states near the charge-neutral dirac point in graphene. *Physical Review Letters*, 99(10):106802, September 2007. ISSN 1079-7114. doi: 10.1103/physrevlett.99.106802.

[88] Edward McCann. Asymmetry gap in the electronic band structure of bilayer graphene. *Phys. Rev. B*, 74:161403, Oct 2006. doi: 10.1103/PhysRevB.74.161403. URL `https://link.aps.org/doi/10.1103/PhysRevB.74.161403`.

[89] Edward McCann and Mikito Koshino. The electronic properties of bilayer graphene. *Reports on Progress in Physics*, 76(5):056503, April 2013. ISSN 1361-6633. doi: 10.1088/0034-4885/76/5/056503.

[90] Heike Kammerlingh Onnes. *Leiden comm.*, 120b, 1911.

[91] W. Meissner and R. Ochsenfeld. Ein neuer effekt bei eintritt der supraleitfähigkeit. *Die Naturwissenschaften*, 21(44):787–788, nov 1933. doi: 10.1007/bf01504252.

[92] Michael Tinkham. *Introduction To Superconductivity*. McGraw-Hill College, 1995. ISBN 0-07-064878-6.

[93] Brian D. Josephson. Possible new effects in superconductive tunnelling. *Physics Letters*, 1(7):251–253, jul 1962. doi: 10.1016/0031-9163(62)91369-0.

[94] M. J. Zhu, A. V. Kretinin, M. D. Thompson, D. A. Bandurin, S. Hu, G. L. Yu, J. Birkbeck, A. Mishchenko, I. J. Vera-Marun, K. Watanabe, T. Taniguchi, M. Polini, J. R. Prance, K. S. Novoselov, A. K. Geim, and M. Ben Shalom. Edge currents shunt the insulating bulk in gapped graphene. *Nature Communications*, 8:14552, feb 2017. doi: 10.1038/ncomms14552.

[95] D. I. Indolese, R. Delagrange, P. Makk, J. R. Wallbank, K. Wanatabe, T. Taniguchi, and C. Schönenberger. Signatures of van hove singularities probed by the supercurrent in a graphene-hbn superlattice. *Phys. Rev. Lett.*, 121:137701, Sep 2018. doi: 10.1103/PhysRevLett.121.137701. URL `https://link.aps.org/doi/10.1103/PhysRevLett.121.137701`.

[96] Rainer Kraft, Jens Mohrmann, Renjun Du, Pranauv Balaji Selvasundaram, Muhammad Irfan, Umut Nefta Kanilmaz, Fan Wu, Detlef Beckmann, Hilbert von Löhneysen, Ralph Krupke, Anton Akhmerov, Igor Gornyi, and Romain Danneau. Tailoring supercurrent confinement in graphene bilayer weak links. *Nature Communications*, 9(1), apr 2018. doi: 10.1038/s41467-018-04153-4.

[97] Rudolf Gross and Achim Marx. Applied superconductivity lecture notes. Walther Meissner Institute, 2025.

[98] Juhani Kurkijärvi. Intrinsic fluctuations in a superconducting ring closed with a josephson junction. *Physical Review B*, 6(3):832–835, August 1972. ISSN 0556-2805. doi: 10.1103/physrevb.6.832.

[99] T. A. Fulton and L. N. Dunkleberger. Lifetime of the zero-voltage state in josephson tunnel junctions. *Physical Review B*, 9(11):4760–4768, June 1974. ISSN 0556-2805. doi: 10.1103/physrevb.9.4760.

[100] A.O Caldeira and A.J Leggett. Quantum tunnelling in a dissipative system. *Annals of Physics*, 149(2):374–456, September 1983. ISSN 0003-4916. doi: 10.1016/0003-4916(83)90202-6.

[101] John Clarke, Andrew N. Cleland, Michel H. Devoret, Daniel Esteve, and John M. Martinis. Quantum mechanics of a macroscopic variable: The phase difference of a josephson junction. *Science*, 239(4843):992–997, February 1988. ISSN 1095-9203. doi: 10.1126/science.239.4843.992.

[102] Gil-Ho Lee, Dongchan Jeong, Jae-Hyun Choi, Yong-Joo Doh, and Hu-Jong Lee. Electrically tunable macroscopic quantum tunneling in a graphene-based josephson junction. *Physical Review Letters*, 107(14):146605, September 2011. ISSN 1079-7114. doi: 10.1103/physrevlett.107.146605.

[103] J. C. Fenton and P. A. Warburton. Monte carlo simulations of thermal fluctuations in moderately damped Josephson junctions: Multiple escape and retrapping, switching- and return-current distributions, and hysteresis. *Phys. Rev. B*, 78:054526, Aug 2008. doi: 10.1103/PhysRevB.78.054526. URL `https://link.aps.org/doi/10.1103/PhysRevB.78.054526`.

[104] A. F. Andreev. Electron spectrum of the intermediate state of superconductors. *Sov. Phys. - JETP (Engl. Transl.)*, Vol: 49, 08 1965.

[105] I. O. Kulik. Macroscopic quantization and the proximity effect in sns junctions. *Sov. Phys. - JETP (Engl. Transl.)*, Vol: 30, 05 1970.

[106] Elsa Prada, Pablo San-Jose, Michiel W. A. de Moor, Attila Geresdi, Eduardo J. H. Lee, Jelena Klinovaja, Daniel Loss, Jesper Nygård, Ramón Aguado, and Leo P. Kouwenhoven. From andreev to majorana bound states in hybrid superconductor–semiconductor nanowires. *Nature Reviews Physics*, 2(10):575–594, September 2020. ISSN 2522-5820. doi: 10.1038/s42254-020-0228-y.

[107] A. A. Golubov, M. Yu. Kupriyanov, and E. Il'ichev. The current-phase relation in josephson junctions. *Reviews of Modern Physics*, 76(2):411–469, April 2004. ISSN 1539-0756. doi: 10.1103/revmodphys.76.411.

[108] R. Haller, G. Fülöp, D. Indolese, J. Ridderbos, R. Kraft, L. Y. Cheung, J. H. Ungerer, K. Watanabe, T. Taniguchi, D. Beckmann, R. Danneau, P. Virtanen, and C. Schönenberger. Phase-dependent microwave response of a graphene josephson junction. *Physical Review Research*, 4(1):013198, March 2022. ISSN 2643-1564. doi: 10.1103/physrevresearch.4.013198.

[109] Asbjørn Rasmussen, Jeroen Danon, Henri Suominen, Fabrizio Nichele, Morten Kjaergaard, and Karsten Flensberg. Effects of spin-orbit coupling and spatial symmetries on the josephson current in sns junctions. *Physical Review B*, 93(15):155406, April 2016. ISSN 2469-9969. doi: 10.1103/physrevb.93.155406.

[110] D. B. Szombati, S. Nadj-Perge, D. Car, S. R. Plissard, E. P. A. M. Bakkers, and L. P. Kouwenhoven. Josephson 0-junction in nanowire quantum dots. *Nature Physics*, 12(6):568–572, May 2016. ISSN 1745-2481. doi: 10.1038/nphys3742.

[111] Alexandre Assouline, Cheryl Feuillet-Palma, Nicolas Bergeal, Tianzhen Zhang, Alireza Mottaghizadeh, Alexandre Zimmers, Emmanuel Lhuillier, Mahmoud Eddrie, Paola Atkinson, Marco Aprili, and Hervé Aubin. Spin-orbit induced phase-shift in bi2se3 josephson junctions. *Nature Communications*, 10(1), January 2019. ISSN 2041-1723. doi: 10.1038/s41467-018-08022-y.

[112] S. Reinhardt, T. Ascherl, A. Costa, J. Berger, S. Gronin, G. C. Gardner, T. Lindemann, M. J. Manfra, J. Fabian, D. Kochan, C. Strunk, and N. Paradiso. Link between supercurrent diode and anomalous josephson effect revealed by gate-controlled

interferometry. *Nature Communications*, 15(1), May 2024. ISSN 2041-1723. doi: 10.1038/s41467-024-48741-z.

[113] Muhammad Nadeem, Michael S. Fuhrer, and Xiaolin Wang. The superconducting diode effect. *Nature Reviews Physics*, 5(10):558–577, September 2023. ISSN 2522-5820. doi: 10.1038/s42254-023-00632-w.

[114] Christian Baumgartner, Lorenz Fuchs, Andreas Costa, Simon Reinhardt, Sergei Gronin, Geoffrey C. Gardner, Tyler Lindemann, Michael J. Manfra, Paulo E. Faria Junior, Denis Kochan, Jaroslav Fabian, Nicola Paradiso, and Christoph Strunk. Supercurrent rectification and magnetochiral effects in symmetric josephson junctions. *Nature Nanotechnology*, 17(1):39–44, November 2021. ISSN 1748-3395. doi: 10.1038/s41565-021-01009-9.

[115] Kun-Rok Jeon, Jae-Keun Kim, Jiho Yoon, Jae-Chun Jeon, Hyeon Han, Audrey Cottet, Takis Kontos, and Stuart S. P. Parkin. Zero-field polarity-reversible josephson supercurrent diodes enabled by a proximity-magnetized pt barrier. *Nature Materials*, 21(9): 1008–1013, July 2022. ISSN 1476-4660. doi: 10.1038/s41563-022-01300-7.

[116] Heng Wu, Yaojia Wang, Yuanfeng Xu, Pranava K. Sivakumar, Chris Pasco, Ulderico Filippozzi, Stuart S. P. Parkin, Yu-Jia Zeng, Tyrel McQueen, and Mazhar N. Ali. The field-free josephson diode in a van der waals heterostructure. *Nature*, 604(7907):653–656, April 2022. ISSN 1476-4687. doi: 10.1038/s41586-022-04504-8.

[117] Lorenz Bauriedl, Christian Bäuml, Lorenz Fuchs, Christian Baumgartner, Nicolas Paulik, Jonas M. Bauer, Kai-Qiang Lin, John M. Lupton, Takashi Taniguchi, Kenji Watanabe, Christoph Strunk, and Nicola Paradiso. Supercurrent diode effect and magnetochiral anisotropy in few-layer nbse2. *Nature Communications*, 13(1), July 2022. ISSN 2041-1723. doi: 10.1038/s41467-022-31954-5.

[118] Banabir Pal, Anirban Chakraborty, Pranava K. Sivakumar, Margarita Davydova, Ajesh K. Gopi, Avanindra K. Pandeya, Jonas A. Krieger, Yang Zhang, Mihir Date, Sailong Ju, Noah Yuan, Niels B. M. Schröter, Liang Fu, and Stuart S. P. Parkin. Josephson diode effect from cooper pair momentum in a topological semimetal. *Nature Physics*, 18(10): 1228–1233, August 2022. ISSN 1745-2481. doi: 10.1038/s41567-022-01699-5.

[119] J. Díez-Mérida, A. Díez-Carlón, S. Y. Yang, Y.-M. Xie, X.-J. Gao, J. Senior, K. Watanabe, T. Taniguchi, X. Lu, A. P. Higginbotham, K. T. Law, and Dmitri K. Efetov. Symmetry-broken josephson junctions and superconducting diodes in magic-angle twisted bilayer graphene. *Nature Communications*, 14(1), April 2023. ISSN 2041-1723. doi: 10.1038/s41467-023-38005-7.

[120] Bianca Turini, Sedighe Salimian, Matteo Carrega, Andrea Iorio, Elia Strambini, Francesco Giazotto, Valentina Zannier, Lucia Sorba, and Stefan Heun. Josephson diode effect in high-mobility insb nanoflags. *Nano Letters*, 22(21):8502–8508, October 2022. ISSN 1530-6992. doi: 10.1021/acs.nanolett.2c02899.

[121] R. C. Jaklevic, John Lambe, A. H. Silver, and J. E. Mercereau. Quantum interference effects in josephson tunneling. *Physical Review Letters*, 12(7):159–160, February 1964. ISSN 0031-9007. doi: 10.1103/physrevlett.12.159.

[122] R. C. Black, A. Mathai, F. C. Wellstood, E. Dantsker, A. H. Miklich, D. T. Nemeth, J. J. Kingston, and J. Clarke. Magnetic microscopy using a liquid nitrogen cooled yba2cu3o7 superconducting quantum interference device. *Applied Physics Letters*, 62(17):2128–2130, April 1993. ISSN 1077-3118. doi: 10.1063/1.109448.

[123] David Cohen. Magnetoencephalography: Evidence of magnetic fields produced by alpha-rhythm currents. *Science*, 161(3843):784–786, August 1968. ISSN 1095-9203. doi: 10.1126/science.161.3843.784.

[124] M. L. Della Rocca, M. Chauvin, B. Huard, H. Pothier, D. Esteve, and C. Urbina. Measurement of the current-phase relation of superconducting atomic contacts. *Physical Review Letters*, 99(12):127005, September 2007. ISSN 1079-7114. doi: 10.1103/physrevlett.99.127005.

[125] Gil-Ho Lee, Sol Kim, Seung-Hoon Jhi, and Hu-Jong Lee. Ultimately short ballistic vertical graphene josephson junctions. *Nature Communications*, 6(1), January 2015. ISSN 2041-1723. doi: 10.1038/ncomms7181.

[126] Anil Murani, Alik Kasumov, Shamashis Sengupta, Yu A. Kasumov, V. T. Volkov, I. I. Khodos, F. Brisset, Raphaëlle Delagrange, Alexei Chepelianskii, Richard Deblock, Hélène Bouchiat, and Sophie Guéron. Ballistic edge states in bismuth nanowires revealed by squid interferometry. *Nature Communications*, 8(1), July 2017. ISSN 2041-1723. doi: 10.1038/ncomms15941.

[127] G. Nanda, J. L. Aguilera-Servin, P. Rakyta, A. Kormányos, R. Kleiner, D. Koelle, K. Watanabe, T. Taniguchi, L. M. K. Vandersypen, and S. Goswami. Current-phase relation of ballistic graphene josephson junctions. *Nano Letters*, 17(6):3396–3401, May 2017. ISSN 1530-6992. doi: 10.1021/acs.nanolett.7b00097.

[128] F. Nichele, E. Portolés, A. Fornieri, A.M. Whiticar, A.C.C. Drachmann, S. Gronin, T. Wang, G.C. Gardner, C. Thomas, A.T. Hatke, M.J. Manfra, and C.M. Marcus. Relating andreev bound states and supercurrents in hybrid josephson junctions. *Physical Review Letters*, 124(22):226801, June 2020. ISSN 1079-7114. doi: 10.1103/physrevlett.124.226801.

[129] Morteza Kayyalha, Mehdi Kargarian, Aleksandr Kazakov, Ireneusz Miotkowski, Victor M. Galitski, Victor M. Yakovenko, Leonid P. Rokhinson, and Yong P. Chen. Anomalous low-temperature enhancement of supercurrent in topological-insulator nanoribbon josephson junctions: Evidence for low-energy andreev bound states. *Physical Review Letters*, 122 (4):047003, February 2019. ISSN 1079-7114. doi: 10.1103/physrevlett.122.047003.

[130] Ian Babich, Andrei Kudriashov, Denis Baranov, and Vasily S. Stolyarov. Limitations of the current–phase relation measurements by an asymmetric dc-squid. *Nano Letters*, 23 (14):6713–6719, July 2023. ISSN 1530-6992. doi: 10.1021/acs.nanolett.3c01970.

[131] Erik Eriksson, Roman-Pascal Riwar, Manuel Houzet, Julia S. Meyer, and Yuli V. Nazarov. Topological transconductance quantization in a four-terminal Josephson junction. *Phys. Rev. B*, 95:075417, Feb 2017. doi: 10.1103/PhysRevB.95.075417. URL `https://link.aps.org/doi/10.1103/PhysRevB.95.075417`.

[132] Manuel Houzet and Julia S. Meyer. Majorana-weyl crossings in topological multiterminal junctions. *Phys. Rev. B*, 100:014521, Jul 2019. doi: 10.1103/PhysRevB.100.014521. URL `https://link.aps.org/doi/10.1103/PhysRevB.100.014521`.

[133] Hong-Yi Xie, Maxim G. Vavilov, and Alex Levchenko. Topological Andreev bands in three-terminal Josephson junctions. *Phys. Rev. B*, 96:161406(R), Oct 2017. doi: 10.1103/PhysRevB.96.161406. URL `https://link.aps.org/doi/10.1103/PhysRevB.96.161406`.

[134] Hong-Yi Xie, Maxim G. Vavilov, and Alex Levchenko. Weyl nodes in Andreev spectra of multiterminal Josephson junctions: Chern numbers, conductances, and supercurrents.

Phys. Rev. B, 97:035443, Jan 2018. doi: 10.1103/PhysRevB.97.035443. URL https://link.aps.org/doi/10.1103/PhysRevB.97.035443.

[135] Hong-Yi Xie, Jaglul Hasan, and Alex Levchenko. Non-abelian monopoles in the multiterminal Josephson effect. *Phys. Rev. B*, 105:L241404, Jun 2022. doi: 10.1103/PhysRevB.105.L241404. URL https://link.aps.org/doi/10.1103/PhysRevB.105.L241404.

[136] Julia S. Meyer and Manuel Houzet. Nontrivial Chern numbers in three-terminal Josephson junctions. *Phys. Rev. Lett.*, 119:136807, Sep 2017. doi: 10.1103/PhysRevLett.119.136807. URL https://link.aps.org/doi/10.1103/PhysRevLett.119.136807.

[137] Oindrila Deb, K. Sengupta, and Diptiman Sen. Josephson junctions of multiple superconducting wires. *Phys. Rev. B*, 97:174518, May 2018. doi: 10.1103/PhysRevB.97.174518. URL https://link.aps.org/doi/10.1103/PhysRevB.97.174518.

[138] Lucila Peralta Gavensky, Gonzalo Usaj, D. Feinberg, and C. A. Balseiro. Berry curvature tomography and realization of topological Haldane model in driven three-terminal Josephson junctions. *Physical Review B*, 97(22):220505(R), June 2018. ISSN 2469-9969. doi: 10.1103/physrevb.97.220505.

[139] R.L. Klees, G. Rastelli, J.C. Cuevas, and W. Belzig. Microwave spectroscopy reveals the quantum geometric tensor of topological Josephson matter. *Physical Review Letters*, 124 (19):197002, May 2020. ISSN 1079-7114. doi: 10.1103/physrevlett.124.197002.

[140] Valla Fatemi, Anton R. Akhmerov, and Landry Bretheau. Weyl Josephson circuits. *Physical Review Research*, 3(1):013288, March 2021. ISSN 2643-1564. doi: 10.1103/physrevresearch.3.013288.

[141] L. Peyruchat, J. Griesmar, J.-D. Pillet, and Ç. Ö. Girit. Transconductance quantization in a topological Josephson tunnel junction circuit. *Phys. Rev. Res.*, 3:013289, Mar 2021. doi: 10.1103/PhysRevResearch.3.013289. URL https://link.aps.org/doi/10.1103/PhysRevResearch.3.013289.

[142] H. Weisbrich, R.L. Klees, G. Rastelli, and W. Belzig. Second chern number and non-abelian berry phase in topological superconducting systems. *PRX Quantum*, 2(1):010310, January 2021. ISSN 2691-3399. doi: 10.1103/prxquantum.2.010310.

[143] Y. Chen and Y. V. Nazarov. Weyl point immersed in a continuous spectrum: An example from superconducting nanostructures. *Physical Review B*, 104(10):104506, September 2021. ISSN 2469-9969. doi: 10.1103/physrevb.104.104506.

[144] Y. Chen and Y. V. Nazarov. Spin Weyl quantum unit: A theoretical proposal. *Physical Review B*, 103(4):045410, January 2021. ISSN 2469-9969. doi: 10.1103/physrevb.103.045410.

[145] E. V. Repin and Y. V. Nazarov. Weyl points in multiterminal hybrid superconductor-semiconductor nanowire devices. *Phys. Rev. B*, 105:L041405, Jan 2022. doi: 10.1103/PhysRevB.105.L041405. URL https://link.aps.org/doi/10.1103/PhysRevB.105.L041405.

[146] Lucila Peralta Gavensky, Gonzalo Usaj, and C. A. Balseiro. Multi-terminal Josephson junctions: A road to topological flux networks. *Europhysics Letters*, 141(3):36001, January 2023. ISSN 1286-4854. doi: 10.1209/0295-5075/acb2f6.

[147] M. Coraiola, D. Z. Haxell, D. Sabonis, M. Hinderling, S. C. ten Kate, E. Cheah, F. Krizek, R. Schott, W. Wegscheider, and F. Nichele. Spin-degeneracy breaking and parity transitions in three-terminal Josephson junctions. *arXiv (Condensed Matter, Mesoscale and Nanoscale Physics)*, July 2023. doi: 10.48550/ARXIV.2307.06715. 13 July, 2023, `https://arxiv.org/abs/2307.06715` (accessed 2024-05-21).

[148] Sadashige Matsuo, Joon Sue Lee, Chien-Yuan Chang, Yosuke Sato, Kento Ueda, Christopher J. Palmstrøm, and Seigo Tarucha. Observation of nonlocal josephson effect on double inas nanowires. *Communications Physics*, 5(1), September 2022. ISSN 2399-3650. doi: 10.1038/s42005-022-00994-0.

[149] Sadashige Matsuo, Takaya Imoto, Tomohiro Yokoyama, Yosuke Sato, Tyler Lindemann, Sergei Gronin, Geoffrey C. Gardner, Sho Nakosai, Yukio Tanaka, Michael J. Manfra, and Seigo Tarucha. Phase-dependent andreev molecules and superconducting gap closing in coherently-coupled josephson junctions. *Nature Communications*, 14(1), December 2023. ISSN 2041-1723. doi: 10.1038/s41467-023-44111-3.

[150] Sadashige Matsuo, Takaya Imoto, Tomohiro Yokoyama, Yosuke Sato, Tyler Lindemann, Sergei Gronin, Geoffrey C. Gardner, Michael J. Manfra, and Seigo Tarucha. Josephson diode effect derived from short-range coherent coupling. *Nature Physics*, 19(11):1636–1641, July 2023. ISSN 1745-2481. doi: 10.1038/s41567-023-02144-x.

[151] M. P. Nowak, M. Wimmer, and A. R. Akhmerov. Supercurrent carried by nonequilibrium quasiparticles in a multiterminal Josephson junction. *Physical Review B*, 99(7):075416, feb 2019. doi: 10.1103/physrevb.99.075416.

[152] Régis Mélin, Romain Danneau, Kang Yang, Jean-Guy Caputo, and Benoît Douçot. Engineering the Floquet spectrum of superconducting multiterminal quantum dots. *Phys. Rev. B*, 100:035450, Jul 2019. doi: 10.1103/PhysRevB.100.035450. URL `https://link.aps.org/doi/10.1103/PhysRevB.100.035450`.

[153] Régis Mélin. Inversion in a four-terminal superconducting device on the quartet line. I. Two-dimensional metal and the quartet beam splitter. *Phys. Rev. B*, 102:245435, Dec 2020. doi: 10.1103/PhysRevB.102.245435. URL `https://link.aps.org/doi/10.1103/PhysRevB.102.245435`.

[154] Régis Mélin, Romain Danneau, and Clemens B. Winkelmann. Proposal for detecting the π-shifted Cooper quartet supercurrent. *Phys. Rev. Res.*, 5:033124, Aug 2023. doi: 10.1103/PhysRevResearch.5.033124. URL `https://link.aps.org/doi/10.1103/PhysRevResearch.5.033124`.

[155] Benoît Douçot, Romain Danneau, Kang Yang, Jean-Guy Caputo, and Régis Mélin. Berry phase in superconducting multiterminal quantum dots. *Phys. Rev. B*, 101:035411, Jan 2020. doi: 10.1103/PhysRevB.101.035411. URL `https://link.aps.org/doi/10.1103/PhysRevB.101.035411`.

[156] André Melo, Valla Fatemi, and Anton Akhmerov. Multiplet supercurrent in Josephson tunneling circuits. *SciPost Physics*, 12(1), January 2022. ISSN 2542-4653. doi: 10.21468/scipostphys.12.1.017.

[157] A. H. Pfeffer, J. E. Duvauchelle, H. Courtois, R. Mélin, D. Feinberg, and F. Lefloch. Subgap structure in the conductance of a three-terminal Josephson junction. *Phys. Rev. B*, 90:075401, Aug 2014. doi: 10.1103/PhysRevB.90.075401. URL `https://link.aps.org/doi/10.1103/PhysRevB.90.075401`.

[158] Yonatan Cohen, Yuval Ronen, Jung-Hyun Kang, Moty Heiblum, Denis Feinberg, Régis Mélin, and Hadas Shtrikman. Nonlocal supercurrent of quartets in a three-terminal Josephson junction. *Proceedings of the National Academy of Sciences*, 115(27):6991–6994, June 2018. ISSN 1091-6490. doi: 10.1073/pnas.1800044115.

[159] Ethan G. Arnault, Sara Idris, Aeron McConnell, Lingfei Zhao, Trevyn F.Q. Larson, Kenji Watanabe, Takashi Taniguchi, Gleb Finkelstein, and François Amet. Dynamical stabilization of multiplet supercurrents in multiterminal Josephson junctions. *Nano Letters*, 22(17):7073–7079, aug 2022. doi: 10.1021/acs.nanolett.2c01999.

[160] Gino V. Graziano, Mohit Gupta, Mihir Pendharkar, Jason T. Dong, Connor P. Dempsey, Chris Palmstrøm, and Vlad S. Pribiag. Selective control of conductance modes in multiterminal Josephson junctions. *Nature Communications*, 13(1), oct 2022. doi: 10.1038/s41467-022-33682-2.

[161] Ko-Fan Huang, Yuval Ronen, Régis Mélin, Denis Feinberg, Kenji Watanabe, Takashi Taniguchi, and Philip Kim. Evidence for 4e charge of Cooper quartets in a biased multiterminal graphene-based Josephson junction. *Nature Communications*, 13(1), may 2022. doi: 10.1038/s41467-022-30732-7.

[162] John Chiles, Ethan G. Arnault, Chun-Chia Chen, Trevyn F. Q. Larson, Lingfei Zhao, Kenji Watanabe, Takashi Taniguchi, François Amet, and Gleb Finkelstein. Nonreciprocal supercurrents in a field-free graphene Josephson triode. *Nano Letters*, 23(11):5257–5263, may 2023. doi: 10.1021/acs.nanolett.3c01276.

[163] Mohit Gupta, Gino V. Graziano, Mihir Pendharkar, Jason T. Dong, Connor P. Dempsey, Chris Palmstrøm, and Vlad S. Pribiag. Gate-tunable superconducting diode effect in a three-terminal Josephson device. *Nature Communications*, 14(1), may 2023. doi: 10.1038/s41467-023-38856-0.

[164] Sadashige Matsuo, Takaya Imoto, Tomohiro Yokoyama, Yosuke Sato, Tyler Lindemann, Sergei Gronin, Geoffrey C. Gardner, Michael J. Manfra, and Seigo Tarucha. Phase engineering of anomalous josephson effect derived from andreev molecules. *Science Advances*, 9(50), December 2023. ISSN 2375-2548. doi: 10.1126/sciadv.adj3698.

[165] Marco Coraiola, Aleksandr E. Svetogorov, Daniel Z. Haxell, Deividas Sabonis, Manuel Hinderling, Sofieke C. ten Kate, Erik Cheah, Filip Krizek, Rüdiger Schott, Werner Wegscheider, Juan Carlos Cuevas, Wolfgang Belzig, and Fabrizio Nichele. Flux-tunable josephson diode effect in a hybrid four-terminal josephson junction. *ACS Nano*, 18 (12):9221–9231, 2024. doi: 10.1021/acsnano.4c01642. URL `https://doi.org/10.1021/acsnano.4c01642`. PMID: 38488287.

[166] Anne W. Draelos, Ming-Tso Wei, Andrew Seredinski, Hengming Li, Yash Mehta, Kenji Watanabe, Takashi Taniguchi, Ivan V. Borzenets, François Amet, and Gleb Finkelstein. Supercurrent flow in multiterminal graphene Josephson junctions. *Nano Letters*, 19(2): 1039–1043, jan 2019. doi: 10.1021/acs.nanolett.8b04330.

[167] Jonas Kölzer, Abdur Rehman Jalil, Daniel Rosenbach, Lisa Arndt, Gregor Mussler, Peter Schüffelgen, Detlev Grützmacher, Hans Lüth, and Thomas Schäpers. Supercurrent in Bi_4Te_3 topological material-based three-terminal junctions. *arXiv (Condensed Matter, Superconductivity)*, January 2023. doi: 10.48550/ARXIV.2301.01115. 3 January, 2023, `https://arxiv.org/abs/2301.01115` (accessed 2024-05-21).

[168] Fan Zhang, Asmaul Smitha Rashid, Mostafa Tanhayi Ahari, Wei Zhang, Krishnan Mekkanamkulam Ananthanarayanan, Run Xiao, George J. de Coster, Matthew J.

Gilbert, Nitin Samarth, and Morteza Kayyalha. Andreev processes in mesoscopic multi-terminal graphene Josephson junctions. *Physical Review B*, 107(14):L140503, apr 2023. doi: 10.1103/physrevb.107.l140503.

[169] Thomas C. Achee, Wanmei Sun, Joshua T. Hope, Samuel G. Quitzau, Charles Brandon Sweeney, Smit A. Shah, Touseef Habib, and Micah J. Green. High-yield scalable graphene nanosheet production from compressed graphite using electrochemical exfoliation. *Scientific Reports*, 8(1), September 2018. ISSN 2045-2322. doi: 10.1038/s41598-018-32741-3.

[170] Keith R. Paton, Eswaraiah Varrla, Claudia Backes, Ronan J. Smith, Umar Khan, Arlene O'Neill, Conor Boland, Mustafa Lotya, Oana M. Istrate, Paul King, Tom Higgins, Sebastian Barwich, Peter May, Pawel Puczkarski, Iftikhar Ahmed, Matthias Moebius, Henrik Pettersson, Edmund Long, João Coelho, Sean E. O'Brien, Eva K. McGuire, Beatriz Mendoza Sanchez, Georg S. Duesberg, Niall McEvoy, Timothy J. Pennycook, Clive Downing, Alison Crossley, Valeria Nicolosi, and Jonathan N. Coleman. Scalable production of large quantities of defect-free few-layer graphene by shear exfoliation in liquids. *Nature Materials*, 13(6):624–630, April 2014. ISSN 1476-4660. doi: 10.1038/nmat3944.

[171] Md. Anamul Hoque, Antony George, Vasudev Ramachandra, Emad Najafidehaghani, Ziyang Gan, Richa Mitra, Bing Zhao, Satyaprakash Sahoo, Maria Abrahamsson, Qiuhua Liang, Julia Wiktor, Andrey Turchanin, Sergey Kubatkin, Samuel Lara-Avila, and Saroj P. Dash. All-2d cvd-grown semiconductor field-effect transistors with van der waals graphene contacts. *npj 2D Materials and Applications*, 8(1), August 2024. ISSN 2397-7132. doi: 10.1038/s41699-024-00489-2.

[172] P. Blake, E. W. Hill, A. H. Castro Neto, K. S. Novoselov, D. Jiang, R. Yang, T. J. Booth, and A. K. Geim. Making graphene visible. *Applied Physics Letters*, 91(6), August 2007. ISSN 1077-3118. doi: 10.1063/1.2768624.

[173] Mikhail N. Polyanskiy. Refractiveindex.info database of optical constants. *Scientific Data*, 11(1), January 2024. ISSN 2052-4463. doi: 10.1038/s41597-023-02898-2.

[174] L. Wang, I. Meric, P. Y. Huang, Q. Gao, Y. Gao, H. Tran, T. Taniguchi, K. Watanabe, L. M. Campos, D. A. Muller, J. Guo, P. Kim, J. Hone, K. L. Shepard, and C. R. Dean. One-dimensional electrical contact to a two-dimensional material. *Science*, 342(6158): 614–617, November 2013. ISSN 1095-9203. doi: 10.1126/science.1244358.

[175] Mei-Yan Tian, Yu-Meng Gao, Yue-Jiao Zhang, Meng-Xue Ren, Xiao-Huan Lv, Ke-Xin Hou, Chen-Dong Jin, Hu Zhang, Ru-Qian Lian, Peng-Lai Gong, Rui-Ning Wang, Jiang-Long Wang, and Xing-Qiang Shi. Toward direct band gaps in typical 2d transition-metal dichalcogenides junctions via real and energy spaces tuning. *Communications Materials*, 5(1), September 2024. ISSN 2662-4443. doi: 10.1038/s43246-024-00631-z.

[176] D. G. Purdie, N. M. Pugno, T. Taniguchi, K. Watanabe, A. C. Ferrari, and A. Lombardo. Cleaning interfaces in layered materials heterostructures. *Nature Communications*, 9(1), December 2018. ISSN 2041-1723. doi: 10.1038/s41467-018-07558-3.

[177] Satoru Masubuchi, Masataka Morimoto, Sei Morikawa, Momoko Onodera, Yuta Asakawa, Kenji Watanabe, Takashi Taniguchi, and Tomoki Machida. Autonomous robotic searching and assembly of two-dimensional crystals to build van der waals superlattices. *Nature Communications*, 9(1), April 2018. ISSN 2041-1723. doi: 10.1038/s41467-018-03723-w.

[178] Bálint Fülöp. *Van der Waals heterostructures: from fabrication to hydrostatic pressure experiments*. PhD thesis, Budapest University of Technology and Economics, 2022.

[179] Tosson Elalaily, Martin Berke, Máté Kedves, Gergő Fülöp, Zoltán Scherübl, Thomas Kanne, Jesper Nygård, Péter Makk, and Szabolcs Csonka. Signatures of gate-driven out-of-equilibrium superconductivity in ta/inas nanowires. *ACS Nano*, 17(6):5528–5535, March 2023. ISSN 1936-086X. doi: 10.1021/acsnano.2c10877.

[180] Edward McCann and Vladimir I. Fal'ko. $z \rightarrow -z$ symmetry of spin-orbit coupling and weak localization in graphene. *Phys. Rev. Lett.*, 108:166606, Apr 2012. doi: 10.1103/PhysRevLett.108.166606. URL `https://link.aps.org/doi/10.1103/PhysRevLett.108.166606`.

[181] Matthew Yankowitz, Jeil Jung, Evan Laksono, Nicolas Leconte, Bheema L Chittari, K Watanabe, T Taniguchi, Shaffique Adam, David Graf, and Cory R Dean. Dynamic band-structure tuning of graphene moiré superlattices with pressure. *Nature*, 557:404–408, 5 2018. doi: 10.1038/s41586-018-0107-1.

[182] Stephen Carr, Shiang Fang, Pablo Jarillo-Herrero, and Efthimios Kaxiras. Pressure dependence of the magic twist angle in graphene superlattices. *Physical Review B*, 98(8): 085144, aug 2018. doi: 10.1103/physrevb.98.085144.

[183] Mengqiao Sui, Guorui Chen, Liguo Ma, Wen-Yu Shan, Dai Tian, Kenji Watanabe, Takashi Taniguchi, Xiaofeng Jin, Wang Yao, Di Xiao, and Yuanbo Zhang. Gate-tunable topological valley transport in bilayer graphene. *Nature Physics*, 11:1027–1031, 12 2015. ISSN 1745-2473. doi: 10.1038/nphys3485.

[184] K. S. Novoselov, E. McCann, S. V. Morozov, V. I. Fal'ko, M. I. Katsnelson, U. Zeitler, D. Jiang, F. Schedin, and A. K. Geim. Unconventional quantum hall effect and berry's phase of 2π in bilayer graphene. *Nature Physics*, 2(3):177–180, feb 2006. doi: 10.1038/nphys245.

[185] B. M. Hunt, J. I. A. Li, A. A. Zibrov, L. Wang, T. Taniguchi, K. Watanabe, J. Hone, C. R. Dean, M. Zaletel, R. C. Ashoori, and A. F. Young. Direct measurement of discrete valley and orbital quantum numbers in bilayer graphene. *Nature Communications*, 8(1): 948, 10 2017. ISSN 2041-1723. doi: 10.1038/s41467-017-00824-w. URL `https://doi.org/10.1038/s41467-017-00824-w`.

[186] Jun Yong Khoo and Leonid Levitov. Tunable quantum hall edge conduction in bilayer graphene through spin-orbit interaction. *Physical Review B*, 98:115307, 9 2018. doi: 10.1103/physrevb.98.115307.

[187] Sergey Slizovskiy, Aitor Garcia-Ruiz, Alexey I. Berdyugin, Na Xin, Takashi Taniguchi, Kenji Watanabe, Andre K. Geim, Neil D. Drummond, and Vladimir I. Fal'ko. Out-of-plane dielectric susceptibility of graphene in twistronic and bernal bilayers. *Nano Letters*, 21(15):6678–6683, jul 2021. doi: 10.1021/acs.nanolett.1c02211.

[188] Ron Bessler, Urs Duerig, and Elad Koren. The dielectric constant of a bilayer graphene interface. *Nanoscale Advances*, 1(5):1702–1706, 2019. doi: 10.1039/c8na00350e.

[189] Javier D. Sanchez-Yamagishi, Jason Y. Luo, Andrea F. Young, Benjamin M. Hunt, Kenji Watanabe, Takashi Taniguchi, Raymond C. Ashoori, and Pablo Jarillo-Herrero. Helical edge states and fractional quantum hall effect in a graphene electron–hole bilayer. *Nature Nanotechnology*, 12(2):118–122, oct 2016. doi: 10.1038/nnano.2016.214.

[190] Louis Veyrat, Corentin Déprez, Alexis Coissard, Xiaoxi Li, Frédéric Gay, Kenji Watanabe, Takashi Taniguchi, Zheng Han, Benjamin A. Piot, Hermann Sellier, and Benjamin Sacépé. Helical quantum hall phase in graphene on srtio$_3$. *Science*, 367(6479):781–786, feb 2020. doi: 10.1126/science.aax8201.

[191] Sean Hart, Hechen Ren, Timo Wagner, Philipp Leubner, Mathias Mühlbauer, Christoph Brüne, Hartmut Buhmann, Laurens W. Molenkamp, and Amir Yacoby. Induced superconductivity in the quantum spin hall edge. *Nature Physics*, 10(9):638–643, aug 2014. doi: 10.1038/nphys3036.

[192] Xiao Li, Zhenhua Qiao, Jeil Jung, and Qian Niu. Unbalanced edge modes and topological phase transition in gated trilayer graphene. *Phys. Rev. B*, 85:201404, May 2012. doi: 10.1103/PhysRevB.85.201404. URL `https://link.aps.org/doi/10.1103/PhysRevB.85.201404`.

[193] V. E. Calado, S. Goswami, G. Nanda, M. Diez, A. R. Akhmerov, K. Watanabe, T. Taniguchi, T. M. Klapwijk, and L. M. K. Vandersypen. Ballistic Josephson junctions in edge-contacted graphene. *Nature Nanotechnology*, 10(9):761–764, July 2015. ISSN 1748-3395. doi: 10.1038/nnano.2015.156.

[194] Peter Rickhaus, Romain Maurand, Ming-Hao Liu, Markus Weiss, Klaus Richter, and Christian Schönenberger. Ballistic interferences in suspended graphene. *Nature Communications*, 4(1), August 2013. ISSN 2041-1723. doi: 10.1038/ncomms3342.

[195] Clevin Handschin, Péter Makk, Peter Rickhaus, Ming-Hao Liu, K. Watanabe, T. Taniguchi, Klaus Richter, and Christian Schönenberger. Fabry-pérot resonances in a graphene/hbn moiré superlattice. *Nano Letters*, 17(1):328–333, December 2016. ISSN 1530-6992. doi: 10.1021/acs.nanolett.6b04137.

[196] H. J. Suominen, J. Danon, M. Kjaergaard, K. Flensberg, J. Shabani, C. J. Palmstrøm, F. Nichele, and C. M. Marcus. Anomalous fraunhofer interference in epitaxial superconductor-semiconductor josephson junctions. *Phys. Rev. B*, 95:035307, Jan 2017. doi: 10.1103/PhysRevB.95.035307. URL `https://link.aps.org/doi/10.1103/PhysRevB.95.035307`.

[197] Simon Zihlmann, Péter Makk, Mirko K. Rehmann, Lujun Wang, Máté Kedves, David I. Indolese, Kenji Watanabe, Takashi Taniguchi, Dominik M. Zumbühl, and Christian Schönenberger. Out-of-plane corrugations in graphene based van der waals heterostructures. *Phys. Rev. B*, 102:195404, Nov 2020. doi: 10.1103/PhysRevB.102.195404. URL `https://link.aps.org/doi/10.1103/PhysRevB.102.195404`.

[198] William Mayer, Matthieu C. Dartiailh, Joseph Yuan, Kaushini S. Wickramasinghe, Enrico Rossi, and Javad Shabani. Gate controlled anomalous phase shift in al/inas josephson junctions. *Nature Communications*, 11(1), January 2020. ISSN 2041-1723. doi: 10.1038/s41467-019-14094-1.

[199] Claudia D. Tesche and John Clarke. dc SQUID: Noise and optimization. *Journal of Low Temperature Physics*, 29(3-4):301–331, nov 1977. ISSN 1573-7357. doi: 10.1007/bf00655097.

[200] Rudolf Gross and Achim Marx. Lecture notes on applied superconductivity, October 2005. URL `https://www.wmi.badw.de/teaching/lecture-notes`.

[201] Marco Coraiola, Daniel Z. Haxell, Deividas Sabonis, Hannes Weisbrich, Aleksandr E. Svetogorov, Manuel Hinderling, Sofieke C. ten Kate, Erik Cheah, Filip Krizek, Rüdiger Schott, Werner Wegscheider, Juan Carlos Cuevas, Wolfgang Belzig, and Fabrizio Nichele. Phase-engineering the Andreev band structure of a three-terminal Josephson junction. *Nature Communications*, 14(1):6784, 2023. ISSN 2041-1723. doi: 10.1038/s41467-023-42356-6. URL `https://doi.org/10.1038/s41467-023-42356-6`.

[202] E. Strambini, S. D'Ambrosio, F. Vischi, F. S. Bergeret, Yu. V. Nazarov, and F. Giazotto. The ω-SQUIPT as a tool to phase-engineer Josephson topological materials. *Nature Nanotechnology*, 11(12):1055–1059, sep 2016. doi: 10.1038/nnano.2016.157.

[203] Natalia Pankratova, Hanho Lee, Roman Kuzmin, Kaushini Wickramasinghe, William Mayer, Joseph Yuan, Maxim G. Vavilov, Javad Shabani, and Vladimir E. Manucharyan. Multiterminal Josephson effect. *Phys. Rev. X*, 10:031051, Sep 2020. doi: 10.1103/PhysRevX.10.031051. URL https://link.aps.org/doi/10.1103/PhysRevX.10.031051.

[204] Ethan G. Arnault, Trevyn F. Q. Larson, Andrew Seredinski, Lingfei Zhao, Sara Idris, Aeron McConnell, Kenji Watanabe, Takashi Taniguchi, Ivan Borzenets, François Amet, and Gleb Finkelstein. Multiterminal inverse AC Josephson effect. *Nano Letters*, 21(22): 9668–9674, nov 2021. doi: 10.1021/acs.nanolett.1c03474.

[205] Christopher B. McKitterick, Daniel E. Prober, and Michael J. Rooks. Electron-phonon cooling in large monolayer graphene devices. *Phys. Rev. B*, 93:075410, Feb 2016. doi: 10.1103/PhysRevB.93.075410. URL https://link.aps.org/doi/10.1103/PhysRevB.93.075410.

[206] D. Z. Haxell, E. Cheah, F. Křížek, R. Schott, M. F. Ritter, M. Hinderling, W. Belzig, C. Bruder, W. Wegscheider, H. Riel, and F. Nichele. Measurements of phase dynamics in planar Josephson junctions and SQUIDs. *Phys. Rev. Lett.*, 130:087002, Feb 2023. doi: 10.1103/PhysRevLett.130.087002. URL https://link.aps.org/doi/10.1103/PhysRevLett.130.087002.

[207] I. V. Borzenets, F. Amet, C. T. Ke, A. W. Draelos, M. T. Wei, A. Seredinski, K. Watanabe, T. Taniguchi, Y. Bomze, M. Yamamoto, S. Tarucha, and G Finkelstein. Ballistic graphene josephson junctions from the short to the long regime. *Phys. Rev. Lett. 117, 237002 (2016)*, 117(23):237002, dec 2016. doi: 10.1103/physrevlett.117.237002. URL https://link.aps.org/doi/10.1103/PhysRevLett.117.237002.